Realization of Rydberg-dressed quantum magnets

Johannes Zeiher

München 2017

Realization of Rydberg-dressed quantum magnets

Johannes Zeiher

Dissertation
an der Fakultät für Physik
der Ludwig–Maximilians–Universität
München

vorgelegt von
JOHANNES ZEIHER
aus Freiburg i. Br.

München, 02.10.2017

Erstgutachter: Prof. Dr. Immanuel Bloch
Zweitgutachter: Prof. Dr. Thomas Pohl
Tag der mündlichen Prüfung: 20.11.2017

Zusammenfassung

Wechselwirkende, ultrakalte atomare Quantengase bieten ideale Bedingungen für die Untersuchung stark korrelierter Quantenmaterie. Die Wechselwirkungen zwischen Atomen in einem ultrakalten Quantengas sind dabei typischerweise kurzreichweitig und können gut durch ein effektives Kontaktpotential angenähert werden. Länger reichweitige Wechselwirkungen versprechen die Verwirklichung neuartiger Quantenphasen, die in Systemen mit ausschließlich kurzreichweitigen Wechselwirkungen nicht auftreten.
Gefangene, durch Laser an hoch angeregte, stark wechselwirkende Rydberg Zustände gekoppelte Atome sind als vielseitige Systeme zur Realisierung solch langreichweitig wechselwirkender Quantenmaterie vorgeschlagen worden. Im ersten in dieser Arbeit vorgestellten Experiment wurden die Einzelatomempfindlichkeit eines Quantengasmikroskopes sowie die durch diese Technik ermöglichte räumlich aufgelöste Präparation und Detektion kombiniert, um ein im optischen Gitter gefangenes Ensemble von Rubidium-87 Atomen im Grenzfall starker Rydberg Blockade mikroskopisch zu untersuchen. Dabei konnten kollektiv verstärkte Kopplung an das Lichtfeld im Rahmen eines effektiven Zwei-Niveau Systems, dem sogenannten „Superatom", beobachtet, sowie auf das Vorhandensein von Quantenverschränkung geschlossen werden.
Verstimmte optische Kopplung an Rydberg Zustände, „Rydberg dressing" genannt, wurde als alternativer Ansatz zur Erzeugung langreichweitiger Wechselwirkungen vorgeschlagen. Dabei werden, im Gegensatz zur direkten Anregung eines Rydberg Zustandes, die Eigenschaften des letzteren dem Grundzustand beigemischt, welcher in der Folge langreichweitige Wechselwirkungen ausbildet. Im Rahmen dieser Arbeit wurde ein Lasersystem im ultravioletten Spektralbereich entwickelt, um dem Grundzustand von Atomen in einem optischen Gitter Rydberg P-Zustands-Charakter beizumischen. In einem sich ergebenden Ising Quantenmagneten wurden Rydberg-beigemischte Wechelwirkungen mittels Interferometrie kombiniert mit der Messung räumlich aufgelöster Spin Korrelationsfunktionen direkt nachgewiesen. Die theoretisch erwartete Kontrolle über Isotropie sowie Reichweite der Wechselwirkungen konnte dabei experimentell bestätigt werden.
Während diese ersten Messungen noch unerwartet starke Dissipation aufwiesen, konnte letztere in einem nachfolgenden Experiment in einer eindimensionalen Spin-Kette unterdrückt werden. Der Nachweis von verbesserten Kohärenzzeiten gelang dabei durch Messung der Zeitentwicklung der Magnetisierung nach einem plötzlichen Anschalten der Wechselwirkungen sowie der Beobachtung von kohärentem Zerfall gefolgt von einem Wiederaufleben der Magnetisierung – einem wesentlichen Merkmal kohärenter Zeitentwicklung eines Quantensystems. Die vorgestellten Ergebnisse etablieren Rydberg-beigemischte Wechselwirkungen in ultrakalten Gasen und ebnen den Weg zur Realisierung und Untersuchung neuartiger, exotischer Quantenphasen.

Abstract

Interacting ultracold atomic quantum gases provide an ideal test bed to study strongly correlated quantum matter. The interactions between atoms in such an ultracold quantum gas are typically short-ranged and well described by an effective contact potential. Introducing longer-range interactions promises the realization of novel quantum phases which are absent in systems with only short-range interactions.
Trapped atoms, resonantly laser-coupled to highly excited, strongly interacting Rydberg states have been proposed as a versatile platform to realize such long-range interacting quantum matter. In a first experiment presented in this thesis, we combined the single-atom-sensitive local preparation and detection enabled by a quantum gas microscope to prepare and microscopically characterize an ensemble of rubidium-87 atoms trapped in an optical lattice in the regime of strong Rydberg blockade. There, we observe collectively enhanced optical coupling in an effective two-level system, the so-called "superatom", and infer the presence of entanglement.
Detuned optical coupling to Rydberg states, termed "Rydberg dressing", has been proposed as an alternative approach to induce long-range interactions. Rather than directly exciting an atom to a Rydberg state, the properties of the latter are admixed to a ground state, which consequently acquires long-range interactions. In the context of this thesis, we have designed a laser system in the ultraviolet spectral range to admix Rydberg P-state character to the ground state of atoms in an optical lattice. In an emerging Ising quantum magnet, the presence of Rydberg-dressed interactions was demonstrated by an interferometric technique combined with spatially resolved spin correlation measurements. The theoretically predicted tunability of the isotropy and range of the interaction were confirmed experimentally.
While these initial measurements exhibited unexpected dissipation, in a subsequent experiment in a one-dimensional spin chain this dissipation was overcome. We substantiated the improved coherence times by tracking the time evolution of the magnetization upon suddenly switching on interactions and observing coherent collapse and revival dynamics, one of the hallmarks of coherent quantum evolution. Our results establish Rydberg-dressed interactions in ultracold gases and pave the way to realize and study novel exotic quantum phases.

Contents

Chapter 1

Introduction

The first experimental realization of Bose-Einstein condensates in dilute bosonic gases [1, 2] has resulted in an impressive development of the field of ultracold atomic gases in recent years [3, 4]. The availability of well-isolated quantum systems combined with excellent controllability and detection techniques has on the one hand enabled quantum simulations [5] of phenomena occurring in solid state systems, for example the superfluid to Mott insulator transition [6, 7], but on the other hand also proven to be a unique platform for experimentally tackling fundamental theoretical problems like out-of-equilibrium dynamics of closed quantum systems in an unparalleled way [8, 9].
Regarding the detection, the recent advent of quantum gas microscopes for bosonic [10–12] and fermionic species [13–17] has revolutionized the way to extract information from such quantum gases. The direct imaging of single atoms provides single-atom-sensitive measurements as well as access to local observables, enabling for example the study of correlations near the quantum phase transition from the superfluid to the Mott insulator [18, 19], or the discovery of antiferromagnetic correlations in an Ising model [20] and the Hubbard regime of ultracold Fermi gases [21–26]. At the same time, microscopic local control of spin and density of unity-filling Mott insulators with exactly one atom per lattice site was achieved [27], paving the way for studying out-of-equilibrium spin dynamics in low-dimensional spin systems [28, 29] or thermalization in disordered [30] and clean [31] isolated quantum systems.
Interactions between the atoms form an essential cornerstone of the "toolbox" for manipulating ultracold atomic gases [32, 33]. For example, the aforementioned superfluid to Mott insulator transition is driven by a changing ratio of tunnelling and interaction energy [7]. Tunable interactions allowed in further seminal experiments also for reaching the regime of fermionic pairing [34], followed by the observation of condensation and superfluidity of fermion pairs [35]. Here, the tunability of the interactions was achieved by working in the vicinity of magnetic Feshbach resonances [36]. In all of these examples, the interactions at play were short-ranged, well approximated by a contact potential with the scattering length as an associated length scale [3]. Surpassing the established techniques and enriching the available toolbox of systems of ultracold gases by novel forms of interactions with additional associated

characteristic length scales has been shifting to the focus of research recently. As an example, dipolar interactions in quantum gases promise the realization of novel states of quantum matter, including crystalline or even supersolid phases with density order at an emerging dipolar length scale [37–39]. Several experimental platforms allow for studying dipolar physics, among them are magnetic atoms [40–43], polar ground state molecules [44, 45] and neutral atoms excited to high-lying Rydberg states, so-called Rydberg atoms [46].
Rydberg atoms in particular have received much attention recently due to their strong long-range interactions, with a focus both on quantum information [46] but also on quantum simulation [47, 48]. Due to their short lifetimes on the order of tens of microseconds, experiments involving Rydberg atoms have been limited to the so-called frozen gas regime [49, 50], where all motional dynamics, typically occurring on time scales of tens of milliseconds, is frozen out. In this regime, the interplay of optical coupling and interactions leads to the appearance of a strong excitation blockade [51, 52], which has been utilized to implement quantum gates between isolated pairs of atoms [53, 54]. For more atoms, the development of local microscopic detection of Rydberg atoms recently led to the observation of ordered structures in many-body systems [55, 56], followed by the preparation of low energy many-body states both in our experiment [57] and recently also for atoms trapped in optical microtraps [58]. As part of the work presented in this thesis, we have combined the excellent preparation and detection capabilities provided by our quantum gas microscope to prepare and microscopically study atomic ensembles smaller than the blockade distance. In this regime, the interactions completely dominate the dynamics and, as a result, in our experiment more than one hundred atoms share a single excitation and form an effective collective two-level system, the so-called "superatom" [59]. Increasing the system size, we could observe the coherent breakdown of the Rydberg blockade, connecting the superatom regime with the many-body regime explored in earlier work [55, 57]. Our findings are summarized in the publication [60].
While these experiments were limited to durations of few microseconds to remain well within the frozen gas regime, pulsed Rydberg excitation [61] or the off-resonant optical admixture of Rydberg states was proposed as a route to induce dipolar interactions in quantum gases with motional dynamics [62, 63]. The main idea is that in presence of an off-resonant optical coupling, the emerging "Rydberg-dressed" eigenstates contain a small amount of Rydberg state admixture, which induces Rydberg interactions but also results in a finite lifetime. The presence of these Rydberg-dressed interactions combined with lifetimes long enough to reach motional time scales have for a long time been the driving force for the realization of Rydberg-dressed interactions. Only recently, it was realized that Rydberg dressing also allows for the implementation of spin systems [64, 65], featuring even novel, highly tunable spin interactions [66, 67], with the prospect of enabling coherent quantum annealing [68]. As

such, Rydberg-dressed spin interactions have the potential to complement or enrich superexchange-based spin interactions [69], which have up to now set the standard for exploring quantum magnetism of atoms in optical lattices [28, 29, 70–72]. While in a pioneering experiment Rydberg-dressed interactions were employed to entangle and demonstrate a quantum gate between two atoms [73], they had lacked experimental confirmation in a many-body setting.

In the second part of the thesis we will describe our experiments on establishing Rydberg-dressed interactions in a many-body system, summarized in the publication [74]. Still working in the frozen gas regime, we implemented an Ising spin model with the spin directions encoded in two different ground states of rubidium-87 atoms. Interactions were induced by coupling one of the spins to a Rydberg P-state on a single-photon transition with ultraviolet light. Employing Ramsey interferometry [75] combined with microscopic spin-correlation measurements, we could directly map out the Rydberg-dressed interactions and show their tunability. While first experiments in a two-dimensional ensemble of approximately 200 atoms showed strong collective dissipation and so far only allowed for exceeding the bare Rydberg state lifetime by a factor of five, in a subsequent experiment on a one-dimensional spin chain of ten atoms published in [76] we were able to achieve lifetimes exceeding 40 times the bare Rydberg state lifetime. The ratio between interaction and decoherence was simultaneously increased by two orders of magnitude. From the observation of coherent collapse and revivals of the magnetization of the spin chain, we conclude that dressed interaction potential as well as coherence properties of the system are well understood.

Next to the demonstrated tunability of their isotropy and strength, Rydberg-dressed interactions can also be switched optically. Combined with the controlled disorder utilized recently to study many-body localization in our experiment [30], this could enable the study of novel quantum phases existing solely in disordered stroboscopically driven systems [77, 78], among them the recently discovered time crystal [79, 80]. In the appendix of this thesis, we briefly discuss the experimental prospects of stroboscopic dressing.

The long achieved lifetime in the one-dimensional spin system mark an important step towards bridging the enormous gap between the Rydberg state lifetime and the motional time scale of atoms, and unfreezing the frozen Rydberg gas has come well within experimental reach. Moreover, the demonstrated tunability and switchability of the interactions, combined with well-established detection of ground state atoms and their spins, renders Rydberg-dressing a versatile part enriching the ultracold atom toolbox and promises to open up many new directions to explore.

Outline

In the first part of this thesis we will focus on the two cornerstones of the presented experiments, Rydberg atoms and our quantum gas microscope. Chapter 2 will give a brief introduction to the former, their interactions and especially the effects emerging and the capabilities offered when interacting Rydberg states are optically coupled to ground states. The following chapter 3 will introduce the experimental platform of the quantum gas microscope for bosonic rubidium-87 atoms, which provides the enabling technology for all experiments described thereafter. The microscopic study of a Rydberg gas in the strongly interacting "superatom" regime presented in chapter 4 will set a first example of the potential of combining Rydberg excitation in an optical lattice with single-atom-sensitive preparation and detection. Extending our experimental toolbox by an ultraviolet laser, the single-photon excitation of Rydberg P-states and their optical detection with a quantum gas microscope are described in the subsequent chapter 5. The final two chapters present two experiments building on this technology: First, we report on the successful realization and measurement of Rydberg-dressed interactions in a many-body system in chapter 6. While these initial experiments were plagued by unexpectedly strong dissipation, in a second experiment with fewer atoms we were able to achieve long coherence times and observe coherent collapse and revival dynamics in a long-range interacting one-dimensional Ising spin-1/2 chain. The corresponding experiment, described in chapter 7, paves the way for studying more complex many-body systems.

List of publications

The following articles have been published in refereed journals in the context of this thesis. The articles most relevant for this thesis are shown in bold font.

Many-body interferometry of a Rydberg-dressed spin lattice
J. Zeiher, R. van Bijnen, P. Schauß, S. Hild, J.-y. Choi, T. Pohl, I. Bloch, C. Gross
Nature Physics 12, 1095-1099 (2016)

Exploring the many-body localization transition in two dimensions
J.-y. Choi, S. Hild, J. Zeiher, P. Schauß, A. Rubio-Abadal, T. Yefsah, V. Khemani, D. A. Huse, I. Bloch, C. Gross
Science 352, 1547-1552 (2016)

Microscopic Characterization of Scalable Coherent Rydberg Superatoms
J. Zeiher, P. Schauß, S. Hild, T. Macrì, I. Bloch, C. Gross
Phys. Rev. X 5, 031015 (2015)

Spatially Resolved Detection of a Spin-Entanglement Wave in a Bose-Hubbard Chain
T. Fukuhara, S. Hild, J. Zeiher, P. Schauß, I. Bloch, M. Endres, C. Gross
Phys. Rev. Lett. 115, 035302 (2015)

Crystallization in Ising quantum magnets
P. Schauß, J. Zeiher, T. Fukuhara, S. Hild, M. Cheneau, T. Macrì, T. Pohl, I. Bloch, C. Gross
Science 347, 1455-1458 (2015)

Far-from-Equilibrium Spin Transport in Heisenberg Quantum Magnets
S. Hild, T. Fukuhara, P. Schauß, J. Zeiher, M. Knap, E. Demler, I. Bloch, C. Gross
Phys. Rev. Lett. 113, 147205 (2014)

The following article has appeared as a pre-print.

Coherent many-body spin dynamics in a long-range interacting Ising chain
J. Zeiher, J.-y. Choi, A. Rubio-Abadal, T. Pohl, R. van Bijnen, I. Bloch, C. Gross
arXiv:1705.08372 (2017)

Chapter 2

Rydberg atoms and their interactions

2.1 Introduction

In this chapter, resonant and off-resonant optical coupling of neutral atoms to Rydberg states are presented as an approach to generate long-range interactions in ultracold gases. Starting from a description of the dipolar interactions between Rydberg states, we show how this interaction can be transferred to ground states by including an off-resonant optical coupling. Within the framework of this so-called "Rydberg dressing", the interaction between Rydberg states is optically admixed to ground state atoms, allowing for a novel type of interaction between ultracold atoms. Rydberg-dressed interactions can in principle be used both for the implementation and simulation of spin systems, as well as for systems exhibiting motional dynamics, and their optical switchability endows them with unique control features.

2.1.1 Long-range interactions in the ultracold

In quantum simulation experiments with ultracold atoms, interactions are usually well approximated by a contact interaction potential [3, 4]. This implies that they are of short-range nature and particles have to come very close to each other before the interaction becomes effective. Extending the toolbox of ultracold atomic quantum simulators with dipolar interactions has been a long-standing goal [37, 39] and experimental breakthroughs were achieved recently. Among these is the demonstration of spin interactions between ultracold polar molecules [45]. Furthermore, highly magnetic species like chromium [40], dysprosium [41, 42] or erbium [43] have recently been cooled to quantum degeneracy, and the finite-range dipolar nature of the interactions was demonstrated in a series of beautiful experiments [81–85]. Another well-studied platform featuring long-range interactions are strings of ions trapped in radio-frequency traps [86]. Manipulation and detection in these system has matured to an impressive degree, yet, up to now, simulations have been limited to different variants of spin-systems [79, 87–89], and the simulation of motional dynamics seems difficult if not impossible.

Quantity	Symbol	Scaling	Ref.	Values for $31P_{3/2}$
Energy	$E_{n,L,J}$	n^{-2}	[90, 91]	-4.1 THz
Orbital radius	$\langle r^2 \rangle^{1/2}$	n^2	[91]	67 nm
Coupling to $5S_{1/2}$	$\mathcal{R}^{n',1,J'}_{5,0,1/2}$	$n^{-3/2}$	[92]	$0.0036\, ea_0$
Coupling to $nS_{1/2}$	$\mathcal{R}^{n,1,J'}_{n,0,1/2}$	n^2	[92]	$899\, ea_0$ (to $31S_{1/2}$)
Effective lifetime	τ	n^2	[93]	28 µs
Radiative lifetime	τ_{rad}	n^3	[91, 93]	58 µs
Black-body lifetime	τ_{BB}	n^2	[91, 93, 94]	53 µs
Energy splitting	$\Delta E_{n,L,J}$	n^{-3}	[90, 91]	-145 GHz (to $31S_{1/2}$)
C_6-coefficient	C_6	n^{11}	[92, 95]	$-h\,201$ MHz µm^6
Blockade radius	R_b, R_c	$\sim n^{1.8}$		1.43 µm ($\Delta/2\pi = 6$ MHz)

Table 2.1: Scaling laws with principal quantum number. Approximate scaling of properties of Rydberg atoms with principal quantum number n for rubidium-87. The fifth column shows concrete numbers for the Rydberg state $31P_{3/2}$. The effective and black-body lifetimes are calculated at a temperature of 300 K. For the scaling of the blockade radius, the Rabi frequency is assumed to be constant. The cut-off radius R_c relevant for dressed interactions has the same scaling in this case. The given scaling relations can be used to find the scaling of many derived quantities.

2.2 Rydberg atoms

The term "Rydberg atom" refers to an atom excited to a high-lying electronic state close to the ionization threshold. Rydberg atoms very often exhibit exaggerated properties compared to ground state atoms, many of which can be traced back to their much larger size. Generally, also properties like interaction strength or sensitivity to the environment are strongly enhanced, and lifetimes on the order of several microseconds allow for coherent manipulations of the transition between ground and Rydberg states. The remainder of the chapter will be dedicated to substantiating many of these points, with special focus on interactions.

2.2.1 Level structure and scaling

For rubidium-87, the ionization energy of the single valence electron in the $5S$-shell with respect to the lowest hyperfine ground state is $E_i/h = 1010.029164$ THz [97] and the binding energies of the high-lying states close to the threshold to the continuum

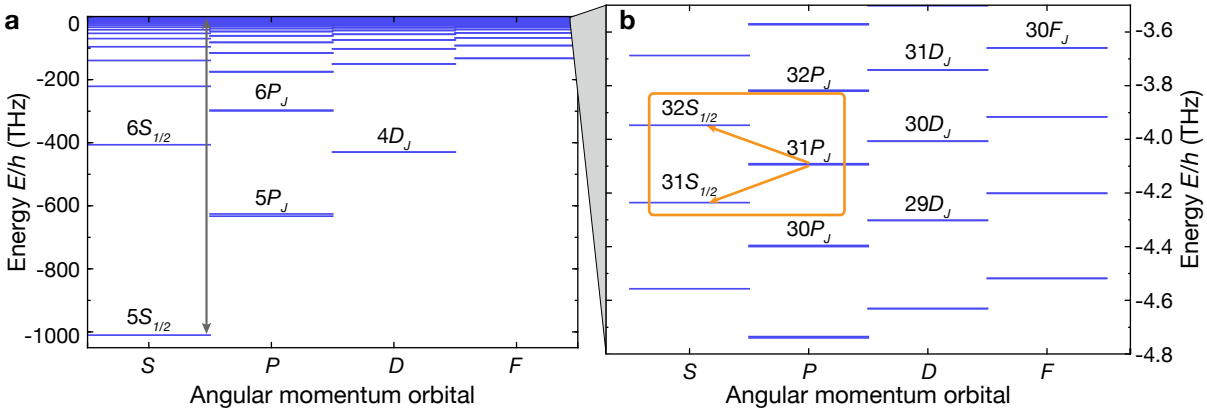

Figure 2.1: Energy levels of rubidium-87. a Energy levels of rubidium-87 for different orbital angular momentum states (quantum number L) are shown as blue horizontal lines, with specific states labelled in spectroscopic notation nL_J, where L denotes the letter representing the orbital angular momentum. The vertical gray arrow marks the ionization energy. For the $5S$-, $5P$- and $4D$-states, and the $6S$- and $6P$-states, the energies were taken from the NIST database [96], for all other levels, quantum defect theory was used to calculate the energies. **b** Zoom into the Rydberg manifold in the vicinity of the states $31P_J$. The quantum defect leads to a larger binding energy for S-states as compared to states with higher angular momenta. The strongest two transitions to neighoring states for $31P$ are to $32S$ and $31S$, yielding the main contribution to the van-der-Waals interaction of $31P$, see section 2.3. The orange rectangle marks this minimal model system, from which van-der-Waals interactions and their isotropy can be deduced, see section 2.3.

follow the simple scaling formula [90, 91]

$$E_{n,L,J} = -\frac{R_\star}{(n-\delta_{n,L,J})^2} \equiv -\frac{R_\star}{(n^\star)^2}. \tag{2.1}$$

Here, $R_\star = h \cdot 3289.82119466(2)\,\mathrm{THz}$ denotes the Rydberg constant in frequency units for rubidium-87 [97, 98]. The principal quantum number is denoted as n, L represents the orbital angular momentum and J the sum of spin and orbital angular momenta of the electron. Despite the complex electronic structure of rubidium with 37 electrons in total, the inner-shell electrons in filled orbitals shield most of the nuclear charge. In consequence, the single valence electron in the $5S$-orbital is bound in the Coulombic field of a screened, singly positively charged nucleus, similar to the single electron in the field of the proton in atomic hydrogen. To account for the shielding effect, the hydrogenic principal quantum number n is corrected by the so-called "quantum defects" $\delta_{n,L,J}$ [99], and an effective principal quantum number $n^\star$ is introduced. The quantum defects have to be determined from the spectroscopically

measured energy levels by fitting empirical models [97, 98, 100]. Generally, they are non-vanishing for $L < 4$, whereas for all larger L the spectrum becomes hydrogenic, up to the reduced-mass correction in the Rydberg constant [98]. The resulting energy level structure is shown in Fig. 2.1. Next to the simple scaling of the energy with the principal quantum number, also other quantities follow similar scaling laws [91, 92]. The most important ones for the work presented in this thesis are summarized in table 2.1, along with concrete numbers evaluated for the Rydberg state $31P_{3/2}$.

2.2.2 Rydberg state wavefunctions

In addition to the eigenenergies given by equation (2.1), the calculation of many properties of Rydberg atoms also requires detailed knowledge about the states corresponding to the energy levels. In the quantum defect approximation, the state of a Rydberg atom is described by the quantum numbers of the valence electron. For an energy $E_{n,L,J}$ it can be written as $|n,\ L,\ J, m_J\rangle$, where we have added the quantum number m_J describing the projection of the total angular momentum J on the z-axis. While in the absence of external fields, all states with different m_J are degenerate, typical experiments work at finite field and the m_J are split in energy. Assuming that the screening of the nuclear charge is isotropic, as can be expected for filled inner shells, we can furthermore separate the angular and radial dependence and write the state as

$$|n, L, J, m_J\rangle = |R_{n,L,J}(r)\rangle \otimes |L, J, m_J\rangle. \tag{2.2}$$

In this notation, $|R_{n,L,J}(r)\rangle$ denotes the vector whose real space representation is the radial wavefunction $R_{n,L,J}(r)$, while $|L, J, m_J\rangle$ contains all angular dependence and we have omitted the spin $S = 1/2$ for the valence electron for the sake of a simpler notation. The J-dependence of the radial wavefunction is a consequence of the J-dependent quantum defects and usually very weak, yet we still write it explicitly in the following to keep it in mind. Calculating physical quantities like transition matrix elements (see section 2.2.3) generally requires knowledge of the explicit form of the radial wavefunctions [101]. Transition matrix elements between Rydberg states are for example important for the calculation of interaction properties of Rydberg atoms. Because, unlike for ground states [102], precise measurements of the oscillator strengths are missing in this case, an *ab-initio* calculation of wavefunctions is required. This can be achieved by numerically solving the Schrödinger equation for the valence electron in a simple Coulomb potential with the eigenenergies $E_{n,L,J}$ determined from quantum defect theory. To account for the screening and the polarizability of the screened core, empirical model potentials can be used, see reference [103] for the explicit form of a widely used potential, whose parameters are empirically optimized by fitting spectroscopic data. The required numerical integration of the Schrödinger equation is then frequently accomplished with the aid of the Numerov split-step method [103–107]. To improve the accuracy of the results, usually a scaled grid is implemented

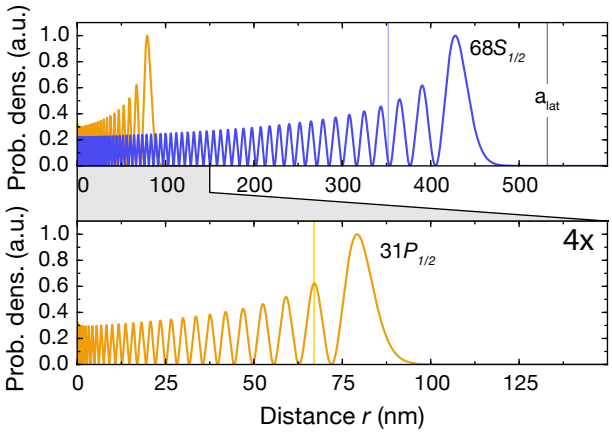

Figure 2.2: Radial wavefunctions for $68S$ and $31P$ Rydberg states. The upper panel shows the absolute value of the calculated scaled radial wave functions $|\chi_{n,L,J}|^2 = r^2|R_{n,L,J}|^2$, normalized to the maximum, for $68S_{1/2}$ (blue line) and $31P_{1/2}$ (yellow line). Both curves were obtained by numerically integrating the radial Schrödinger equation. The lower panel shows a zoom by a factor of four to the $31P_{1/2}$ wave function. The blue and orange vertical lines mark the root mean square radius $\langle r^2\rangle^{1/2} = 67(352)\,\mathrm{nm}$ for $31P_{1/2}$ and $68S_{1/2}$ and the gray vertical line marks the lattice spacing a_{lat}.

for the integration with a more dense sampling for small r [105, 106], because the wavefunction exhibits fast oscillations in that regime, see Fig. 2.2. The wavefunctions displayed in Fig. 2.2 were calculated using this approach with the quantum-defect energies in equation (2.1) and the quantum defects and ionization energy taken from references [100] and [97] respectively. Comparing the wavefunctions of the states $31P_{1/2}$ and $68S_{1/2}$, a large difference in size is directly apparent. This is a direct manifestation of the scaling $\langle r^2\rangle^{1/2} \propto n^2$ of the mean square radius with principal quantum number. More quantitatively, for $31P_{1/2}$ we obtain $\langle r^2\rangle^{1/2} \approx 67\,\mathrm{nm}$ while for $68S_{1/2}$, $\langle r^2\rangle^{1/2} \approx 352\,\mathrm{nm}$. For comparison, the typical extension of a rubidium atom in the ground state is on the order of few Bohr radii, $a_0 = 4\pi\epsilon_0\hbar^2/(m_e e^2) \approx 53\,\mathrm{pm}$, such that the spatial extent of the Rydberg states discussed before is approximately three orders of magnitude larger. In an optical lattice with lattice constant $a_{\mathrm{lat}} = 532\,\mathrm{nm}$ as used in all experiments presented in this thesis, the $31P_{1/2}$-state can be considered well localized within a lattice site, while the outermost maximum of the wavefunction of $68S_{1/2}$-state reaches close to the lattice distance. Increasing the principal quantum number further, one might reach the interesting regime where the maximum coincides with the lattice distance, potentially allowing for efficient generation and spectroscopy of exotic molecules [108, 109].

2.2.3 Transition dipole matrix elements

The calculation of matrix elements of the dipole operator $\hat{\boldsymbol{d}} = e\hat{\boldsymbol{r}}$ between two states $|i\rangle$ and $|j\rangle$ is a particularly important case where accurate knowledge of the Rydberg wavefunctions is required. These matrix elements read

$$\boldsymbol{d}_{ji} \equiv \langle j|e\hat{\boldsymbol{r}}|i\rangle, \tag{2.3}$$

and they are relevant because they determine the interaction properties of Rydberg atoms as well as the optical coupling strength when exciting them from an electronic ground state. For example, the calculation of the interaction between two Rydberg atoms requires the calculation of $\boldsymbol{d}_{ij}$ between many pairs of Rydberg states, e.g. $|i\rangle \equiv |n, L, J, m_J\rangle$ and $|j\rangle \equiv |n', L', J', m'_J\rangle$ see Section 2.3 and references [95, 110–114]. Specifically, one has to evaluate

$$\begin{aligned}\boldsymbol{d}_{ji} &= \langle n', L', J', m'_J|\hat{\boldsymbol{d}}|n, L, J, m_J\rangle \\ &= e\mathcal{R}^{n',L',J'}_{n,L,J} \times \delta_{|L-L'|,1}(-1)^{J'+J+L_>+S+1-m'_J} \begin{Bmatrix} L' & 1 & L \\ J & S & J' \end{Bmatrix} \times \sum_q \boldsymbol{e}^{\boldsymbol{q}} \begin{pmatrix} J' & 1 & J \\ -m'_J & q & m_J \end{pmatrix} \\ &\equiv \sum_q \boldsymbol{e}^{\boldsymbol{q}} d_q,\end{aligned} \tag{2.4}$$

where the angular dependence has been separated from the radial dependence using the Wigner-Eckhart theorem by introducing Wigner-6j and Wigner-3j symbols following the description and notation in reference [101], c. f. eq. (49). Here, $L_> = max(L,L')$ denotes the larger of L and L', whose difference has to equal unity, ensured by the Kronecker-delta $\delta_{|L-L'|,1}$. This is well known for optical transitions and a consequence of the parity symmetry of the dipole operator. The vector $\boldsymbol{e}^{\boldsymbol{q}}$ with $q = \pm 1, 0$ is a spherical unit vector defined by $\boldsymbol{e}^{\pm\mathbf{1}} = \mp\frac{1}{\sqrt{2}}(\boldsymbol{e_x} \mp i\boldsymbol{e_y})$ and $\boldsymbol{e}^{\mathbf{0}} = \boldsymbol{e_z}$ and the radial matrix element can be obtained from the radial wavefunctions $R_{n,L,J}(r)$ by integrating $\mathcal{R}^{n',L',J'}_{n,L,J} = \int_0^\infty \mathrm{d}r\, r^3 R^\star_{n',L',J'}(r) R_{n,L,J}(r)$. Finally, in the last step we have defined the components d_q of the dipole operator in the spherical basis. It is quite instructive to investigate the structure of equation (2.4) further. The overall strength of the dipole moment is determined by the radial matrix elements $\mathcal{R}^{n',L',J'}_{n,L,J}$. The typical size of such a radial matrix element between two different ground states in rubidium-87 is on the order of few ea_0 (e being the elementary charge), e.g. for states $5S_{1/2}$ coupled to $5P_{3/2}$, it becomes $\mathcal{R}^{5,1,3/2}_{5,0,1/2} \approx 5.18\, ea_0$ [102], whereas for two neighboring Rydberg states, e.g. $31P_{3/2}$ and $31S_{1/2}$, it reaches up to $\mathcal{R}^{31,1,3/2}_{31,0,1/2} \approx 900\, ea_0$. This explains partly the much larger interaction strength of two Rydberg atoms compared to ground state atoms. The direction of the dipole moment is contained in the magnitude of the Wigner-3j

symbols, which are the vectorial components in the spherical basis spanned by the $\boldsymbol{e}^q$. From the properties of the Wigner-3j symbols, it follows that for the dipole moment to be non-vanishing, $|J - J'| \leq 1$ and $m'_J = q + m_J$, also entailing the well-known polarization selection rules for optical transitions. These imply, for example, that a dipole moment along the z-direction with $q = 0$ can only be present between two states with the same $m_J = m'_J$. Intuitively, this makes sense because two charge distributions with $m_J = m'_J$ have the same symmetry about the z-axis and thus cannot exhibit a dipole moment which is not directed in the z-direction. In section 2.3 we will see in more detail how the dipole moments between two atomic states determine the interaction properties of atoms.

For calculating the strength of Rydberg-dressed interactions or the size of the blockade radius (see section 2.4), also the optical coupling between a Rydberg state and a ground state is relevant. It is quantified by the Rabi frequency $\hbar\Omega_{ij} = E_0\langle i|\boldsymbol{\epsilon}\cdot\hat{\boldsymbol{d}}|j\rangle$, where $E_0 = (2I/c\epsilon_0)^{1/2}$ is the amplitude of the light field with intensity I and the vector $\boldsymbol{\epsilon}$ encodes the polarization of the light [101]. While the subscript order can be understood as specifying a transition from state $|j\rangle$ to $|i\rangle$, we will usually drop the indices and choose $\Omega \equiv \Omega_{ij}$ to be real.

At the magnetic field strength used in all experiments presented in this thesis, the ground states of rubidium-87 are well described by quantum numbers $|n, L, J, F, m_F\rangle$ because of the hyperfine coupling of J with the nuclear spin $I = 3/2$ to the total hyperfine spin F. As shown in reference [92] combined with the notation used in [101], in this case the Rabi coupling between a ground state $|g\rangle$ and a Rydberg state $|r\rangle$ can be calculated as

$$\begin{aligned}\hbar\Omega_{rg} &= eE_0\langle n', L', J', m'_J|\boldsymbol{\epsilon}\cdot\hat{\boldsymbol{d}}|n, L, J, F, m_F\rangle \\ &= eE_0\mathcal{R}^{n',L',J'}_{n,L,J} \times (-1)^{J+2J'-I+m_F+m'_J+S+L_>}\sqrt{(2F+1)(2J+1)(2J'+1)(L_>)} \\ &\times \begin{Bmatrix} L & L' & 1 \\ J' & J & S \end{Bmatrix} \sum_q \epsilon^q \begin{pmatrix} J & I & F \\ m'_J - q & m_F - m'_J + q & -m_F \end{pmatrix} \times \begin{pmatrix} J' & 1 & J \\ m'_J & -q & -m'_J + q \end{pmatrix},\end{aligned} \tag{2.5}$$

with the same definitions as above for equation (2.4). The circular polarizations $\sigma_\pm$ thereby correspond to $q = \pm 1$ respectively, linear polarization along z corresponds to $q = 0$, and the ϵ^q is the coordinate of the polarization along direction q in the spherical basis. In equation (2.5) the matrix element $\mathcal{R}^{n',L',J'}_{n,L,J}$ is to be calculated between a ground and a Rydberg state. Contrary to the matrix elements between two Rydberg states, these can be quite sensitive to the effects of screening and the details of the numerical calculation, for example the lower bound of the integration region used to calculate the wavefunctions. Especially regarding the transition matrix elements from ground S-states to Rydberg P-states there appear discrepancies between numerical calculations based on quantum-defect energies and more sophisticated methods [115],

where the former tend to consistently overestimate the matrix elements. While corrections to the dipole operator due to core polarization [103] reduce this discrepancy, further calculations using a different model potential [116–118] or including relativistic and many-body corrections [119–122] and a thorough comparison to experimental measurements as done in reference [123] would be desirable for larger principal quantum numbers.

2.2.4 Lifetime of Rydberg atoms

The lifetimes of Rydberg states crucially determine their usefulness for quantum simulation or quantum information. The decay of Rydberg states occurs via two main processes [91, 93]. The first is a direct radiative decay back to the ground states with rate $1/\tau_{\text{rad}}$ upon emission of a photon in the visible or ultraviolet spectral range. The second possible path is a decay to neighboring Rydberg states with rate $1/\tau_{BB}$ after stimulated emission of a microwave photon to the thermal black-body microwave background. Both processes contribute to the overall effective decay time

$$\tau = \left(\frac{1}{\tau_{\text{rad}}} + \frac{1}{\tau_{BB}} \right)^{-1}. \tag{2.6}$$

Generally, the decay rate of a Rydberg state $|i\rangle = |n, L, J, m_J\rangle$ corresponds to a redistribution of population to other states, either directly to the ground states due to the radiative decay or to other nearby Rydberg states. Atoms in the latter can interact with those left in the initially excited states, which can lead to unwanted and uncontrolled loss, see chapter 6.
The radiative lifetime is obtained by summing all decay rates to lower-lying states. The rate for transitions to each individual state is independent of the magnetic quantum number and quantified by the Einstein A coefficient [91–93]

$$A_{ji} = \frac{16\pi^3 e^2 \nu_{ji}^3}{3\epsilon_0 h c^3} \frac{L_>}{2L+1} |\mathcal{R}_i^j|^2. \tag{2.7}$$

Here, ν_{ji} is the transition frequency and $\mathcal{R}_i^j$ denotes the radial matrix element between the Rydberg state $|i\rangle$ and a different state $|j\rangle$ and $L_>$ stands for the larger of the two involved orbital angular momenta, see equation (2.4). Due to the large transition frequency ν_{ji} to the ground states, these contribute most strongly to the spontaneous decay rate. Furthermore, as ν_{ji} is approximately independent of n, the scaling is dominated by the scaling of the radial matrix elements. Inspecting table 2.1, we find [91, 93]

$$\tau_{\text{rad}} \propto n^3. \tag{2.8}$$

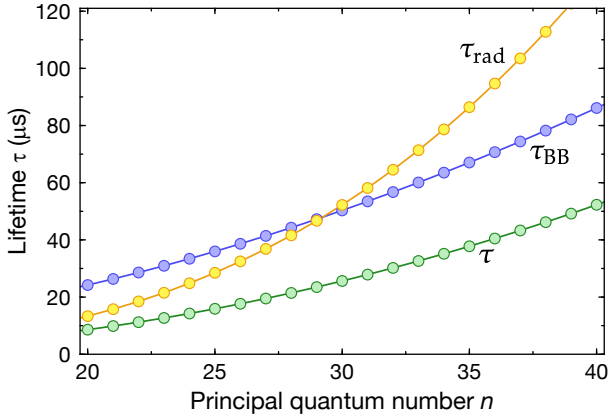

Figure 2.3: Lifetime of Rydberg $nP_{3/2}$-states. Scaling of effective lifetime τ, radiative lifetime τ_{rad} and black-body-radiation-induced lifetime τ_{BB}. Around $n = 29$, the two contributions to the effective lifetime become equal.

For the black-body-radiation-induced decay, the spontaneous transition rate is negligible due to the small transition frequencies, despite large transition matrix elements. Focussing on Rydberg states around $n = 31$, typical matrix elements between neighboring Rydberg states are 10^5 times larger than those between Rydberg and ground states, whereas the transition frequencies are smaller by 10^{-4}. Combining these scalings with their respective powers in the Einstein A coefficient in equation (2.7), we see that the spontaneous transition rates between two Rydberg states are smaller by a factor 10^{-2}. However, at room temperature ($T \approx 300\,\text{K}$), the average number of photons per thermally occupied mode with a frequency close to the transition frequencies to neighboring Rydberg states is approximately 10^2. Multiplying this with the Einstein A coefficient yields the stimulated emission rate [93], bringing it to the same scale as the spontaneous transition rate to the lower-lying electronic states. More quantitatively, the mean photon number n per mode with frequency ν at temperature T is given by the Bose-Einstein distribution $n(\nu)$ and the rate for stimulated emission from state $|i\rangle$ into other Rydberg states becomes

$$\tau_{BB} = \left[\sum_j n(\nu_{ji}) A_{ji}(\nu_{ji})\right]^{-1} = \left[\sum_j \frac{A_{ji}(\nu_{ji})}{\exp\left(h\nu_{ji}/k_B T\right) - 1}\right]^{-1}. \tag{2.9}$$

The scaling in the limit of small ν for high-lying Rydberg states with large n amounts to [93, 94]

$$\tau_{BB} \propto n^2. \tag{2.10}$$

Comparing both scalings (2.8) and (2.10), we see that for small principal quantum number n the radiative decay rate dominates, whereas for large n, the black-body

decay is the stronger source of decay and also determines the scaling of the total decay time τ. Empirical relations have been put forward to predict the two rates [93] and using the parameters given there, we obtained the numbers shown in Fig. 2.3. At $n \approx 29$, the two rates become equal, marking the transition from the regime of radiation-dominated to black-body-dominated decay. Suppressing the black-body radiation can drastically increase lifetimes of Rydberg states for large principal quantum numbers. This can be achieved in a cryogenic environment, due to the exponential decrease in population of photon modes with decreasing temperature. In fact, experiments for studying many-body physics with Rydberg states of rubidium-87 in a cryogenic environment are en route [124, 125].

2.3 Interactions between Rydberg atoms

Atoms excited to Rydberg states are especially attractive for quantum simulations due to their exaggerated interaction properties [46, 92]. The interaction strength is orders of magnitude larger than for atoms in their electronic ground state and the interaction potential can be tuned from van-der-Waals to dipolar character, as well as made repulsive or attractive, isotropic or even anisotropic. The strength and the tunability explain to a large extent the interest in ultracold Rydberg atoms. Recently, easy-to-use codes for the calculation of Rydberg interaction potentials have become publicly available [95, 114], accompanied by tutorial-style introductions to the subject with further references [95, 112, 114]. This section reviews the basic ideas necessary to understand the interactions between two Rydberg atoms, with explicit discussions of model systems for the cases relevant for this thesis.

2.3.1 Interaction between two classical charge distributions

Before introducing the quantum mechanical description of the interaction between two atoms, we first present a classical treatment which allows to understand the essential physics and to build some intuition on how the interaction arises. To this end, the atoms are described as extended negative charge distributions $\rho(\boldsymbol{r}_1)$ and $\rho(\boldsymbol{r}_2)$ for the valence electrons, each with a localized positively charged screened nucleus in the center, separated by a distance vector $\boldsymbol{R}$. From classical electrodynamics, it is well known that in this case, the interaction energy between the charge distributions reads [126, 127]

$$V(\boldsymbol{R}, \boldsymbol{r}_1, \boldsymbol{r}_2) = \frac{1}{4\pi\epsilon_0} \int d\boldsymbol{r}_1 d\boldsymbol{r}_2 \frac{\rho(\boldsymbol{r}_1)\rho(\boldsymbol{r}_2)}{|\boldsymbol{R} + \boldsymbol{r}_2 - \boldsymbol{r}_1|}. \tag{2.11}$$

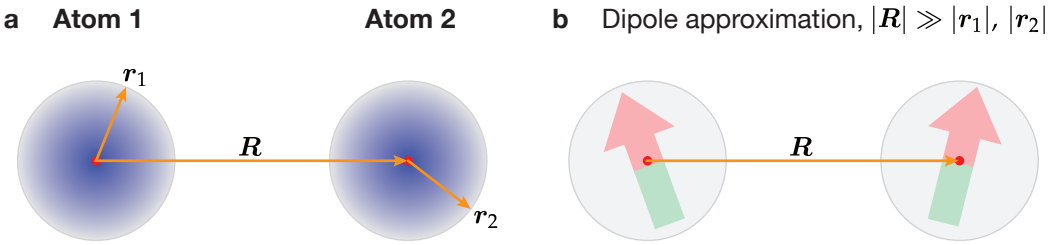

Figure 2.4: Schematic overview of relevant quantities for calculating dipolar interactions between two atoms. **a** Schematic for two interacting atoms with extended electron density (blue shading) distributed around the screened nuclei (red dots). The vectors $\boldsymbol{r}_1$ and $\boldsymbol{r}_2$ specify the distances between an electron density element and the screened nuclei, which are themselves separated by $\boldsymbol{R}$. Distances are not to scale. **b** Approximating the interactions between electrons and nuclei for $|\boldsymbol{R}| \gg |\boldsymbol{r}_1|, |\boldsymbol{r}_2|$, the dipole-dipole interaction replaces the full interaction potential as the dominant interaction term, schematically indicated by replacing the continuous charge distribution displayed in a by dipoles (red-green arrows). See main text for further details.

For large distances $|\boldsymbol{R}| \gg |\boldsymbol{r}_1|, |\boldsymbol{r}_2|$, this expression can be expanded in multipole moments as follows [127]

$$V(|\boldsymbol{R}|,\theta,\phi) = \sum_{l_1,l_2,m_1,m_2} (-1)^{l_1} \left[\frac{4\pi}{2L+1}\right]^{1/2} C^{L,M}_{l_1,m_1,l_2,m_2} (Y^M_L)^\star(\theta,\phi) \frac{(\rho)_{l_1,m_1}(\rho)_{l_2,m_2}}{4\pi\epsilon_0|\boldsymbol{R}|^{L+1}}. \tag{2.12}$$

Here, the angles θ and ϕ denote the polar and azimuthal angles of the vector $\boldsymbol{R}$ in the reference frame, we have defined the sum of angular momentum $L = l_1 + l_2$ and its z-projection $M = m_1 + m_2$ and $C^{L,M}_{l_1,m_1,l_2,m_2} = \langle l_1, m_1, l_2, m_2 | L, M\rangle$ is a Clebsch-Gordan coefficient [128]. The angular dependence is fully encoded in the spherical harmonic $Y^M_L(\theta,\phi)$ [128]. The multipole moments of the charge distributions are defined as

$$(\rho)_{l,m} = \sqrt{\frac{4\pi}{2l+1}} \int d\boldsymbol{r} |\boldsymbol{r}|^l (Y^m_l)^\star(\theta,\phi)\rho(\boldsymbol{r}). \tag{2.13}$$

The expansion in inverse powers of $|\boldsymbol{R}|$ in equation (2.12) allows for a systematic treatment of the interaction orders. In systems with special symmetries or for large enough distances only few terms in the expansion are relevant to describe the interactions. In the example of interacting atoms, we immediately conclude that because the atoms as a whole are neutral, the monopole vanishes $(\rho)_{0,0} = 0$ and hence so do also monopole-monopole ($l_1 = 0, l_2 = 0, L = 0$) and monopole-dipole ($l_1 = 0, l_2 = 1, L = 1$) contributions to the interactions. The first non-zero contribution is the dipole-dipole interaction ($l_1 = 1, l_2 = 1, L = 2$) provided that $(\rho)_{1,m} \neq 0$, see Fig. 2.4 b. Later in the chapter,

employing the full quantum mechanical description, we will see how to induce non-zero dipole moments in neutral atoms, either permanent or perturbatively in the form of induced dipole moments. For all cases discussed in this chapter, higher order interactions, such as dipole-quadrupole ($L = 3$) or quadrupole-quadrupole ($L = 4$), will be neglected. For general systems, this approximation has to be carefully checked, especially for experimental configurations with high density and therefore sensitive to short interatomic distances, as higher order interactions can strongly modify the interaction landscape in this regime in a way relevant for specific experiments [129, 130].

2.3.2 Dipole interaction between two atoms

The classical picture presented above illustrates the expansion of an electrostatic interaction in terms of multipole moments and directly identifies dipole-dipole interactions as the first possibly relevant interactions for neutral atoms. Yet, a full description has to take into account the quantization of the electronic states for the interacting atoms. The basic idea of the quantum mechanical treatment is that the electrostatic interaction between valence electrons and screened nuclei perturb the eigenstates of the individual atoms. We are thus interested in matrix elements of the interaction operator, which in the most general form contains all Coulomb interactions between nuclei and electrons of the two different atoms and reads

$$\hat{V} = \frac{e^2}{4\pi\epsilon_0}\left(\frac{1}{|\boldsymbol{R}|} + \frac{1}{|\boldsymbol{R} - \hat{\boldsymbol{r}}_1 + \hat{\boldsymbol{r}}_2|} - \frac{1}{|\boldsymbol{R} - \hat{\boldsymbol{r}}_1|} - \frac{1}{|\boldsymbol{R} + \hat{\boldsymbol{r}}_2|}\right). \tag{2.14}$$

Here, we use the same parametrization of the coordinates of valence electrons and nuclei as in the previous section, see Fig. 2.4, however $\hat{\boldsymbol{r}}_1$ and $\hat{\boldsymbol{r}}_2$ are now to be understood as the position operators for the valence electron in atom 1 and 2 respectively. Performing the same expansion for large interatomic distances $|\boldsymbol{R}|$ as in the previous section and keeping only the dipole-dipole contribution, the interaction operator becomes [127, 131]

$$\hat{V} \approx \hat{V}_{dd} = \frac{e^2\hat{\boldsymbol{r}}_1 \cdot \hat{\boldsymbol{r}}_2 - 3e^2(\hat{\boldsymbol{r}}_1 \cdot \boldsymbol{e}_R)(\hat{\boldsymbol{r}}_2 \cdot \boldsymbol{e}_R)}{4\pi\epsilon_0|\boldsymbol{R}|^3}, \quad |\boldsymbol{R}| \gg \langle\hat{\boldsymbol{r}}_1^2\rangle^{1/2}, \langle\hat{\boldsymbol{r}}_2^2\rangle^{1/2}, \tag{2.15}$$

and we have defined the dipole-interaction operator $\hat{V}_{dd}$ and $\boldsymbol{e}_R = \boldsymbol{R}/|\boldsymbol{R}|$ as a unit vector pointing along the interatomic axis in the direction of $\boldsymbol{R}$. Acting on two atoms at the same time, the dipole interaction operator can be expressed in a product basis of two atomic eigenstates $|i\rangle \otimes |j\rangle = |i, j\rangle$. As before, here and in the following discussion we implicitly assume that all relevant quantum numbers of the Rydberg states are contained in $|i\rangle$, so $|i\rangle \equiv |n, L, J, m_J\rangle$. In this simplified notation, the matrix

elements of $\hat{V}_{dd}$ read

$$\begin{aligned}(\hat{V}_{dd})_{ij,kl} &= \langle i, j|\hat{V}_{dd}|k, l\rangle \\ &= \frac{\boldsymbol{d}_{ik}^{(1)} \cdot \boldsymbol{d}_{jl}^{(2)} - 3(\boldsymbol{d}_{ik}^{(1)} \cdot \boldsymbol{e}_R)(\boldsymbol{d}_{jl}^{(2)} \cdot \boldsymbol{e}_R)}{4\pi\epsilon_0|\boldsymbol{R}|^3}.\end{aligned} \tag{2.16}$$

In analogy to two interacting classical charge distributions, the dipole interaction is caused by dipole moments in atoms 1 and 2, which in the quantum case are quantified by the matrix elements $\boldsymbol{d}_{ik}^{(1,2)}$ of the dipole operator. As described in section 2.2.3, the directionality of these expectation values is conveniently expressed in a spherical basis, due to the symmetry properties of the atomic eigenstates [128], see equation (2.4). Motivated by this, one can also decompose the dipole operators appearing in equation (2.15) in their spherical components $\hat{d}_p^{(1,2)} = \boldsymbol{e_p} \cdot \hat{\boldsymbol{d}}^{(1,2)}$, which are straightforwardly connected to the atomic eigenstates. In doing so, one obtains [112]

$$\hat{V}_{dd} = -\sqrt{\frac{24}{5\pi}} \sum_{p,q} C_{1,p,1,q}^{2,p+q} (Y_2^{p+q})^\star(\theta, \phi) \frac{\hat{d}_p^{(1)} \hat{d}_q^{(2)}}{4\pi\epsilon_0|\boldsymbol{R}|^3}. \tag{2.17}$$

Here, p and q can take integer values -1, 0 or 1, enforcing the selection rule that the absolute value of the difference in magnetic quantum numbers m_J for each atom of a pair with non-vanishing dipole-dipole interaction is 0 or 1. All angular dependence is encoded in the spherical harmonic $Y_L^M(\theta, \phi)$, where θ and ϕ describe the orientation of the interatomic connection vector $\boldsymbol{R}$ in the reference frame, and $C_{1,p,1,q}^{2,p+q}$ is a Clebsch-Gordan coefficient.

Before continuing the discussion, some remarks can elucidate implications of the equations presented before. First, from the symmetry of the dipole operator [128] and the resulting selection rule $\boldsymbol{d}_{ii} = 0$ it directly follows that

$$(\hat{V}_{dd})_{ii,ii} = 0. \tag{2.18}$$

This implies that two atoms in the same state $|i\rangle$ do not interact via direct dipole-dipole interaction. We will see in the next sections that an interaction in this case only appears in second order in the form of a so-called a "van-der-Waals interaction".

A special configuration is the one with aligned atomic dipoles $\boldsymbol{d}_{ik}^{(1)} = \boldsymbol{d}_{jl}^{(2)} \equiv \boldsymbol{d}$, oriented along the same direction $\boldsymbol{d} \cdot \boldsymbol{e}_R = \cos(\theta)$. In this case one obtains from equation (2.16) the well-known formula for the interaction between two aligned dipoles

$$(\hat{V}_{dd})_{ij,ji} = V_{dd}(|\boldsymbol{R}|, \theta) = \frac{|\boldsymbol{d}|^2}{4\pi\epsilon_0|\boldsymbol{R}|^3}(1 - 3\cos^2(\theta)). \tag{2.19}$$

The same form is of course reproduced by equation (2.17), where two aligned dipoles in the z-direction would correspond to $p = q = 0$. In this case, the angular dependence is given by the spherical harmonic $Y_2^0(\theta, \phi) = \sqrt{5/(16\pi)}(3\cos^2(\theta) - 1)$, indeed with the same dependence as equation (2.19). It should be noted again that for dipoles oriented along z, both equations are equally handy in predicting the angular dependence. The description in spherical coordinates is most useful for dipoles oriented in arbitrary directions other than z.

2.3.3 Numerical calculation of interaction

For the complete description of two atoms interacting via dipole-dipole interaction, the interaction energy operator has to be added to the total energy of the two-atom system,

$$\hat{H} = \hat{H}_1 + \hat{H}_2 + \hat{V}_{dd}, \tag{2.20}$$

and it perturbs the two-atom eigenstates $|i, j\rangle$ and the respective eigenenergies of the isolated atomic Hamiltonians $\hat{H}_1 + \hat{H}_2$ with eigenenergies $\langle i, j|\hat{H}_1 + \hat{H}_2|k, l\rangle = (E_i + E_j)\delta_{i,k}\delta_{j,l}$. The task is therefore to find the eigenstates of $\hat{H}$ defined by equation (2.20), which for large distances and hence small perturbation by $\hat{V}_{dd}$ adiabatically connect to the pair atomic eigenstates. Specifically, one has to diagonalize [74]

$$\begin{aligned} \hat{H} &= \sum_{ij,kl} |i, j\rangle\langle i, j|\hat{H}_1 + \hat{H}_2 + \hat{V}_{dd}|k, l\rangle\langle k, l| \\ &= \sum_{ij,kl} \left((E_i + E_j)\delta_{i,k}\delta_{j,l} + (\hat{V}_{dd})_{ij,kl}\right) |i, j\rangle\langle k, l|. \end{aligned} \tag{2.21}$$

The atomic eigenenergies E_i are obtained from quantum defect theory, see section 2.2, equation (2.1), and the matrix elements of the dipole interaction operator have to be calculated using the radial matrix elements, see section 2.2. The resulting eigenenergies are distance dependent and reflect the increasing interaction energy for short interatomic distances but connecting asymptotically to the uncoupled atomic eigenstates, see also Fig 6.2 for concrete examples. The numerical challenge lies in the diagonalization of the matrix defined in equation (2.21), which can become large if many pair states have to be considered. A proper choice of basis as well as the use of conservation laws and symmetries can significantly improve the performance of the calculation and the accuracy of the potential curves [95, 113, 114], especially if external fields are applied [114].

2.3.4 Interaction in a two-state model

To get a more clear picture, in the following we want to consider a simple two-state model, concentrating on just two isolated states $|i\rangle$ and $|j\rangle$ in each of the two interact-

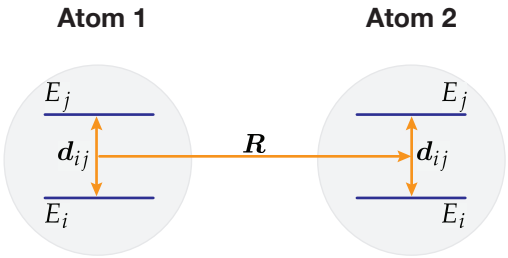

Figure 2.5: Model system. For describing interacting atoms, the quantized level structure of the atoms has to be taken into account. The simplest model for dipole-dipole interactions between two atoms replaces the classical dipoles displayed in Fig. 2.4 b by two two-state atoms with two eigenstates with energies E_i and E_j and dipole moments $\boldsymbol{d}_{ij}$ separated by distance $\boldsymbol{R}$. See main text for further details on the dynamics and limits.

ing atoms, see Fig. 2.5. Even though this might seem like a poor approximation for the complex structure of an atom, c.f. Fig. 2.1, it nevertheless captures the essential physics and helps to understand some basic properties of the interaction. To manifest the model, we first express $\hat{H}$ in the atomic pair state basis $|i,\, j\rangle$, assuming for simplicity that for the chosen states $(\hat{V}_{dd})_{ii,jj} = (\hat{V}_{dd})_{ji,ij} = V = V(R) = |\boldsymbol{d}|^2/(4\pi\epsilon_0 R^3)$. The last approximation requires dipole matrix elements $\boldsymbol{d}$ orthogonal to the plane of the interatomic connection axis, or $\boldsymbol{d} \cdot \boldsymbol{e}_{\boldsymbol{R}} = 0$. Choosing $E_i = 0$ as the energy reference in a rotating frame and setting $E_j = \Delta$, we obtain the following matrix

$$H = \begin{array}{c} \\ |i,\, i\rangle \\ |i,\, j\rangle \\ |j,\, i\rangle \\ |j,\, j\rangle \end{array} \begin{array}{c} \begin{array}{cccc} \langle i,\, i| & \langle i,\, j| & \langle j,\, i| & \langle j,\, j| \end{array} \\ \begin{pmatrix} 0 & 0 & 0 & V \\ 0 & \hbar\Delta & V & 0 \\ 0 & V^\star & \hbar\Delta & 0 \\ V^\star & 0 & 0 & 2\hbar\Delta \end{pmatrix} \end{array}. \tag{2.22}$$

The eigenenergies and eigenstates of this matrix exhibit both exchange oscillations as well as induced dipole-dipole interactions, as discussed in the following.

Resonant dipole interactions – Exchange oscillations

We focus first on the case where the two atoms start out in two different states, i.e. an initial state $|i,\, j\rangle$, see Fig. 2.6 a, b. One can see that the dynamics is constrained to the subspace spanned by $|i,\, j\rangle$ and $|j,\, i\rangle$. In this subspace, the eigenstates are given by (see appendix A)

$$|\pm\rangle = \frac{1}{\sqrt{2}} \left(|i,\, j\rangle \pm |j,\, i\rangle\right) \tag{2.23}$$

with eigenenergies $E_\pm = \Delta \pm |V|$. Thus, starting in state $|i,\, j\rangle$, the system undergoes dipole-interaction-driven state exchange dynamics between $|i,\, j\rangle$ and $|j,\, i\rangle$ with a frequency $\nu_{ex}/h = 2|V|$. The experimental challenge to realize these state exchange reactions lies in the necessity to prepare two atoms in two different Rydberg states. This can be accomplished experimentally for example by laser exciting both atoms in the same Rydberg state to prepare $|i,\, i\rangle$ and then performing a state transfer of one of the atoms to a different Rydberg state [132]. With the aid of the necessary microwave coupling of two Rydberg states, the exchange reaction has been directly observed in experiments in optical microtraps [133] and indirectly inferred from the spin depolarization dynamics of a frozen gas [134]. The exchange dynamics is also suspected to be responsible for the enhanced loss present in a Rydberg-dressed many-body system, see chapter 6. Important in this respect is the fact that the eigenenergies $E_\pm$ split symmetrically about Δ, the energy of the initial state $|i,\, j\rangle$, which can induce unwanted resonances, see chapter 6 and reference [135].

Off-resonant interactions – The van-der-Waals regime

Another experimentally relevant situation is encountered if two atoms are prepared in the same Rydberg state, in our model described by $|i,\, i\rangle$, see Fig. 2.6 c, d. Contrary to the states in the mixed subspace, this state can in principle be prepared directly by a laser excitation of two atoms starting in the same ground state. As previously, inspection of the Hamiltonian (2.22) shows that together with $|j,\, j\rangle$ an isolated subspace is formed. In this subspace, the Hamiltonian reads

$$H_{\mathrm{vdW}} = \begin{matrix} \\ |i,\, i\rangle \\ |j,\, j\rangle \end{matrix} \begin{matrix} \begin{matrix} \langle i,\, i| & \langle j,\, j| \end{matrix} \\ \begin{pmatrix} 0 & V \\ V^\star & 2\hbar\Delta \end{pmatrix} \end{matrix}. \tag{2.24}$$

Contrary to the previously discussed case of exchange oscillations, here the dynamics is described by a detuned coupling of the two levels. Assuming that state $|j\rangle$ lies energetically above $|i\rangle$ and hence $\Delta > 0$, the eigenenergy of the state asymptotically connecting to $|i,\, i\rangle$ for large positive detunings is given as (see appendix A)

$$\begin{aligned} E_- &= \hbar\Delta - \sqrt{(\hbar\Delta)^2 + |V|^2} \\ &\approx \hbar\Delta - \hbar|\Delta| - \frac{|V|^2}{2\hbar|\Delta|} = -\frac{|\boldsymbol{d}|^4}{32\pi^2\epsilon_0^2\hbar|\Delta|R^6} \equiv -\frac{C_6}{R^6}, \end{aligned} \tag{2.25}$$

where we have assumed $|\Delta| \gg |V|$ to approximate the square root and inserted the explicit expression for $V(R)$. Due to the distance dependence of the dipole-dipole interaction element, $V \propto 1/R^3$, we expect this approximation to yield good results as the first correction to the energy for large distances between the two atoms. Analysing

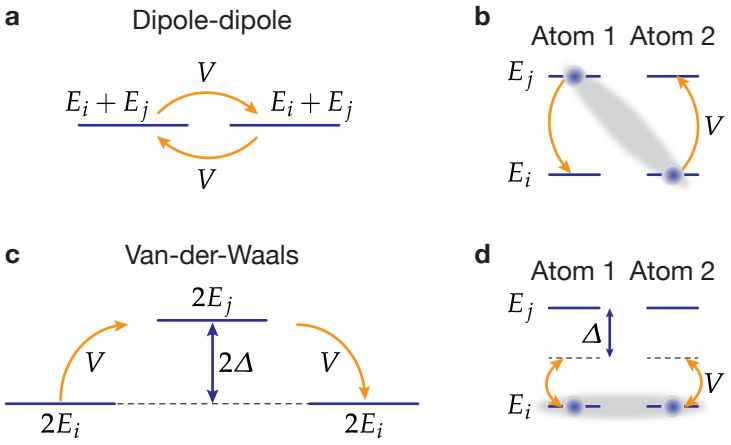

Figure 2.6: Illustration of processes present in model system. a For two atoms starting in a pair state $|i, j\rangle$, the system is constrained to a degenerate subspace of two-atom states (purple lines), where resonant exchange oscillations take place, driven by the dipole interaction V (orange arrows). **b** Considering the states, the atoms are always found in different single-particle states, indicated by purple disks on purple lines and gray shading, and undergo anti-correlated oscillations, driven by the dipole interaction (orange arrow). **c** For two atoms initially in the same pair state $|i, i\rangle$, the dynamics is detuned by twice the single-particle detuning 2Δ (purple arrow) and the doubly excited state is only admixed by the dipolar interaction, resulting in the second-order van-der-Waals interactions. **d** Contrary to the case of exchange oscillations, here the atoms are always found in the same single-particle state and undergo detuned correlated oscillations.

the scaling of the interaction with distance in this limit yields $V_{\mathrm{vdW}} \propto 1/R^6$, characteristic for induced dipole-dipole interactions, also known as "van-der-Waals interaction". Furthermore, we have combined all distance-independent constants to define the so-called "C_6-coefficient", which quantifies the strength of the interaction. In our example, the restriction to positive detunings, $\Delta > 0$, leads to attractive van-der-Waals interactions with $V(R) < 0$ while a negative detuning would have led us to find repulsive interactions. The former case applies for two interacting ground state atoms, which generally have attractive van-der-Waals interactions. For Rydberg atoms, however, Δ can both be positive or negative, and, hence, the interaction is repulsive or attractive depending on the specifically chosen state. Furthermore, the C_6-coefficient is defined negative for repulsive interactions and positive for attractive interactions, see also equation (2.25).
An intuitive picture of the effect of the interaction on the states of two atoms can be obtained by considering the eigenstate corresponding to the perturbed eigenenergy

E_-. We obtain (see equation (A.3) in appendix A)

$$\begin{aligned} |-\rangle &\approx -|i,\, i\rangle + \theta/2|j,\, j\rangle \quad (|\Delta| \gg |V|) \\ &\approx -|i,\, i\rangle + |V|/(2\Delta)|j,\, j\rangle, \end{aligned} \tag{2.26}$$

where $\theta \approx |V|/\Delta$ is valid in the limit of large detunings. Physically, this implies that the doubly excited state $|j,\, j\rangle$ is only weakly admixed to the state $|i,\, i\rangle$. Hence, exciting to the state $|i,\, i\rangle$, the dipole interaction will cause the atoms to undergo correlated detuned oscillation dynamics with a maximal probability $|V|^2/(\Delta^2 + |V|^2)$ of finding both in the state $|j,\, j\rangle$. These correlated dipole oscillations are at the heart of the induced dipole-dipole or van-der-Waals interaction.
Note also that while capturing the essential qualitative features of the interaction of two atoms, for a quantitative description of the interaction this simple model is not sufficient. The most obvious shortcoming of the approximation is the fact that the correlated oscillations leading to the van-der-Waals interaction do not have to happen between the same two states $|i\rangle$ and $|j\rangle$ in each atom. The typical case in alkali atoms is the one where one level lies between two coupled levels, see Fig. 2.1 b. A simple expansion of the described model by including a third level with eigenenergy E_k can be used for example to explain so-called Förster resonances [46, 136], for which a resonant dipolar exchange is found when $\Delta_F = E_j + E_k - 2E_i = 0$, i.e. when the so-called "Förster-defect" Δ_F vanishes. Experimentally, this condition is usually met by tuning the energies of the atomic eigenstates via electric fields [137].
In the following we will generalize the concept of the interaction between two Rydberg states via dipole-dipole interaction to many channels and also detail the origin of anisotropic interactions.

2.3.5 Anisotropic van-der-Waals interactions

The interaction between two dipoles is captured by equation (2.15). The discussion of the simple model system above shows that for two atoms in the same state, the interaction appears for large interatomic separations as a second-order perturbation to the energy eigenstates. This is a consequence of the energetic penalty for inducing correlated dipole moments in two atoms. In consequence, the off-resonant generation of dipole moments leads to characteristic van-der-Waals interactions, see equation (2.25). Extending the exactly solvable two-state system discussed above, the general expression for the van-der-Waals interaction operator between two atoms in the same state $|i\rangle$ including several intermediate states can be obtained perturbatively in second order of $|V_{dd}(R)|/|\Delta|$, yielding for the matrix elements $(\hat{V}_{\mathrm{vdW}})_{ii,ii} = \langle i,\, i|\hat{V}_{\mathrm{vdW}}|i,\, i\rangle$ of

the van-der-Waals interaction operator $\hat{V}_{\mathrm{vdW}}$ [110, 111, 138, 139]

$$\begin{aligned}(\hat{V}_{\mathrm{vdW}})_{ii,ii} &= \sum_{mn} \frac{\langle i,\, i|\hat{V}_{dd}|m,\, n\rangle\langle m,\, n|\hat{V}_{dd}|i,\, i\rangle}{\Delta_{ii,mn}} \\ &= \sum_{mn} \frac{|(V_{dd})_{ii,mn}|^2}{\Delta_{ii,mn}} \equiv \frac{C_6}{R^6} \times D(\theta,\phi).\end{aligned} \tag{2.27}$$

The two-state detuning $\Delta_{ii,mn}$ now depends on all the involved two-atom states $|m,\, n\rangle$ coupled to $|i,\, i\rangle$. The last equality adopts the insight of [111] that the angular dependence of the interaction and the distance dependence can be separated. The C_6-coefficient thereby contains all radial matrix elements between initial and intermediate states, see also section 2.2, as well as the two-state detunings $\Delta_{ii,mn}$. All angular dependence due to the relative orientation of the induced dipoles and hence the dependence on the specific Rydberg Zeeman substates in the two atoms is contained in the factor $D(\theta,\phi)$ [111, 139]. Contrary to the direct dipole interaction, the perturbative coupling now also allows interactions between two atoms in the same state, i.e. $(\hat{V}_{\mathrm{vdW}})_{ii,ii} \neq 0$, which is of course the interaction used by numerous experiments involving Rydberg blockade between two atoms.

Anisotropic interactions of $31P_{3/2}$

As a simple example for anisotropic van-der-Waals interactions we consider two atoms initially prepared in their Rydberg state $31P_{3/2}$, $m_J = -3/2$. To lift the degeneracy of the Zeeman sublevels and define a quantization axis, we assume an externally applied magnetic field. Inspecting the level structure in the neighborhood of the initial state, see Fig. 2.1 b, we can expect the channel $|i,\, i\rangle = |31P_{3/2}, 31P_{3/2}\rangle \rightarrow |m,\, n\rangle = |31S_{1/2}, 32S_{1/2}\rangle$ to dominate the van-der-Waals interactions because of the minimal two-state detuning $\Delta_{ii,mn}$. Of the two Zeeman sublevels of the S-states, only $m_J = -1/2$ has a non-vanishing dipole moment with the initial state $31P_{3/2}$, $m_J = -3/2$, due to the dipole selection rules. In the notation of equations (2.4) and (2.17), the resulting dipole moments are $d_{-1}^{(1,2)}$ and from equation (2.17), we can read off an angular dependence $V_{dd}(\theta,\phi) \propto Y_2^{-2}(\theta,\phi) \propto \sin(\theta)^2$. As there is only one strongly coupled channel, the perturbative sum (2.27) reduces to a simple two-state model as the one discussed above and we can see that in the van-der-Waals regime for large distances, the angular dependence of the interaction becomes

$$D(\theta,\phi) \propto (V_{dd}(\theta,\phi))^2 \propto \sin(\theta)^4. \tag{2.28}$$

This angular dependence is shown in Fig. 2.7 and can be experimentally measured, provided that the quantization axis can be chosen such that the angle θ is probed by the relative positions of the atoms, as shown in chapter 6.

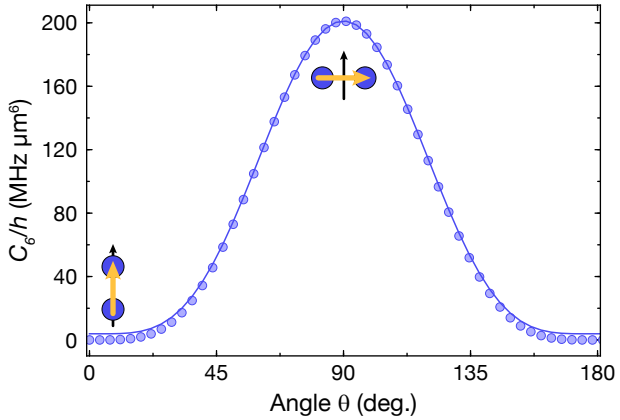

Figure 2.7: Anisotropic interaction for $31P_{3/2}$. The C_6-coefficient of two interacting atoms in state $31P_{3/2}$, $m_J = -3/2$ shows a strong modulation versus the angle θ between quantization axis and connection vector $\boldsymbol{R}$. The solid line is obtained using the ARC-package [95] and shows excellent agreement with the $\sin(\theta)^4$-dependence expected in the single-channel approximation (blue data points), see main text. For angles $\theta = 0°$ and $\theta = 180°$, other channels lead to a finite contribution to the interaction. The pictograms indicate the geometry of the two atoms (blue) with connection vector $\boldsymbol{R}$ (orange arrow) and quantization axis (black arrow). For the calculation of the solid blue line, states with maximal $|\Delta n| = 2$ and a pair state detuning $\Delta/2\pi = 5\,\mathrm{THz}$ were taken into account.

There is also a quite intuitive way to understand the angular dependence of equation (2.28). In the spherical basis, the dipole matrix element between $31P_{3/2}$, $m_J = -3/2$ and $31S_{1/2}$, $m_J = -1/2$ with $q = -1$ can be associated with the emission of a σ_--polarized photon. This cannot be absorbed by the second atom for $\theta = 0$ ($\boldsymbol{R}$ aligned with the quantization axis) in the channel to $32S_{1/2}$, as there is no $m_J = -5/2$ state in the S-state manifold. If, however, the atoms are next to each other with $\theta = \pi/2$, the $q = -1$ dipole projected in this orthogonal direction appears as an emitter of linearly polarized light, whose σ_+-component can be absorbed by the second atom, leading to a finite interaction energy V_{vdW}.

2.3.6 Validity of the dipole approximation

To obtain the results presented in this chapter, the Rydberg atoms have been described as non-overlapping charge distributions, interacting via electrostatic interactions. This approximation is valid as long as their separation $R = |\boldsymbol{R}|$ is small enough to neglect retardation effects caused by the finite speed of light of the photons mediating the interactions [140]. For Rydberg states with $n \approx 30$ this is the case if the

separation of two atoms is less than approximately 100 µm, and this bound increases like n^3, analogous to the inverse of the nearest-neighbor level spacing [113, 141].
For smaller separations, within the framework of electrostatic interaction, higher order multipole interactions become relevant, see equation (2.12). While higher order terms in principle always improve the accuracy of the calculated potentials, once the corrections are below an a priori set level in the region of interest for R, the expansion can be terminated.
Finally, for the electrostatic approximation for the atoms to be valid it is necessary that R exceeds the so-called "Le-Roy-radius" $R \gg R_{LR} = 2(2\langle r^2 \rangle)^{1/2}$, where $\langle r^2 \rangle^{1/2}$ denotes the root-mean-square radius of the charge distributions, which are here considered to be identical for the sake of simplicity [95, 114, 142]. Below this distance, quantum mechanical exchange processes between the atomic electrons gain importance and the description by a simple electrostatic interaction is not sufficient.
Taking as an example two atoms in the state $31P_{1/2}$, from the atomic wave function we obtain $\langle r^2 \rangle^{1/2} \approx 68\,\text{nm}$, yielding $R_{LR} \approx 190\,\text{nm}$ as an approximation of the Le-Roy-radius. This is significantly smaller than the separation $a_{\text{lat}} = 532\,\text{nm}$ of two neighboring atoms in the optical lattice used for all experiments (see chapter 3). Of course, for higher principal quantum numbers n, the validity of the approximation has to be verified due to the scaling $\langle r^2 \rangle^{1/2} \propto n^2$ (see section 2.2). For the state $68S_{1/2}$ used for the measurements of the fully blockaded ensemble presented in chapter 4, we obtain $\langle r^2 \rangle^{1/2} \approx 350\,\text{nm}$ and an increased $R_{LR} \approx 1\,\mu\text{m}$. This implies that the simple van-der-Waals interaction scaling cannot assumed to be valid for atoms occupying neighboring sites in the optical lattice any longer, even if higher order multipole interactions are taken into account. This might cause imperfect blockade and contribute to decoherence.

2.4 From dipole blockade to Rydberg dressing

In the following, the interaction between two atoms in their Rydberg states will be extended by including an optical coupling to a ground state. This will lead to the important concept of the so-called "Rydberg blockade", as well as an effective "Rydberg-dressed" interaction between two ground states coupled to Rydberg states. Both effects have been extensively used and studied in the experiments described in this thesis, see chapters 4, 6 and 7.

2.4.1 Rydberg interactions in the presence of a light field

We start the discussion by introducing a general model of many atoms, each optically coupled to a Rydberg state. The atoms are assumed to be distinguishable, as it

is for example the case if they are held in an optical lattice in different lattice sites. In developing this model, we constrain the discussion to a single ground state $|g\rangle$ coupled to a single Rydberg state $|r\rangle$, with a coupling strength Ω for each atom. As in the previous section, we do not explicitly write out all quantum numbers for the two states, but implicitly assume that $|g\rangle$ embraces all quantum numbers to uniquely describe the ground state and equivalently for $|r\rangle$. Equation (2.5) shows how to calculate the Rabi frequency in this setting. We will furthermore allow for a detuned coupling of ground and Rydberg state and therefore introduce a detuning Δ, which we assume to be positive if the light is blue detuned with respect to the atomic transition. For the interaction between two atoms in their Rydberg states at positions $\boldsymbol{i}$ and $\boldsymbol{j}$ separated by a distance $R_{\boldsymbol{ij}} = |\boldsymbol{i} - \boldsymbol{j}|$, we will for simplicity assume an isotropic van-der-Waals interaction $V(R) = -C_6/R_{\boldsymbol{ij}}^6$, which can be realized experimentally by a proper choice of the quantization axis. Taken together, the Hamiltonian describing N interacting two-level atoms in the rotating-wave approximation at lattice position $\boldsymbol{i}$ reads [55, 57, 143–145]

$$\begin{aligned}\hat{H} &= \frac{\hbar\Omega}{2}\sum_{\boldsymbol{i}}^{N}\left(|g\rangle_{\boldsymbol{i}}\langle r|_{\boldsymbol{i}} + |r\rangle_{\boldsymbol{i}}\langle g|_{\boldsymbol{i}}\right) - \hbar\Delta\sum_{\boldsymbol{i}}^{N}|r\rangle_{\boldsymbol{i}}\langle r|_{\boldsymbol{i}} - \sum_{\boldsymbol{i}<\boldsymbol{j}}^{N}\frac{C_6}{R_{\boldsymbol{ij}}^6}|r\rangle_{\boldsymbol{i}}\langle r|_{\boldsymbol{i}}|r\rangle_{\boldsymbol{j}}\langle r|_{\boldsymbol{j}} \\ &\equiv \hat{H}_\Omega + \hat{H}_\Delta + \hat{H}_{\text{int}}.\end{aligned} \tag{2.29}$$

Without further approximations, the exact treatment of this Hamiltonian is a formidable task due to the exponential increase of the Hilbert space size in the number of atoms like 2^N. We will therefore discuss a simpler model of only two atoms with two states each, which contains the essential physics and allows for gaining some intuition. The N-atom model will be considered again in the case of dominating interactions and resonant excitation in the so-called superatom regime in chapter 4. The emergence of dressed interactions for off-resonant coupling in many-body systems will be discussed in more detail in chapter 6.

2.4.2 Blockade and dressed interactions in a two-atom system

Constraining the number of atoms to $N = 2$, the Hamiltonian defined in equation (2.29) becomes much simpler, see Fig. 2.8 for an illustration of this configuration. In the basis of two-atom states $|g, g\rangle$, $|r, g\rangle$, $|g, r\rangle$ and $|r, r\rangle$, and assuming the same detuning Δ for the two atoms, we obtain

$$H = \begin{array}{c} \\ |g,g\rangle \\ |g,r\rangle \\ |r,g\rangle \\ |r,r\rangle \end{array} \begin{array}{c} \begin{array}{cccc} \langle g,g| & \langle g,r| & \langle r,g| & \langle r,r| \end{array} \\ \begin{pmatrix} 0 & \hbar\Omega/2 & \hbar\Omega/2 & 0 \\ \hbar\Omega/2 & -\hbar\Delta & 0 & \hbar\Omega/2 \\ \hbar\Omega/2 & 0 & -\hbar\Delta & \hbar\Omega/2 \\ 0 & \hbar\Omega/2 & \hbar\Omega/2 & -2\hbar\Delta + V(R) \end{pmatrix} \end{array}. \tag{2.30}$$

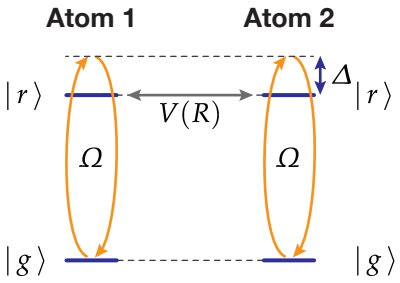

Figure 2.8: Schematics for two light-coupled interacting atoms. Two atoms with a ground state $|g\rangle$ coupled to a Rydberg state $|r\rangle$ (blue solid lines) with coupling Ω (curved orange arrows) detuned by Δ (vertical arrow). In presence of Rydberg interactions $V(R)$, this system exhibits both Rydberg blockade and dressed interactions (see main text).

Investigating the structure of equation (2.30), we note that the coupling of the states $|g,\, r\rangle$ and $|r,\, g\rangle$ to the states $|g,\, g\rangle$ and $|r,\, r\rangle$ is completely symmetrical. This motivates the introduction of the symmetrical and antisymmetrical superpositions $|\pm\rangle = 1/\sqrt{2}(|g,\, r\rangle \pm |r,\, g\rangle)$, for which it is easy to show by direct calculation that $\langle g,\, g|\hat{H}_\Omega|+\rangle = \sqrt{2}\hbar\Omega/2 = \langle r,\, r|\hat{H}_\Omega|+\rangle$ and $\langle g,\, g|\hat{H}_\Omega|-\rangle = 0 = \langle r,\, r|\hat{H}_\Omega|-\rangle$. This implies that the antisymmetric superposition forms a "dark-state" not coupled to light, whereas the symmetric one exhibits an enhanced coupling $\sqrt{2}\Omega$. Considering the coupled states in the symmetric subspace only, the matrix (2.30) can be simplified to

$$H = \begin{array}{c} \\ |g,\, g\rangle \\ |+\rangle \\ |r,\, r\rangle \end{array} \begin{array}{c} \begin{array}{ccc} \langle g,\, g| & \langle +| & \langle r,\, r| \end{array} \\ \begin{pmatrix} 0 & \sqrt{2}\hbar\Omega/2 & 0 \\ \sqrt{2}\hbar\Omega/2 & -\hbar\Delta & \sqrt{2}\hbar\Omega/2 \\ 0 & \sqrt{2}\hbar\Omega/2 & -2\hbar\Delta + V(R) \end{pmatrix} \end{array}. \tag{2.31}$$

Despite its simplicity, this Hamiltonian contains the phenomenology of Rydberg blockade including the superatom dynamics (see also chapter 4), as well as the physics of Rydberg dressing, experimentally studied in chapters 6 and 7.

Rydberg blockade and collective enhancement

We want to start our discussion of these phenomena for vanishing detuning, $\Delta = 0$. The eigenenergies of Hamiltonian (2.31) are shown in Fig. 2.9. For large distances, the eigenenergies of the system are given as the sum of the eigenenergies of two independent atoms in the presence of a light field and the energy of a third symmetric but uncoupled state. Up to a global phase, we explicitly get for the corresponding eigenstates

$$\begin{aligned} |\pm\Omega\rangle &= \frac{1}{\sqrt{2}}(|g\rangle \pm |r\rangle) \otimes \frac{1}{\sqrt{2}}(|g\rangle \pm |r\rangle) \quad (R \gg R_b) \\ |0\rangle &= \frac{1}{\sqrt{2}}(|g,g\rangle - |r,r\rangle). \end{aligned} \tag{2.32}$$

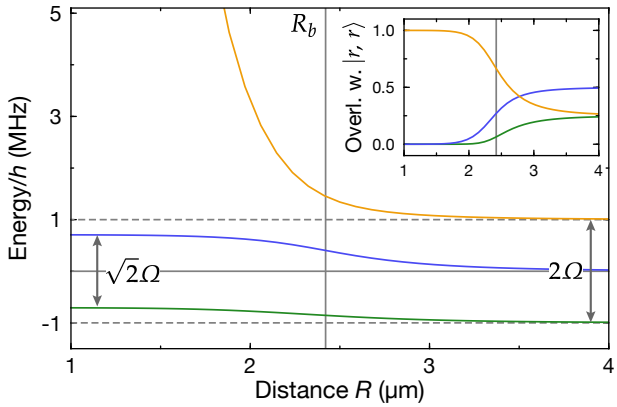

Figure 2.9: Rydberg blockade for two atoms. The main panel shows the eigenenergies of the Hamiltonian (2.31) for $\Omega/2\pi = 1\,\text{MHz}$, $\Delta = 0$ and $C_6 = -h\,201\,\text{MHz}\,\mu\text{m}^6$. For large distances R, the system describes two independent two-level atoms in the presence of a Rabi drive Ω, whereas for small distances R the Rydberg blockade leads to an effective two-level system (blue and green curve), as the doubly excited state $|r, r\rangle$ (orange curve) is detuned by the interaction. The inset illustrates this transition by showing the overlap $|\langle\lambda|r, r\rangle|^2$ of the eigenstates $|\lambda\rangle$ corresponding to the eigenenergies (color-coded) with $|r, r\rangle$. For small distances, $|r, r\rangle$ becomes a good eigenstate and isolates the two remaining states in the "superatom" subspace. The gray vertical line marks the blockade radius R_b as the distance at which this transition happens. The gray horizontal lines are guides to the eye.

It is well known that starting in the state $|g, g\rangle$, independent Rabi oscillations of the individual atoms lead to population of the state $|r, r\rangle$ after half the period $T/2 = \pi/\Omega$. These Rabi oscillations can also be interpreted as a quench to the eigenbasis of Hamiltonian (2.31). In order to reach the doubly excited state $|r, r\rangle$ during the time evolution it has to have finite weight in the eigenstates to which the initial state is projected. Whereas this is the case for two atoms at large separations R, as can be seen in the eigenstates (2.32) and the inset of Fig. 2.9, the situation changes for distances below the so-called "blockade radius", $R < R_b$. Here, the dipole interaction shift renders the state $|r, r\rangle$ an eigenstate and isolates the states $|g, g\rangle$ and $|+\rangle$ in the "superatom subspace", forming an effective two-level system. Specifically, the two eigenstates different from $|r, r\rangle$ are

$$|SA\pm\rangle = \frac{1}{\sqrt{2}}(|g, g\rangle \pm |+\rangle) \quad (R \ll R_b). \tag{2.33}$$

Considering the energies of the two states in Fig. 2.9, the splitting is now enhanced compared to a simple two-level system. This enhanced splitting can be detected by driving Rabi oscillations, i.e. quenching the two-atom ground state now into the su-

peratom basis $|SA\pm\rangle$. As a result, the single atom Rabi frequency acquires the collective enhancement factor $\Omega_2 = \sqrt{2}\Omega$. The missing amplitude of the doubly excited state $|r, r\rangle$ of course also implies that starting in the ground state $|g, g\rangle$, the doubly excited state is not reached during the Rabi cycle. This is the origin of the so-called excitation "blockade", as the maximal number of excitations is limited to one. The blockade radius R_b marks the distance at which the transition from independent atoms to the collective superatom happens, which is the region where the doubly excited state shifts out of resonance. More quantitatively, it can be found by equating interaction energy and coherent coupling and becomes

$$R_b = \left(\frac{|C_6|}{\hbar\Omega}\right)^{1/6}. \tag{2.34}$$

For typical experimental parameters and the Rydberg van-der-Waals interaction of two rubidium-87 atoms, the size of the blockade radius is typically between $1\mu\text{m} < R_b < 10\mu\text{m}$ and hence can be much larger than the interparticle distance. It should be noted that this derivation of the blockade distance relies on resonant and coherent excitation dynamics. In case of incoherent excitation with a dephasing rate $\Gamma > \Omega$, the blockade is given by $R_b = (|C_6|/\hbar\Gamma)^{1/6}$. For off-resonant excitation, the blockade can also be significantly reduced and in the so-called "anti-blockade" regime, the detuning is set to compensate the interaction shift of $|r, r\rangle$, which can then be excited again [146]. This effect has been used in numerous experiments studying facilitated excitation in cold Rydberg gases [147–151].

Rydberg-dressed interactions: Dipolar interactions for the ground state

The second regime where the Hamiltonian (2.31) exhibits interesting physics is the regime of large detunings $|\Delta|/\Omega \gg 1$. In the following, we will derive Rydberg-dressed interactions between two ground state atoms present in this setting and compare them to bare van-der-Waals interactions discussed before.

Rydberg-dressed interactions arise as a distance-dependent modification of the eigenstates and energies of Hamiltonian (2.31) due to Rydberg blockade and hence rely on the interactions between two Rydberg atoms. Considering first large distances where $V \approx 0$, two of the eigenstates of the system are again product states of two independent atoms in a light field with coupling Ω and detuning Δ, see also equation (2.32). Contrary to the preceding discussion in section 2.4.2, however, for large detuning the eigenstates are now close to the three basis states $|g, g\rangle$, $|r, r\rangle$ and $|+\rangle$. The eigenenergies for $\Delta < 0$ are shown in Fig. 2.10 a, and one can see that for large separations R, they are approximately split by $|\Delta|$. In the absence of light coupling, the lowest-energy eigenstate would exactly correspond to the state $|g, g\rangle$ with vanishing energy. For small optical coupling $\Omega \ll |\Delta|$, one can also easily work out the explicit form

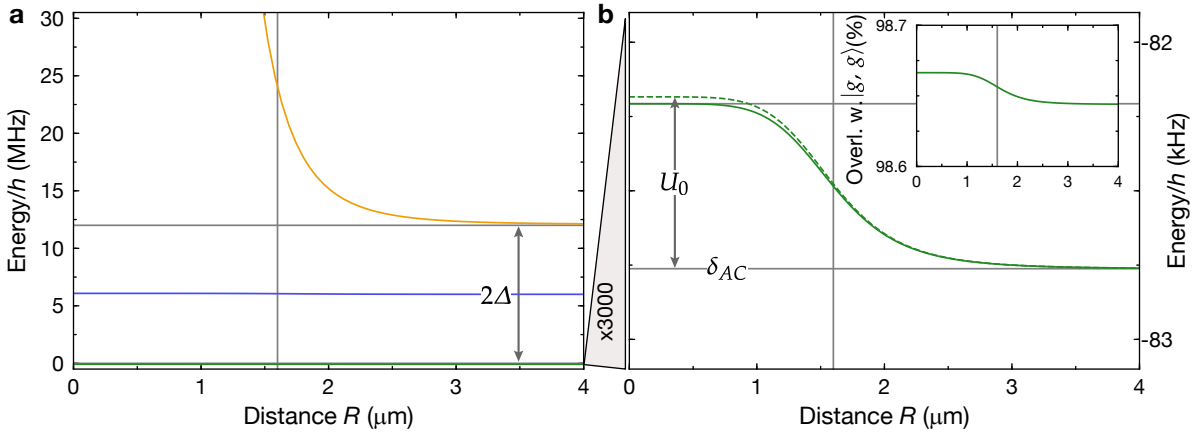

Figure 2.10: Rydberg-dressed potential for two atoms. **a** The three eigenenergies of the Hamiltonian (2.31) are shown for $\Delta/2\pi = -6\,\mathrm{MHz}$, $\Omega/2\pi = 1\,\mathrm{MHz}$ and $C_6 = -h\,201\,\mathrm{MHz}\,\mu\mathrm{m}^6$, see also Fig. 2.9. While at the energy scale of the bare Rydberg-Rydberg interaction no distance dependence is visible, a zoom by a factor 3000 to the lowest-energy eigenstate, indicated by the gray triangle, bears out a distance dependence, see **b**. This distance dependence corresponds to the dressed interaction $U(R)$. The perturbative result (2.38) (dashed green) is in good agreement with the exact eigenenergy (green solid line). The corresponding eigenstate has a large probability overlap with the state $|g, g\rangle$, as indicated in the inset. The characteristic range of the dressed interaction, R_c, is indicated as the vertical gray line in all panels, the horizontal lines are guides to the eye. See main text for further details.

of the eigenstates adiabatically connected to $|g, g\rangle$ up to a normalization constant of order unity (see appendix A), obtaining

$$\begin{aligned} |\tilde{g}, \tilde{g}\rangle &\approx (-|g\rangle + \theta/2|r\rangle) \otimes (-|g\rangle + \theta/2|r\rangle) \quad (R \gg R_c) \\ &= (-|g\rangle + \beta|r\rangle) \otimes (-|g\rangle + \beta|r\rangle). \end{aligned} \tag{2.35}$$

In the last step, we have introduced the small parameter of the "admixture" $\beta = \Omega/(2|\Delta|) \ll 1$ by replacing the mixing angle $\theta = \Omega/|\Delta|$. While the admixture corresponds to the probability amplitude, the actual probability of finding an atom in state $|r\rangle$ is given as β^2. For example for $\Omega/2\pi = 1\,\mathrm{MHz}$ and $\Delta/2\pi = -6\,\mathrm{MHz}$, the probability of finding at least one of the two atoms in a Rydberg state is only approximately $\beta^2 = 1.35\%$, see the inset in Fig. 2.10 b. For the eigenenergies, a finite $\Omega \ll |\Delta|$ leads to an overall negative shift, which corresponds to a light-induced AC-Stark potential [152], see Fig. 2.10 b. One can easily work out that in fourth order of $\Omega/|\Delta|$ this shift amounts to

$$\delta_{AC} = -2 \times \frac{\hbar}{2}(\Delta + \sqrt{\Delta^2 + \Omega^2}) \approx 2 \times \left(\frac{\hbar\Omega^2}{4\Delta} - \frac{\hbar\Omega^4}{16\Delta^3}\right) \quad (R \gg R_c, \Delta < 0). \tag{2.36}$$

The approximation in the last step is valid in the regime $\Omega/|\Delta| \ll 1$ and from Fig. 2.10 b we see that δ_{AC} approaches the eigenenergy of $|\tilde{g}, \tilde{g}\rangle$ asymptotically for large distances $R \gg R_c$, where R_c marks a cut-off distance similar to the blockade radius to be defined below.
Using the dressed pair state $|\tilde{g}, \tilde{g}\rangle$ allows to find the matrix element of the interaction Hamiltonian $\hat{H}_{\text{int}}$ for two atoms, which can be treated as a perturbation as long as it is small enough and provides a first distance-dependent correction to the trivial constant offset,

$$U(R) \approx \langle \tilde{g}, \tilde{g}|V(R)|r, r\rangle\langle r, r|\tilde{g}, \tilde{g}\rangle \approx \beta^4 V(R) \quad (R > R_c). \tag{2.37}$$

This shows that for large separations R between the two atoms, the interaction potential between the dressed ground state atoms has the same character $V(R)$ as the one between the two Rydberg states, however its strength is reduced by the fourth power of the admixture β. This scaling sparks the quite intuitive interpretation that the superposition of ground and Rydberg state in the state $|\tilde{g}\rangle$ admixes some of the interaction between two Rydberg atoms to the dressed ground state atoms. However this cannot be true for all distances, as the previously discussed Rydberg blockade strongly suppresses the admixture of the $|r, r\rangle$ amplitude to the state $|\tilde{g}, \tilde{g}\rangle$ for small R. The eigenenergy obtained by diagonalizing the Hamiltonian (2.31) shown in Fig. 2.10 b rather displays a saturation behavior in that regime.
A better approach to understand the specific shape of the interaction is a perturbative treatment as done in reference [62]. To this end, we start from the states $|g, g\rangle$, $|+\rangle$ and $|r, r\rangle$, eigenstates of $\hat{H}_\Delta + \hat{H}_{\text{int}}$, and treat the light-coupling $\hat{H}_\Omega$ as a perturbation, focussing on the corrections to the energy of the state $|g, g\rangle$. The motivation thereby is that in a typical experiment, all atoms are prepared in the ground state and we assume that the light field is turned on adiabatically with a rate slow enough to not induce diabatic excitations into $|+\rangle$, or $|r, r\rangle$, protected by a gap Δ, see Fig. 2.11. Using the matrix elements $\langle g, g|\hat{H}_\Omega|+\rangle = \hbar\Omega/\sqrt{2} = \langle r, r|\hat{H}_\Omega|+\rangle$, one arrives at the energy corrections to the ground state up to fourth order in the small parameter β [62, 128, 131]

$$\begin{aligned} E_{gg}^{(1)} &= E_{gg}^{(3)} = 0 \\ E_{gg}^{(2)} &= \frac{|\langle g, g|H_\Omega|+\rangle|^2}{-E_+} = \frac{\hbar\Omega^2}{2\Delta} \\ E_{gg}^{(4)} &= \frac{|\langle g, g|H_\Omega|+\rangle\langle +|H_\Omega|r, r\rangle|^2}{E_+^2(-E_{rr})} - \frac{|\langle g, g|H_\Omega|+\rangle|^4}{E_+^2(-E_+)} \\ &= \frac{\hbar\Omega^4}{4\Delta^2(2\Delta - V(R)/\hbar)} - \frac{\hbar\Omega^4}{4\Delta^3}. \end{aligned} \tag{2.38}$$

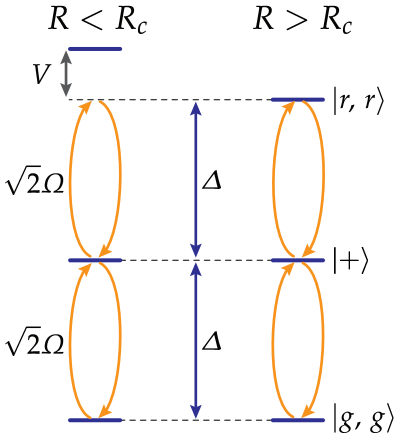

Figure 2.11: Illustration of perturbative derivation of dressed potential. Perturbing the eigenstate $|g, g\rangle$ (blue solid line) by the light coupling $\hat{H}_\Omega$ yields the dressed interaction. The coupling Ω (orange curved arrows) to the states $|+\rangle$ and $|r, r\rangle$ is detuned by Δ. For small distances $R < R_c$, the interaction V adds to the detuning of $|r, r\rangle$, resulting in the characteristic soft-core interaction (see main text). Four photons have to be off-resonantly absorbed and emitted to reach $|r, r\rangle$ starting in and returning to $|g, g\rangle$, resulting in a fourth-order effect.

The perturbative result $E_{gg}^{(4)}$ contains the interaction potential and a constant offset. Comparing the perturbative corrections to the ground state energy $E_{gg}^{(2)} + E_{gg}^{(4)}$ for large R with the expansion of the exact light shift δ_{AC}, see equation (2.36), we notice that both agree up to fourth order. Hence, the light shift can be subtracted, yielding the interaction potential

$$\begin{aligned} U(R) &= E_{gg}^{(2)} + E_{gg}^{(4)} - \delta_{AC} \\ &\approx \frac{\hbar\Omega^2}{2\Delta} + \frac{\hbar\Omega^4}{4\Delta^2(2\Delta - V(R)/\hbar)} - \frac{\hbar\Omega^4}{4\Delta^3} - 2\left(\frac{\hbar\Omega^2}{4\Delta} - \frac{\hbar\Omega^4}{16\Delta^3}\right) \\ &= \frac{U_0}{1 + (R/R_c)^6}. \end{aligned} \tag{2.39}$$

In the last step, we have assumed $\Delta < 0$ and a repulsive potential $V(R) = |C_6|/R^6$ to define the cut-off distance R_c and the soft-core height U_0 to which the interaction potential saturates for $R \to 0$. They are given as

$$R_c = \left(\frac{|C_6|}{2\hbar|\Delta|}\right)^{1/6}. \tag{2.40}$$

and

$$U_0 = 2\hbar\Delta\beta^4 = \frac{\hbar\Omega^4}{8\Delta^3}. \tag{2.41}$$

Using these relations and expanding the potential $U(R)$ for large distances $R > R_c$, we obtain $U(R) \approx \beta^4 C_6/R^6$, consistent with equation (2.37). Interestingly, the bare interaction strength of the two atoms in the Rydberg state, quantified by C_6, does not enter the height U_0 of the soft core, which only depends on the light coupling parameters Ω and Δ. The cut-off distance R_c, however, increases with the van-der-Waals interaction strength. Looking at the expression for R_c, one notices that it is very similar

to the blockade radius defined in equation (2.34). The interpretation of the similarity between R_b and R_c is straightforward: Analogous to the blockade, also the dressed potential is caused by a change in the structure of the eigenstates due to the interaction shift of $|r, r\rangle$, see also the inset of Fig. 2.10 b. For the dressing, the crossover can be found by matching the interaction energy with the detuning 2Δ of the pair state. This equality defines R_c.
Comparing the perturbative result for $U(R)$ with the exact eigenenergy shown in Fig. 2.10 b, one can see that both are in very good agreement. However, the exact interaction strength is slightly smaller as, of course, the approximate result derived above is expected to break down when increasing the small perturbation parameter β. To find the soft-core height U_0 also for larger admixtures, we note that analogous to the discussion of the blockade, for $R \ll R_c$, the two-atom system is limited to the superatom subspace with enhanced coupling $\Omega_2 = \sqrt{2}\Omega$ to the symmetric superposition $|+\rangle$. The eigenenergy there is $E_{SA-} = -\frac{\hbar}{2}(\Delta + \sqrt{\Delta^2 + 2\Omega^2})$. This allows to find the soft-core height for two atoms at arbitrary admixture as the difference to the AC-Stark shift [153, 154]

$$\begin{aligned} U_0 = E_{SA-} - \delta_{AC} &= -\frac{\hbar}{2}(\Delta + \sqrt{\Delta^2 + 2\Omega^2}) + 2 \times \frac{\hbar}{2}(\Delta + \sqrt{\Delta^2 + \Omega^2}) \\ &\approx \frac{\hbar\Omega^4}{8\Delta^3}. \end{aligned} \tag{2.42}$$

The expansion in the second step shows that in the weak dressing regime $\beta \ll 1$, the same result as in the perturbative treatment is recovered.
In the preceeding derivation of the dressed interaction potential we have assumed a repulsive van-der-Waals interaction and red-detuned light $\Delta < 0$ to derive the soft-core potential. A similar result could have been obtained with an attractive van-der-Waals potential and blue detuning, however the soft core would have become attractive as well. In the cases where $\Delta \cdot V(R) > 0$, i.e. attractive interactions and red detuning or repulsive interactions and blue detuning, resonances appear where the energies of $|g, g\rangle$ and $|r, r\rangle$ become equal. In the presence of light coupling, an avoided crossing opens. For blue detuning and repulsive interactions, this results in a "blue-shield potential" which has been proposed to be used for quantum simulation of roton physics in a cold quantum gas [63]. In the experiments described in this thesis, we only work with either attractive interactions and blue detuning or repulsive interactions and red detuning, see chapters 6 and 7. Finally, even though the discussion above was limited to two atoms, the interaction potential in a many-body setting can be reduced to a sum of two-body terms [62]. This will be shown and discussed in chapter 6.

2.4.3 Lifetime of a dressed atom

In the last section we have derived the dressed interaction between two atoms off-resonantly coupled to a Rydberg state. The question one may immediately ask is: What has been gained by using off-resonant admixture rather than a direct excitation into the Rydberg states via resonant light? One possible answer lies in the lifetime of a Rydberg-dressed atom. If separated further than R_c, inspection of the dressed eigenstates $|\tilde{g}\rangle \approx (-|g\rangle + \beta|r\rangle)$ defined in equation (2.35) allows to conclude that due to the small probability β^2 of populating the Rydberg state $|r\rangle$, the lifetime τ_{eff} of $|\tilde{g}\rangle$ is given by extending the bare Rydberg state lifetime τ to [62, 63]

$$\tau_{\text{eff}} = \tau/\beta^2. \tag{2.43}$$

In the limit of weak Rydberg state admixture, this increased effective lifetime can be on the order of milliseconds. For coherent quantum simulations of many-body dynamics, the decoherence time has to be compared to the time scale set by the interaction strength to figure out whether coherent interaction-driven dynamics is possible. For dressed interactions, one obtains by combining equations (2.37) and (2.43)

$$U(R) \cdot \tau_{\text{eff}} = \beta^2 V(R)\tau \quad R \gg R_c. \tag{2.44}$$

The product $V(R)\tau$ is the lifetime-interaction product for direct excitation and in the weak dressing regime with $\beta \ll 1$, the interaction to lifetime product is reduced compared to what could be achieved with resonant excitation. Despite this apparent drawback, there are also arguments in favor of an off-resonant admixture. We will briefly discuss them in the following and compare dressed and bare interactions.

2.4.4 Rydberg-dressed versus bare Rydberg interactions

Motional time scales

Inducing interactions via off-resonant coupling to a light field has originally been discussed for generating dipolar Bose-Einstein condensates or lattice gases [61–63, 155]. These systems exhibit a time scale associated with the motion of the particles, given by e.g. the trap frequency or a hopping rate in presence of the lattice. For the interaction to be effective, the lifetime of the gas has to be larger than the motional time scale, which typically exceeds the bare Rydberg state lifetime by orders of magnitude. To be specific, the time scale associated with tunneling in an optical lattice is typically on the order of few milliseconds, whereas the bare Rydberg lifetimes are only tens of microseconds. Off-resonant admixture allows in principle to extend the bare Rydberg state lifetime to exceed the motional time scale, see equation (2.43), such that dipolar effects become relevant for the dynamics.

Switchability of the interactions

If optically admixed, the interactions can be switched on and off controlled by the light field. This is different from the case of the bare dipolar interactions between Rydberg states, which are always present. Optical control allows for example the periodic modulation of the interaction and therefore potentially Floquet-engineered quantum systems [78, 156].

Trapping

For alkali atoms, bare Rydberg states experience a ponderomotive light potential [157–159] due to their nearly free electrons and are therefore attracted to intensity minima of optical traps. Consequently, in red-detuned optical lattices or dipole traps, where the trap minima and hence equilibrium positions of ground state atoms coincide with the intensity maxima of the light field [3, 152] atoms excited to Rydberg states are repelled from those positions [160]. This induces motional dephasing and sets a limit on achievable coherence [161] unless specially designed traps are implemented [162–165] or the lattice is inverted after exciting the Rydberg state [160]. For atoms interacting via optically admixed interactions, the trapping is automatically guaranteed for small β if the undressed ground state is trapped [166], and the small admixture of anti-trapped Rydberg state only slightly reduces the trap depth.

Detection

Next to the problematic trapping, achieving high detection fidelity, potentially with spatial resolution, has proven difficult to achieve for Rydberg states. The used techniques span from ionizing Rydberg states and detection of the produced ions [147, 148, 167–169] to indirect detection of the Rydberg states due to trap loss [51, 52, 58] and depumping Rydberg atoms back to a ground state, which can then be imaged [55], see also chapter 5. While progress has been made to improve all these techniques, they do not yet match the detection capabilities achieved for ground state atoms, among them time-of-flight detection [3] of momentum distributions, or the powerful techniques provided by quantum gas microscopes [10, 11]. For Rydberg-dressed ground state atoms, all of these techniques can be immediately employed if the dressed ground state is adiabatically transformed to a bare ground state for detection.

Character of the interaction

The bare Rydberg interaction in absence of Förster resonances with its van-der-Waals characteristic $V(R) = -C_6/R^6$ exhibits a fast drop with distance. This has consequences for the complexity of resulting many-body models, as very often the interaction is extremely strong (see e.g. chapter 4) and dominates on length scales small com-

pared to the blockade radius. This can strongly reduce the size of the relevant Hilbert space [55, 57]. For larger separations, however, the interaction is too weak to significantly influence the dynamics on the rather short experimentally accessible time scales. To be more specific, the interaction strength reduces by a factor of $2^{-6} = 1/64$ when the internuclear distance of two atoms is doubled. Rydberg-dressed interactions are of different character, mainly due to the saturation of the interaction energy at small distances. As an example, in chapter 7 we work with a potential where the ratio between the interaction energies of two atoms separated by one and two lattice sites respectively is only $1/5$. Thus, the Hilbert space size cannot generally be reduced much and the resulting dynamics is more difficult to model. Furthermore, the extended soft-core plateau is a very unusual type of interaction, leading to predictions of exotic many-body phases like supersolidity [62, 63] or cluster liquids with large degeneracies [170].

Exotic interaction potentials

Using light-induced interactions in the vicinity of Förster resonances has been proposed as a way to engineer interactions with an exotic distance dependence between ground state atoms [67]. It has been proposed that this can also be exploited for implementing many-body models with dynamical gauge constraints, paving the way to performing coherent quantum annealing tasks [68].

2.5 Summary and outlook

In this chapter, we have described Rydberg atoms, their dipolar interaction and the resulting effective van-der-Waals potential. Including a light field in the description, the concepts of Rydberg blockade and Rydberg-dressed interactions were introduced. Both were described in a simple two-atom system, which, however, captures the most important effects. These simple two-atom systems will be extended to more atoms in chapter 4, where the experiments on a collective superatom with many atoms within the blockade volume will be described. Chapters 6 and 7 will treat the generalized model for Rydberg-dressed interactions. In the following chapter we will start tackling this route by describing the technology necessary for the preparation and detection of many-body systems in the ground state (chapter 3), the starting point of all experiments described thereafter.

Chapter 3

Single-site-resolved detection of ultracold gases

3.1 Introduction

Ultracold quantum gases have become a very successful platform to study quantum systems from the non-interacting to the strongly correlated regime. The advent of quantum gas microscopes for bosonic [10–12] and fermionic [13–17] atoms has provided access to microscopic quantities such as spin and density correlations [17, 18, 22, 24–26, 171] but also proven extremely beneficial for the preparation of non-equilibrium initial states [28, 29], whose time evolution can then be studied. In this chapter, we will review the details of the experimental platform – a bosonic quantum gas microscope for rubidium-87 atoms – which was used to obtain the results presented in this thesis. The discussion will be kept to an absolute necessary minimum and emphasize the aspects relevant for the experiments described in this thesis. Technical details of the setup, both for preparation and detection of the quantum gas, have been described in other theses emerging from the same experiment [115, 172–174].

3.2 Preparation of two-dimensional quantum gases

Reaching the quantum degenerate regime of an atomic gas of rubidium-87 requires several cooling stages. Details of the exact procedure can be found in reference [173] and references therein and here we summarize only the main steps.
The preparation started by loading a $2D^+$-magneto-optical trap (MOT) [175] from the background pressure of gaseous rubidium at room temperature in the 2D-MOT chamber, forming an atomic beam along one axis. Passing through a differential pumping section, this beam loaded a 3D-MOT. After a compressed-MOT phase and molasses cooling, the atoms were loaded into a magnetic trap and forced radio-frequency (RF) evaporation to the untrapped $|F = 2, m_F = -2\rangle \equiv |2, -2\rangle$ ground state of rubidium-87 was performed for a duration of 6 s, which was decreased compared to what is described in reference [173] by using faster frequency ramps and higher RF power.

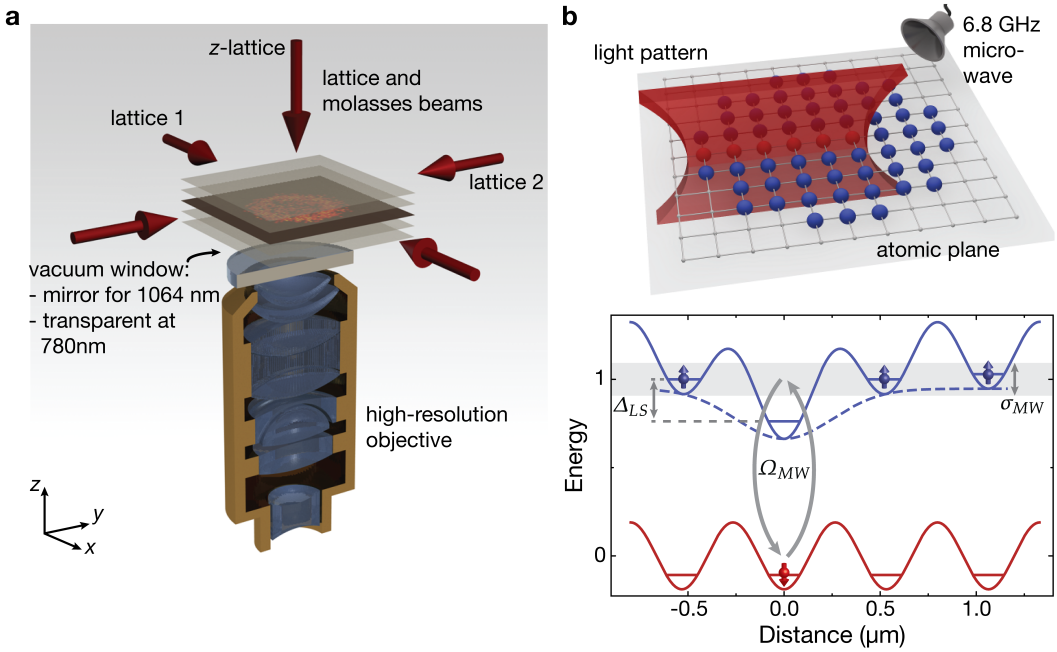

Figure 3.1: Quantum gas microscope and single-site addressing. **a** Single plane of the vertical z-lattice holding a two-dimensional degenerate quantum gas with lattice and molasses axes indicated. The fluorescence photons are collected with the high-resolution objective ($NA = 0.68$) located below the atoms. Figure adapted from [11]. **b** Illustration of single-site addressing. A controlled spatially varying light pattern is engineered with a digital micromirror device (DMD). This creates local differential AC-Stark shifts, which can be used to selectively flip the spin of the atoms with a microwave at a frequency of 6.835 GHz (see lower panel). Figure adapted from [27].

From the magnetic trap, the atoms were transferred into an optical transport trap and conveyed to the "science chamber" using a moving stage to shift the focus of the trap. After that, the atoms were loaded into a crossed optical dipole trap and, following a subsequent evaporation, a retro-reflected vertical optical lattice with lattice constant $a_{\mathrm{lat}} = 532\,\mathrm{nm}$ and lattice depth V_z propagating along the z-direction was switched on. The beam of the vertical optical lattice was directly reflected off the lower vacuum window, see Fig. 3 a. From the resulting two-dimensional atomic planes, a single one was selected by combining a vertical magnetic field gradient and a microwave sweep narrow enough in frequency to discriminate a single plane in the vertical optical lattice from the others, which were then removed from the trap via a resonant push-out on the D_2-cycling transition [102]. The final two evaporation steps were performed first in the vertical lattice and subsequently in a tight dimple trap, by applying a magnetic field gradient in the atomic plane. The dimple also stabilized the atom number via three-body collisions, which limit the atomic density in

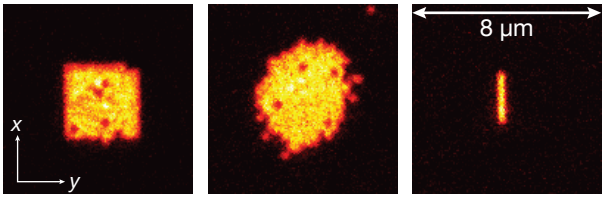

Figure 3.2: Fluorescence images. Representative single shots of atomic distributions. The images from left to right show an addressed array of 12×12 atoms, a Mott insulator of approximately 170 atoms and a one-dimensional spin chain of 10 atoms. These samples were used as starting states in the experiments described in chapters 4, 6 and 7 respectively.

the tight trap volume. After the dimple evaporation, two-dimensional spin-polarized degenerate gases in the state $|1, -1\rangle$ with up to 500 atoms and temperatures of few nano-Kelvin were obtained. For most of the experiments described in this thesis, we prepared degenerate gases of about 200 atoms and drove them quasi-adiabatically to a Mott insulating state with exactly one atom per filled site [11, 176, 177]. To this end, two retro-reflected lattices along the x- and y-directions with lattice constant $a_{\mathrm{lat}} = 532\,\mathrm{nm}$ and depths V_x and V_y were ramped up in an s-shape to slowly cross the transition from the superfluid to the Mott insulator. A second s-shape ramp was then used to bring the system deep into the atomic limit, where tunneling of the atoms between sites is strongly suppressed, see also Fig. 3.1 a. For example, in the configuration $(V_x, V_y, V_z) = (40, 40, 80)\,E_{\mathrm{r}}$ used for the experiments in chapters 4, 6 and 7, the tunnelling rate was 0.23 Hz along the x- or y-lattice and therefore negligible for the duration of a typical experiment of maximally 4 ms. Typically, by the described preparation procedure more than 97 % of the sites in the optical lattice were filled with exactly one atom within the Mott-insulating region.

3.3 Fluorescence imaging of atoms in optical lattices

Details of the imaging can be found in reference [172]. To detect the atomic distribution after an experiment, all three lattices were simultaneously increased to depths of about $3000\,E_{\mathrm{r}}$ per axis to tightly trap the atoms. Then, optical molasses cooling was performed on the D_2-transition of rubidium-87 with two counter-propagating molasses beams in $\sigma_+ - \sigma_-$-polarization configuration along the lattice axes in the atomic plane, see Fig. 3.1 a. A third beam was shone in through the objective to couple and therefore also cool along the z-axis. However, when blocking this beam no negative effects on the cooling were observed. The scattered photons were collected with a high-resolution objective with a numerical aperture of $NA = 0.68$, providing a resolution of approximately 700 nm at a wavelength of 780 nm. While by itself this would

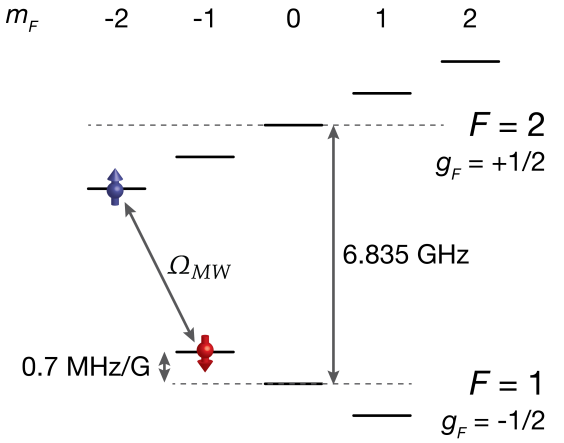

Figure 3.3: Spin system in rubidium-87. The ground state manifold $5S_{1/2}$ of rubidium-87 provides a pseudo-spin-1/2 system consisting of the magnetic hyperfine structure levels $|F = 2, m_F = -2\rangle = |\uparrow\rangle$ and $|F = 1, m_F = -1\rangle = |\downarrow\rangle$ with opposite Landé g_F-factors leading to opposite shifts in the magnetic field. Transitions are driven via a microwave with coupling Ω_{MW} at a frequency of 6.835 GHz [102].

not be sufficient to optically resolve two atoms on neighboring sites of the optical lattice with lattice spacing $a_{\mathrm{lat}} = 532\,\mathrm{nm}$, a reconstruction algorithm [57] based on the known underlying lattice structure allowed for a full reconstruction of the parity of the local occupation number of a given site in the optical lattice. The full density distribution is inaccessible by the fluorescence detection due to a pairwise loss of atoms via light-assisted collisions [178]. Thereby, molecules of two rubidium-87 atoms in the $5S$ and $5P$ state respectively are formed far from their equilibrium distance. Releasing their excess kinetic energy, they are subsequently lost from the trap within approximately 100 µs, which is well below the imaging time scale of approximately 1 s. In the experiments described in this thesis, in most cases the local occupation was kept at or below one atom per site and hence the light-assisted loss is not immediately relevant.

3.4 Single-site addressing

The high resolution of the quantum gas microscope described before enables next to the local detection of individual atoms also a local addressing of selected atoms. Details of the addressing procedure and the underlying technology are described in [27, 172, 174, 179]. Local addressing here means that the spins of selected atoms in the optical lattice can be flipped. In order to achieve this, a spatially varying controllable light pattern is generated in the atomic plane using an addressing laser, which creates spatially dependent differential AC-Stark shifts between the states $|2, -2\rangle$ and $|1, -1\rangle$. To be able to selectively shift only one of the two states, the wavelength of the addressing laser is chosen close to the magic wavelength of rubidium-87 at 787.56 nm [27], see Fig. 3.1 b. Depending on the microwave detuning, either the spin of the shifted or the unshifted atoms can be flipped. The resulting spin pattern is converted to a density distribution with a spin-selective resonant optical push-out on the

D_2-transition. The spatially dependent programmable light pattern is created with a digital mirror device (DMD) [179] and then imaged to the atomic plane through the high-resolution objective. The DMD is an array of 1024×768 mirrors, which can be switched individually "bright" or "dark", allowing for the creation of the required patterns. Gray-scale values are realized by oversampling every lattice site area of size a_{lat}^2 with approximately $7.7 \times 7.7 = 60$ DMD pixels and applying an error diffusion algorithm [179]. In order to optimize the performance, residual inhomogeneities on the light pattern are corrected in the atomic plane via spatially resolved microwave spectroscopy [174] and the relative position of light pattern and the lattice structure is stabilized via a phase feedback algorithm [172]. The good spatial control over the addressed region combined with the unity-filling initial state allows for preparation of samples with sub-shot-noise total-atom-number fluctuations, see chapter 4. Exemplary density distributions which were obtained by the addressing technique are shown in Fig. 3.2.

3.5 Spin physics in the ground state

Rubidium-87 offers in total eight different spin states in the two hyperfine ground state manifolds $F = 1$ and $F = 2$, see Fig. 3.3. In the experiments discussed in chapters 6 and 7, we use the two states $|2, -2\rangle$ and $|1, -1\rangle$ to encode spin up, $|\uparrow\rangle$, and spin down, $|\downarrow\rangle$, respectively. This spin basis was used before in our experiment with superexchange-mediated spin interactions [28, 29, 71, 72]. Spin changing collisions [180] are absent for single atoms in single sites. The spin relaxation of the $F = 2$ state is also negligible for all experiments performed. The magnetic offset field is applied to set a quantization axis and to isolate the spin basis, such that spin flips can be induced via a microwave. Here, coupling strengths of up to $\Omega_{MW}/2\pi = 40\,\mathrm{kHz}$ can be reached for the transition between $|\uparrow\rangle$ and $|\downarrow\rangle$ in our experiment. The differential magnetic field shift of the transition is $2.1\,\mathrm{MHz/G}$. For typically realized interactions and microwave couplings on the order of 20 kHz in our experiments, magnetic field stabilities of roughly 1 mG are required in order to be able to control the spin dynamics. Both homogeneous and inhomogeneous effects [181] limit the achievable Ramsey dephasing times to approximately $T_2 = 110\,\mu\mathrm{s}$, dominated by shot-to-shot global magnetic field fluctuations which lead to inhomogeneous spin dephasing. Their effect can be suppressed by applying a spin echo pulse, increasing the dephasing times significantly to approximately $T_2' = 3\,\mathrm{ms}$. Alternatively, the spin system could be encoded on the the clock ($|1, 0\rangle \leftrightarrow |2, 0\rangle$) or magnetic field insensitive transitions ($|1, -1\rangle \leftrightarrow |2, 1\rangle$) with the disadvantage of lower microwave coupling strength and generally also less optical coupling strength to the Rydberg manifold due to reduced Clebsch-Gordan coefficients. Furthermore, a large differential magnetic moment of the two atoms allows for implementing a spin-selective detection by applying a mag-

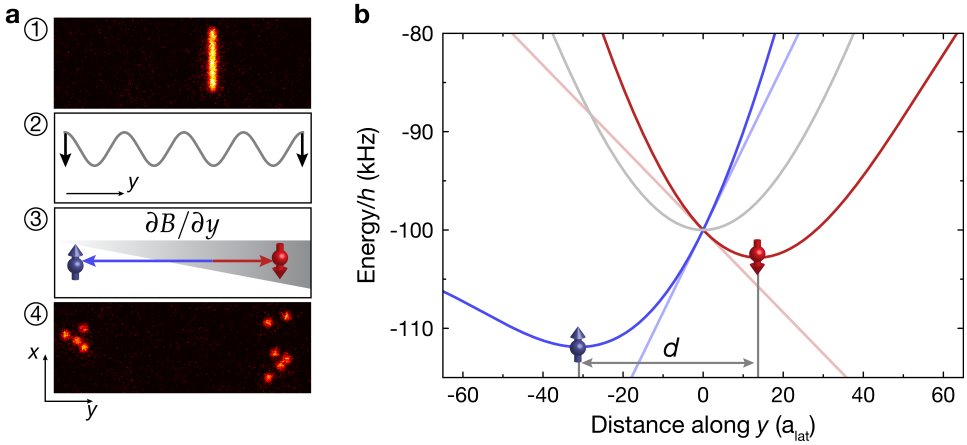

Figure 3.4: Separation in Stern-Gerlach sequence. **a** Schematic of *in-situ* Stern-Gerlach spin-selective detection of a spin chain after a measurement (1), followed by (2) switch-off of y-lattice to induce tunneling along y, (3) adiabatic ramp-up of magnetic field gradient to separate the atoms in the states $|2,-2\rangle$ and $|1,-1\rangle$ respectively and (4) fluorescence image of frozen density with spin encoded in the position along y. **b** Calculation of spin-dependent potentials. The combined potential of the Gaussian envelope of lattices along the x- and z-direction is shown in gray (waist and depth $w_x = 70\,\mu\text{m}/w_z = 55\,\mu\text{m}$ and $V_x = 40\,E_\text{r}/V_z = 60\,E_\text{r}$ respectively). The magnetic field gradient of $11.25\,\text{G/cm}$ leads to a spin-dependent shift of the minimum of the potential. The resulting potentials for $|2,-2\rangle$ and $|1,-1\rangle$ are shown in blue and red, the separation of their minima is denoted as d. The respective gradients are displayed in light blue and light red. The gradient for $|2,-2\rangle$ is so strong that the full Gaussian shape of the potential becomes relevant, leading in this case to a softer trap.

netic field gradient, which will be discussed in the next section.

3.5.1 Spin-selective detection

In order to read out the spin states of the atoms, one spin component can be removed from the optical lattice. In our experiments we typically apply a resonant optical push-out to the $F = 2$ manifold on the D_2-transition. If the system is initially prepared with approximately unity filling and no atom loss occurs before detection, this procedure allows to infer the spin populations directly by associating the left-over atoms with one spin component and the holes with the other. If, however, there is atom loss present or the initial filling is significantly below unity, the attainable information is restricted to the left-over spin component.
For isolated one-dimensional samples as shown in Fig. 3.2, an *in-situ* Stern-Gerlach sequence circumvents this problem. There, the spin and density in the system can be

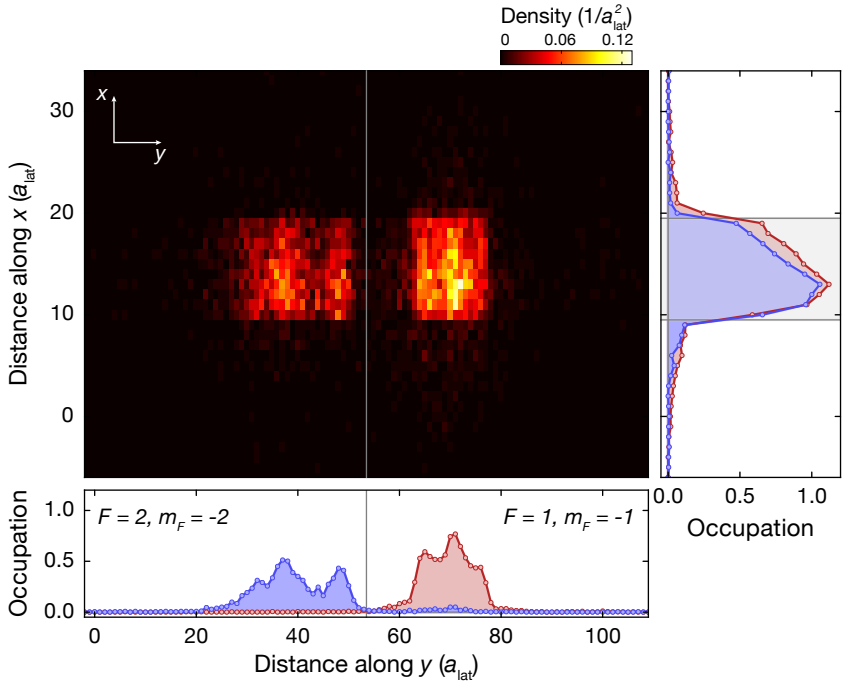

Figure 3.5: Spin-selective detection. The main panel shows the mean density of atoms detected after the *in-situ* Stern-Gerlach sequence for an initially prepared spin chain of length $10\,a_{\mathrm{lat}}$ along the x-direction, averaged over many experimental runs. The panel on the right shows the density of atoms in state $|2,-2\rangle$ and $|1,-1\rangle$, averaged along the y-direction, in blue and red respectively. The lower panel equivalently displays the average along the x-direction. The vertical line marks the line of separation between assigning the state $|2,-2\rangle$ or $|1,-1\rangle$ to a detected atom.

read out at the same time. The sequence for this type of detection has been described in [174]. The main steps are summarized in Fig. 3.4 a. At the end of the experiment which requires spin-selective readout, see e.g. the spin dynamics measurement discussed in chapter 7, the optical lattice along the y-direction is adiabatically switched off, such that the atoms are only subjected to the combined potential of the x-and z-lattices due to their Gaussian beam envelope. Subsequently, a magnetic field gradient of strength $\partial B/\partial y \approx 11.25\,\mathrm{G}$ is adiabatically switched on in the atomic plane, resulting in a spin-dependent additional potential $U(y) = -m_F g_F \mu_B\, y\, \partial B/\partial y$, where μ_B denotes the Bohr magneton. This potential adds to the trapping potential and shifts the minima for the two states $|2,-2\rangle$ and $|1,-1\rangle$ in opposite directions, see Fig. 3.4 b. Provided that the field is ramped slowly enough, the two spin components settle to their new equilibrium positions, separated by a distance d. The spin information is hence encoded in the spatial position in a subsequently acquired fluorescence image. As tunnelling along the initially prepared chain in the x-direction is inhib-

ited throughout the detection sequence, the information of the initial position in the chain is preserved. The spatial separation d between the two spin components can be optimized by slightly lowering the confinement induced by the x- or z-lattice. We found values of approximately $V_z = 60E_\mathrm{r}$ optimal for the latter, leaving the x-lattice at $V_x = 40\,E_\mathrm{r}$.
An experiment performed to asses the quality of the spin-selective imaging is displayed in Fig. 3.5. The initially prepared spin chain was spin-polarized either in the state $|2,-2\rangle$ or in $|1,-1\rangle$. The separation d acquired in the detection sequence is large enough to clearly discriminate the two components, with the overlap small enough to estimate a probability to falsely detect a spin of the order of 2 %. To obtain optimal values for discriminating the two spin components, the position of the line of separation between the two spin components was optimized along the y-direction. The spatial spin distribution along the y-direction is significantly wider for the state $|2,-2\rangle$ compared to $|1,-1\rangle$. This would not be expected if the harmonic approximation for the Gaussian lattice traps was true, as in this case the gradients would just add a translational offset without changing the trap stiffness. Looking at Fig. 3.4 b, it becomes clear, however, that for the full Gaussian potential the strong gradient induces non-linearities in the trapping potential of $|2,-2\rangle$. Effectively, the trap becomes considerably shallower, which explains the striking difference of the widths of the two distributions. Furthermore, the trap softening makes a fully adiabatic detection increasingly difficult. The residual modulation of the average density along the y-direction could be a consequence of non-adiabatic transitions to higher harmonic oscillator levels.

3.6 Summary and outlook

The presented experimental setup and the discussed techniques form the basis of the subsequent chapters. The interactions between Rydberg atoms and especially the Rydberg-dressed interactions discussed in chapter 2 will be harnessed to build spin models in the presented rubidium-87 ground state manifold. The single-atom sensitivity, excellent spatial resolution and near-unity detection efficiency combined with the preparation capabilities provided by the quantum gas microscope will prove indispensable for the described experiments. As a first example, in the next chapter we will present our experimental results on a microscopic study of the so called "superatom", which requires high-fidelity preparation of the atomic density distribution combined with Rydberg excitation and their spatially resolved, single-atom-sensitive detection.

Chapter 4

Microscopic characterization of a superatom

4.1 Introduction

The strong interactions between Rydberg atoms discussed in chapter 2 can dominate other energy scales in a cold quantum gas over large distances. Combining these interactions with the preparation and detection capabilities offered by the quantum gas microscope discussed in chapter 3 enables the production and characterization of strongly correlated quantum states. In particular, in the regime of strong Rydberg blockade, the interactions between Rydberg atoms constrain the dynamics to a subspace with maximally one single excitation. The resulting two-level system has been termed "superatom". Its main characteristic feature is a collectively enhanced coupling to light. Next to demonstrating this enhancement, we perform Ramsey spectroscopy to test the coherence of the superatom and infer the presence of entanglement in the involved states. Finally, we illustrate how the Rydberg blockade breaks down when doubly excited states begin to become optically coupled. The experimental results presented in this chapter are based on the publication [60].

4.1.1 From Rydberg blockade to Rydberg superatoms

Rydberg blockade is one of the most widely studied effects resulting from the interaction between two Rydberg atoms. It was initially observed spectroscopically as a saturation of the number of Rydberg excitations with increasing ground state density [182–184]. Later, the attention was directed towards its use for quantum information, and after its observation for pairs of atoms in optical tweezers [51, 52], the implementation of first coherent quantum gates soon followed [53, 54]. While these experiments were showing the blockade in the minimal two-atom system discussed in chapter 2, Rydberg-blockaded many-body systems exhibit even richer phenomenology, exploited for example for quantum simulation of many-body spin systems [55, 56, 58]. In these experiments, detection was performed by directly or indirectly imaging Rydberg atoms. Combining Rydberg blockade with the detection of photonic states al-

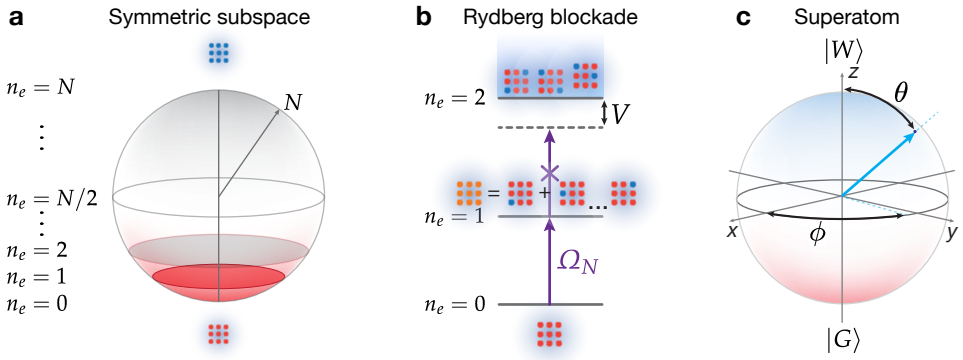

Figure 4.1: The fully blockaded regime. a Symmetrical coupling by a light field gives access to all states invariant under particle exchange. They are represented on the collective Bloch sphere for N atoms and characterized by their number of excitations n_e. **b** In the regime of strong interactions V, all states with $n_e > 1$ are detuned from the optical coupling and the system is restricted to the lowest two symmetrical states $|G\rangle$ and $|W\rangle$ with $n_e = 0$ and $n_e = 1$. The pictograms indicate the spatial structure of the respective states (a red dot represents an atom in the ground state, a blue dot one in a Rydberg state). **c** The resulting two-level system can be represented with angles (θ, ϕ) on a simple two-level Bloch sphere in the basis spanned by the collective ground state $|G\rangle$ and the entangled W-state $|W\rangle$.

lowed for the realization of an efficient single-photon source [185] and even for creating effective interactions between photons [186–188]. Furthermore, the characteristic enhanced many-body Rabi oscillations expected in the fully blockaded regime [59] were for the first time observed in a photonic signal [185], overcoming difficulties limiting the oscillation contrast in previous experiments [189–192]. Observing the involved atomic states in the fully blockaded regime is of particular interest due to the entanglement which is expected to be present in those states. Experimentally, however, this is challenging due to the required single-atom sensitivity. Only recently has progress been made by detecting the collectively enhanced oscillation frequency in optical tweezers directly via the created Rydberg excitations [56, 58, 193] and by demonstrating blockade between ensemble qubits [194]. In the following, we will give a brief introduction to the background of the superatom, and describe the experimental measurements performed to characterize it with the quantum gas microscope.

4.2 The superatom

As discussed before in chapter 2, optically coupling ground and Rydberg states in the presence of interactions leads to particularly rich physics. To shed light on the super-

atom regime, we start by assuming first a non-interacting system where N identical atoms are trapped in an optical lattice. If their electronic ground state $|g\rangle$ is coupled with the same coupling Ω to a Rydberg state $|r\rangle$, it is clear that in this case all accessible N-atom states must be symmetrical with respect to particle exchange. The symmetric subspace of N atoms consists of $N+1$ substates characterized by their number of excitations n_e, which naturally takes values between zero and N. The states $|N, n_e\rangle$ can be conveniently represented as rings on a collective Bloch sphere with radius N, in analogy to collective spin states [195], see Fig. 4.1 a. Adding Rydberg interactions between the atoms leads to a spatially varying detuned coupling and hence breaks the symmetry between the atoms. The symmetry is restored only if the Rydberg blockade is strong enough to act globally. This is the case if the blockade radius $R_b = (|C_6|/(\hbar\Omega))^{1/6}$ exceeds the system size D,

$$R_b \gg D. \tag{4.1}$$

Then, higher excited states with $n_e > 1$ are detuned entirely and the system is constrained to the collective ground state $|G\rangle$ with $n_e = 0$ and the excited state $|W\rangle$ with $n_e = 1$, see Fig. 4.1 b.
The symmetric states $|G\rangle = |g_1, \ldots, g_N\rangle$ and $|W\rangle = 1/\sqrt{N}\sum_{i=1}^{N}|g_1, \ldots, r_i, \ldots, g_N\rangle$ (subscripts label the atoms) form an effective two-level system with a corresponding two-level Bloch sphere and all accessible states can be represented as superpositions of these two states on the surface of the sphere, see Fig. 4.1 c. The Hamiltonian describing the dynamics in this case is the same as for a simple two-level system and reads (see appendix B for the derivation)

$$\hat{H} = \frac{\hbar\sqrt{N}\Omega}{2}\left(|G\rangle\langle W| + |W\rangle\langle G|\right) - \hbar\Delta|W\rangle\langle W|, \tag{4.2}$$

where the collective nature appears in the collectively enhanced coupling

$$\Omega_N \equiv \sqrt{N}\Omega. \tag{4.3}$$

This explicitly depends on the number of involved atoms N and the detuning Δ is the usual single-particle detuning in the transition from $|g\rangle$ to $|r\rangle$. The collectively enhanced coupling gives rise to the phenomenon of superradiance, according to which an ensemble of atoms coupled symmetrically to light radiates with a higher rate than an isolated atom [196]. It has also been discussed in the context of quantum information as providing a valuable link between storage qubits and photons for quantum state transmission [197].
Next to the enhanced optical coupling, also the excited state $|W\rangle$ of the superatom has intriguing properties. Its entanglement is particularly robust against local perturbations [198], a feature which could make it useful for storage protocols of quantum

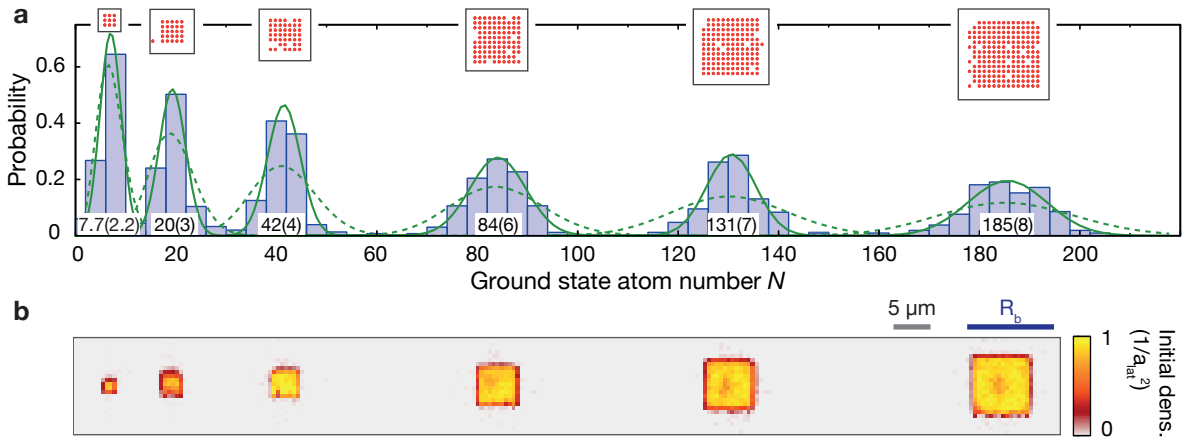

Figure 4.2: Preparation of superatoms. a Histograms of the initial atom number distributions (blue bars) are shown together with a Gaussian fit (solid green line) and the respective expectation for a Poissonian number distribution for the same mean number (green dashed line). The mean and standard deviation of the atom number are indicated. The pictograms illustrate the reconstructed site occupations of a representative initial atom distribution. **b** Average density of initially prepared samples corresponding to respective histograms above.

information [199, 200] and robust encoding of the spin degree of freedom in novel quantum simulation platforms [201]. The W-state has so far been prepared successfully in several experimental platforms, among them trapped ions [202] and neutral atoms in optical cavities [203, 204].

4.3 Experimental techniques

4.3.1 Initial state preparation

To prepare the ground state $|G\rangle$ of the superatom as an array of atoms in their electronic ground state $|g\rangle$, we employed the single-site addressing scheme described in chapter 3 [27]. We started with $200 - 500$ atoms in a single two-dimensional plane, prepared in a unity-filling Mott-insulating state. Transverse motion was suppressed by the lattices along x and y, which to this end were both ramped to depths of $40\,E_\mathrm{r}$. The lattice in the third (z) direction was kept at a depth of $80\,E_\mathrm{r}$ for all experiments. The local addressing then allowed for preparing approximately square-shaped samples of varying diameter D and atom number N, see Fig. 4.2 a. Sample sizes with atom numbers between one and $N = 185(8)$ atoms were realizable, spanning almost two orders of magnitude. The initial local number squeezing of the Mott insulator [11] to-

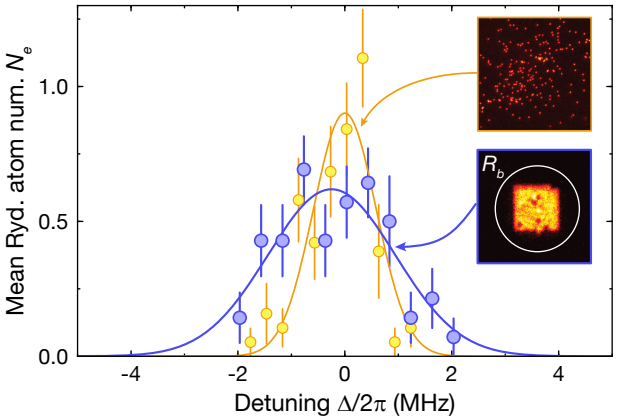

Figure 4.3: Resonance in a superatom. Mean detected Rydberg atom number N_e versus two-photon detuning Δ for a $12 \times 12\, a_{\mathrm{lat}}^2$ superatom (blue data points) and a dilute cloud (yellow data points). The solid lines represent Gaussian fits. Representative images of the two starting states are shown on the right (images not to scale relative to each other). The relevant blockade radius $R_b = 11.7(1)$ µm for $68S_{1/2}$ is additionally indicated. Error bars denote the standard error of the mean (s.e.m.).

gether with the shape control via spatial addressing enabled us to reach fluctuations in the total atom number N down to 4 dB below shot noise. Subsequently, all particles were prepared in the hyperfine ground state $|F = 2, m_F = -2\rangle$. This ensemble formed the collective superatom ground state $|G\rangle$.

4.3.2 Excitation and detection of Rydberg states

Excitation and detection of the Rydberg states was achieved analogous to references [55, 57, 115], where the technical details are described. Starting in the ground state $|g\rangle \equiv |2, -2\rangle$, the Rydberg state $68S_{1/2}$, $m_J = -1/2$ was coupled in a two-photon scheme via the intermediate state $5P_{3/2}$, $m_F = -3$. The two transition wavelengths were 780 nm and 480 nm and the intermediate state detuning was +742 MHz. Detailed parameters for coupling and estimated decoherence rate are given in table 5.1. The measured single-atom two-photon Rabi frequency was $\Omega/2\pi = 240(30)$ kHz, approximately 30 % below the estimate based on beam parameters. Together with the repulsive C_6-coefficient of $C_6 = -h\,630\,\mathrm{GHz}\,\mu\mathrm{m}^6$, the blockade radius was estimated to be $R_b = 11.7(1)$ µm, exceeding the lattice spacing $a_{\mathrm{lat}} = 532$ nm in our system significantly. The lifetime of the $68S_{1/2}$ Rydberg state is approximately 139 µs [93], however we expect the coherence to be limited by laser frequency noise and intensity fluctuations rather than Rydberg state decay, see table 5.1. Compared to the technology described in [57, 115], the system was upgraded by reducing the linewidth of the

laser for the lower transition by about a factor of five via a lock to a laser at the same wavelength, which was stabilized to a ULE cavity [205].
Detection of the Rydberg atoms was achieved *in-situ* by first removing all ground state atoms within 8 µs and then optically depumping the Rydberg states for 2 µs. To this end, a sideband was added to the laser for the upper transition to obtain light resonant with the transition to $5P_{3/2}$, from where the atoms rapidly decay to the ground state. Subsequent fluorescence imaging revealed their position to within ± 1 lattice site and provides an overall detection efficiency of $\eta = 0.67(5)$ for the Rydberg state, extracted from the measurements described in the following.

4.4 Experimental results

4.4.1 Superatom spectroscopy

A simple spectroscopy experiment provides a first test of the developed superatom picture, see Fig. 4.3. Comparing the resonance taken in a dilute cloud with the one for a $12 \times 12\, a_{\mathrm{lat}}^2$ superatom ($N = 131(5)$ atoms), the resonance is broadened by approximately a factor of two. This can be attributed to the collective coupling, which is less pronounced in the dilute sample. The residual interactions and the too high density in the dilute cloud prevent a quantitative confirmation of the collective enhancement based on the spectroscopic data alone. However, for the superatom initial state, the maximal detected Rydberg atom number stays below one, consistent with the expectation for the fully blockaded regime.

4.4.2 Collective enhancement

As further, unequivocal evidence for the superatom description we seek to demonstrate the collective enhancement of the Rabi frequency from Ω to $\sqrt{N}\Omega$. To this end, we coupled the superatom ground state for variable times T to the Rydberg state by switching on the excitation lasers. The observed Rabi oscillations, see Fig. 4.4 a, exhibit the characteristic enhancement and show a dramatically increased oscillation frequency when the number of atoms is increased. At the same time, the spatial distribution of the detected Rydberg atoms homogeneously fills the density profile of the initially prepared square samples. This is a direct test and verification of the assumption that all atoms are coupled to the Rydberg state homogeneously, as required for the simplified superatom description of equation (4.2) to be valid. Furthermore, the number statistics of the detected excitations indicate that the blockade is active and the system is indeed restricted almost exclusively to the subspace spanned by $|G\rangle$ and $|W\rangle$. Only for the largest sample with $N = 185(8)$ do we detect a significant fraction of double excitations, which is expected as there the diameter of the system D starts

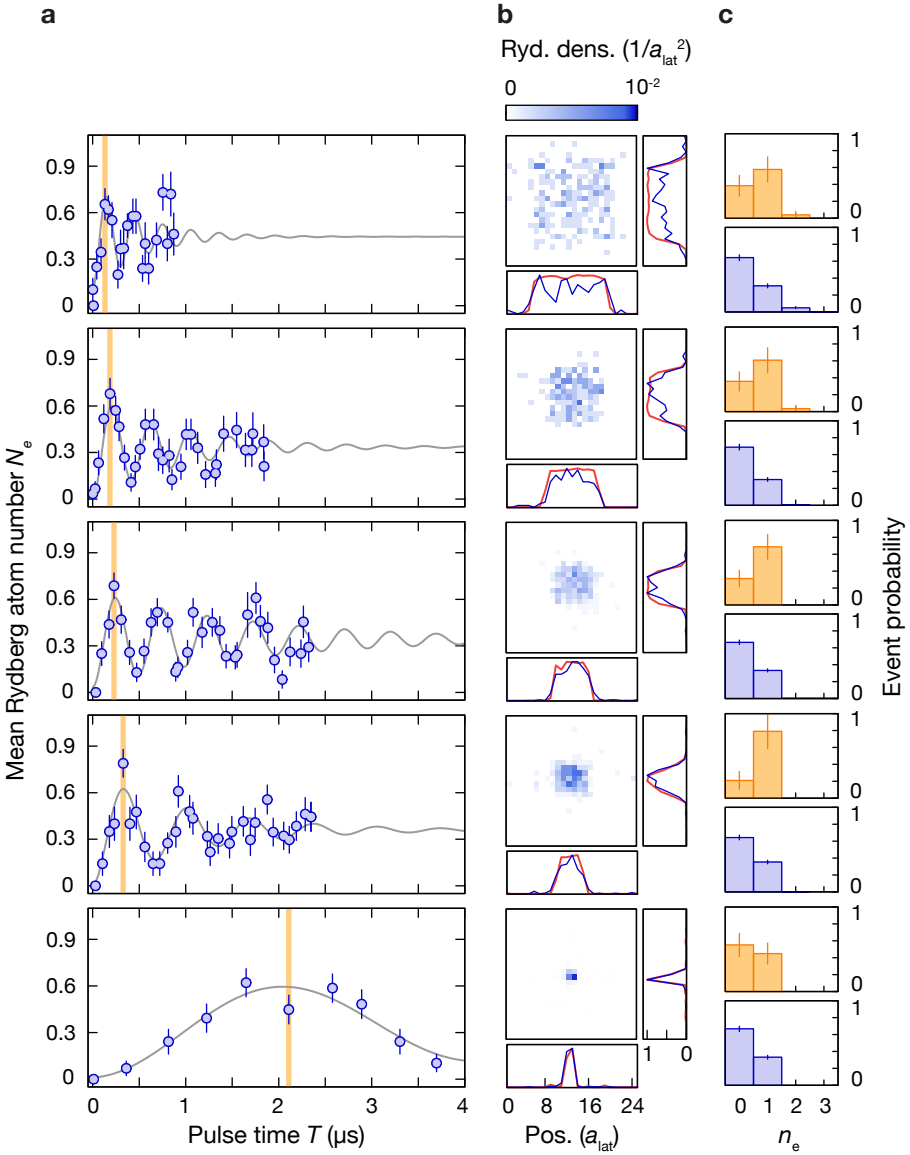

Figure 4.4: Collectively enhanced oscillations. **a** Mean Rydberg atom number N_e versus excitation pulse time T (blue data points) with an exponentially decaying sinusoidal fit (gray solid line). The initial atom numbers were $N = 185(8), 84(6), 42(4), 20(3), 0.74(0.60)$ from top to bottom. Error bars on the data represent one s.e.m.. **b** Spatial distribution of Rydberg atoms. The panels to the right (below) show normalized horizontal (vertical) averages (solid blue line) together with the averaged initial density (solid red line). **c** Number histograms for full oscillation (blue bars) and first maximum (orange bars, position marked by orange line in a).

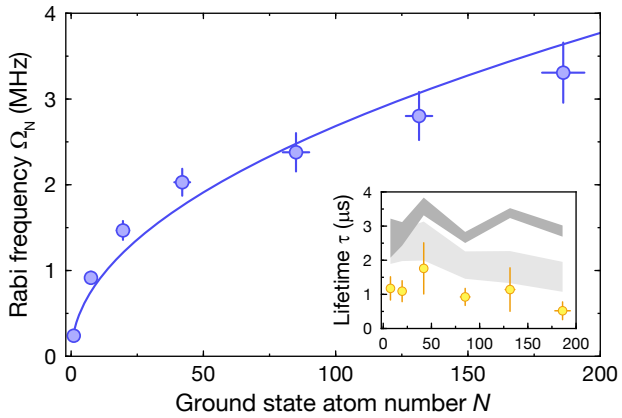

Figure 4.5: Square root scaling. Collective Rabi frequency Ω_N extracted from the oscillations shown in Fig 4.4 a versus initial atom number N (blue data points), calibrated by independent reference measurements. The solid blue line represents a power-law fit with an extracted exponent of $0.49(10)$. Error bars on the data points take into account day-to-day fluctuations of the Rabi frequency Ω (10 %) and the detuning ($\pm$200 kHz). The inset shows the measured lifetime (orange data points) together with the expected lifetime taking into account initial atom number fluctuations (dark-gray shaded area) and additionaly noise in the single-particle Rabi coupling of $4(1)$ % (light-gray shaded area).

approaching the blockade radius R_b and the simple superatom description has to be modified.

In order to evaluate the observed oscillations more quantitatively, we fit an exponentially decaying oscillation of the form $N_e = \eta \left[A - e^{-T/\tau} \cos\left(\Omega_N T/2\right)\right]$ to the average detected Rydberg atom number N_e. The collective enhancement is directly visible when plotting the extracted oscillation frequency Ω_N versus the independently calibrated initial atom number N, see Fig. 4.5. The scaling can be quantified by a power-law fit $\Omega_N = \Omega\, N^{\alpha}$, from which we extract an exponent $0.49(10)$ in excellent agreement with the expected square root scaling. Deviations for the largest atom numbers could be due to spatial inhomogeneities of the coupling laser intensity, which we expect to lead to spatial variations of the coupling of up to 10 % for these system sizes, see also appendix B for a discussion of the superatom with inhomogeneous coupling. An interesting arising question is whether the collectively enhanced coupling can be harnessed for higher fidelity quantum operations. Extracting the lifetime τ from the oscillation allows for answering this question by determining optimal regime where the ratio between coupling and decoherence is maximized. Interestingly, the extracted values for τ are on the order of $\tau \approx 1$ μs and change little with increasing atom num-

ber, see inset of Fig. 4.5. The optimum ratio of coupling and decoherence is achieved for $N = 131(5)$, still in the fully blockaded regime, such that we conclude that the enhancement is indeed favourable. One of the limiting factors for the lifetime is a shot-to-shot fluctuation in the atom number, which appears as an effective dephasing due to the number-dependent coupling. For example, in the case of a Poissonian intial atom number distribution the effective dephasing time would be on the order of 1.5 µs. Our preparation with sub-shot-noise fluctuations extends this time by a factor of two, leading to expected dephasing times of approximately 3 µs, see dark-gray shaded area in inset of Fig. 4.5. Yet, based on this effect alone and otherwise coherent evolution, we cannot reproduce the observed short coherence times. Taking additionally into account estimated Rabi frequency fluctuations of $4(1)$ % reproduces the trend of the data, but there still remains a discrepancy. Further sources of dephasing are laser frequency noise and residual couplings to Rydberg potentials of higher angular momentum Rydberg states, which can become (near) resonant at shorter distances [194]. Both could explain the nearly size-independent offset between data and theoretical model.

4.4.3 Ramsey spectroscopy

The sensitivity of the superatom towards laser frequency noise can be tested with Ramsey spectroscopy [75]. To this end, the superatom was prepared in an equal superposition of the two states $|G\rangle$ and $|W\rangle$ by a laser pulse with an adjusted time to match the collective $\pi/2$-pulse time $T = \pi/(2\Omega_N)$. After that, the superposition was left to evolve freely for a duration T_R. The acquired precession phase was then read out with a second $\pi/2$ pulse identical to the first. The resulting detected mean Rydberg atom number versus hold time is displayed in Fig. 4.6. It exhibits clear oscillations whose frequency is determined by the AC-Stark shift of the red laser, which is naturally switched on for the preparation pulse but then switched off for the remainder of the evolution until the readout pulse. The contrast of the Ramsey fringe decays with a time constant of $\tau_R = 2.2(4)$ µs, which would be consistent with a dephasing rate of approximately $2\pi \times 50$ kHz. This is slightly above the expected combined two-photon laser-noise of $2\pi \times 30$ kHz [115], which, however, clearly constitutes the main source of dephasing in this case. Still, even if this is included in the model for the expected decay of the Rabi-oscillation constrast, the discrepancy observed there between data and model is not resolved and further decoherence sources seem to be present.

4.4.4 Entanglement in the superatom

Entanglement is one of the fundamental concepts in quantum theory. It has recently been identified as a resource for quantum information tasks such as teleportation

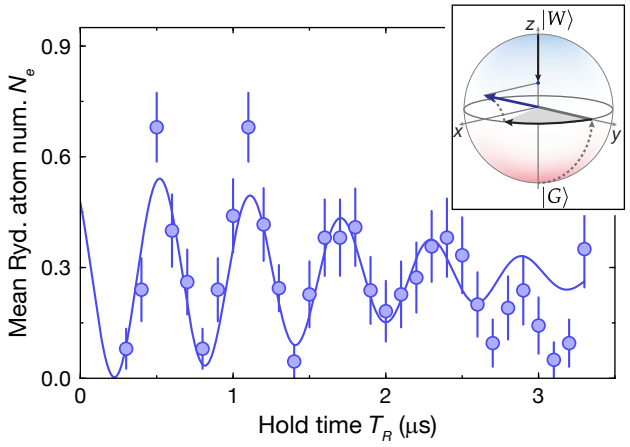

Figure 4.6: Ramsey coherence of superatom. The mean Rydberg atom number N_e oscillates with hold time T_R (blue data points) in a Ramsey sequence. The solid blue line is a fit of a decaying sinusoidal oscillation. The spin trajectory is illustrated on the two-level Bloch sphere in the inset. The precession angle (black arrow and gray shading) is converted to population in $|W\rangle$ and $|G\rangle$ respectively (blue dot). Dashed arrows illustrate trajectory during the collective $\pi/2$ pulses, the blue arrow denotes the final spin direction. The initial atom number for the measurement was $N = 38(3)$. Error bars on the data points denote the s.e.m..

or computation [206]. The role of entanglement in many-body systems is an active field of study [207], focussing for example on the relevance of entanglement at quantum phase transitions [208, 209], its development and dynamics after quantum quenches [9, 210, 211], especially in quantum thermalization [212] or its use for quantum-enhanced metrology [213]. Verifying the presence of entanglement in a quantum system experimentally is generally a very difficult task and there are different approaches to achieve this [214]. In small samples, full quantum state tomography [215] is feasible, however the excessive number of required measurements makes this impractical for larger systems. Here, measurements of entanglement entropy [216] or spin squeezing [195, 217] have been performed successfully. An alternative strategy is provided by measuring system-specific entanglement witnesses [72, 202]. Entanglement is present in the system if the measured value for such a witness is above (or below) some critical bound, usually zero [214].
In order to experimentally infer the entanglement expected to be present in the superatom dynamics, we employ an entanglement witness developed in the context of atoms coupled to a cavity [203]. Generally, we know that any fully separable state $|\Psi\rangle$ of N parties, here we focus on atoms, can be written as a direct product of single-particle states $|\psi\rangle_i$. This, however, is not the case if some entanglement is present in

$|\Psi\rangle$, which hence implies for an entangled state

$$|\Psi\rangle \neq \bigotimes_{i=1}^{N} |\psi\rangle_i. \tag{4.4}$$

This inequality tells a priori nothing about which or how many particles are entangled in the system described by $|\Psi\rangle$, just that entanglement has to be there. The witness developed in reference [203] builds on the idea that any separable state, i.e. a state that does factorize into single-particle states, has a maximal overlap with a W-state. This can be shown by explicit calculation using the known structure of the W-state and the general expression for separable states analogous to equation (4.4). If the overlap of a prepared state with a W-state is known, and it exceeds this maximal overlap expected for any separable state, the presence of entanglement in the system is proven. A simple extension of this concept allows to go beyond this rather qualitative statement by considering the overlap of a state with at least k entangled atoms with the W-state. Such a state with k-particle entanglement can be written as a tensor product similar to equation (4.4), but with at least one state with k entangled particles as a factor. Then, similar bounds to the overlap with a W-state exist and allow for determining the minimal number of entangled particles k in the system. This number is also known as the entanglement depth of a state [204, 218]. The preceeding discussion can also simply be extended to the experimentally relevant case of mixed states, see the Supplementary Materials of [203], and our experimental results are always compared to this generalized version in the following.

Experimental results

In our experiment we can, under three conditions discussed below, extract the W-state overlap from the measured collective oscillations as the oscillation amplitude at the oscillation maxima $C(T) = \eta e^{-T/\tau}$, which we extracted from the fit to the measured oscillations, see Fig. 4.4 a. Comparing with the bound for at least bipartite ($k = 2$-particle) entanglement, the extracted amplitudes at the first oscillation maximum are clearly above this bound, demonstrating incompatibility with a classical state, see Fig. 4.7. For maxima reached at later times T, the decoherence present in the system leads to a decay of the amplitude C into the classically allowed region. Correcting the oscillation amplitude by the detection efficiency η allows for the conclusion that at least approximately 100 particles are entangled in the sample containing $131(5)$ atoms in total. Furthermore, we extract a preparation fidelity of $0.78(18)$ for the W-state at the first oscillation maximum, averaged over all atom numbers. Interestingly, the boundary between classical and entangled states is nearly independent of the actual number of particles in the system and close to 0.37. This is equal to the overlap of the W-state with a coherent state of N atoms with a mean of one, which is in fact

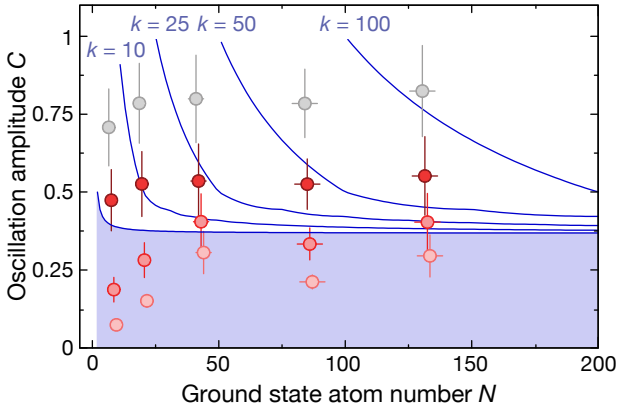

Figure 4.7: Entanglement in the superatom. The extracted oscillation amplitudes C of the oscillations shown in Fig. 4.4 a, evaluated at the first, second, third oscillation maximum are shown in red with decreasing color intensity (data points slightly offset horizontally for clarity). The gray points denote the amplitude at the first maximum, corrected by the known detection efficiency. The blue shaded area denotes the region of oscillation amplitudes consistent with a classical state with a fully separable density matrix. Different upper bounds for at least k-particle separability are shown as solid blue lines. Error bars on data points denote the 1σ-confidence interval of the fit.

the classical state with maximal W-state overlap.
In the following we want to justify that the W-state overlap can be extracted from the measured oscillation traces. To this end, three conditions have to be met: First, the system has to be constrained to the subspace with maximally one single excitation, second, the light has to couple to all atoms symmetrically and, third, shot-to-shot fluctuating relative phases between the atoms have to be absent. The first condition is fulfilled, as the histograms shown in Fig. 4.4 c exhibit vanishing occurrence of events with $n_e = 2$ for all but the largest sample, which we have therefore excluded from the analysis of the entanglement presented in Fig. 4.7. Here, the single-atom-sensitive detection enabled by our quantum gas microscope is crucial. This becomes even more clear when revisiting the example of a coherent state with a mean of one. Such a state is realized for example at the Rabi-oscillation maxima in a non-interacting N-atom ensemble with off-resonantly driven two-level systems, with a *detuning* of $\Delta = \sqrt{N}\Omega$ (to reduce the maximal mean atom number to $\Omega^2/(\Omega^2 + N\Omega^2) \approx 1$). As the effective Rabi frequency $\sqrt{\Omega^2 + \Delta^2}$ of such an ensemble would also increase with the square root of the number of particles, the dynamics of the mean atom number appears nearly identical to the one observed for the superatom. Yet, in a coherent state with a mean atom number of one, the contribution of events with $n_e = 2$ is approximately 0.18, incompatible with our measurement, see Fig. 4.4 c. The second criterion is also met, given that the coupling inhomogeneities present can be neglected on the

time scale of the performed experiment. The observed square root scaling with the number of atoms N, see Fig. 4.5, as well as the nearly homogeneous spatial distribution of excited Rydberg atoms strongly suggests that this is the case, see Fig. 4.4 b. The last condition is met because the effective two-photon wave vector is orthogonal to the atomic plane, as both excitation beams are counter-propagating along the z-direction. This implies that no phase gradients or spin waves are imprinted during excitation, contrary to the case when the laser excitation is performed transverse to the extent of the atomic sample [54]. As the atoms are in their respective motional ground states in the optical lattice, motional dephasing can also be excluded. Therefore we assume that the phase is stable, up to irrelevant global fluctuations. Furthermore, a dominating phase dynamically accumulating during the Rabi-oscillation dynamics can be excluded on the grounds of the visibility of the Ramsey fringe, which would be strongly damped in such a case. Under these three assumptions, it is clear that following the same arguments as in the introductory paragraph 4.2, the system dynamics is constrained to the two symmetric states $|G\rangle$ and $|W\rangle$. All $N-1$ other states with maximally a single excitation are not coupled by the light and therefore do not contribute to the oscillation but rather dephase the Rabi oscillations [219, 220]. Consequently, the oscillatory dynamics has to occur in the subspace spanned by $|G\rangle$ and $|W\rangle$, and the prepared state has maximal overlap with the latter at the oscillation maxima. This holds true even in the case of a possibly present homogeneous detuning in the experiment, which can only reduce the overlap. Thus, the measured oscillation amplitude constitutes a lower bound to the W-state overlap, demonstrating that the observed dynamics in our experiment is incompatible with classical product states. Similarly, the W-state overlap can also be deduced from the contrast of Ramsey fringes, which has been accomplished in the fully blockaded regime in reference [194].

4.4.5 Breakdown of the blockade

If the system diameter D of the prepared system reaches close to the blockade radius $R_b = 11.7(1)\,\mu\text{m}$, doubly excited states start to be significantly coupled and the isolated superatom picture breaks down, see Fig. 4.8 a. We probe this regime in our experiment with the largest sample size with $N = 185(8)$ and $D = 9.8(7)\,\mu\text{m}$. Even though the strict application of $R_b > D$ still suggests a blockaded ensemble, we detect experimentally a non-vanishing fraction of $4.8(1.0)\,\%$ of events with $n_e = 2$, see Fig. 4.4 c. This can be understood as a dynamical breaking of the blockade, as the interaction-induced detuning V for these states approaches the Rabi coupling Ω, resulting in a finite effective coupling and therefore population of these states for longer excitation times. Our measurements show that the doubly excited states exhibit a significantly altered dynamics compared to the singly excited states in the blockade regime, see Fig. 4.8 b. While the latter are coupled with a slightly reduced but still collective coupling rate on the order of Ω_N well above the single-particle Rabi frequency

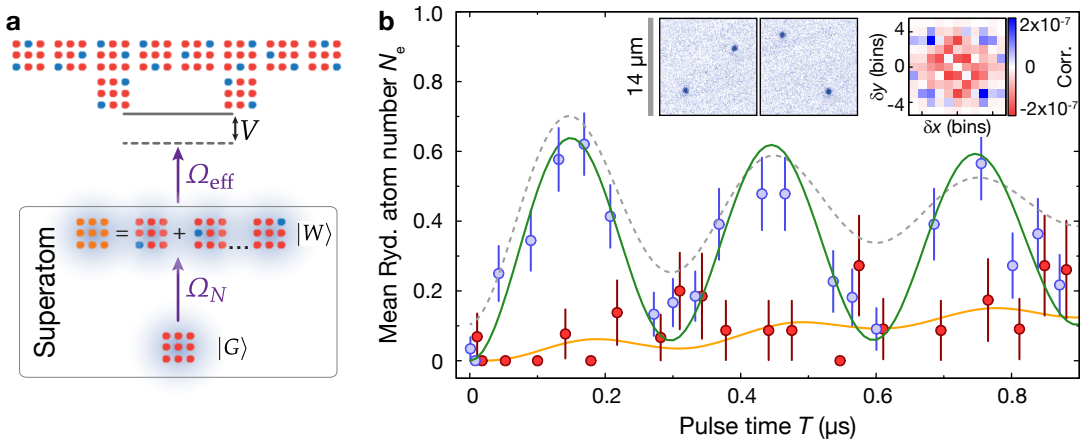

Figure 4.8: Breakdown of blockade and symmetric-subspace approximation. **a** Schematic illustrating the interaction-detuned coupling Ω_{eff} from the symmetric superatom subspace to higher excited states when the system size approaches the blockade radius. Atoms in ground and Rydberg states are represented by red and blue dots, respectively. **b** Collective oscillation for $N = 185(8)$ atoms, post-selected on only the contributions from states with $n_e = 1$ (blue data points) and $n_e = 2$ (red data points, slightly offset horizontally for better visibility). The theoretical calculation in a truncated Hilbert space [55], scaled by the detection efficiency, agrees well with the data (green and orange solid lines). The fit to the mean (gray dashed line) shows faster dephasing than observed in the $n_e = 1$ subspace alone. The inset shows exemplary single shots with $n_e = 2$ (field of view $14 \times 14\ \mu\text{m}^2$) and the translationally averaged density-density correlation evaluated for $n_e = 2$ events only versus the coordinates $(\delta x, \delta y)$ of the shift vector $\boldsymbol{R}$. The data was binned in 4×4 sites. The error bars denote the s.e.m..

Ω, the dynamics of the former is slower. This is due to the absence of enhancement for the coupling of the symmetry-breaking doubly excited states. In fact, there are only two energetically equivalent configurations with the two atoms occupying positions with maximal separation along the diagonal of the initially prepared ensemble, which is apparent in the observed single shots, see inset of Fig. 4.8, and can be quantified by evaluating the density-density correlation

$$g^{(2)}_{ij} = \langle \hat{n}^e_i \hat{n}^e_j \rangle - \langle \hat{n}^e_i \rangle \langle \hat{n}^e_j \rangle, \tag{4.5}$$

where $\hat{n}^e_i$ measures the number of Rydberg atoms at site i. The correlation displayed in the inset of Fig. 4.8 is additionally translationally averaged by restricting the distance between two atoms to the shift vector $\boldsymbol{R} = \boldsymbol{i} - \boldsymbol{j}$. As there are only two equivalent doubly excited states, the coupling Ω_{eff} to these states starting in the symmetric W-state is now inversely proportional to the square root of the number of atoms,

$\Omega_{\text{eff}} \propto \Omega/\sqrt{N}$ [221, 222]. Symmetry-induced enhancement by $\sqrt{M}\Omega_{\text{eff}}$ for M equivalent doubly excited states increases the coupling rate and, taking into account sufficiently many doubly excited states, such a model can explain the slow rise of the $n_e = 2$ states to a good extent [222]. The immediate consequence of the different dynamics of the doubly excited fraction compared to the singly excited states is an apparent dephasing in the mean Rydberg atom number [223], see Fig. 4.8, which was observed in several other experiments in the imperfectly blockaded regime [190–192].

4.5 Summary and outlook

In this chapter we have described the microscopic characterization of a Rydberg superatom in the regime of strong Rydberg blockade. The detection sensitivity and spatial resolution provided by the quantum gas microscope have allowed for showing the characteristic many-body Rabi oscillations, which are a consequence of multiple atoms coupling in unison to the same light field. Furthermore, the entanglement of the involved states has been inferred from the measurements of the oscillations and the breakdown of the blockade was demonstrated. Increasing the sample size, or, equivalently, decreasing the blockade radius further naturally leads to the theoretically well studied regime where crystalline order is expected in the excitations [144, 145, 224–227] which was indeed demonstrated experimentally in our group [55, 57] and elsewhere [56, 58]. Studying the fully blockaded regime further might be interesting if combined with a coherent mapping of the Rydberg excitation to the ground state [194]. There, the lifetime of the W-state would be much longer and could be studied via global microwave rotations analogous to [203, 204]. Furthermore, Rydberg blockade can be exploited for parallel gate operations on multiple qubits [228] or the generation of highly entangled Schrödinger cat states [229, 230] useful for quantum metrology [213].
In the next chapter, we will describe the direct single-photon excitation as an alternative to the two-photon excitation employed to study the superatom. We will compare the two strategies and show that the single-photon excitation has a number of advantages, among them much higher achievable Rabi frequencies. This will be of fundamental importance for the implementation of Rydberg-dressed spin systems described in the subsequent chapters.

Chapter 5

Single-photon excitation and detection of Rydberg P-states

5.1 Introduction

In the last chapter, we have seen how the interaction between Rydberg states can be harnessed to study the so-called superatom in the regime of dominating interactions. Whereas in those experiments the Rydberg state was coupled on a two-photon transition, in this chapter we present the direct single-photon excitation of Rydberg P-states as an alternative. We start by first comparing the performances of the two excitation pathways in our setup and show that the single-photon excitation combines the advantages of a higher achievable coupling rate with longer coherence times. Indeed, the increased decoherence due to the intermediate state in the two-photon excitation contributes to the dephasing observed in the superatom experiments described before. Even though it promises to achieve larger coherence times, the single-photon excitation is technically more challenging because the required wavelengths lie in the ultraviolet spectral range. As part of the work presented in this thesis, a laser system suitable for the generation of light in the ultraviolet spectral range has been developed. Guiding principles in its design as well as the characterization and performance of the system will be described briefly, followed by results on the direct optical detection of Rydberg P-states in an optical lattice by depumping via a short-lived intermediate state.

5.1.1 Comparison of single- and two-photon excitation

Rydberg states lie closely below the ionization threshold, see section 2.2. This implies that, starting in the ground state, large energies are necessary to excite them. For example, for rubidium-87, the transition frequency to Rydberg P-states lies in the ultraviolet spectral range, with a wavelength of approximately 298 nm. Continuous wave laser sources in the ultraviolet have recently been developed in several groups for the Rydberg excitation of cesium [231, 232], strontium via a long-lived intermediate state [233] and rubidium [234]. An alternative strategy to excite Rydberg S-

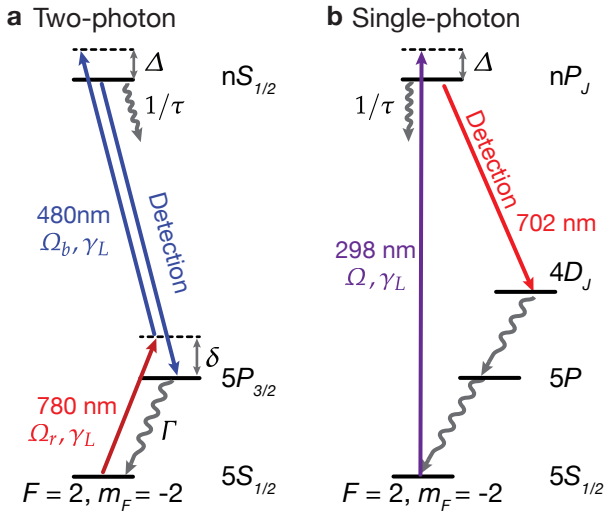

Figure 5.1: Excitation and detection schemes. a A two-color excitation scheme is used to excite Rydberg S-states starting in the ground state $F = 2$, $m_F = -2$, coupling off-resonantly via $5P_{3/2}$ with an intermediate-state detuning δ. For detection, the laser of the upper transition at 480 nm is shifted by $-\delta$ to pump atoms into $5P_{3/2}$, from where they spontaneously decay back to the ground state. **b** The Rydberg state nP_J is excited on the single-photon transition starting in $F = 2$, $m_F = -2$ with a wavelength of 298 nm. Detection is performed by depumping atoms in the Rydberg state to $4D_{3/2}$ or $4D_{5/2}$ using a laser at 702 nm. From there they cascade via $5P$ spontaneously back to the ground state $5S_{1/2}$. Rabi frequencies Ω_i and decay rates are indicated where necessary for the discussion in the main text.

or D-states consists in a two-photon stepwise excitation. For alkali atoms, there are two main pathways, either via the lowest- or the second-lowest-lying P-state. For rubidium-87, the former requires wavelengths of 780 nm and 480 nm and the excitation occurs via the $5P_J$ state, while the latter proceeds via the $6P_J$ with photons at 420 nm and 1014 nm. Due to the readily available laser sources, the 780 nm + 480 nm pathway is nowadays routinely used in experiments, but also the inverted scheme 420 nm + 1014 nm has been explored [58, 192].
In the following, we summarize some important differences between the single-photon and the two-photon excitation scheme. We thereby focus on the two-photon scheme via the $5P$-state, which has been used to obtain the results presented in chapter 4 and is displayed schematically in Fig. 5.1 a. Most results can be straightforwardly generalized to the inverted scheme. We limit our discussion to off-resonant excitation with respect to the intermediate state. The resonant configuration has recently been explored in the framework of electromagnetically induced transparency [235–238]. To provide an overview of the experimental significance of the discussed effects, table 5.1

Quantity	Two-photon [60]			Single-photon
	780 nm	480 nm	Combined	298 nm
Rabi freq., $\Omega/2\pi$ (MHz)	82(6)	6(1)	0.33(4)	7.50(8)
Laser dephasing, γ_L (μs^{-1})	0.06	0.12	0.18	0.18
Rydberg decay, $1/\tau$ (μs^{-1})	-	-	0.007	0.037
Add. dephasing, $\frac{\Omega_r^2}{4\delta^2}\Gamma$ (μs^{-1})	0.116(19)	-	0.116(19)	-
Add. decay, $\frac{\Omega_b^2}{4\delta^2}\Gamma$ (μs^{-1})	-	0.0006(2)	0.0006(2)	-
Eff. decoh., Γ_{eff} (μs^{-1})	-	-	0.15(2)	0.12
Recoil freq. (kHz)	3.8	10.0	6.2	25.8
AC-Stark, $\delta_{AC}/2\pi$ (MHz)	2.26(33)	$-0.012(4)$	2.25(37)	-
Good-to-bad ratio	-	-	2.2(3)	63(1)

Table 5.1: Comparison of numbers for single- and two-photon excitation. Experimental figures for the two excitation pathways coupling to $68S_{1/2}$ and $31P_{3/2}$ respectively for two- and single-photon scheme with $\Delta = 0$. The AC-Stark shift adds to the detuning on the ground to Rydberg state transition. For the intermediate state $5P_{3/2}$, the detuning used was $\delta/2\pi = 742\,\text{MHz}$ [55] and the decay rate is given as $\Gamma = 2\pi \times 6.067\,\text{MHz}$ [102]. The Rydberg state decay rates were calculated with the formulae from reference [93] and the numbers for laser-linewidth-induced dephasing are estimated upper bounds. The good-to-bad ratio is approximately the number of full Rabi cycles expected per $1/e$-decoherence time. It is calculated as the ratio of Rabi frequency and effective decoherence $\Omega/(2\pi\Gamma_{\text{eff}})$, where $\Gamma_{\text{eff}} = (3\Gamma_{\text{dec}} + 2\gamma_{\text{dep}})/4$ is a weighted sum of dephasing and decay rates, see p. 60ff in reference [181]. Numbers in brackets denote uncertainty.

also summarizes concrete numbers relevant for our measurements.

Rabi coupling

The off-resonant two-photon excitation is performed with a detuning δ from the intermediate $5P_{3/2}$-state and with Rabi couplings Ω_r and Ω_b for the red and blue beams respectively. In the limit of large intermediate-state detunings $\delta \gg \Omega_r, \Omega_b$, the intermediate state can be adiabatically eliminated to yield an effective coupling Ω from the ground state to the Rydberg state given by [92]

$$\Omega = \frac{\Omega_r \Omega_b}{2|\delta|}. \tag{5.1}$$

The bottleneck to achieve high two-photon Rabi coupling is usually the achievable Rabi coupling Ω_b on the upper transition, as here the transition matrix elements are

approximately two orders of magnitude smaller than for the lower transition.
The single-photon coupling provides larger achievable Rabi frequencies, exceeding those obtained by the two-photon excitation by up to an order of magnitude, see table 5.1. This is crucial for the realization of Rydberg dressing due to the strong scaling of the dressed interaction strength like $U_0 \propto \Omega^4$, see section 2.4.

Decoherence

For the two-photon excitation, the admixture of the short-lived intermediate state with linewidth Γ effectively decreases the Rydberg state lifetime by increasing the Rydberg state decay rate to [62, 131]

$$\Gamma_{\mathrm{dec}} = \frac{\Omega_b^2}{4\delta^2}\Gamma + 1/\tau. \tag{5.2}$$

Furthermore, the admixture of the intermediate state adds to the dephasing due to laser noise γ_L via

$$\gamma_{\mathrm{dep}} = \frac{\Omega_r^2}{4\delta^2}\Gamma + \gamma_L. \tag{5.3}$$

These relations show that for fixed laser powers for the two transitions, the decoherence decreases faster with increasing δ than the effective two-photon Rabi frequency given by equation (5.1) and hence a large intermediate state detuning is favourable. As the Rydberg state lifetime and the laser-linewidth-induced dephasing set lower bounds to the overall decoherence, there is an optimum intermediate state detuning where the ratio of Rabi coupling and decoherence is maximized. Inspecting the decoherence sources, it is also clear that species with long-lived intermediate states such as strontium are advantageous for increasing the ratio between coupling and decoherence due to a small admixed decoherence rate Γ. In this respect, the single-photon transition constitutes the limit of vanishing intermediate state admixture and so there the only decoherence sources are laser linewidth and Rydberg state decay.

Light shifts

For the two-photon excitation, the off-resonant coupling to the intermediate state can also introduce considerable trapping or anti-trapping potentials of strength

$$\delta_{AC} = \frac{\Omega_r^2}{4\delta} - \frac{\Omega_b^2}{4(\delta - \Delta)}, \tag{5.4}$$

where weak effects of the 480 nm beam on the lower and of the 780 nm beam on the upper transition are neglected. The light shift can in principle be avoided by choosing

appropriate Rabi frequencies, for example in the usual case $|\delta/\Delta| \gg 1$ they should be matched [46]. However, due to these light shifts, intensity noise on the excitation beams is detrimental, as it will act as a considerable effective dephasing source. The light shift can be problematic even in the absence of intensity noise due to inhomogeneous Gaussian beam shapes and resulting (anti-)trapping of atoms. Next to the trapping effect induced by the intermediate state coupling, there is of course also the trapping due to the effective Rabi coupling between ground and Rydberg state in case of off-resonant two-photon excitation with $\Delta \neq 0$. This is of the order $\Omega^2/(4\Delta)$ and exactly the same as for the single-photon excitation with the same coupling and detuning.

Detection

Detection of the Rydberg atoms is possible in our setup via the previously described optical depumping [55, 57, 115], see section 4.3.2, following a fast resonant push-out of all ground state atoms. While for the two-photon excitation scheme, depumping can be achieved by frequency-shifting the laser at 480 nm by $-\delta$, this is not possible for the single-photon excitation. There, an independent laser at a wavelength of 702 nm is required, see Fig. 5.1 b, which couples atoms in the nP-states resonantly to the $4D$ manifold, from where they decay in a cascade via $5P$ back to the ground state. The final section of the chapter will be dedicated to a brief summary of this technology.

Photon recoil

Due to the small wavelength, the photon recoil energy $E_\mathrm{r} = h^2/(2m_{Rb}\lambda^2)$ is considerably larger for the single-photon excitation compared to the two-photon excitation. This assumes that the two-photon excitation is performed in a counter-propagating configuration of the two photons, where the recoil momenta partially cancel. The large photon recoil likely constitutes a significant factor to decrease the optical detection efficiency, as the untrapped Rydberg atoms start moving upon absorption of the photons [115].

Conclusion

As a conclusion of the comparison, in view of the numbers displayed in table 5.1, the single-photon excitation seems to be advantageous for achieving large good-to-bad ratios between Rabi coupling and decoherence in our experiment due to the missing admixed intermediate state decay and induced light shifts. This implies that for example in a blockade gate [51, 52], more coherent operations should be possible. In this, the large recoil energy involved in the single-photon excitation and resulting motional dephasing have not been considered and could be problematic for the direct ex-

citation, at least on a time scale exceeding several microseconds [115]. Furthermore, comparing the scaling of Rabi frequency and decoherence sources, the two-photon coupling scheme can be improved by increasing the intermediate state detuning. In our and many other experiments, this is at one point limited by the achievable laser power on either of the two transitions involved.

5.2 Excitation of Rydberg P-states

As shown in the previous section, the single-photon excitation has advantages over the two-photon excitation. However, the generation of light at the required wavelength in the ultraviolet spectral range at approximately 298 nm is not straightforward and only very recently have commercial laser systems with sufficient power and stability become available. In the following we describe the necessary technology for the generation of ultraviolet light used for our experiments, focussing first on the second-harmonic generation cavity, its design principles and its performance. After that, the essential parts of the whole laser system including infrared, visible and ultraviolet spectral range are discussed in more detail. The presented system has large enough output power and sufficiently narrow linewidths to implement Rydberg-dressed interactions and study interacting Rydberg gases. The reader not interested in the technical details, many of them in fact relevant for the performed experiments, could skip the following sections up to section 5.2.6, where we present results on the first single-photon excitation of Rydberg states in a rubidium vapor.

5.2.1 The path to the ultraviolet

The generation of the required light in the ultraviolet at 298 nm is achieved via two frequency doubling stages, see Fig. 5.2. Starting point is infrared light at a wavelength of 1192 nm, which is used to seed a Raman fiber amplifier and single-pass frequency-doubled to a wavelength of 596 nm in the visible spectral range using a single-pass doubling stage with periodically poled lithium niobate (PPLN) as the nonlinear medium. The light in the ultraviolet used to excite Rydberg P-states is then generated by a home-built optical resonator with beta barium borate (BBO) as a nonlinear crystal.
Next to our approach of starting with a solid state laser source in the infrared, alternative routes are the use of a dye laser for generating visible light directly [234], or the use of sum-frequency generation of two different infrared sources [231–233]. Advantages of a dye-laser approach are the wide tuning range, which allows for exciting a range of many Rydberg states, and the large available powers. Due to the larger effort necessary for maintenance of daily operation and for achieving frequency and intensity stability comparable to the solid-state-based approach, we decided to pursue the

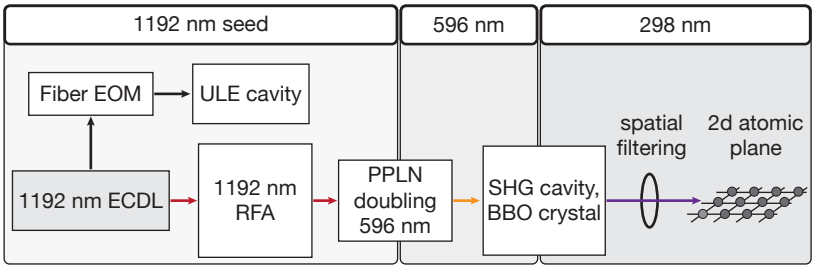

Figure 5.2: Generation of light at 298 nm. The generation of ultraviolet light proceeds in two doubling stages. The seed light at 1192 nm seeds a Raman fiber amplifier (RFA) followed by a single-pass doubling to 596 nm in a periodically poled lithium niobate crystal (PPLN). The second doubling is achieved in a resonant second-harmonic-generation (SHG) enhancement cavity with a beta barium borate crystal (BBO). After spatial filtering, the light is sent to the atoms. The fundamental at 1192 nm is frequency stabilized by locking the sideband of a fiber-EOM to a cavity made of ultralow-expansion glass (ULE).

latter.

5.2.2 The second-harmonic generation cavity

Frequency doubling in non-linear media

The frequency conversion of light requires optical media with a non-vanishing non-linearity. In such media, harmonic radiation can be generated at sufficiently high intensity of the fundamental light, provided that the so-called phase-matching condition is fulfilled [239]. This implies that for effective conversion, the refractive indices for the fundamental and the harmonic frequency have to be matched, which can be achieved in birefringent crystals in combination with specific polarizations for the fundamental and the harmonic [240]. For generating the light in the ultraviolet spectral range, beta-barium borate (BBO) has been introduced as an appropriate crystal [241], providing good transparency in the ultraviolet and visible spectral range [242], large effective non-linearities [243, 244] and relatively easy handling. This explains, next to the wide range of phase-matchable wavelengths, the widespread use of BBO for generating light in the ultraviolet spectral range [231, 232, 245–247], even down to wavelengths as low as 229 nm [248]. Therefore, we have decided to use BBO for the resonant doubling stage.

To estimate the achievable power conversion to the second harmonic for a laser, the Gaussian spatial mode of the fundamental light has to be taken into account. In a seminal paper, Boyd and Kleinman developed a model for this situation. According to their and subsequent work [250–252], the non-linear coefficient relating the funda-

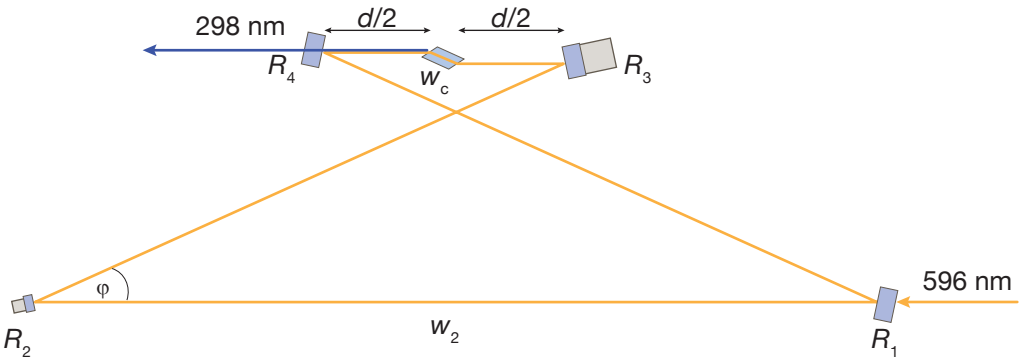

Figure 5.3: Cavity geometry of the bow-tie cavity. The path of the fundamental at 596 nm (orange) is traversed in the order $R_1 \rightarrow R_2 \rightarrow R_3 \rightarrow R_4 \rightarrow R_1$. The second harmonic (blue) is generated in the crystal. The short arm d is symmetrically split to $d/2$ each before and after passing the Brewster-cut crystal (light blue). The approximate positions of the waist in the crystal (w_c) and in the collimated arm (w_2) are indicated. Mirrors are represented as darker blue rectangles. The gray rectangles behind mirrors R_2 and R_3 respectively mark a fast and a slow piezo for stabilizing the cavity length.

mental power P_f to the square of the generated harmonic power P_{SH} is given as

$$\kappa_{NL} = P_{SH}/P_f^2 = \frac{16\pi^2 d_c d_{\text{eff}}^2}{c\lambda_f^3 n^2 \epsilon_0}\, h. \tag{5.5}$$

The non-linear medium enters explicitly via its length d_c, refractive index n and effective non-linearity d_{eff}. All geometric dependences of the non-linear coefficient are thereby contained in the parameter h, which can be calculated numerically if the waist of the Gaussian beam and the properties of the non-linear medium are known. For obtaining a good estimate of h without performing the numerical optimization, heuristic expressions reproducing the exact numerical results with good accuracy have been found [252]. Generally, tighter focussing increases h, but for too tight foci with large beam divergence, the reduced effective volume of high intensity decreases h again. Consequently, there is an optimum focus size that maximizes the conversion. For a BBO crystal of length $d_c = 10\,\text{mm}$ and with refractive index $n = 1.668$, the optimal waist is around 20 µm for the doubling of 596 nm to 298 nm. Using these values, the non-linear coefficient becomes $\kappa_{NL} = 1.44 \times 10^{-4}\,1/\text{W}$, so only a small fraction of the fundamental power is converted to the harmonic. To boost the conversion efficiency, enhancement cavities can be used. The power build-up in the resonator effectively increases the intensity in the doubling crystal and hence results in a larger generated harmonic power [253]. An alternative strategy to increase the conversion efficiency is

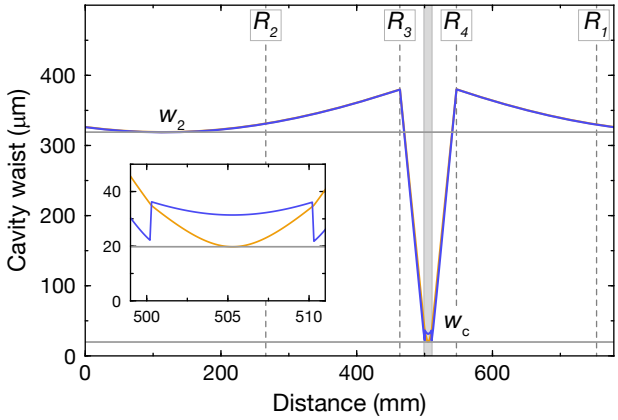

Figure 5.4: Waist in the cavity. The calculated waist at each position in the cavity illustrates the small waist in the crystal, w_c, and the large second waist w_2 in the collimated arm, see also Fig. 5.3, both for sagital and tangential plane (orange and blue). The second waist is identical for both planes for the chosen optimal opening angle $\varphi = 25.12\,^\circ$. The gray vertical dashed lines indicate the approximate positions of the four mirrors in the cavity. The inset shows a zoom to the crystal region, marked by the gray-shaded area in the main graph. There, the two waists differ, only the sagital waist is close to the optimal waist (gray horizontal line). Due to the Brewster-cut crystal, the tangential waist is projected to the crystal surfaces and hence there its size jumps discontinuously [249].

the use of quasi-phase-matched periodically poled crystals like PPLN [254, 255], used for the doubling of 1192 nm to 596 nm but not described further in the following.

Cavity geometry

To find the optimal geometry of the enhancement cavity, the calculated optimal Boyd-Kleinman focal spot size of 20 µm in the doubling crystal serves as the reference point. Larger waists might be advantageous to avoid effects like thermal lensing and reduce the stress in the crystal due to the incident optical power [256]. The decrease in h for larger waists is modest, amounting to approximately 30% when increasing the waist by a factor of two.
In our case, the optimal waist is chosen as the target in order to reach the maximum possible output power. The designed resonator is of "bow-tie" type, schematically displayed in Fig. 5.3, with four mirrors. Two of them are planar (R_1, R_2) and two are spherical (R_3, R_4), with a radius of curvature of $r_3 = r_4 = -75\,\text{mm}$. We use a Brewster-cut BBO crystal to avoid anti-reflection coatings which could be damaged at the high ultraviolet and visible intensities present in the cavity. Together with the radii of the two curved mirrors, the optimal target waist in the non-linear crystal fixes the

Table 5.2: Properties of crystal and geometry of the cavity. The relevant crystal properties are taken from the database of SNLO [259]. The phase-matching angle θ_{PM} is for type I ($o + o = e$) critical phase matching, for second-harmonic generation of 596 nm at a temperature of 353 K, to which the crystal was stabilized. The length d of the short arm is excluding the crystal length d_c. The Brewster angle $\theta_B = \arctan(n)$ is only effective for 596 nm due to polarization. The walk-off angle ρ enters the Boyd-Kleinman factor and is given for the sake of completeness. The radii of curvature of mirrors R_3 and R_4 are denoted as r_3 and r_4.

Quantity	Value
d_c	10 mm
n	1.668
θ_{PM}	40.9 °
d_{eff}	18.7 pm/V
θ_B	59 °
ρ	82.36 mrad
w_c	20 µm
w_2	320 µm
d	73.2 mm
u	695 mm
$r_3 = r_4$	−75 mm
φ	25.12°
κ_{NL}	1.44×10^{-4} 1/W

distances between the cavity mirrors by requiring maximal resonator stability [257]. For this optimally stable configuration, the target waist w_c in the crystal lies in the center between mirrors R_3 and R_4, on the "short arm", see Fig. 5.4. The strongly diverging beam is collimated by the mirror R_4. The collimated "long arm" u extends between the mirrors $R_4 \rightarrow R_1 \rightarrow R_2 \rightarrow R_3$ and exhibits a large second waist $w_2 \approx 320\,\mu\text{m}$, situated approximately in the middle between mirrors R_1 and R_2. The opening angle φ of the cavity causes astigmatic distortions to the two waists w_c and w_2 due to the different effective focal lengths of curved mirrors in the sagital and tangential plane for non-zero angle of incidence [258]. Choosing in our case $\varphi = 25.12\,^\circ$ allows for achieving a round w_2, see Fig. 5.4, where the waist in the sagital and tangential plane are shown and have almost identical sizes close to the location of w_2. As the light entering the cavity through the incoupling mirror R_1 has to be spatially mode-matched to the cavity, a symmetric second waist w_2 is advantageous to minimize the effort of coupling light into the cavity. In this case a single spherical lens is sufficient for achieving optimal overlap [247]. For the optimal angle and symmetric w_2, the waist in the crystal is asymmetric, leading to a slightly smaller non-linear coefficient than in the optimal configuration, but also less stress due to high light intensities (see inset of Fig. 5.4). Experimentally, the large achieved coupling efficiencies seem to be in favour of our strategy of optimizing for symmetric w_2, see Fig. 5.7 b, despite compromising on the maximal achievable single-pass conversion. Finally, to make sure that the cavity is operable, also the stability criterion for the round trip was checked again including the optimal opening angle φ. Table 5.2 gives an overview of some relevant quantities calculated for the optimal cavity design.

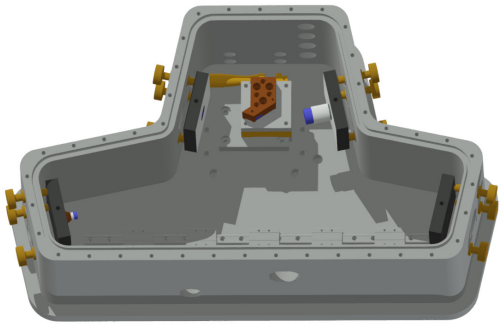

Figure 5.5: Monolithic mechanical design of the SHG cavity. The incoupling mirror R_1 is on the lower right, the outcoupler R_4 for the ultraviolet on the upper left. The crystal heater made of copper is in the center between the upper two mirrors. The cavity body is made of aluminium. See main text for further details.

Impedance matching

In order to provide maximal power enhancement and conversion efficiency, the cavity has to be impedance matched, see appendix C. This implies that the round-trip power losses of the fundamental light in the cavity have to be matched by the incoupled power. Power losses in the cavity occur both due to conversion to harmonic and due to linear absorption or reflection off the crystal surfaces. Technically, the reflectivity R_1 of the incoupling mirror has to be chosen appropriately, dependent on input power and estimated losses. A formula for this is given in reference [260] and based on this we calculated an optimal reflectivity of $R_1^{\mathrm{opt}} = 98.8\,\%$. The specified reflectivity of the used incoupling mirror of $R_1 = 98.70(25)$ is slightly below the optimal value. Generally, choosing lower reflectivities than the R_1^{opt} is advisable, as the power enhancement strongly drops if the resonator is undercoupled, i.e. for too large R_1.

Mechanical cavity design

With the optimal waist in the crystal and a stable round trip, the foundation of the mechanical design of the cavity is laid. The main criteria for this were the achievement of a large output power, stable day-to-day operation with a tight and high-bandwidth locking of the cavity, the possibility of evacuating or purging the cavity if necessary and a flexible alignment of the crystal. Furthermore, the crystal holder should allow for a heating in order to avoid damage to the crystal induced by ambient humidity.
To achieve these goals, a monolithic cavity design was chosen similar to reference [261], see Fig 5.5. The mirror mounts (RD2-HS, Radiant Dyes) for the cavity mirrors are attached to the aluminium housing and their position can be controlled with fine-thread screws (Model 5, Radiant Dyes). The diameter of the mirrors were selected to be $0.5''$ for R_1, R_3 and R_4. The high-reflectivity coating for R_2 to R_4 is specified for $R > 99.95\,\%$ at 596 nm. To achieve impedance matching, the incoupler R_1 has a specified reflectivity of $R = 98.70(25)\,\%$. The crystal was placed in a heating made of copper, which allows for operation at stabilized crystal temperatures

up to 200 °C. For BBO, however, the temperature was set to a considerably lower value of approximately 80 °C, to avoid damage due to ambient air humidity and to allow for a temperature stabilization via a resistive heater without cooling. To avoid heat transfer from the heater to the cavity body, the adapters were made of MACOR. For alignment of the crystal position and orientation, the heating assembly containing the crystal was placed on two independent manipulation stages, one linear stage (M-SDS40, Newport) for z-translations of the crystal along the direction of the short cavity arm and a five-axis manipulator (9071-V, Newport) for all other relevant degrees of freedom. To achieve fast and stable locking of the cavity length, a two-piezo design was pursued with a slow piezo actuator with large stroke (HPSt150/14-10/12, piezomechanik, specified resonance frequency 75 kHz), combined with a fast piezo with smaller stroke (HPCh-150/6-2/2, piezomechanik, specified resonance frequency > 500 kHz). The small piezo was placed on a heavy mounting structure and holding a smaller mirror substrate R_2 with diameter 0.25 ″ and thickness 3 mm. With a similar design, large stabilization bandwidths of up to 180 kHz have already been demonstrated [262]. To allow in principle for evacuating the cavity, the input port and output port were closed with fused silica windows (WG41050-UV and WG41050-A, Thorlabs Inc., respectively).

5.2.3 Performance of the doubling cavity

In the following, the benchmarked performance of the doubling cavity will be presented briefly.

Conversion efficiency

The realization of Rydberg dressing requires large powers in the ultraviolet. Therefore, the generated power in the cavity is a very important benchmark. A measurement of the output power of the cavity P_{out} in the ultraviolet at 298 nm versus the incident power P_{in} at 596 nm is shown in Fig. 5.6. While for small incident powers, the converted power increases quadratically as expected for second-harmonic generation, the dependence becomes linear for larger P_{in}. This is characteristic for the enhancement cavity: An increased conversion of fundamental light to the ultraviolet adds effectively to the loss of the fundamental and therefore counteracts the power enhancement in the cavity via a decrease of the finesse [251], see also appendix C. The largest measured output power is approximately $P_{\text{out}} = 300$ mW for an incident power of $P_{in} = 980$ mW. The resulting conversion efficiency saturates in this regime at approximately $\eta = 30$ %. As the achievement of phase matching in the BBO crystal requires the fundamental and the harmonic to have orthogonal polarizations, the Brewster angle is not effective for the ultraviolet. Due to the resulting idle reflection, approximately 22 % of harmonic power created in the crystal is lost and does not exit

the resonator. Correcting the measured power for this and including approximately 10 % loss of ultraviolet power before the measurement point, we obtain conversion efficiencies on the order of 40 %, comparable to what has been achieved in other experiments, e.g. in references [231, 245, 251] but slightly lower than reported in references [232, 247].

Cavity reflection

For high conversion efficiency, the light entering the cavity has to be as well spatially mode-matched as possible to the cavity mode, i.e. the beam has to be focussed to match the cavity waist $w_2 = 320\,\mu\text{m}$. The quality of the mode matching can be assessed by quantifying the minimal reflected light when the cavity is scanned over the resonance. In our case Fig. 5.7 shows a coupling efficiency of approximately 95 %, indicating excellent spatial-mode and power impedance matching. In fact, the observed reflection dip seems to be saturating compared to the fit function at the central point of minimal reflection. This could be attributed to variable losses when the frequency of the laser is scanned over the cavity resonance. On resonance, when the maximal second-harmonic power is generated, the losses are maximal, therefore the reflection effectively broadens over a small range of detunings and the peak saturates. From the fitted free spectral range $\Delta\nu_{\text{FSR}} = 376(5)\,\text{MHz}$ and the width $\delta\nu = 1.35(8)\,\text{MHz}$ of the reflection dip, we calculate a finesse of $\mathcal{F} = \Delta\nu_{\text{FSR}}/\delta\nu = 278(17)$.

Possible future improvements

The measured conversion efficiency in the constructed cavity is lower than the optimum predicted by the Boyd-Kleinman model. The solid line in Fig. 5.6 is obtained by a theoretical model of the generated harmonic power for a down-scaled Boyd-Kleinman factor h to 67 % of the calculated optimal value. A reason for this could be the elliptical waist in the BBO crystal. Optimizing the cavity parameters for elliptical waists in the crystal has been discussed and even predicted to lead to larger conversion efficiencies [247, 263, 264]. Furthermore, the larger conversion efficiency compared to the expectation for smaller incident powers could imply thermal effects coming into play for larger P_{in}. These can be reduced by increasing the waist w_c in the crystal [256]. To reproduce the power characteristics in Fig. 5.6 and the observed finesse $\mathcal{F} = 278(17)$ within the same model, the intra-cavity losses have to be as high as $\alpha \approx 0.7\,\%$. Combining reported absorption losses in the BBO crystal [241, 242], estimated reflections at the Brewster crystal surfaces and losses at the high-reflectivity cavity mirrors, we would expect smaller intra-cavity losses of maximally 0.1 %. Possible sources for additional losses are damage in the crystal or losses at the crystal surface, both could be reduced by using a different crystal.

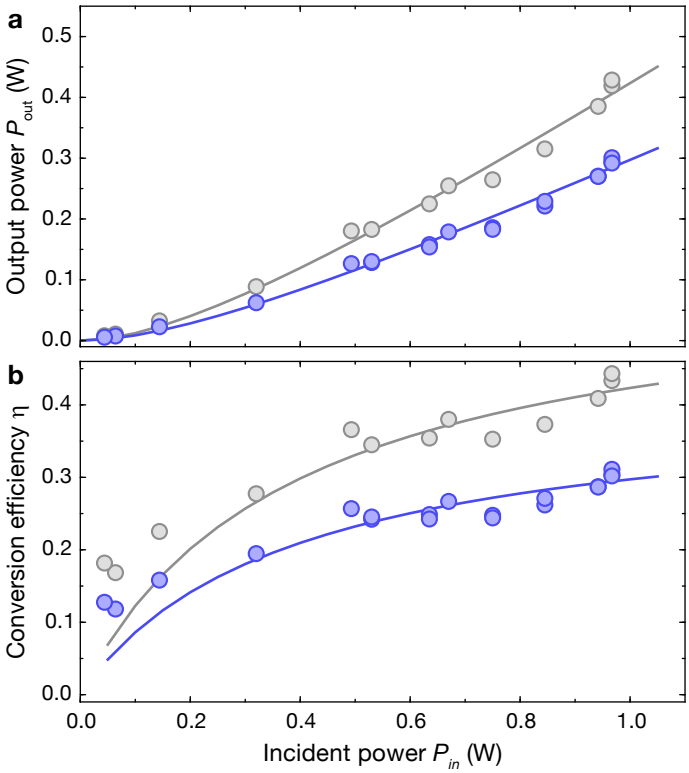

Figure 5.6: Output power and conversion efficiency of doubling resonator. a Output power P_{out} at 298 nm versus incident power P_{in} in the visible, measured behind and before the cavity (blue data points). The solid blue line represents the expected characteristics based on an *ab-initio* calculation of the cavity properties, taking into account the power dependence as well as the measured finesse of $\mathcal{F} = 278(17)$, see also appendix C. Best agreement with the data is achieved for a total round-trip loss of $\alpha \approx 0.7\,\%$, a down-scaled Boyd-Kleinman factor $h_{sc} = 0.67\,h$ and an input reflectivity of $R_1 = 99.17\,\%$, slightly above the value specified by the manufacturer. The gray data points and solid line show the same data, but scaled to take into account the reflection loss of the converted harmonic light at the second crystal surface (22%) as well as loss before the measurement point of the ultraviolet power (estimated to be 10%). **b** Resulting conversion efficiency $\eta = P_{\text{out}}/P_{in}$ without (blue) and with these losses taken into account (gray).

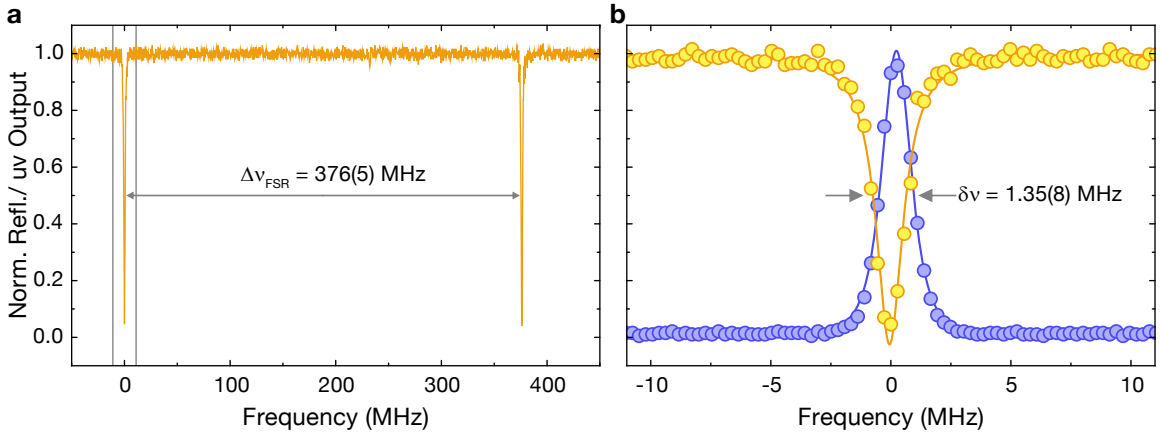

Figure 5.7: SHG cavity reflection. a The reflection signal of light at 596 nm is shown for a broad frequency scan (orange). The free spectral range $\Delta\nu_{\mathrm{FSR}} = 376(5)$ MHz is extracted from a fit of the theoretically expected reflection curve. **b** Zoom into the region marked by two vertical lines in a. A single reflection dip is shown (yellow data points), together with the fitted theoretical expectation (orange solid line). This yields the width $\delta\nu = 1.35(8)$ MHz. The generated ultraviolet light after the cavity is shown in blue. The solid blue line guides the eye.

5.2.4 Laser setup – Seed and doubling to 596 nm

The next sections describe the laser setup, providing further technical details for the overview given in section 5.2.1.

Sideband lock to reference cavity

The light of the seed laser at 1192 nm is derived from a commerical external cavity diode laser (DL 100 PRO, TOPTICA Photonics). A small amount of the light is used for measuring the wavelength with a commercial wavelength meter (HighFinesse WS7), see Fig. 5.8.
For linewidth reduction and frequency stabilization of the seed, approximately 20 µW of the seed light are split off and sent through a fiber-coupled electro-optic modulator (f-EOM, PM-0K5-10-PFA-PFA-1190, EOSPACE Inc.) to a reference cavity made of ultralow expansion (ULE) glass (ATFilms) with a measured finesse of $\mathcal{F} \approx 10800$ and a free spectral range of $\Delta\nu_{\mathrm{FSR}} = 1496.6$ MHz. Spacers made of ULE glass have been becoming popular recently due to the insensitivity of their length to temperature and a zero-crossing of the thermal expansion coefficient, which makes them excellent tools for absolute frequency stabilization [205]. To provide isolation against acoustic and thermal perturbations, our reference cavity is temperature stabilized and kept under vacuum at a pressure below 10^{-7} mbar.

For frequency stabilization, the f-EOM is driven by a radio-frequency (RF) signal at a frequency of $f_{\mathrm{PDH}} = 15\,\mathrm{MHz}$. The sideband is used to stabilize the seed light to the ULE cavity using the Pound-Drever-Hall locking scheme [265]. In order to provide frequency tunability, a second, stronger RF signal with variable frequency f_0 and power 16 dBm is applied to the f-EOM. Locking one of the two sidebands at $\pm f_0$ to the ULE cavity provides the desired frequency tunability by changing f_0, which shifts the carrier relative to the absolutely frequency-stabilized sideband. We achieve this by remotely controlling the RF-source (SG384, Stanford Research Systems) via the experiment control software. The two RF modulation signals result in a total of nine frequencies (carrier plus two sidebands at $\pm f_0$ and each of them with two sidebands at $\pm f_{\mathrm{PDH}}$). If Rydberg resonances come to fall close to the carrier or half the free spectral range of the ULE-cavity, stable locking might be complicated due to interferences between the sidebands. In those cases, single optical sideband generation might be useful, however comes with significant technical overhead [266, 267]. An alternative strategy is the addition of offset frequencies by acousto-optic modulators.

Single-pass doubling

Approximately 20 mW of the seed light in the infrared are used to seed a Raman fiber amplifier system (VRFA-P-2-595.4-SF, MPB Communications Inc.), which outputs approximately 10 W of infrared power and up to 2.2 W (typically 1.6 W at the wavelength required to excite the Rydberg state $31P$) in the visible spectral range at 596 nm. The phase matching for the single-pass doubling stage from the infrared to 596 nm in periodically poled lithium niobate (PPLN) is achieved by temperature tuning, with typical temperatures in the range between $50 - 70\,^{\circ}\mathrm{C}$. The light at 596 nm is sent through an optical isolator to prevent damage of the single-pass doubling stage by back reflections and then passing through an acousto-optic modulator (AOM) which is driven with a frequency of 200.674 MHz. The -1^{st} order is then coupled with a coupling efficiency of approximately 65 % into a polarization-maintaining, single-mode photonic crystal fiber (PMJ-A3HPC.A3AHPC-1064-15/230-3AS-3-1-CSP-SP, OZ Optics) in order to clean the spatial mode and to keep the system modular and flexible.

5.2.5 Laser setup – 298 nm

Coupling to the cavity

The light at 596 nm coupled out of the photonic crystal fiber is beam shaped for optimal mode matching with the mode of the second-harmonic resonator cavity (SHG cavity) using the collimation lens ($f = 4.51\,\mathrm{mm}$) in combination with a telescope, see Fig. 5.8. To adjust the polarization of the light for optimal conversion efficiency in

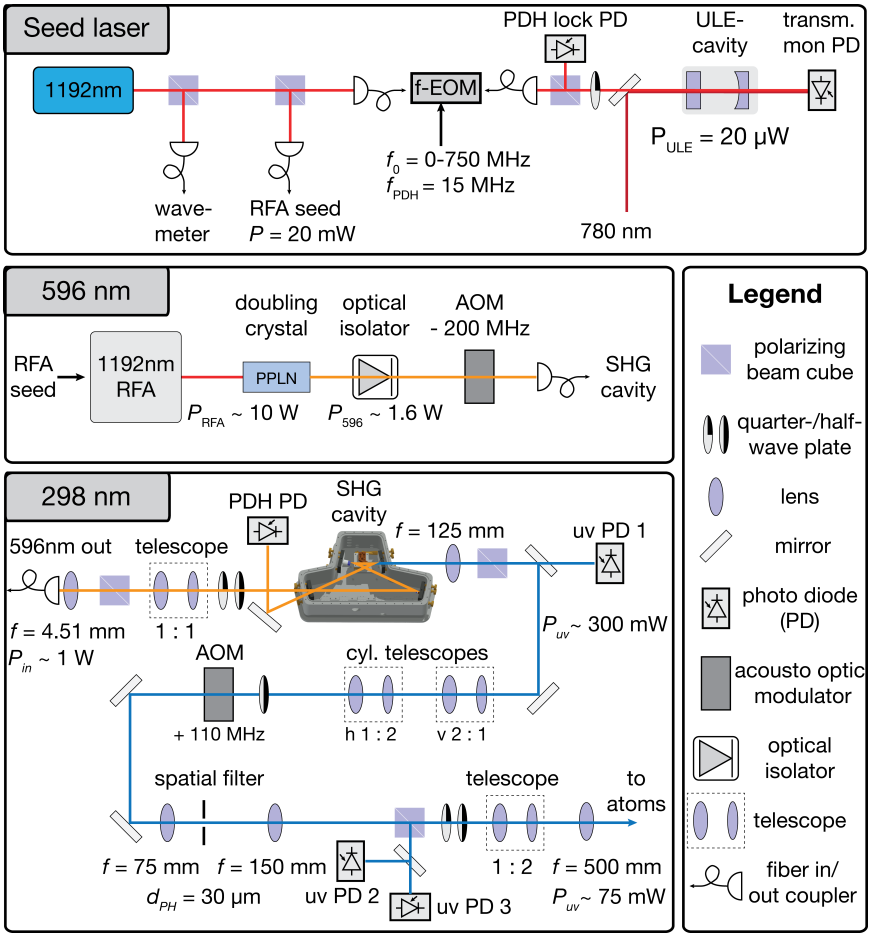

Figure 5.8: Optical setup of Rydberg excitation laser system. The generation of the ultraviolet light starts with the seed laser at a wavelength of 1192 nm (top panel), which is frequency stabilized via the sideband of a fiber-coupled electro-optic modulator (f-EOM) to a cavity made of an ultra-low expansion glass spacer. The 780 nm laser driving the lower transition in the two-photon Rydberg excitation scheme is also locked to the ULE cavity. Part of the light at 1192 nm is used to seed a Raman fiber amplifier system (RFA), which outputs a power of approximately 10 W and is then frequency doubled using a periodically poled lithium niobate (PPLN) crystal, yielding typically 1.6 W of light at a wavelength of 596 nm (middle panel). This light is then again frequency doubled using a home-built resonator, which outputs up to more than 300 mW of ultraviolet light (bottom panel). After beam-shaping and mode cleaning with a pin hole of size $d_{PH} = 30\,\mu$m, approximately 75 mW of the ultraviolet light are focused to the two-dimensional atomic plane (power measured before an uncoated fused silica vacuum viewport). See main text for details.

the second-harmonic stage, half- and quarter-wave plates are added. The achieved coupling into the SHG cavity is excellent, the nearly vanishing reflection upon scanning over a cavity resonance, displayed in Fig. 5.7, shows that most of the light sent to the resonator is coupled into it, suggesting a very high spatial mode overlap between resonating cavity mode and incoming beam. To achieve stable ultraviolet light generation, the SHG cavity length is stabilized to the 596 nm light using the Pound-Drever-Hall locking scheme [265]. The RF sidebands required for the lock are generated via current modulation of the infrared seed at $f_{\mathrm{uvPDH}} = 20\,\mathrm{MHz}$.

Ultraviolet collimation

To separate the fundamental light and the generated ultraviolet light after the doubling resonator, the high-reflectivity ultraviolet mirrors (custom coating HR297-323, Laseroptik) are sufficient, as they are nearly perfectly transmitting the fundamental at 596 nm. This is fortunate as therefore no specific dichroic coating has to be used. After several ultraviolet mirrors, when all fundamental light has been filtered, we use the small transmitted fraction of ultraviolet light of one of the mirrors for monitoring the ultraviolet power. In order to suppress background light, a colored glass filter (FGUV5, Thorlabs Inc.) is used before the photo diode (DET10A, Thorlabs Inc.). The ultraviolet light generated in the SHG cavity is strongly divergent due to walk-off in the non-linear medium and the rather tight focus in the non-linear crystal. To achieve collimation, we first use a spherical lens with a focal length of 125 mm, followed by two telescopes of cylindrical lenses to individually correct the waists of the beams in the two directions. Empirically, we found that the waist in the vertical direction has to be increased by a factor of two whereas the waist in the horizontal direction has to be decreased by a factor of two. This approach of shaping waists individually is complementary to using a single cylindrical lens for collimation as done e.g. in reference [247] and in some commercially available systems.

Spatial filtering

For switching and intensity modulation of the 298 nm light, an AOM (I-M110-3C10BB-3-GH27, Gooch and Housego) is used, operated at a frequency of 110.162 MHz. The $+1^{\mathrm{st}}$ order is focussed with a lens of focal length 75 mm through a pin hole with a diameter of $d_{PH} = 30\,\mu\mathrm{m}$. This pin hole has two important functions. First, it acts as a mode cleaner for the spatial mode of the ultraviolet light. After the pin hole, the spatial mode is close to a symmetric Gaussian with a residual ellipticity of less than 6%, see the inset of Fig. 5.12. The second important function of the pin hole is to provide a fixed reference point. The lenses after the pin hole are arranged so as to form an image of the pin hole at the position of the atoms. This implies that as soon as the ultraviolet beam is transmitted through the pin hole, it will also be aligned to

the atoms. This has been verified experimentally many times and proven very useful for fast alignment of the ultraviolet beam. The image is realized by a collimation lens with a focal length of 150 mm, a telescope expanding the beam by a factor of two and the final lens with focal length of 500 mm to focus the beam to the atoms, where a final waist of $w = 18(3)$ µm is measured, see Fig. 5.12. To set the correct polarization of the light for exciting targeted Rydberg states, a combination of a half- and a quarter-wave plate is used. All used lenses for collimation and focussing are standard fused-silica lenses, anti-reflection-coated for the ultraviolet spectral range.

Intensity stabilization

For achieving optimal intensity stability of the ultraviolet light, it has proven very useful to pre-stabilize its power by feeding back the signal recorded by the photo diode directly after the SHG cavity to the AOM controlling the intensity of the 596 nm light before the photonic crystal fiber. The advantage is that this scheme allows to use the AOM in the ultraviolet without a stabilization loop for faster intensity switching, not limited by a stabilization loop bandwidth. The results described in chapter 7 rely critically on very good intensity stability and fast switching and most likely could not have been achieved without this trick. The frequency lock of the SHG cavity seems not to be affected negatively by the intensity stabilization, as long as the intensity is not modulated too much. In the experiments described in chapter 7, the intensity was not modulated by more than approximately 10 %. The two photo diodes in the ultraviolet path after the pin hole serve either for further stabilization or for monitoring the ultraviolet beam.

5.2.6 Rydberg spectroscopy in vapor cells

As a first fast and easy test whether the laser system is suitable for excitation of Rydberg states, a spectroscopy of rubidium-87 in a gas cell was performed. To detect the weak signals of the Rydberg state $36P_{3/2}$ with a natural linewidth of $1/\tau = 25\,\mathrm{ms}^{-1}$ in a rubidium vapor, we performed a shelving spectroscopy experiment similar to reference [268]. Thereby, the weak signal of a narrow line with long natural lifetime is detected via the suppression of absorption on a stronger, broad line. The technique relies on shelving atoms in the long-lived state and thereby removing their contribution to the strong line, hence the name "shelving spectroscopy". This concept was introduced and successfully demonstrated for state detection of (individual) ions [269, 270]. The principle and setup for the spectroscopy of rubidium Rydberg states is shown in Fig. 5.9 a and b. The frequency of an infrared laser at 780 nm was stabilized to the cycling transition of the D_2-line of rubidium-87 with a natural linewidth of $\Gamma = 2\pi \times 6.067\,\mathrm{MHz}$ and a saturation intensity $I_\mathrm{s} = 2.5030\,\mathrm{mW/cm^2}$ [102]. To enhance the sensitivity, we performed a differential measurement. To this end, the infrared

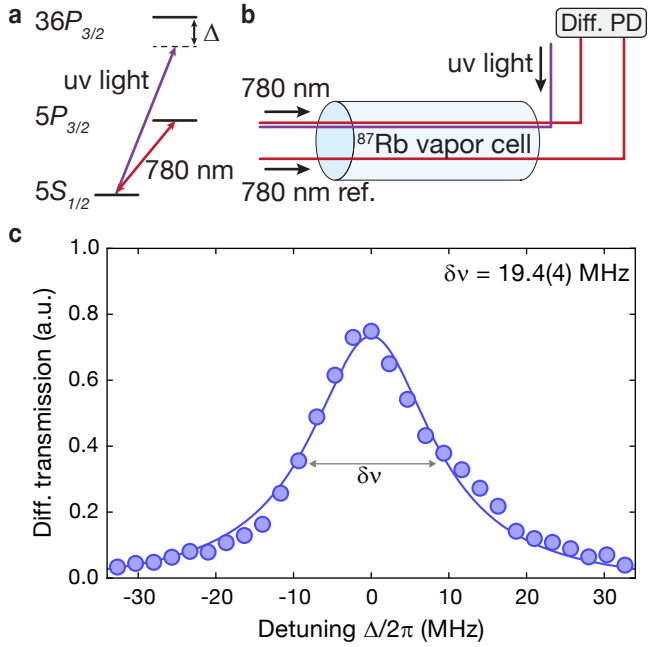

Figure 5.9: Rydberg spectroscopy in rubidium vapor. a Schematic of bleaching spectroscopy with an infrared probe beam locked to the D_2-line and the ultraviolet beam exciting the Rydberg state $36P_{3/2}$. **b** The infrared is split in two beams and sent to a differential photo diode. One beam is overlapped in a vapor cell with the counter-propagating ultraviolet. **c** Differential transmission signal. On resonance, the depletion of the $5S_{1/2}$ population due to the excitation of the Rydberg state results in enhanced transmission on the D_2 line. The width $\delta\nu = 19.4(4)$ MHz is limited by the natural linewidth of the D_2 cycling transition, up the residual Doppler-shift-induced broadening.

light was split in two equal parts with an approximate intensity $I_s/2$ per beam and sent through the cell to a differential photo diode (PDB210A/M, Thorlabs Inc.). One of the two infrared beams was overlapped with a counter-propagating ultraviolet beam with a larger beam diameter and an intensity $I \approx 5000\,\mathrm{mW/cm^2}$, whose frequency was varied, see Fig. 5.9 b. In order to increase the signal-to-noise ratio, we additionally modulated the ultraviolet power with a chopper wheel and performed a lock-in detection. The differential absorption signal obtained upon varying the ultraviolet frequency is displayed in Fig. 5.9 c and shows a spectral feature of enhanced transmission at the frequency corresponding to the $5S_{1/2}$ to $36P_{3/2}$ transition. The feature is fitted with a Lorentzian, yielding a width $\delta\nu = 19.4(4)$ MHz. As both beams interact with the zero-velocity class of atoms, the feature is expected to be Doppler-free, up to a residual Doppler broadening due to the different wavelengths of infrared and

ultraviolet beam [268]. The observed width is only slightly larger than the expected $780\,\mathrm{nm}/297.7\,\mathrm{nm} \times \Gamma = 15.9\,\mathrm{MHz}$. The most likely broadening mechanism responsible for the deviation is saturation broadening on the infrared probe line [271], but also other mechanisms like collisional broadening or transit-time broadening could contribute.

5.2.7 Rydberg spectroscopy in optical lattices

The spectroscopy in the vapor cell provides a good initial benchmark of the ultraviolet system and a starting point for detecting Rydberg resonances in the optical lattice. The goal for the latter is to locate transitions from the ground state $5S_{1/2}$, $F = 2$ to the Rydberg states as precisely as possible. Limiting factors are generally the natural linewidth of the transitions, finite laser linewidth, power broadening and, specifically for Rydberg states, interaction-induced broadening. Doppler broadening can be neglected in the optical lattice as the atoms are cooled to the ground states of the respective lattice wells and movement is frozen at the chosen lattice depths of $(V_x,V_y,V_z) = (40, 40, 80)\,E_\mathrm{r}$, with the lattice recoil energy $E_\mathrm{r} = h^2/(8m_{Rb}a_\mathrm{lat}^2)$.
A typical resonance scan obtained for a Mott-insulating initial state with unity filling of atoms prepared in the spin state $F = 2$, $m_F = 0$ in the optical lattice is shown in Fig. 5.10. The detected signal is the fraction of atoms leaving the optical lattice after excitation due to the recoil kick, hence the resonances appear as dips. The four observed lines corresponding to the m_J Zeeman states of $31P_{3/2}$ are clearly distinguished. Their approximately equal splittings are consistent with the expectation for the linear Zeeman shift in the applied bias magnetic field of $B_{xy} = 0.43\,\mathrm{G}$ oriented along the excitation beam in the atomic plane. The hyperfine structure of the Rydberg states is not resolved, but responsible for the observed broadening of the resonances for $m_J = -3/2$ and $m_J = +3/2$ to full widths at half maximum (FWHM) of approximately 250 kHz. Extrapolating previously measured magnetic dipole hyperfine-structure constants A for small principal quantum numbers n [272] using the expected scaling $A \sim n^{-3}$ [98], we arrive at $A \approx 43\,\mathrm{kHz}$ for $31P_{3/2}$. This sets the scale $AF(F+1)/2 \approx 258\,\mathrm{kHz}$ for the shift of $F = 3$ relative to $F = 0$ in the Rydberg manifold and is consistent with the observed broadening of the extremal m_J states. The full calculation of the shifts of all levels confirms this simple estimate and furthermore also predicts the observed narrower features for $m_J = -1/2$ and $m_J = +1/2$, see Fig. 5.10.
To obtain the most narrow resonances with widths (FWHM) down to approximately 80 kHz [74], the excitation pulse was applied for 3 ms with an estimated Rabi frequency of $\Omega/2\pi \approx 10\,\mathrm{kHz}$. In this regime, neglecting power broadening, the FWHM $\delta\nu$ of the resonances is determined by $2\pi\delta\nu = 1/\tau + 2\gamma_L$ [181, 273], dominated by laser dephasing γ_L and the natural linewidth $1/\tau = 37\,\mu\mathrm{s}^{-1}$ of the Rydberg states. This allows for concluding that the laser dephasing $\gamma_L/2\pi$ is below 40 kHz. Residual power broadening of approximately 25 % for our Rabi-frequency estimate reduces

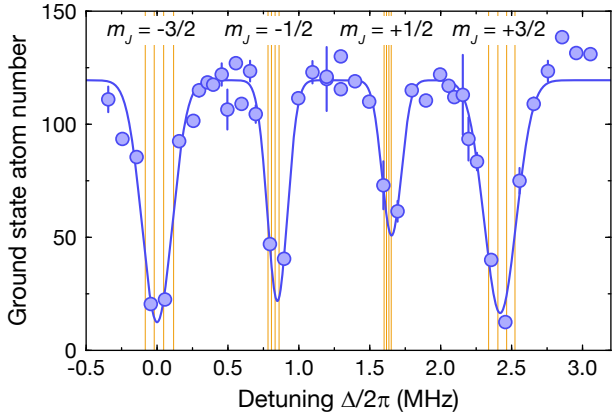

Figure 5.10: Rydberg resonance in optical lattice. Rydberg resonance for $31P_{3/2}$ for a Mott insulator as starting state versus excitation laser detuning Δ (blue data points). The resonance features are dips corresponding to a loss of atoms from the optical lattice upon excitation to a Rydberg state with Zeeman sublevel m_J as indicated. The orange lines are the result of a calculation of the expected level shifts in the applied magnetic field of $B_{xy} = 0.43\,\mathrm{G}$ in the plane of the atoms. The shifts of the m_J Zeeman states at this field are responsible for the large-scale splitting of approximately 800 kHz. Considering additionally the hyperfine interaction with a magnetic dipole constant $A = 43\,\mathrm{kHz}$, also the broadening of the measured resonances can be explained because the individual sublevels are not resolved. Such a resonance scan can be recorded very efficiently, only two shots were averaged per point. The error bars on the data points denote the standard error of the mean.

this value to 30 kHz, and additionally present interaction-induced broadening would lead to an even smaller inferred linewidth.

5.2.8 Rabi frequency calibration

With precisely determined resonance positions, also the Rabi frequency Ω for the transition between the ground and the Rydberg state can be calibrated accurately. This is one of the most crucial steps as the dressed interaction potential depends strongly on the Rabi coupling and scales like Ω^4. Therefore, the calibration of the interaction strength requires very precisely calibrated Rabi frequencies. The measurement we perform for the calibration is based on the dispersive AC-Stark shift of the ultraviolet beam on the ground state. If the coupling to the Rydberg state is detuned with a detuning Δ large compared to the Rabi frequency Ω, the shift is given as $\delta_{AC} = \Omega^2/4\Delta$, see also appendix A, equation (A.4) for the full expression for arbitrary Δ. The shift can be measured employing Ramsey spectroscopy [74], where the light-shift-induced phase difference between two ground states leads to a periodic oscillation in the pop-

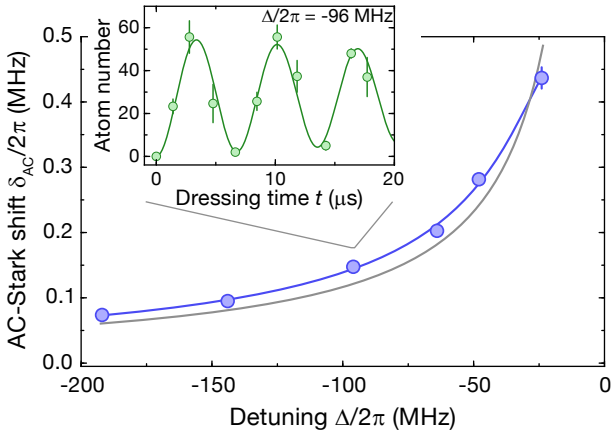

Figure 5.11: Extraction of ultraviolet Rabi frequency. A measurement of the AC-Stark shift δ_{AC} versus dressing laser detuning Δ (blue data points) allows to extract the Rabi frequency Ω of the dressing laser. To this end, the expression for the two-level light shift is fitted to the data, including a correction term due to the interaction (blue solid line). If the interaction correction is not taken into account, the behaviour cannot be captured (gray solid line). The extracted Rabi frequency is $\Omega/2\pi = 7.50(8)\,\mathrm{MHz}$. The inset shows an exemplary oscillation trace for $\Delta/2\pi = -96\,\mathrm{MHz}$, from which the AC-Stark shift is extracted as the oscillation frequency by fitting a damped sine-function. For this measurement, the measured ultraviolet power before entering the experimental chamber was $77(5)\,\mathrm{mW}$ and the waist at the position of the atoms $w = 18(3)\,\mu\mathrm{m}$. The error bars on the data points in the inset are the standard error of the mean, in the main figure they denote the 1σ-confidence interval of the fit.

ulations of a coupled and an uncoupled ground state with a frequency corresponding to δ_{AC}, see also Fig. 6.3 a in chapter 6. One exemplary oscillation is shown in the inset of Fig. 5.11. Repeating the measurement for various detunings allows to extract the Rabi frequency by a fit of $\delta_{AC}(\Delta)$. An exemplary set of measurements with a corresponding fit to extract Ω is displayed in Fig. 5.11 for the coupling from $5S_{1/2}$, $F = 2$, $m_F = -2$ to the Rydberg state $31P_{3/2}$. For the Ramsey sequence, the state $F = 1$, $m_F = -1$ is used as a non-shifted reference. Inspecting the shift, one can see that the simple model of non-interacting two-level atoms does not capture the observed dependence $\delta_{AC}(\Delta)$ fully. Rather, the observed light shift seems to saturate when the detuning is decreased. This is due to the van-der Waals interactions between nearby Rydberg atoms, which modifies the light shift. Only upon taking the interactions into account can one reproduce the data. This effect is in fact the first manifestation of Rydberg-dressed interactions and will be explained later, see chapter 6. With the interaction correction taken into account, we obtain an estimated Rabi

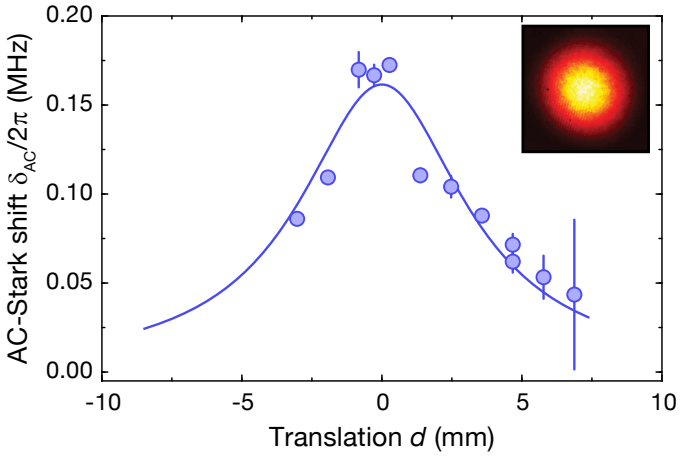

Figure 5.12: Extraction of ultraviolet beam waist. The AC-Stark shift δ_{AC} is measured versus a longitudinal shift d of the focus along the beam propagation (blue data points). The solid line is a fit of the form $\delta_{AC}(d) = a/(1 + (d/z_r))^2$. From the extracted value of the Rayleigh range $z_r = \pi w_0^2/\lambda$, the waist can be calculated to be $w_0 = 18(3)\,\mu$m, where the error is an estimate based on the fit-error and the systematic uncertainty in the determination of d. The error bars on the data points denote the 1σ-confidence intervals of the fit used to extract δ_{AC}. The inset shows the measured beam profile before focussing it into the cell. The shape is very well fitted by a Gaussian and has a residual ellipticity of 6%.

frequency of $\Omega/2\pi = 7.50(8)$ MHz, with a calibration uncertainty of approximately 1 %.

5.2.9 Waist calibration

Using the interferometric sequence described in the previous section, we can also optimize the focus position along the propagation direction of the ultraviolet laser to achieve maximal Rabi coupling at the position of the atomic plane. At the same time, this measurement allows to extract the waist of the focussed beam directly from the signal of the atoms. To achieve this, the light shift δ_{AC} was measured as a function of the longitudinal shift d of the ultraviolet focus, which was varied by changing the position of the last lens before the atoms with a z-translator. The measurement is summarized in Fig. 5.12. For each point along d, the two directions orthogonal to the propagation direction were optimized for maximal δ_{AC}. To extract the waist from the dependence of the light shift on the focus position, the Lorentzian intensity dependence expected for a Gaussian beam along the propagation direction was fitted to

the data and allowed for extracting a waist of $w = 18(3)$ µm for the ultraviolet beam at the position of the atoms. The inset of the same figure shows a measured beam profile of the ultraviolet beam after mode cleaning before the last lens, justifying the assumption of a Gaussian beam profile and demonstrating the functioning of the pinhole cleaning. For the experiments presented in chapter 7, the waist was calibrated to be $w = 18(3)$ µm, see Fig. 5.12, whereas for the experiments presented in chapter 6 a larger waist $w = 44(5)$ µm was used.

5.3 Direct detection of Rydberg P-states in an optical lattice

5.3.1 Introduction

While the previously discussed results were obtained by detecting ground state atoms, much insight can also be gained by detecting the Rydberg atoms directly in the optical lattice. This can be achieved in the case of Rydberg S-states excited via the two-photon excitation scheme by using the upper transition laser at a wavelength of 480 nm as a depumper, rapidly shifting its frequency by the intermediate state detuning $-\delta$, such that it resonantly couples the excited Rydberg atoms to their ground state, see the schematic in Fig. 5.1. Before the frequency is shifted, the non-excited atoms are rapidly removed from the lattice typically within 10 µs by a resonant light pulse on the cycling transition of the D_2-line, such that the depumped Rydberg atoms can be detected without background. This technique has been successfully applied for Rydberg S- and D-states of rubidium [55, 57, 115, 274, 275], and also in the experiments presented in chapter 4 of this thesis.
One natural question arising is whether an analogous scheme can be used to detect Rydberg P-states excited via the single-photon transition. Similar to the detection scheme for the two-photon excitation, a rapidly decaying intermediate state is required. In the case of Rydberg P-states, contrary to the two-photon scheme, an additional laser has to be used, which couples and hence depumps to the $4D$-state of rubidium. Due to screening of the nucleus in rubidium, the $5S$- and $5P$-states lie below $4D$, such that the latter can rapidly decay via a cascade down to $5S$, which can be detected by subsequent fluorescence imaging. Lifetimes of the $4D$- and $5P$-states are approximately 80 ns and 27 ns [276], such that the total cascade is expected to take approximately $100 - 110$ ns. Next to the advantage of direct optical detection, the depumper can also be used for spectroscopy of excited many-body states [274, 275, 277] or to induce controlled dissipation by admixing the decay of the $4D$-state to the Rydberg states. The latter could be interesting in the context of opening new directions in the study of non-equilibrium dynamics in cold dissipative Rydberg gases [278–

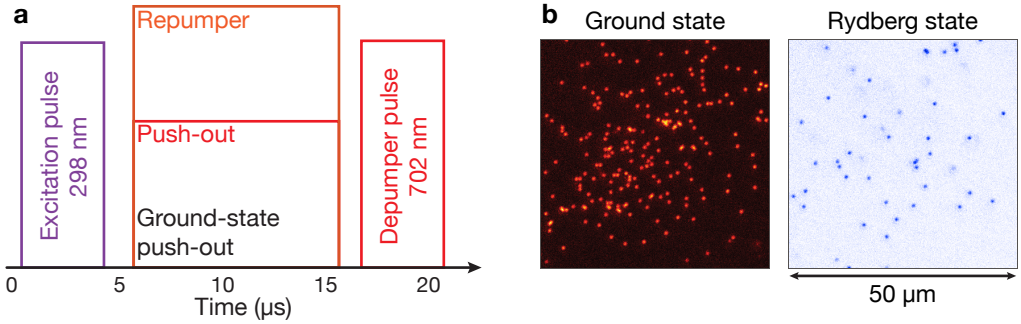

Figure 5.13: Detection scheme for Rydberg P-state atoms. **a** To detect the Rydberg atoms directly in the optical lattice, the excitation pulse (purple box) is followed by a ground-state push-out [55]. Finally, the atoms are depumped with a laser running at a wavelength of 702 nm. **b** Single shots obtained by fluorescence imaging of a dilute cloud of ground state atoms (left picture). After depumping, the Rydberg state $31P_{1/2}$ can be imaged (right picture).

285], which has recently been investigated experimentally [135, 151, 168, 286]. In ultracold cesium, depumping of P-states via the short-lived $7S$ has already been demonstrated experimentally [277].

5.3.2 Experimental excitation and depumping parameters

The following section briefly summarizes the results obtained for optical detection of the $31P$ Rydberg states. In order to increase the Rydberg signal and minimize interaction effects, a dilute cloud of approximately 250 atoms was prepared as a starting state in the optical lattice with the motional degrees of freedom frozen out, see Fig. 5.13 b. The laser at 702 nm used for depumping was frequency-stabilized relative to a locked laser at 780 nm via a transfer cavity, and its frequency could be freely tuned to match the required depumping resonances. The experimental sequence proceeded analogous to the schematic shown in 5.13. The Rydberg states were excited via the single-photon transition starting in $5S_{1/2}$, $F = 2$, $m_F = -2$ with a Rabi coupling of $\Omega/2\pi = 250(100)$ kHz and typical excitation pulse lengths of 4 μs. For the shown spectra, the excitation parameters were held constant. To define a quantization axis, a magnetic field was applied, oriented in the z-direction orthogonal to the atomic plane, and set to a value of $B_z = 0.27$ G. The excitation was followed by a 10 μs push-out of the ground state atoms [55] and a depumper pulse of 4 μs. The depumper propagated along the z-direction, was σ_--polarized and had a power of approximately $P_{\mathrm{dep}} \approx 600$ μW at a beam waist of $w_0 \approx 75$ μm.

5.3.3 Hyperfine-structure spectra of the $4D$-states

Depumping of Rydberg states allows for performing spectroscopy of the short-lived intermediate states, which is particularly interesting for the case of $4D$ as it cannot be excited with a single photon starting in the $5S_{1/2}$ ground state. For the low magnetic offset field, the $4D_{5/2}$- and the $4D_{3/2}$-states are well described in the hyperfine-structure basis. Level schemes with ground state, Rydberg state and $4D$-states with their respective level splitting and lifetimes are shown in Fig. 5.14 a, b. In the experimentally recorded spectra, the individual hyperfine states of both $4D_{5/2}$ and $4D_{3/2}$ are well resolved, see Fig. 5.14 c, d. The signal for successful depumping consists in an increase in the number of Rydberg atoms when the depumping is successful. The data displayed in Fig. 5.14 exhibit a gain in the detected Rydberg atom number by approximately a factor of two over the background of spontaneously decaying Rydberg atoms present even without active depumping.

Focussing on the spectral features, we observe that at the low applied magnetic field, individual magnetic Zeeman substates are within the width of the resonance features and, in particular for the state $4D_{5/2}$, $F = 4$, lead to a slight broadening of the depumping resonance. The observed splitting of the lines is in excellent agreement with the theoretical prediction based on measurements of the magnetic dipole and electric quadrupole hyperfine-structure constants in a magneto-optical trap via excitation from $5P_{3/2}$ [290], both for $4D_{5/2}$ [287, 289] and for $4D_{3/2}$ [288]. Vice versa, in principle the hyperfine-structure constants could also be extracted from the splitting of our measured spectroscopy lines for both $4D$-states. While the low statistics of our measurements seems to preclude an improvement of the accuracy of the known hyperfine-structure constants at present, the spectroscopy via the Rydberg state in principle allows for narrower spectral features and could be advantageous, provided that all systematics can be sufficiently well characterized. This might be relevant for improving bounds on known hyperfine anomalies, i.e. small differences in hyperfine constants for different isotopes due to the screened core [272, 289]. Indeed, considering for example the full width at half maximum of the resonances shown in Fig. 5.14 d, we extract for the states $F = 1$, $F = 2$ and $F = 3$ values between 2 MHz and 4 MHz, significantly smaller than the widths obtained in references [271, 290].

5.3.4 Rydberg blockade of P-states

In images with multiple atoms excited to Rydberg states, for example like the one shown in Fig. 5.13 b, the van-der-Waals interaction between Rydberg atoms leads to Rydberg blockade. The ability to directly image Rydberg atoms after depumping allows for quantifying the blockade by evaluating a density-density correlation func-

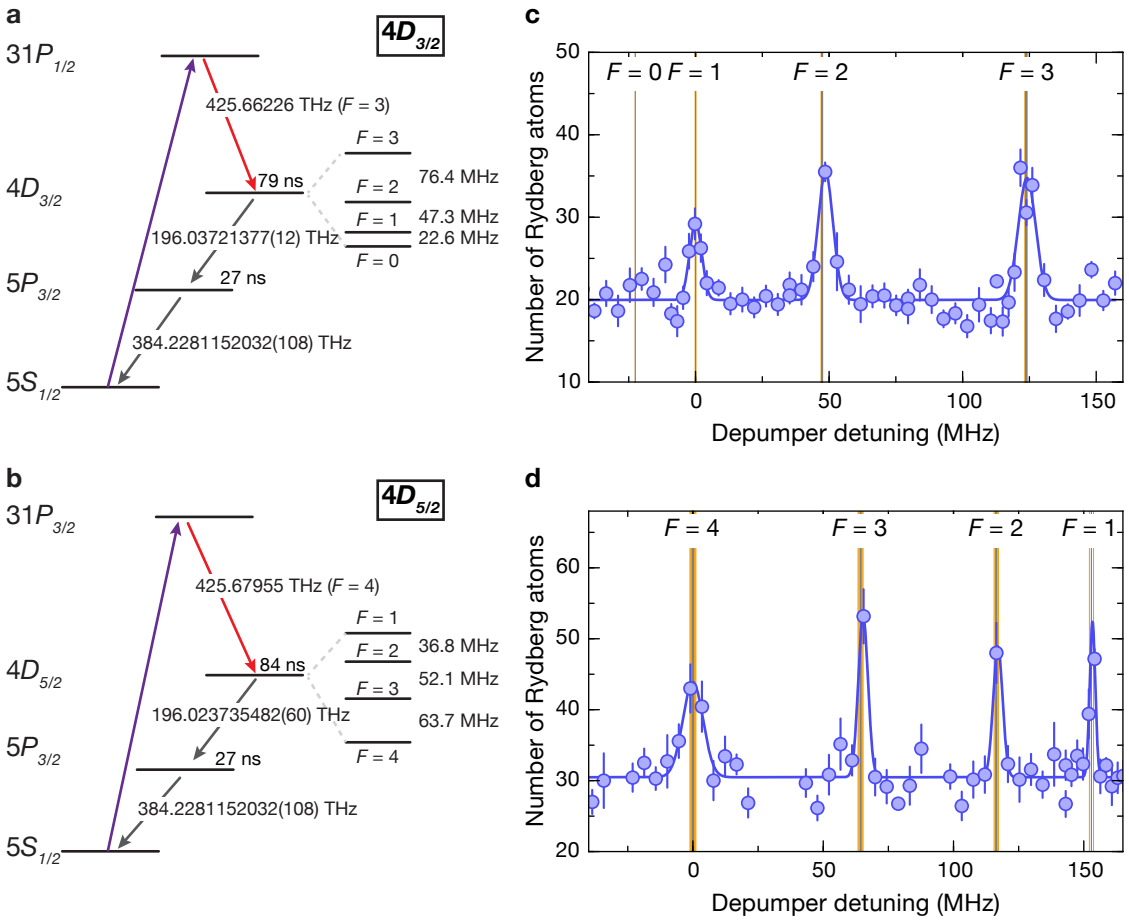

Figure 5.14: Hyperfine-structure spectra of $4D_{3/2}$ and $4D_{5/2}$ in rubidium-87. **a** and **b** Excitation and detection schematic displaying absolute transition frequencies [102, 287, 288], lifetimes [276] and hyperfine-structure splitting of $4D_{3/2}$ [288] (a) and $4D_{5/2}$ [289] (b). Rydberg level energies are calculated using quantum defect theory, see chapter 2. **c** Measured spectrum of $4D_{3/2}$ by depumping atoms from $31P_{1/2}$. The solid line is a fit of three Gaussian peaks with the same constant offset. The gray vertical lines are the resonance positions expected from a calculation of the $4D_{3/2}$ hyperfine structure at zero field, orange vertical lines mark the split Zeeman states. The fitted position of the $F = 1$ resonance marks the zero of the frequency axis for data and theory. Depumping via $4D_{3/2}, F = 0$ is impossible due to dipole selection rules. **d** Measured spectrum of $4D_{5/2}$ by depumping from $31P_{3/2}$ with same colors as in c together with expected lines. The fitted position of the $F = 4$ resonance is taken as the zero of the frequency axis for data and theory. The Zeeman substructure leads to a measurable broadening of the observed resonances, most pronounced for $F = 4$.

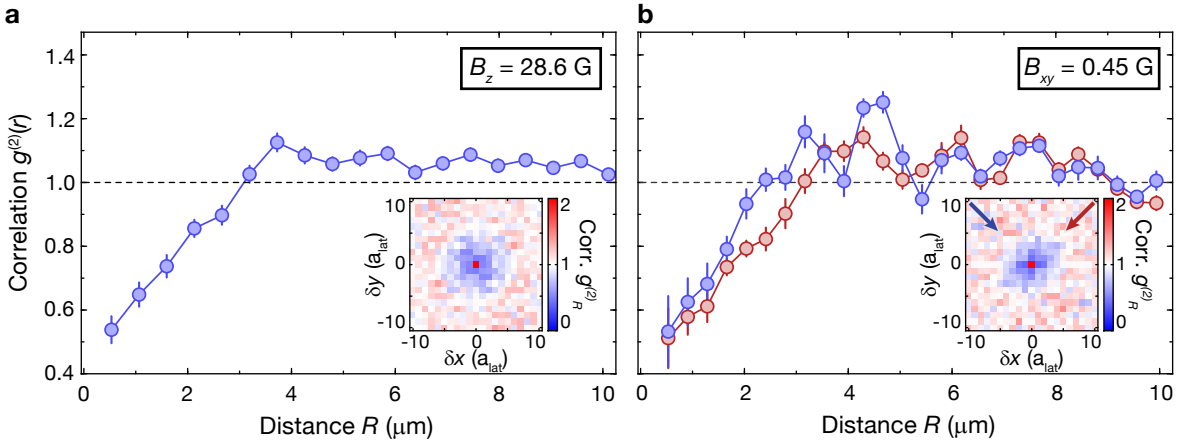

Figure 5.15: Rydberg blockade of $31P_{3/2}$ in different magnetic field configurations. **a** Azimuthally averaged density-density correlation $g^{(2)}_{\boldsymbol{R}}$. The measurement was performed with a dilute cloud as starting state and with the magnetic field oriented along the z-direction with strength $B = 28.66\,\mathrm{G}$. The excitation pulse had an area $\Omega t = 7.8(3)$ with a peak Rabi frequency of $\Omega/2\pi = 550(50)\,\mathrm{kHz}$. The inset shows the full two-dimensional correlation for different distance vectors $\boldsymbol{R}$ with components $(\delta x, \delta y)$ connecting two sites. **b** One-dimensional correlations with the three sites neigboring the center averaged along two orthogonal directions (red and blue data points). The magnetic field had a strength $B_{xy} = 0.45\,\mathrm{G}$ and was aligned with the direction of the excitation laser, which was σ_--polarized. The pulse area was $\Omega t = 4.0(5)$ and the peak Rabi frequency $\Omega/2\pi = 330(30)\mathrm{kHz}$. The inset shows the two-dimensional correlation analogous to a, with the two averaging directions indicated by red and blue arrows. Depumping was done via the state $4D_{5/2}$, $F = 4$ both for data shown in a and b. Error bars denote the standard error of the mean.

tion [55, 60, 291]

$$g^{(2)}_{i,j} = \frac{\langle \hat{n}^e_i \hat{n}^e_j \rangle}{\langle \hat{n}^e_i \rangle \langle \hat{n}^e_j \rangle}, \tag{5.6}$$

where $\hat{n}^e_i$ measures whether an atom at site $\boldsymbol{i}$ in the optical lattice was detected in a Rydberg state. For our experimental data, it is advantageous to increase statistics by evaluating the translationally averaged version

$$g^{(2)}_{\boldsymbol{R}} = \frac{\sum_{i \neq j} \delta_{ij,\boldsymbol{R}}\, g^{(2)}_{i,j}}{\sum_{i \neq j} \delta_{ij,\boldsymbol{R}}}. \tag{5.7}$$

Here, the Kronecker symbol $\delta_{ij,\boldsymbol{R}}$ constrains the distance between the two lattice sites $\boldsymbol{i}$ and $\boldsymbol{j}$ to the vector $\boldsymbol{R} = (\delta x, \delta y)$. A correlation signal of one indicates uncorrelated

densities, whereas larger (smaller) values than one signal correlation (anticorrelation). In the event of Rydberg blockade, the simultaneous excitation of close-by atoms is suppressed by the interaction, see chapter 2, which results in a "correlation hole" in the density-density correlation with low correlation values for short interatomic distances. This was observed in a unity-filling initial state in reference [55]. Evaluating the correlation for the Rydberg state $31P_{3/2}$, we find a similar suppression of joint excitation of nearby Rydberg atoms, qualitatively different for two different experimental configurations, see Fig. 5.15 a, b. For the first case, the quantization was set orthogonal to the plane of the atoms. The resulting correlation hole is symmetric with respect to the azimuthal angle, see inset of Fig 5.15 a. This can be understood from the fact that in this configuration, the van-der-Waals interaction between two Rydberg atoms is independent of their relative orientation. Quite the contrary, if the magnetic field specifying the quantization axis is rotated to lie in the atomic plane and aligned with the excitation beam, the van-der-Waals interaction becomes anisotropic, which results in an anisotropic blockade, visible in Fig. 5.15 b, especially in the inset. Later in this thesis, the same effect will be described in the context of Rydberg-dressed interactions admixed to the ground state, which inherit these isotropy properties of the bare van-der-Waals interaction. This is quite clear because, as explained in chapter 2, the blockade is responsible for the dressed interactions. In the symmetric blockade configuration, the reduced correlation signal extends up to about $R = 3\,\mu\text{m}$, roughly in agreement with the expected blockade radius $R_b = 2.7(1)\,\mu\text{m}$ for $31P_{3/2}$ at the used Rabi coupling of $\Omega/2\pi = 550(50)\,\text{kHz}$. Considering the data shown in Fig. 5.15, there is a quite considerable residual correlation signal within the range of the blockade for small separations between two atoms. This is not expected in case of perfect Rydberg blockade and possible reasons for the non-zero correlation might be motion induced by the excitation recoil or van-der-Waals repulsion, as well as residual movement before and during the fluorescence imaging. A further, more detailed analysis of these effects is missing thus far.

5.4 Summary and outlook

In this chapter, we have introduced and described the underlying technologies for excitation and detection of Rydberg P-states in an optical lattice. The presented direct optical detection of Rydberg P-states with the depump laser at 702 nm might be useful for engineering controlled dissipation in future experiments. Another open route is the study of ordered structures emerging in Rydberg gases [55]. Compared to the previously studied Rydberg S-states, the P-states used here have a smaller blockade radius, allowing for more excitations and hence larger structures to emerge. A comparison of single shots of the previously observed structures of Rydberg atoms in the

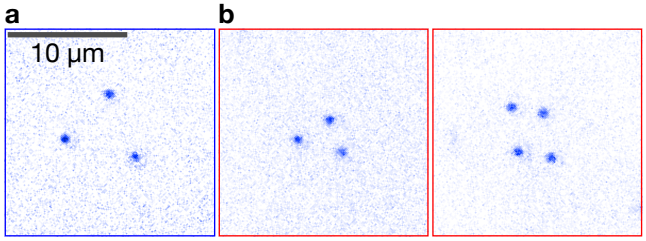

Figure 5.16: Comparison of ordered structures between $43S$ and $31P$. Fluorescence image of depumped **a** $43S_{1/2}$ and **b** $31P_{3/2}$ Rydberg atoms. Comparing the size of the ordered structures, the larger blockade radius as a consequence of the stronger interaction of $43S_{1/2}$ is apparent.

state $43S$ with more recently observed structures for $31P$ is shown in Fig. 5.16, highlighting the smaller blockade radius of the latter. Also, exploiting the anisotropy of the interactions of Rydberg P-states, anisotropic crystalline structures [292] or magic distances [139] could be studied.
Combining the optically detected Rydberg blockade of P-states with the strong Rabi coupling achievable on the single-photon transition, we were able to realize and measure Rydberg-dressed interactions for the first time in an ultracold gas of rubidium-87. The experimental techniques and the results of those measurements will be described in the subsequent chapters.

Chapter 6

Experimental realization of a Rydberg-dressed spin lattice

6.1 Introduction

In this chapter, we will show how the availability of a laser system for the direct single-photon excitation of Rydberg P-states can be exploited to implement Rydberg-dressed interactions in a many-body system. We will discuss the emerging Ising lattices if one out of two spin components of ultracold rubidium-87 in an optical lattice is off-resonantly coupled to a Rydberg state. Thereafter, we will present the first experimental implementation of such systems with dressed interactions. The interaction strength is measured interferometrically, with local spin resolution. This technique allows for demonstrating the tunability of the interaction, whose isotropy and range can be changed. The experimental results presented in this chapter are based on the publication [74].

6.1.1 Rydberg-dressed many-body systems

The idea of admixing Rydberg interactions to ground state atoms was developed with the aim to induce dipolar interactions in a Bose-Einstein condensate [61]. While the initially proposed technique was a stroboscopic admixture with resonant pulses requiring very accurate timing, it was realized later that dressed interactions can also be generated by off-resonant coupling [62–64]. Since then, the main focus has remained on the theoretical study of novel many-body phases in systems with motional dynamics ranging from the celebrated supersolid in two and three spatial dimensions [62, 63, 293, 294] to exotic Luttinger liquids in one dimension [170]. Matching the motional time scale with the much larger interaction energy scale of the Rydberg interaction is achieved by the weak admixture, which also allows for reaching the required lifetimes for the preparation and observation of the respective phases. More recently, also the possibility of realizing quantum spin models with Rydberg-dressed interactions has been explored, with a focus metrological applications [64, 65] or exotic spin interaction characteristics [66, 67]. Experimentally, the presence of Rydberg-

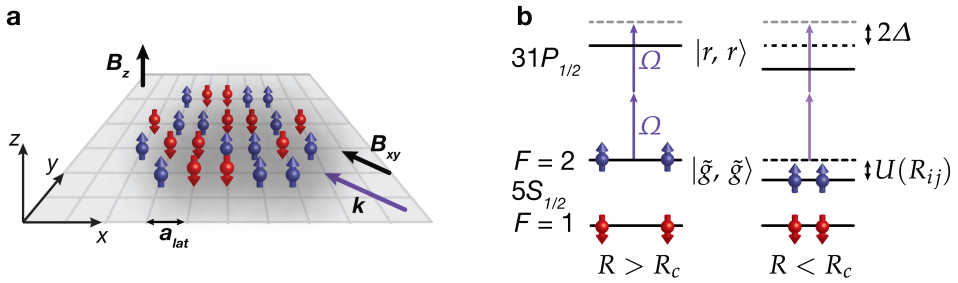

Figure 6.1: Schematic of spin lattice and interaction. a Illustration of the spin lattice with spin up (blue) and spin down (red) indicated as arrows, pinned in an optical lattice with lattice constant $a_{\mathrm{lat}} = 532\,\mathrm{nm}$ and depths $(V_x, V_y, V_z) = (40, 40, 80)E_r$. Two magnetic field directions B_{xy} and B_z (black arrows) are used to tune the isotropy of the interaction. The coupling laser with wavevector $\boldsymbol{k}$ (purple arrow) propagates along the diagonal of the lattice. **b** Illustration of dressed interaction in the spin system, analogous to Fig. 2.11. Only atoms in the spin-up state are interacting with the dressed interaction $U(R_{ij})$, which arises due to the detuning induced by the van-der-Waals interaction between Rydberg atoms for $R < R_c$.

dressed soft-core interactions has been demonstrated for two cesium atoms trapped in microtraps [73]. However, in many-body systems, experiments have not been able to show dressed interactions, but were rather plagued by strong losses and associated linewidth broadening [135, 154, 295]. In the experiments presented here, we study Ising quantum magnets, the most simple quantum spin models and therefore ideally suited to benchmark the novel Rydberg-dressed spin interactions. The following section gives a brief overview on Ising systems in general, before a discussion of their concrete implementation with Rydberg-dressed interactions.

6.1.2 Spin-$1/2$ Ising systems

The Ising model was introduced in the 1920s as a prototypical and simple model to describe magnetic properties of matter [296]. Despite its formal simplicity – it describes essentially interacting constituents with two internal degrees of freedom in external fields – it has become one of the most widely explored spin systems both theoretically and experimentally, providing a playground to study for example critical scaling [297], classical or quantum phase transitions [298] or non-equilibrium statistical mechanics [299]. Going beyond the originally treated model with interactions only between nearest neighbors, more recently also interactions between farther spins have been investigated, uncovering rich phase diagrams of complex ordered structures [300], including the well-known "devil's staircase" [301]. Due to its long history, its wide use and the availability of numerous theoretical tools and results, the Ising

model also constitutes an ideal benchmark to assess the power and capability of quantum simulators [302]. This is one of the prerequisites to allow for quantum simulators exploring regimes inaccessible to exact theoretical treatment.
Recently, several experimental quantum simulation platforms have emerged which are suitable for realizing Ising spin systems with extended-range interactions. Among them are one-dimensional linear ion strings in radio-frequency traps [86–89], ultracold polar molecules trapped in optical lattices [45], magnetic atoms [303] and ultracold atoms in optical lattices [57] or microtraps [56, 58] resonantly coupled to Rydberg states. The approach described in the following constitutes an alternative route to realize an Ising model with extended-range interactions in an optical lattice. The Ising interaction is realized via Rydberg-dressed dipolar interactions in rubidium-87. In a proof of principle experiment, we infer the presence of the interaction by performing Ramsey interferometry in the spin system and show that its characteristics can be tuned in range and isotropy.

6.2 Rydberg-dressed Ising systems

As presented in chapter 2, the interaction between two Rydberg atoms can be transferred to two ground state atoms by off-resonant optical coupling of the ground state $|g\rangle$ to the Rydberg state $|r\rangle$. We have seen that, in this case, the interaction potential between the two dressed atoms assumes the simple soft-core form

$$U(R_{ij}) = \frac{U_0}{1 + (R_{ij}/R_c)^6}, \tag{6.1}$$

where $U_0 = \Omega^4/(8\Delta^3)$ denotes the height of the soft core and $R_c = (|C_6|/(2\hbar|\Delta|))^{1/6}$ is the cut-off distance and sets the characteristic length scale of the interaction potential. Generalizing the discussion of chapter 2, we now consider two particles at different positions $\boldsymbol{i}$ and $\boldsymbol{j}$, as it is the case for example in an optical lattice, see Fig. 6.1 a. Whenever necessary, we explicitly indicate this in the absolute value of the distance vector $R_{ij} = |\boldsymbol{R}_{ij}| = |\boldsymbol{i} - \boldsymbol{j}|$. If not essential, we drop the explicit position dependence and write $R_{ij} \equiv R$. A possible angular dependence of the interaction enters as an angular dependence in R_c, which we have not written explicitly to keep the notation short.
In order to engineer the Ising system with dipolar interactions, we assume that a specific ground state, in our case the state $5S_{1/2}$, $|F = 2, m_F = -2\rangle \equiv |2, -2\rangle$, is off-resonantly coupled to a Rydberg state. Atoms in this state are called "spin up" ($|\uparrow\rangle$). Adding a second, undressed ground state, in our case we work with $|1, -1\rangle$ and call it "spin down", we obtain a two-state system which can be mapped to a spin-1/2 Ising model, see Fig. 6.1 b and also Fig. 3.3 in chapter 3. In the atomic basis and

in the rotating-wave approximation, the Hamiltonian describing a system of multiple atoms with the aforementioned internal states and interactions takes the form

$$\hat{H} = \frac{\hbar\Omega_{MW}}{2}\sum_{\boldsymbol{i}}\hat{\sigma}_{\boldsymbol{i}}^{x} + \hbar\delta_{AC}\sum_{\boldsymbol{i}}\hat{\sigma}_{\boldsymbol{i}}^{(\uparrow)} + \hbar\sum_{\boldsymbol{i}\neq\boldsymbol{j}}\frac{U(R_{\boldsymbol{ij}})}{2}\hat{\sigma}_{\boldsymbol{i}}^{(\uparrow)}\hat{\sigma}_{\boldsymbol{j}}^{(\uparrow)}. \tag{6.2}$$

The vectors $\boldsymbol{i}$ and $\boldsymbol{j}$ denote the position of atoms in a lattice, as exemplified in Fig. 6.1 a. The operators are the Pauli matrices $\hat{\sigma}^{x}$ and $\hat{\sigma}^{z}$ [128], which defines the projector on the spin-up state, $\hat{\sigma}^{(\uparrow)} = \frac{1}{2}(1+\hat{\sigma}^{z})$, and we have dropped the site labels for simplifying the notation. The atomic states are eigenstates with $\hat{\sigma}^{z}|\uparrow\rangle = 1$ and $\hat{\sigma}^{z}|\downarrow\rangle = -1$. We have introduced a transverse driving term containing $\hat{\sigma}^{x}$, which can for example be realized by a microwave coupling of strength Ω_{MW} between the states $|\uparrow\rangle$ and $|\downarrow\rangle$. The dressing-laser-induced light shift δ_{AC} acts as a longitudinal field.
The Hamiltonian (6.3) can be rewritten as an Ising model by symmetrizing the interaction and the longitudinal field for spin up and spin down. To this end, the Pauli matrices are replaced by corresponding spin operators $\hat{\sigma}^{(x,y,z)} = 2\hat{S}^{(x,y,z)}$ and $\hat{\sigma}^{(\uparrow)} = \frac{1}{2}(1+2\hat{S}^{z})$. The eigenstates $|\uparrow\rangle$ and $|\downarrow\rangle$ are then associated with the eigenvalues $\hat{S}^{z}|\downarrow\rangle = -\frac{1}{2}|\downarrow\rangle$ and $\hat{S}^{z}|\uparrow\rangle = \frac{1}{2}|\uparrow\rangle$. Using these relations, one arrives up to an irrelevant and hence neglected energy offset at the following Ising model

$$\hat{H} = B_{x}\sum_{\boldsymbol{i}}\hat{S}_{\boldsymbol{i}}^{x} - \sum_{\boldsymbol{i}}B_{\boldsymbol{i}}^{z}\hat{S}_{\boldsymbol{i}}^{z} + \sum_{\boldsymbol{i}\neq\boldsymbol{j}}J_{\boldsymbol{ij}}\hat{S}_{\boldsymbol{i}}^{z}\hat{S}_{\boldsymbol{j}}^{z}. \tag{6.3}$$

The microwave coupling now takes the role of a transverse magnetic field of strength $B_{x} = \hbar\Omega_{MW}$ and the spin-spin interaction term $J_{\boldsymbol{ij}} = \hbar U(R_{\boldsymbol{ij}})/2$ corresponds to the atomic interaction in equation (6.2). Positive $J_{\boldsymbol{ij}} > 0$ favors antiferromagnetic ordering of the spins while negative $J_{\boldsymbol{ij}} < 0$ leads to a ferromagnetic ground state with all spins aligned. The longitudinal field now acquires an additional term $\Delta_{\boldsymbol{i}}^{(\mathrm{coll})}$ due to the symmetrization and reads

$$B_{\boldsymbol{i}}^{z} = -\hbar\left(\delta_{AC} + \sum_{\boldsymbol{j}\neq\boldsymbol{i}}\frac{U(R_{\boldsymbol{ij}})}{2}\right) \equiv -\hbar\left(\delta_{AC} + \Delta_{\boldsymbol{i}}^{(\mathrm{coll})}\right). \tag{6.4}$$

This "collective field" $\Delta_{\boldsymbol{i}}^{(\mathrm{coll})}$ arises due to the interaction of a given spin with all its neighbors. In a one-dimensional system, the collective contribution will naturally be on the order of the interaction itself, given the experimentally accessible range R_{c} of the potential of a few lattice constants, but in two dimensions it can be considerably larger. In a defect-free infinite system or a system with periodic boundary conditions [56], the collective longitudinal field loses its spatial dependence and becomes homogeneous, such that it can be removed by working in a rotating frame or cancelling it by an externally applied field. The latter can either be a magnetic field

causing a Zeeman shift or a differential AC-Stark shift of an additional laser. Comparing the Ising Hamiltonian (6) with literature [88, 89], we note that it is also commonly expressed in terms of the original Pauli matrices rather than the spin operators used here. The two cases can be compared by the position of the critical point of the transition from the paramagnetic to the ordered phase. Expressed in terms of Pauli matrices, the critical point of the one-dimensional nearest-neighbor interacting transverse Ising model ($J_{i,i+1} = J$ and $B_i^z = 0$ for simplicity) lies at $B_x = J$ [304], whereas for the form given above it would be at $2B_x = J$.
The derivation of the Rydberg-dressed spin model is quite analogous to the one presented in reference [145]. There, the spin basis was constructed from one ground and one Rydberg state and the interaction was the bare van-der-Waals interaction between Rydberg atoms. Our previous experimental work [55, 57] and the results presented in chapter 4 can be rephrased in that language.

6.3 Dressed interactions in experiment

6.3.1 Generalization to many-body systems

Before continuing, we should justify that it is possible to write the bare atomic Hamiltonian in the form of equation (6.2), for which we have implicitly assumed that the interaction potential derived for two particles is also valid in the many-body system. Coming back to the starting point of the two-atom derivation, we consider the general Hamiltonian $\hat{H} = \hat{H}_\Omega + \hat{H}_\Delta + \hat{H}_{\text{int}}$ governing the dynamics of N atoms at different sites $\boldsymbol{i}$ in a lattice, given in chapter 2, see equation (2.29). To derive an effective dressed interaction in the many-body system, the perturbation theory in the small parameter $\beta = \Omega/(2|\Delta|)$ can be applied analogous to the two-particle case. Following the notation of references [62, 131], the perturbation of the eigenenergy of the many-body ground state $|G\rangle = \otimes_k |g\rangle_k$, with the index understood as a label for an atom, requires the off-resonant coupling via singly excited many-body states, $|R_i\rangle = |r_i\rangle \otimes_{k\neq i} |g_k\rangle$ to doubly excited many-body states $|R_{ij}\rangle = |r_i, r_j\rangle \otimes_{k\neq i,j} |g\rangle_k$, see Fig. 2.11 or 6.1 b for the two-atom analog. Restricting the perturbation to these states, the energy correction due to the coupling to Rydberg states interacting via the van-der-Waals potential $V(R_{\boldsymbol{ij}})$ in fourth order of β becomes [62]

$$\begin{aligned} E_G &= 2\sum_{i\neq j}^{N} \frac{|\langle G|\hat{H}_\Omega|R_i\rangle\langle R_i|\hat{H}_\Omega|R_{ij}\rangle|^2}{\hbar^2\Delta^2(2\hbar\Delta - V(R_{\boldsymbol{ij}}))} + \sum_{i}^{N} \frac{|\langle G|\hat{H}_\Omega|E_i\rangle|^2}{\hbar\Delta} \\ &= \frac{\hbar}{2}\sum_{i\neq j}^{N} U(R_{\boldsymbol{ij}}) + \frac{N\hbar^2\Omega^2}{4\hbar\Delta} + \frac{N(N-1)\hbar^4\Omega^4}{16\hbar^3\Delta^3}. \end{aligned} \tag{6.5}$$

Dropping the distance-independent terms, which quantify the AC-Stark shift due to the dressing light, one can see that the perturbative correction to the ground state energy is just the sum of two-body interactions derived for two isolated atoms. We will briefly discuss modifications to this at high atomic densities in section 6.4.4, after the respective section with experimental results where this correction might be relevant.

6.3.2 Generalization to multi-level atoms

Besides the required justification of the validity of the two-body interaction potential in the many-body system, it is furthermore also clear that the two-level approximation used for deriving Rydberg-dressed interactions with a single Rydberg state and a single ground state per atom is a simplification and has to be validated or refined. In a realistic system there are many Rydberg states and the van-der-Waals interactions are more complex, see chapter 2, and so are the Rydberg-dressed interactions. An overview of calculated van-der-Waals potentials taking into account the multi-level structure is displayed in Fig. 6.2, together with derived Rydberg-dressed potentials. It is apparent that the interaction characteristics depend on the different possible combinations of pairs of Zeeman components and the applied magnetic fields. Taking the numerically calculated bare van-der-Waals potentials as a starting point, the dressed potentials are influenced by two factors. In complete analogy to the two-level treatment, the distance-dependent detuning due to the interaction is responsible for the overall soft-core dependence of the calculated potential. In addition, the dipole-dipole interaction also alters the optical coupling dependent on the distance between the two atoms. In particular, states not optically coupled at large separations can become coupled for shorter distances, which can modify the dressed potentials, see Fig. 6.2 d. The distance dependence in the coupling arises because the dipole interaction operator is diagonalized in a basis of superpositions of the atomic eigenstates which determine the Rabi coupling, see equation (2.5) [66, 67, 74]. The coefficients of these superpositions are distance and angle dependent and have to be taken into account for the calculation of the dressed potentials. For carefully chosen laser parameters, the calculated potentials very closely resemble the approximate soft-core shape, and the latter typically provides a good estimate for the interaction in those cases, see Fig. 6.2. The presence of other, high angular momentum Rydberg states can also cause resonances appearing at short internuclear distances. These distances are unproblematic if atoms are kept at a distance larger than the position of the first occurring resonance, as is indeed the case in our optical lattice for the states $31P_J$ for example. Even without optical lattice, the influence of the additional resonances is questionable due to the expected small coupling [62]. An experimental study of these resonances and possible associated loss processes at short distances is highly desirable.

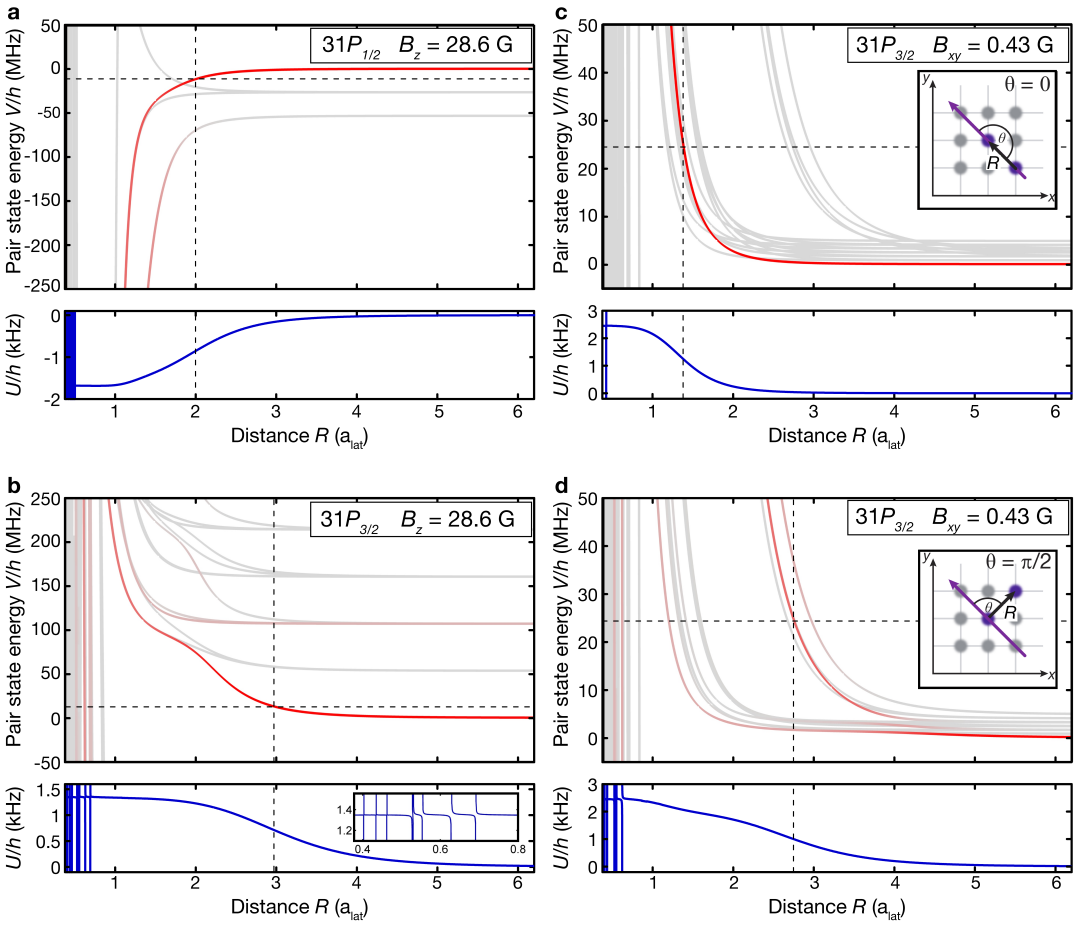

Figure 6.2: Calculated interaction potentials. **a** and **b** indicate the multilevel van-der-Waals Rydberg interaction potentials for pairs of atoms in $31P_{1/2}$ or $31P_{3/2}$ in a magnetic field of $B_z = 28.6\,\mathrm{G}$ aligned with the z-axis. Due to the Zeeman splitting of the m_J levels, there are several potential curves corresponding to combinations of two different m_J states. The intensity of the red coloring indicates the distance-dependent Rabi coupling Ω to the pair ground state. The lower panels show the resulting dressed potential $U(R_{ij})$ between two ground state atoms. The dashed vertical line marks the cut-off distance R_c of the dressed interaction. The inset of b provides a zoom to small R. **c** and **d**, Same plots as a and b, for a magnetic field $B_{xy} = 0.43\,\mathrm{G}$ aligned in-plane with the atoms, and the atomic separation vector R_{ij} either aligned with the magnetic field c, or perpendicular to it d, as depicted in the insets. The dressed interactions were calculated for Rabi frequencies of a $\Omega/2\pi = 1.33\,\mathrm{MHz}$, b $\Omega/2\pi = 1.25\,\mathrm{MHz}$ and c, d $\Omega/2\pi = 2.45\,\mathrm{MHz}$ and detunings of a $\Delta/2\pi = 6\,\mathrm{MHz}$, b $\Delta/2\pi = -6\,\mathrm{MHz}$ and c, d $\Delta/2\pi = -12\,\mathrm{MHz}$. Figure adapted from [74].

6.4 Experimental results for dressed spin model

6.4.1 Many-body interferometry

In the first experiments, our goal is to validate the Rydberg-dressed spin model defined in equation (6.3). The core of the experimental sequence is a Ramsey interferometry scheme [75, 305]. It combines the excellent control over the internal states available in a system of cold atoms with the single-particle-sensitive, local detection of our quantum gas microscope. The sequence consists of a sequential application of the transverse field in equation (6.3), followed by a variable time of Rydberg dressing. Two exemplary schematic sequences are shown in Fig. 6.3. We prepared the system for all measurements in $|1,\ -1\rangle = |\downarrow\rangle$, which was coupled to $|2,\ -2\rangle = |\uparrow\rangle$ with a microwave Rabi coupling of $\Omega_{MW}/2\pi = 12.5\,\mathrm{kHz}$. The interferometric sequence was initialized with a microwave pulse of area $\pi/2$, preparing an equal superposition of the two spin states in the equatorial plane of the Bloch sphere, see Fig. 6.3 b, d. After this initialization, we switched on the dressed interaction for a variable time. The longitudinal field B_i^z, composed of AC-Stark shift and collective longitudinal field, leads to a spin precession in the equatorial plane of the Bloch sphere, whereas the interaction itself causes spin dephasing. To measure the former, we closed the interferometer with a second microwave pulse of area $\pi/2$, mapping the acquired precession phase to the spin population in $|\uparrow\rangle$ and $|\downarrow\rangle$ respectively. In the absence of interactions, a periodic oscillation is expected with the frequency given by the precession frequency. The interaction-induced dephasing leads to a decaying oscillation contrast, see also Fig. 6.5. To detect the interactions directly, it is experimentally advantageous to use a sequence including a spin-echo microwave pulse of area π, which removes the precession, leaving the interactions as the dominating effect in the spin dynamics. Such a spin-echo sequence is illustrated in Fig. 6.3 b, d. In the absence of interactions, all spin population would return to the initial state $|\downarrow\rangle$. The interaction leads to an additional precession angle for spins in the equatorial plane of the Bloch sphere, which therefore pick up a correlated additional phase. The resulting phase correlations are responsible for the interaction-induced dephasing of the magnetization and can be observed as spin correlations in the populations of $|\uparrow\rangle$ or $|\downarrow\rangle$ after the second $\pi/2$-pulse.
In order to detect the spin populations in the S^z-direction, we employ a method similar to the one presented in references [28, 29]. There, atoms in the state $|2,\ -2\rangle$ ($|\uparrow\rangle$) were removed from the optical lattice via a resonant push-out and could then be detected as missing spins. In the case of a unity-filling initial state and no additional loss, the full spin distribution can be inferred.

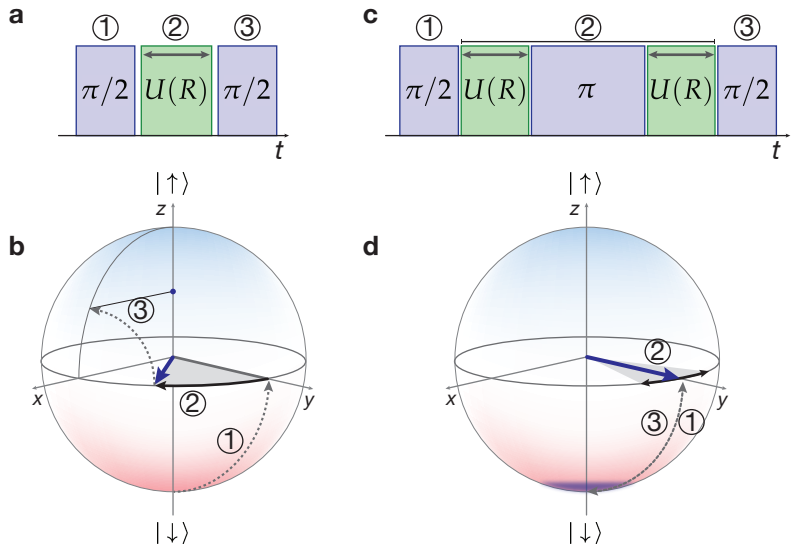

Figure 6.3: Experimental interferometry sequences. **a** Ramsey sequence without spin-echo pulse for Rabi frequency calibration. Two microwave pulses of area $\pi/2$ are used for preparation and readout (blue rectangles). The dressing laser is switched on in between for a variable time (green rectangles). **b** Illustrated trajectory of a single spin (purple arrow) on the Bloch sphere. The gray-shaded area and the black arrow indicate the precession angle, dashed arrows the trajectory of the spin during the microwave pulses. The final state is a superposition of spin up and down. The numbers connect the trajectory with the pulse sequence. **c** If an intermediate π-pulse is added, the single-particle shifts are cancelled. The interaction $U(R)$ in this case translates to correlations between the spins not returning to the initial state. **d** Illustration on the Bloch sphere. The gray-shaded area and the black arrow indicate the interaction-induced dephasing, which translates to correlations in the spin population after the final $\pi/2$-pulse (gray dashed arrow, blue coloring marks resulting depolarization away from spin-down direction).

6.4.2 Laser configuration

Two laser configurations used for inducing Rydberg-dressed interactions are displayed in Fig. 6.4. The states $31P_{1/2}$, $m_J = 1/2$ or $31P_{3/2}$, $m_J = -3/2$ are off-resonantly coupled with Rabi frequency Ω and detuning Δ to the ground state $|2, -2\rangle$. For the state $31P_{1/2}$, we use blue detuning and for $31P_{3/2}$ red detuning in order to fulfil $V(R) \cdot \Delta < 0$ for both cases, which avoids resonant coupling to the Rydberg pair interaction potentials. The dressing laser propagates in the atomic plane, at an angle of 45° with respect to the x and y lattice axes. The polarization is chosen linear in this plane, orthogonal to the magnetic field $B_z = 28.6\,\mathrm{G}$. The latter is applied in the

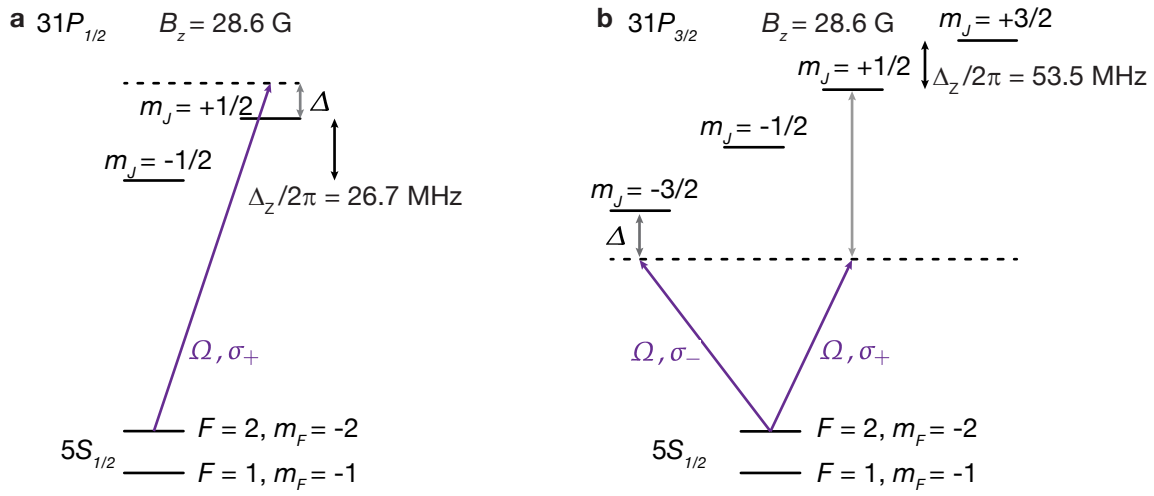

Figure 6.4: Excitation configurations. a The ground state $|\uparrow\rangle$ is off-resonantly coupled to the Rydberg state $31P_{1/2}$, $m_J = 1/2$ with Rabi frequency Ω and detuning Δ. The magnetic field applied in the z-direction defines the quantization axis for the spin system. **b** Same as a but for $31P_{3/2}$. The Zeeman shift is here also necessary to provide laser coupling only to the pair state asymptote with both atoms in $m_J = -3/2$, by detuning the state $m_J = +1/2$ by $2\Delta_Z$.

z-direction to set a quantization axis and realize an isolated spin system in the two ground states, see also Fig. 6.1 a for the geometry. The coupling to the Rydberg state $31P_{1/2}$ is provided by the σ_+-component of the linear polarization with respect to the quantization axis along z. For $31P_{3/2}$, in addition to the desired coupling to the state $m_J = -3/2$, also the state $m_J = +1/2$ is coupled, however the effect of this coupling can be safely neglected as long as $\Delta/(2\Delta_Z) \ll 1$, i.e. in the limit of large Zeeman splitting. For our measurements this is the case, see Fig. 6.4 b.

6.4.3 Collective field

In a first set of experiments aiming at investigating the spin-precession dynamics we employed a Ramsey sequence without spin echo. The dressing laser was switched on for variable time t, sandwiched between two microwave pulses of area $\pi/2$ each. For detection, we performed a spin-resolved measurement of the population in the state $|\downarrow\rangle$. An exemplary trace resulting from such a measurement is displayed in Fig. 6.5. The fast dephasing is caused by the spin-spin interactions and dominated by the collective field, which causes spins at the edge of the system to evolve at different precession frequencies compared to spins in the bulk. This effect is nicely illustrated by the single-shot images of the atomic distribution, where a ring-like structure signals the

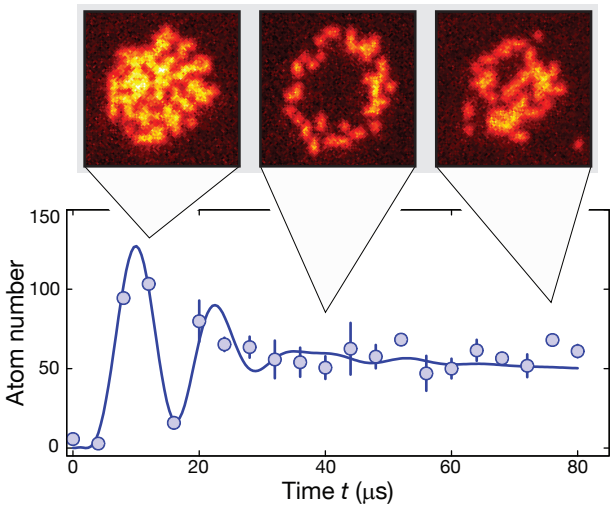

Figure 6.5: Ramsey trace in interacting system. Spin dynamics for dressing to the state $31P_{3/2}$, $m_J = -3/2$ with a detuning of $\Delta/2\pi = -8\,\mathrm{MHz}$ and a Rabi frequency of $\Omega/2\pi = 1.9(1)\,\mathrm{MHz}$. The main panel shows the time evolution of the spin population reflecting the precession phase. The precession frequency corresponds to the magnetic field shift and the dephasing is due to the interactions between the spins. Three exemplary single shots at different times as indicated by the triangles are displayed above the main panel. The polarized initial state develops a ring-like structure due to the collective interaction contribution $\Delta_i^{(\mathrm{coll})}$ to the magnetic field (see central picture). Error bars denote the standard error of the mean (s.e.m.).

time when the bulk and the edge have run out of phase by a differential precession angle amounting to π.
A systematic study of the precession frequency for different detunings Δ reveals the collective-field contribution quantified by equation (6.4) to the spin precession. The results of such a measurement are summarized in Fig. 6.6. The increasing oscillation frequency of the populations are clearly visible in the recorded time traces. Here, the dressing time is scaled to the time τ in order to take into account finite rise times of the dressing laser pulses [74]. For a quantitative analysis, we extract the frequency ν for each detuning via a fit of an exponentially damped sinusoidal oscillation. The dominating dressing laser-induced AC-Stark shift indicates a dependence of this frequency on the detuning,

$$2\pi\nu(\Delta) = \delta_{AC}(\Delta) = -\frac{\Delta}{2} + \frac{1}{2}\sqrt{\Omega^2 + \Delta^2}. \tag{6.6}$$

However, a fit of this formula to the experimental results shows a systematic residual, see Fig. 6.6 b, c. This residual vanishes only upon taking into account the contribution

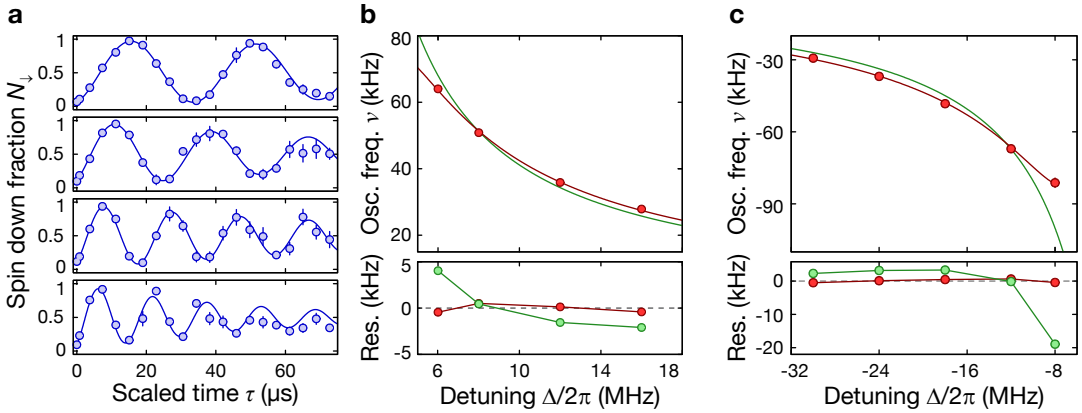

Figure 6.6: Experimentally determined collective-field shift. a Spin precession traces versus scaled time τ corrected for finite rise time of dressing pulses for varying detunings, measured by recording the number of atoms in the state $|\downarrow\rangle$, $N_\downarrow$, after a Ramsey sequence without spin echo. From top to bottom, the detunings were $\Delta/2\pi = 16, 12, 8, 6$ MHz. The oscillation frequencies ν are extracted from a sinusoidal fit and their dependence of Δ is shown in **b** and **c** for $31P_{1/2}$ and $31P_{3/2}$ (red data points, time traces for $31P_{3/2}$ not shown). The red solid line corresponds to the fit including the interaction correction, which removes the systematic residual shown in the lower panels which is present if the fit is performed without it (green solid line both in main and lower panels in b and c).

of the collective field to the precession frequency. Specifically, we include a correction and obtain a modified model

$$2\pi\nu(\Delta) = \delta_{AC}(\Delta) + \frac{N_{\text{eff}}}{2}\frac{\Omega^4}{8\Delta^3}. \tag{6.7}$$

Here, the soft core is approximated by a step function which is non-zero up to its range R_c. The collective-field contribution is then proportional to the effective number of spins N_{eff} within the range, scaled with the soft-core height $\Omega^4/8\Delta^3$. Due to the equal superposition of $|\uparrow\rangle$ and $|\downarrow\rangle$ in the interferometric sequence, the correction is reduced by a factor of one half. Leaving Ω and N_{eff} as fit parameters of the interaction-corrected shift $\nu(\Delta)$ to the data for $31P_{1/2}$, we obtain the best agreement for $N_{\text{eff}} = 11(2)$ particles within the interaction range. This is in good agreement with the simple estimate $\pi R_c^2 = 12.5$ for $31P_{1/2}$ with a calculated cut-off radius of $R_c/a_{\text{lat}} \approx 2$. The slightly smaller experimentally obtained value could be due to the detuning dependence of the effective range $R_c \propto \Delta^{-1/6}$, which has not been considered in the simplified model, or the contribution of particles close to the edge with fewer neighbors. Next to the effective number, we also obtain the Rabi frequency for this configuration as $\Omega/2\pi = 1.33(7)$ MHz. The same procedure can also be applied

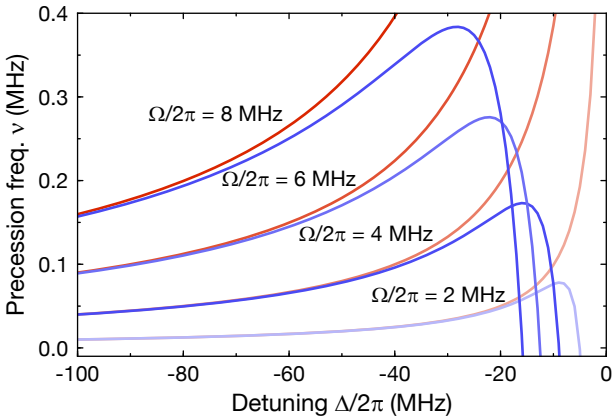

Figure 6.7: Prediction of collective-field shift for $31P_{3/2}$. Calculated expected spin precession frequency versus dressing laser detuning Δ with (blue) and without the interaction included (red) for different Rabi couplings Ω as indicated above the respective curves. For small detunings, the interaction effect dominates, however here also the perturbative dressing approximation $\beta^2 \ll 1$ is expected to break down. The calculation was done for the state $31P_{3/2}$ with $C_6 = -h\,201\,\text{MHz}\,\mu\text{m}^6$, which results in $N_{\text{eff}} = 19$ at $\Delta/2\pi = -20\,\text{MHz}$.

of course for other states, see Fig. 6.6 c for the results for $31P_{3/2}$. In this case, the effective range is larger and amounts to approximately $R_c/a_{\text{lat}} \approx 3$ at $\Delta/2\pi = -6\,\text{MHz}$. For reference, the collective field shift for an approximate step-like soft core but including the detuning dependence of the cut-off radius is shown in Fig. 6.7. It underlines that the collective-field contribution is significant already for quite large $|\Delta|$ and has to be considered to obtain accurate results for the Rabi frequency calibration, see also chapter 5, section 5.2.8.

6.4.4 Correlation growth due to dressed interaction

The measurement of the collective field provides strong evidence for the presence of Rydberg-dressed interactions and the obtained values for the effective number of interacting particles were consistent with the assumption of a simplified dressing potential. Still, a direct measurement of the interaction, also sensitive to the exact shape of the interaction potential, would be more convincing. To achieve this, we insert a spin echo in the interferometric sequence used to measure the collective field, see Fig. 6.3 b. This removes the effect of the longitudinal field including the collective contribution and hence leaves the bare spin-spin interaction of the Hamiltonian (6.3) as the only drive of the dynamics. The resulting correlations between the phases of the

spins are mapped to correlations in the spin-down population, which can be quantified by the spin-spin correlation $g_{ij}^{(2)} = \langle \hat{\sigma}_i^{(\downarrow)} \hat{\sigma}_j^{(\downarrow)} \rangle - \langle \hat{\sigma}_i^{(\downarrow)} \rangle \langle \hat{\sigma}_j^{(\downarrow)} \rangle$, with $\hat{\sigma}_i^{(\downarrow)}$ measuring the spin-down population at site i. Experimentally, we trace the growth of these correlations with the total duration t during which the interaction is induced in both dressing intervals before and after the spin echo, which is conveniently quantified by the total interaction phase $\Phi_0 = U_0\, t$. For short times $\sqrt{N_{\text{eff}}} U_0\, t \ll 1$, the correlations are expected to grow quadratically in the interaction phases [74]

$$g^{(2)}(R) = \frac{\Phi_0^2}{(4(1 + (R/R_c)^6))^2}, \tag{6.8}$$

while at later times the correlation saturates and eventually decreases again.
The interactions are induced by dressing to the state $31P_{1/2}$ with a Rabi frequency of $\Omega/2\pi = 1.33(7)\,\text{MHz}$ and a detuning $\Delta/2\pi = 6\,\text{MHz}$. This is safely in the limit of weak admixture with $\beta = 0.11(1)$, equivalent to approximately 1.2% probability to find a dressed spin-up atom in the Rydberg state. In this setting, the height of the soft-core potential amounts to $|U_0|/2\pi \approx 1.8\,\text{kHz}$ and is attractive due to the attractive van-der-Waals interactions combined with a positive detuning, see Fig. 6.2 a. For these parameters, we varied the dressing time and evaluated the correlation function

$$g^{(2)}(\boldsymbol{R}) = \sum_{i \neq j} \delta_{ij,\boldsymbol{R}}\, g_{ij}^{(2)} / \sum_{i \neq j} \delta_{ij,\boldsymbol{R}}, \tag{6.9}$$

which is obtained from a translational average of $g_{ij}^{(2)}$ constrained to a given distance $\boldsymbol{R}$ by the Kronecker symbol $\delta_{ij,\boldsymbol{R}}$. For the theory comparison, we evaluated the analytic solution for the correlation dynamics beyond the short-time limit, which is given as [74, 88, 306, 307],

$$\begin{aligned} g_{ij}^{(2)} = \frac{1}{8} \left(\prod_{k \neq i,j} \cos\left((\Phi_{ki} + \Phi_{kj})/2\right) + \prod_{k \neq i,j} \cos\left((\Phi_{ki} - \Phi_{kj})/2\right) \right) \\ - \frac{1}{4} \cos\left(\Phi_{ij}/2\right)^2 \prod_{k \neq i,j} \cos\left(\Phi_{ik}/2\right) \cos\left(\Phi_{jk}/2\right). \end{aligned} \tag{6.10}$$

Here, the spatially dependent interaction phases $\Phi_{ij} = U(R_{ij})\, t$ have been introduced for particles at sites i and j in the lattice. Qualitatively, the measured correlations shown in Fig. 6.8 a resemble the soft-core shape as expected from equation (6.8). Non-zero correlation signals extend over several sites in the optical lattice and are, up to a global offset to be discussed later, in good agreement with the theoretical prediction shown in Fig. 6.8 b. For a more quantitative analysis, we evaluated the azimuthally averaged correlations, see Fig. 6.8 c. For all but the smallest and the

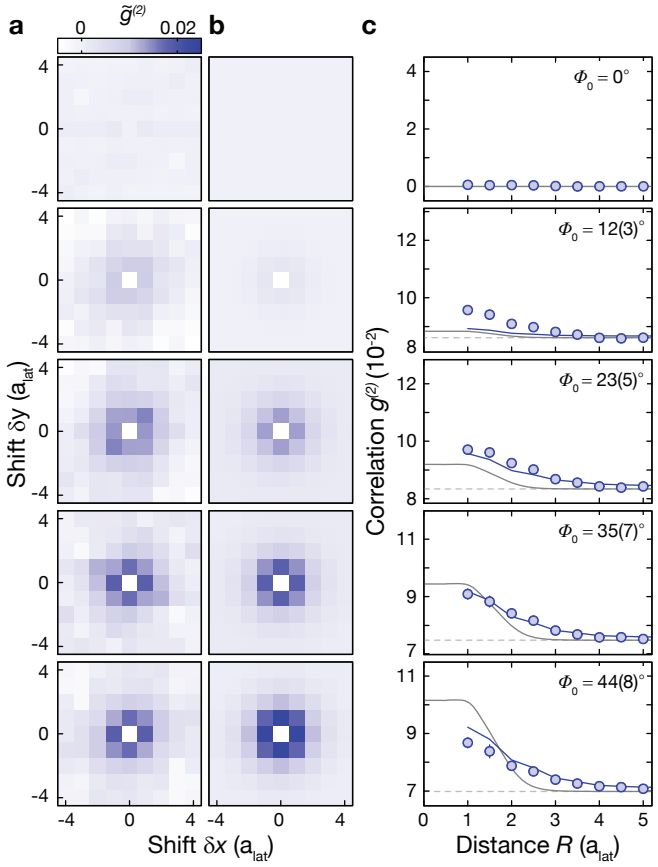

Figure 6.8: Correlation growth due to dressed interactions. **a**, Measured two-dimensional spin-correlation functions $\tilde{g}^{(2)}(\boldsymbol{R}) = g^{(2)}(\boldsymbol{R}) - g^{(2)}_{\infty}$ for increasing interaction phase Φ_0 (top to bottom) evaluated in a region of interest of 9×9 lattice sites. The constant spatial offset $g^{(2)}_{\infty}$ was obtained by azimuthally averaging $g^{(2)}(\boldsymbol{R})$ for $4.5 \leq |\boldsymbol{R}|/a_{\mathrm{lat}} \leq 7.5$ and subtracted for each dataset. The two axes are the shifts $\boldsymbol{R} = (\delta x, \delta y)$. **b**, Theory prediction for $\tilde{g}^{(2)}(\boldsymbol{R})$ including collective loss discussed in section 6.5 with $g^{(2)}_{\infty}$ adjusted to the experimentally determined value. **c**, Azimuthal averages of the two-dimensional correlations in a (blue points), and b (blue solid line) versus distance $R = |\boldsymbol{R}|$. The perturbative estimate (solid dark-gray line) shifted by $g^{(2)}_{\infty}$ (dashed light-gray line) differs significantly from the non-perturbative prediction for the spin correlation (see main text). All error bars denote the s.e.m.. Figure adapted from [74].

largest non-zero Φ_0, the full theoretical calculation agrees well with the data, while the perturbative result of equation (6.8) is qualitatively different, as it predicts smaller

correlations than observed at large distances between $R = 2.5\,a_{\mathrm{lat}}$ and $R = 3\,a_{\mathrm{lat}}$. To understand this deviation, it is interesting to analyse the spin dynamics in the simple case of two isolated spins interacting via a dressed interaction U_0. Here, it is straightforward to show that the time dependence of the correlation is given exactly for all times t as $g^{(2)}(R) = \frac{1}{4}\sin\left(\Phi_0/2\right)^2$, which has the same perturbative expansion (6.8) as the analytical solution of the many-body model on the plateau for small $R \ll R_c$. We are led to conjecture that the deviation in the experimentally measured two-spin correlation is due to interactions of the two spins at positions $\boldsymbol{i}$ and $\boldsymbol{j}$ with other spins in their neighborhood. This is supported by the explicit analytical result (6.10) for the correlation, from which it is clear that the two-body interactions with other spins at sites $\boldsymbol{k}$ explicitly enter and hence modify the correlation between spins at sites $\boldsymbol{i}$ and $\boldsymbol{j}$.

Many-body saturation of the dressing potential

While in all of the previous discussions a valid dressed two-body interaction potential was assumed, many-body corrections to this could be important. For large densities, the dressed interaction is expected to saturate [131, 154]. Neglecting many-body effects would hence lead to a measured correlation signal below the theoretically expected one, which we do in fact observe for the largest interaction phase. Inspecting the validity of the perturbative expansion (6.5) in more detail, it can be shown numerically or by calculating next higher orders in the perturbation series that the correct small parameter for the expansion depends on the density of atoms [154, 308], see chapter 7 of [131] for a nice and more detailed discussion. Explicitly, the above expression in the many-body model is valid if

$$N_{\mathrm{eff}}\beta^2 \ll 1. \tag{6.11}$$

Here, the two-dimensional density ρ explicitly enters the number of atoms within the cut-off radius, $N_{\mathrm{eff}} = \rho\pi R_c^2$. From the analysis of the collective field in section 6.4.3, we know for example for the state $31P_{1/2}$ that $N_{\mathrm{eff}} = 11(2)$ and hence for the measurement presented in Fig. 6.8, $N_{\mathrm{eff}}\beta^2 = 0.13(3)$. For these numbers, the criterion (6.11) is not strictly fulfilled and a correction to the dressed interaction can be expected [154, 308].
An intuitive explanation for the saturation of the strength of the dressed interaction at high densities was given in references [131, 154]. Understanding the dressing potential as a modified light shift due to Rydberg blockade, one can calculate the N-atom potential by subtracting the sum of independent light shifts δ_{AC} of N atoms, corresponding to the dilute limit of dressing without interaction, from the total energy E_N of the system in the fully blockaded regime, i.e. when all particles have been brought close together and behave as a superatom with collectively enhanced coupling $\sqrt{N}\Omega$.

Doing so, one obtains

$$U_{mb}(N) = E_N - N\delta_{AC} = \frac{\hbar\Delta}{2}\left(1 - \sqrt{1 + \frac{N\Omega^2}{\Delta^2}}\right) - N\frac{\hbar\Delta}{2}\left(1 - \sqrt{1 + \frac{\Omega^2}{\Delta^2}}\right) \quad (6.12)$$
$$\approx \frac{\hbar\Omega^4}{16\Delta^3}\left(N^2 - N\right) \quad N\beta^2 \ll 1.$$

The approximate interaction energy in the weak-dressing limit for small $N\beta^2 \ll 1$ scales with N^2, as required to be an extensive quantity, while the full expression scales slower than quadratic with N. Therefore, the dressing interaction saturates, which can also be understood intuitively as a consequence of the diminishing contribution of particles to the total interaction energy when added within the blockade radius of particles already present.
Analysing the measured correlation explicitly for these many-body corrections might be useful for shedding new light on the validity of the weak-dressing assumption. Moreover, higher-order corrections to the binary dressed potentials are expected to be three-body interactions, which could be interesting to study by themselves [309, 310].

6.4.5 Tuning the interaction

As discussed in chapter 2, the van-der-Waals interactions between Rydberg states can be tuned in strength and isotropy, depending on which interaction channels are present. This tunability is directly transferred to Rydberg-dressed interactions. In the following, we demonstrate this by employing the single-site-sensitive interferometric measurement to read out the spin correlations reflecting the interaction potential. In a first experiment, we measured the correlations emerging for dressing to the Rydberg state $31P_{3/2}$, $m_J = -3/2$ in the configuration of Fig. 6.4 b. We used a Rabi frequency of $\Omega/2\pi = 1.16(6)\,\mathrm{MHz}$ and a red detuning of $\Delta/2\pi = -6\,\mathrm{MHz}$ in this case. Due to the stronger interaction of $31P_{3/2}$ with $C_6 = -h\,201\,\mathrm{MHz}\,\mu\mathrm{m}^6$ compared to $C_6 = h\,20\,\mathrm{MHz}\,\mu\mathrm{m}^6$ for $31P_{1/2}$, we expect the cut-off distance to increase by approximately 50 % to $R_c \approx 3\,a_{\mathrm{lat}}$. The measured spin correlations shown in Fig. 6.9 a confirm this in excellent agreement with the theoretical predictions.
For tuning the angular dependence, we changed the orientation of the quantization axis and aligned it in the atomic plane with the direction of the dressing laser, setting it to a value $B_{xy} = 0.43\,\mathrm{G}$. In this configuration, the van-der-Waals interaction between two $31P_{3/2}$, $m_J = -3/2$ states becomes anisotropic with an approximate angle dependence $V \sim \sin(\theta)^4$, due to the dominant coupling to the $32S_{1/2}$-$31S_{1/2}$ interaction channel, as illustrated in chapter 2, section 2.3.5. For the dressing, the laser polarization is in this configuration chosen to be σ_- in order to only couple the state

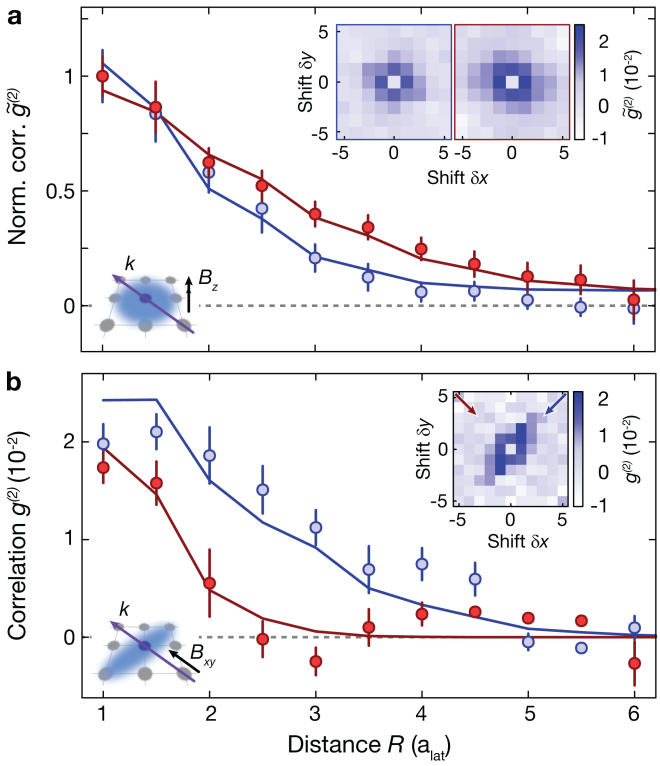

Figure 6.9: Tunability of dressed interaction. **a** Normalized azimuthally averaged spin correlations $31P_{1/2}$ (blue data points) and $31P_{3/2}$ (red data points) together with theory predictions (blue and red solid lines). The inset shows the two-dimensional correlations for the two cases $J = 1/2$ (left) and $J = 3/2$ (right). The inset in the lower left corner illustrates the excitation geometry with magnetic field along z (black arrow) and excitation beam (purple arrow) in the atomic plane (gray disks), which leads to isotropic interaction (light blue area). **b**, One-dimensional averages of an anisotropic spin correlation along two orthogonal directions (red and blue data points), obtained by averaging two neighboring sites, together with the theory prediction (red and blue solid lines). The inset shows the two-dimensional correlation with the two averaging directions indicated by red and blue arrows. The inset in the lower left corner indicates the geometry as in a. All error bars denote the s.e.m.. Figure adapted from [74].

$m_J = -3/2$. The expected anisotropy of the cut-off distance R_c is directly visible in the measured correlations, see Fig. 6.9 b. In agreement with the theoretical prediction, we observe an aspect ratio of $\sim 3/2$ between the strongly and weakly interacting orientations. The much less pronounced angular dependence of the dressed compared to the bare van-der-Waals interactions is a consequence of the strong scaling $R_c \propto |C_6|^{1/6}$,

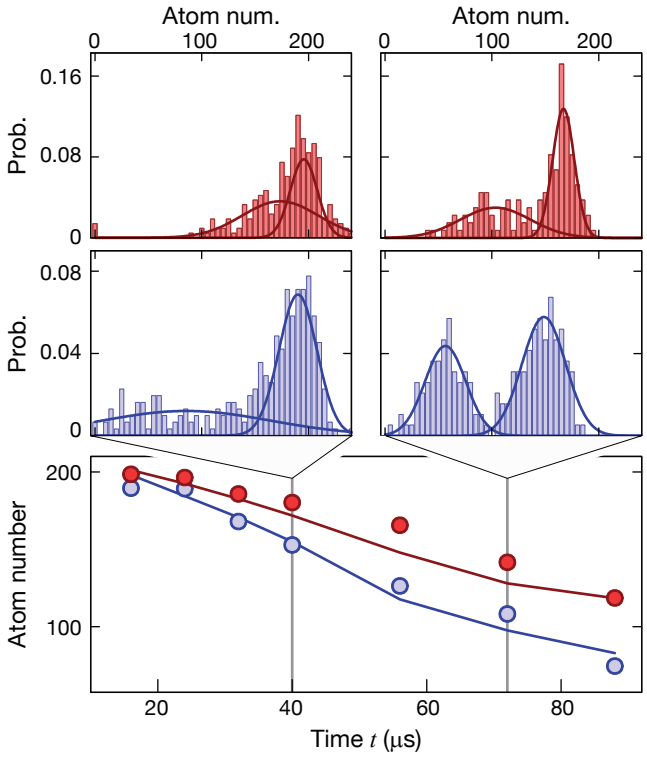

Figure 6.10: Lifetime of dressed ensemble. Measured mean atom number after a spin-echo sequence versus dressing time t with and without spin-resolved detection (blue and red data points respectively) with the theory prediction (blue and red solid lines) and corresponding number histograms above (blue and red filling) at two different times (gray vertical lines). Figure adapted from [74].

which on a relative scale suppresses strongly and enhances weakly interacting orientations. The dressing parameters were in this case $\Omega/2\pi = 2.45(12)\,\mathrm{MHz}$ and $\Delta/2\pi = -12\,\mathrm{MHz}$.

6.5 Lifetime of the dressed ensembles

In order to assess the future applicability of Rydberg dressing for quantum information and quantum simulation purposes, the coherence and lifetime of the dressed ensembles are of paramount importance. In the two-level approximation, the lifetime τ_{eff} of a dressed ground state atom is related to the Rydberg state lifetime via the square of the admixture, $\tau_{\mathrm{eff}} = \beta^{-2}\tau$, see chapter 2, section 2.4.3. Based on this, we expect for our time evolution measurement of the spin correlation $\tau_{\mathrm{eff}} = 2\,\beta^{-2}\tau = 4.4\,\mathrm{ms}$, where an additional factor of two enters due to the equal superposition of

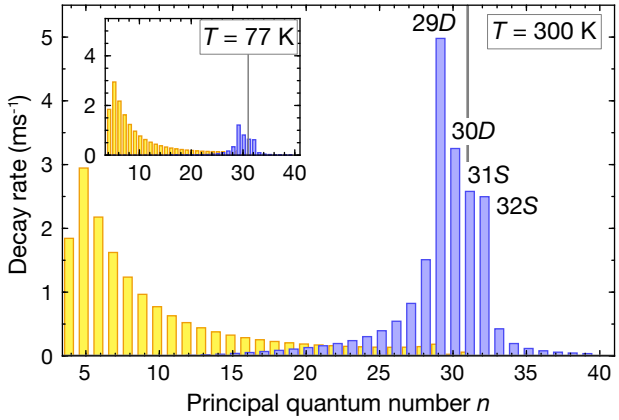

Figure 6.11: Decay channels of $31P_{1/2}$. The decay rates from $31P_{1/2}$ (marked by gray vertical line) to states with principal quantum number n due to radiative (yellow bars) or black-body-radiation-induced decay (blue bars) at a temperature of $T = 300\,\mathrm{K}$ (inset: same calculation for $T = 77\,\mathrm{K}$). The main target states for decay from $31P_{1/2}$ are indicated above or next to the respective bars. The data for the diagram was calculated with the ARC package [95].

dressed and undressed spin states in the spin-echo sequence. Experimentally, we extract the atom number decay from the spin-echo sequence by omitting the final push-out pulse for the spin-selective detection. The resulting time trace of the decaying atom number is displayed in Fig. 6.10, exhibiting a decay with a time constant of $130(20)\,\mu\mathrm{s}$. This is considerably shorter than the expectation based on the simple two-level estimate. Rather, we find agreement by modelling the loss as an exponential decay with a decay constant explicitly dependent on the initial number of atoms $N(0)$, making the loss process "collective" and of the form

$$N(t) = N(0)\mathrm{e}^{-\frac{N(0)}{4}\beta^2\gamma t}. \tag{6.13}$$

We obtain best agreement with our data when $\gamma = 10\,\mathrm{ms}^{-1} \approx \gamma_{BB}/2$, where γ_{BB} is the literature value of the black-body-induced decay rate of the $31P_{1/2}$ state [93]. With the same parameters, we also obtain good agreement for the spin-selective measurement of the spin-down population, see Fig. 6.10.

6.5.1 Modelling the loss

The relation (6.13) predicting a strong collective loss is derived from a model assuming a probabilistically triggered single-particle loss process which then globally affects all atoms in the dressed state $|\uparrow\rangle$. This is motivated by the observed homogeneous offset in the spin correlation, see Fig. 6.8, which can be explained by such an

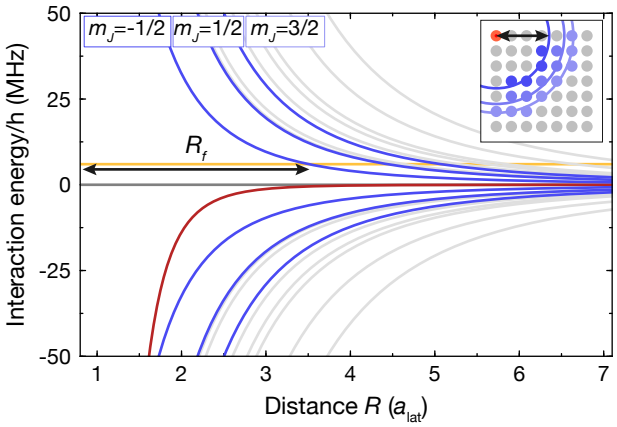

Figure 6.12: Expected dipolar exchange resonances. The blue solid lines are the eigenenergies $E_\pm = \pm C_3/R^3$ for the state exchange reaction of the $31P_{1/2}$, $m_J = 1/2$ state with the most strongly black-body-populated state $29D_{3/2}$. The magnetic quantum numbers of the D-state are indicated at the positive branches. The gray branches indicate the resonances with the other significantly populated states $30D_{3/2}$, $31S_{1/2}$ and $32S_{1/2}$. Additional resonances occur at the intersections of the detuning Δ (orange solid line) and the eigenenergies. For comparison, the van-der-Waals interaction potential between two atoms in $31P_{1/2}$, $m_J = +1/2$ is shown in red. The C_3-coefficients were calculated using the ARC package [95]. The inset illustrates the facilitation process in a filled lattice. There, the interaction with the spontaneously created impurity atom (orange disk) shifts other atoms (grey disks) at a distance R_f (black arrow) in resonance, resulting subsequently in their loss (blue disks). Thus one impurity affects many other atoms. Size of disks and distances not to scale.

infinite-range mechanism and is reproduced quantitatively to within 20 % for the decay rate extracted from the atom loss. Further evidence is provided by the observed bimodal structure both in the atom number and spin distributions, see Fig. 6.10. A plausible process with the required properties is the recently investigated decay of the Rydberg state by stimulated emission of black-body photons followed by strong line broadening [135, 311]. According to this, the dressed ground state decays with small rate $\beta^2\gamma_{BB}$ to Rydberg states with opposite parity, e.g. $29D_{3/2}$ or $31S_{1/2}$ in the case of $31P_{1/2}$, see Fig. 6.11. These loss channels are present at any non-zero temperature, see section 2.2.4 and also admixed to the ground state via the dressing. Population in an opposite-parity impurity state triggers a fast state-exchange reaction between the impurity and the remaining dressed ground state atoms due to the dipolar coupling V_{dd} as described in chapter 2, section 2.3.4. The sudden appearance of two new eigenstates with eigenenergies $E_\pm = \pm V_{dd} \propto \pm 1/R^3$ at positive and negative detunings upon creation of an impurity leads to line broadening [49, 50, 135]

and can render the initially off-resonant dressing laser resonant. This facilitates fast subsequent excitations of Rydberg states at the position of those resonances within a so-called facilitation shell of radius $R_f = (C_3/\Delta)^{1/3}$ and a width determined by the coupling strength to the emerging new eigenstates, analogous to the anti-blockade regime [146, 149, 151, 312, 313]. The subsequently facilitated excitations are then assumed to be quickly lost due to recoil kicks and forces resulting from the dipolar interactions. As an example, Fig. 6.12 displays the exchange interaction potential curves for the exchange between $31P_{1/2}$, $m_J = +1/2$ and the most strongly black-body-populated state $29D_{3/2}$, see also Fig. 6.11. Resonances can be expected for distances larger than approximately $3.5\,a_{\mathrm{lat}}$ and hence within the size of a typical system in our experiment, whose diameter is on the order of $16\,a_{\mathrm{lat}}$. Of course, as shown in Fig. 6.11, more states are populated by the black-body decay and therefore many more resonances than the few shown are expected to appear in a realistic system. Also, a possible angular dependence of the dipolar exchange reaction has been neglected for simplicity.
As such, the loss to interacting states is not a Rydberg-dressing-specific problem and also expected to be present in resonantly coupled Rydberg systems. Generally, considering the multitude of lines with smaller slopes near resonance for large distances R in Fig. 6.12, one could be led to expect a much more severe impact when the detuning is smaller. This would also be consistent with the strong loss observed in previous experiments [135, 154], which were both working in that regime, albeit also with higher particle numbers. The fast light-induced loss encountered in our experiments provides in fact a way to perform post-selection on the data [74], mitigating the effects of the dissipation at least in the post-selected ensemble. A strategy like this to identify if a loss event has occurred seems not directly obvious for resonantly coupled Rydberg states. However, the post-selection procedure is limited to the regime where the time scale over which the avalanche loss occurs, approximately the Rabi frequency Ω, is fast compared to the time scale set by the collective loss process $N\beta^2\gamma_{BB}$. This entails a fast push-out of the density after the initial seed has been created. In our case for $31P_{1/2}$, the two scales are separated by at least two orders of magnitude, justifying our simplified treatment assuming a probabilistic loss of all atoms in the dressed state upon populating the first impurity state.

6.5.2 Improving lifetimes

Based on the findings above and guided by the developed model, in the following we will briefly present and discuss some ideas on how the loss in a dressed system can be reduced significantly.

Larger principal quantum number

The scaling of the black-body-radiation-induced lifetime $\tau_{BB} \propto n^2$, see chapter 2, indicates that larger principal quantum numbers n are favorable. Moreover, in the weak dressing regime, a fixed effective lifetime $\tau_{\text{eff}} = \beta^{-2}\tau \propto \beta^{-2}n^2$ is achieved with a larger Rydberg state admixture $\beta \propto n$. This implies that $\Delta \propto n^{-5/2}$ for fixed optical power, where the Rabi coupling scales as $\Omega \propto n^{-3/2}$ (see table 2.1). Combining these relations, the interaction-to-decay ratio increases as $U_0\tau_{\text{eff}} \propto n^{3/2}$. Yet, bearing in mind that for larger principal quantum number, C_3-coefficients between neighboring states increase strongly with n^4 [314], the outermost exchange resonances shown in Fig. 6.12 will shift outwards, increasing the facilitation radius like $R_f \propto n^{13/6}$ and the facilitation shell correspondingly stronger. Furthermore, the strongly increased sensitivity to electric field fluctuations poses another challenge for increasing principal quantum numbers [92], even though Rydberg states up to $n = 200$ have been excited [315]. To answer the question whether these effects outweigh the advantage of the a priori beneficial scaling with n, experimental studies are demanded.

Cryogenic environment

Due to the exponential decrease of the number of photons per occupied mode with decreasing temperature, the black-body decay channel is expected to be suppressed at small temperatures T. Already at $T = 77\,\text{K}$, the boiling point of liquid nitrogen, the decay rates to neighboring states are reduced by approximately a factor of five, see Fig. 6.11. Decreasing temperatures to $T = 4\,\text{K}$ would gain another factor of approximately 50 and the largest black-body-induced decay rates are there expected to be on the order of $0.02\,\text{ms}^{-1}$, such that the probability of inducing new resonances like those shown in Fig. 6.12 is strongly reduced. In this regime, also the total lifetimes could be expected to be significantly increased, e.g. from $\tau = 27\,\mu\text{s}$ at 300 K to $\tau = 46\,\mu\text{s}$ at $T = 77\,K$ and approaching the radiative lifetime $\tau \approx \tau_{\text{rad}} = 58\,\mu\text{s}$ at $T = 4\,\text{K}$ [93]. In particular, the lifetime scaling for low angular momentum Rydberg states turns from the black-body-dominated $\tau \propto n^2$ over to $\tau \propto n^3$, see chapter 2, which would improve the scaling of the dressed interaction strength $U_0 \propto n^3$ at fixed optical power and effective lifetime and therefore suggest dressing to Rydberg states with higher principal quantum numbers, see previous section.

Smaller systems

As the loss mechanism is collective in a sense that the decay rate of the atoms depends on the total number of atoms, a reduction of the atom number would help considerably. The good coherence properties of only two dressed atoms in optical tweezers [73, 316] seem to indicate that there the collective loss is reduced signifi-

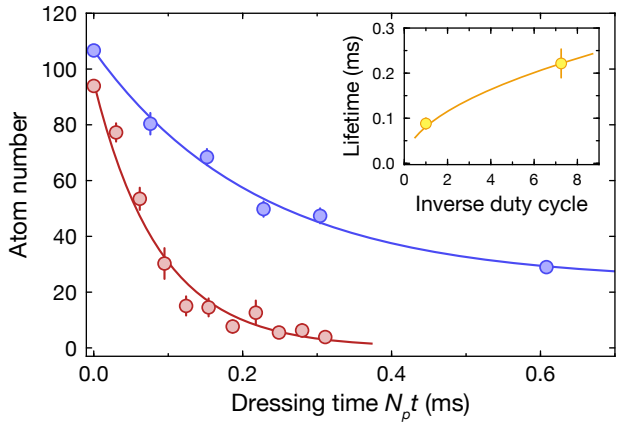

Figure 6.13: Stroboscopic dressing. Measured atom number decay versus the total time $N_p\, t$ during which the dressing light is switched on. The red data points are results for a spin-echo sequence equivalent to the one used to extract the spin correlations shown in Fig. 6.3 a. A stroboscopic sequence, where pulses of duration $t = 8\,\mu$s and dark-time intervals of $T = 50\,\mu$s are alternated, yields considerably longer lifetimes (blue data points). The inset shows the lifetime extracted from exponentially decaying fits (red and blue solid lines in main figure) versus the inverse duty cycle $(t + T)/t$. The orange solid line is a guide to the eye. Error bars in main panel denote the s.e.m., in the inset the 1σ-confidence interval of the fit.

cantly, making the single-particle loss processes the dominating ones. In the following chapter 7, we will show that also for more than two spins, good coherence can be achieved in one dimensional Rydberg-dressed spin chains.

Avoiding resonances

Once identified theoretically or experimentally, the loss due to the resonances at specific distances can be avoided in specifically chosen optical lattices or microtraps. This could be tough considering the multitude of positions at which resonances can occur. The best regime seems to be the one of large detuning, where the emerging potentials become steeper and the resonances are expected to be more localized at smaller distances [317], see Fig. 6.12.

Depumping impurity states

The active removal of atoms in impurity states by a depumper laser similar to those presented in chapter 5 can significantly increase lifetimes, provided that the impurity atoms are depumped fast enough so as to avoid the avalanche process to occur. This

should be unproblematic given the availability of short-lived intermediate states and sufficient available laser power for fast depumping within few microseconds [55, 115], see chapter 5.

Stroboscopic dressing

A stroboscopic-dressing sequence can also help to increase lifetimes significantly [295]. The idea here is to pulse the dressing light. If the dark time T between two pulses of duration t is chosen long enough for the impurity atoms to decay, the lifetimes of Rydberg-dressed systems increase. We have checked this simple idea and found that the atom loss is significantly suppressed for pulsed dressing, see Fig. 6.13. In this case, the state $5S_{1/2}$, $F = 2, m_F = 0$ was coupled to $31P_{1/2}$, $m_J = 1/2$ with Rabi frequency $\Omega/2\pi = 1.17(20)$ MHz and a detuning $\Delta/2\pi = 6$ MHz. The magnetic field was oriented in the atomic plane and had a strength $B_{xy} = 0.43$ G. Instead of applying two equal dressing pulses before and after the spin echo, the dressing light was chopped in N_p pulses of duration $t = 8$ µs each and between two consecutive pulses the dressing laser was off for a duration of $T = 50$ µs. To step the total time, the number of pulses N_p was increased.
Ideally, the stroboscopic pulses are chosen as short as possible with long dark periods, see also appendix D. In order to maintain the same average interaction strength, the detuning has to be reduced. A limit to this procedure is set by the aim of adiabatically connecting the undressed to the dressed state, which is protected by a gap of size Δ. Pulses shorter than the time scale set by $1/\Delta$ will be Fourier broadened enough to result in diabatic transitions to the Rydberg states [311].
Stroboscopic dressing is also interesting in the context of Floquet engineering of spin models, for which the necessary microwave rotations could be performed during the the dark-time periods [78, 318].

6.6 Summary and outlook

The successful realization of Rydberg dressing in a many-body system was demonstrated by directly probing the collective field and the spin-spin interaction in an emergent Ising spin-1/2 system via Ramsey interferometry combined with single-site-resolved spin measurements. The biggest open problem in these large spin lattices is the collectively enhanced decoherence rate. We have discussed some strategies to mitigate the observed loss, as overcoming this in two-dimensional systems would constitute an important step to realize for example quantum annealers based on Rydberg-dressing [68]. In the next section, we will present an important step towards improved lifetimes in smaller systems by investigating coherent magnetization in one-dimensional Rydberg-dressed spin chains.

Chapter 7

Collapse and revivals in a Rydberg-dressed spin chains

7.1 Introduction

Building on the first implementation of Rydberg-dressed interactions in an Ising spin lattice presented in the previous chapter, in the following we describe an experiment aimed at observing coherent spin dynamics in a Rydberg-dressed ensemble. In an attempt to overcome the comparatively short lifetimes of the two-dimensional Rydberg-dressed ensembles studied in chapter 6, here we work with a one-dimensional chain of atoms. It is shown that the lifetime in these one-dimensional quantum magnets is strongly increased compared to the two-dimensional case. This enables the experimental study of non-equilibrium phenomena in isolated quantum systems and, in particular, of collapse and revivals as a special case. The chapter is based on the publication [76], but compared to that work the definitions of spin left and spin right have been interchanged and a factor of 2π has been absorbed in the interaction U_0 for the sake of a consistent notation throughout this thesis.

7.1.1 Collapse and revival dynamics

Coherent superpositions and their unitary quantum evolution lie at the heart of quantum mechanics. In any quantum system described by a Hamiltonian $\hat{H}$, the time evolution of a state $|\psi\rangle$ is determined by its projection to the energy eigenstates $|\lambda\rangle$ of $\hat{H}$ with associated eigenenergies E_λ. The Schrödinger equation then predicts that after a time t the initial state $|\psi\rangle$ has evolved to

$$|\psi(t)\rangle = \sum_\lambda |\lambda\rangle\langle\lambda|\psi\rangle e^{-iE_\lambda t/\hbar}. \tag{7.1}$$

Experimentally, in general the direct measurement of a quantum state is impossible. Accessible are the expectation values of observables, say $\mathcal{O}$, whose time evolution

directly follows and amounts to

$$\langle\psi(t)|\mathcal{O}|\psi(t)\rangle = \sum_{\lambda,\eta}\langle\lambda|\psi\rangle\langle\psi|\eta\rangle e^{-i(E_\lambda - E_\eta)t/\hbar}\langle\eta|\mathcal{O}|\lambda\rangle. \tag{7.2}$$

This shows that the time evolution of any observable is governed by a superposition of oscillations with different frequencies, determined by the eigenenergies of the quantum system. In an experiment, a non-trivial time-evolution follows for example after a quantum quench, where the parameters of the Hamiltonian are suddenly altered, projecting a prepared state to a new eigenbasis and resulting in dynamics described by equation (7.2). It was realized soon after the development of quantum mechanics that, due to the periodic time evolution of the quantum state and derived observables, any finite quantum system returns arbitrarily close to its initial state for special times, possibly very long after starting the dynamics [319]. These so-called revivals or recurrences in finite systems also posses an analogue in classical systems [320, 321] and oppose the intuition that generally, interacting classical and quantum systems of many constituents are expected to thermalize irreversibly [8, 322–325], implying the time averages of observables to be constant. The ensuing so-called "recurrence paradox" played also an important role in the development of the foundational ideas of statistical mechanics [323, 325].
The motivation for the experiment presented in this chapter is to infer the closedness of our quantum system, a Rydberg-dressed Ising chain, from the absence of fast thermalization and the observation of quantum collapse and revival dynamics predicted by equation (7.2). This is guided by the idea that in an open quantum system with strong coupling to an external bath, any coherence in the system is effectively lost as entanglement between system and bath is created [326]. Local measurements of the system alone require tracing over the degrees of freedom of the bath and leave the system in a mixed state, quite analogous to thermalization of subsystems of a closed quantum system [31, 327, 328]. Of course, no laboratory system is truly closed. In this case we refer to the situation where the coupling to the external bath is significantly smaller than the energy scale driving the revival dynamics, and the goal is in fact to quantify these two relevant factors and benchmark Rydberg-dressed interactions in many-body systems.

7.1.2 Previous experimental work

In recent years, the control and degree of isolation achieved for small quantum systems have enabled the observation of collapse and revivals in different settings. Among them are revivals of photonic quantum states in microwave resonators coupled to transmon qubits [329], or of Rabi-oscillation dynamics of a single atom coupled to the radiation field of a microwave cavity [330, 331]. Next to these collapse and revivals involving photon fields, advances in trapping and manipulation of ions en-

abled the observation of revival dynamics in the motional state of a single trapped ion [332]. For atoms, revivals were observed when local coherent states of a superfluid in a given site of an optical lattice at small interaction strength were quenched to the regime of dominating interactions by increasing the lattice depth. There, the dynamics is governed by on-site interactions, resulting in collapse and revivals of the matter wave [176]. Extending this idea to higher densities and longer observation times even led to the observation of multi-body interactions [333].
Common to these experiments is the possibility to describe the underlying system in terms of a symmetric Fock basis with a reduced number of degrees of freedom. More complex dynamics is expected in systems with less symmetries, as for example in spin chains with extended-range interactions. For example, revival dynamics was detected in the magnetization of a three-spin system [133]. Thereby, the spin exchange oscillation dynamics present in a system of two atoms in different Rydberg states described in chapter 2 was extended to the case of three atoms. Furthermore, a revival was detected in the correlation dynamics of a linear ion string [88].

7.2 Observation of collapse and revivals in an Ising chain

7.2.1 Physical system

Here, we focus on the observation of coherent collapse and revival dynamics in an Ising spin-1/2 chain with Rydberg-dressed interactions. The approach taken is similar to a seminal experiment reporting on the observation of collapse and revival dynamics of single atoms passing a microwave cavity [331]. There, the recorded Rabi oscillations between two atomic states were used to extract the statistics of the photon-field in the coupled microwave cavity, i.e. from the measurement of a time trace and its spectrum, the internal structure of the system under consideration was deduced. Guided by this idea, here we aim at studying the time evolution of the one-dimensional spin system shown in Fig. 7.1. Using our local addressing technique [27, 28], we prepared one-dimensional spin chains of approximately $N = 10$ spins oriented along the y-lattice-direction in our optical lattice with lattice constant $a_{\mathrm{lat}} = 532\,\mathrm{nm}$. The motional dynamics was frozen at the chosen lattice depth $(V_x, V_y\, V_z) = (40, 40, 80)E_r$. The spin basis is formed by the two states $|2,\ -2\rangle$, denoted spin up ($|\uparrow\rangle$), and $|1,\ -1\rangle$ as spin down ($|\downarrow\rangle$), analogous to the definition in chapter 6. The spins in the state $|\uparrow\rangle$ were interacting via attractive Rydberg-dressed interactions with a nearest-neighbor interaction strength of $|U_0|/2\pi = 13.1(5)\,\mathrm{kHz}$, induced by optically admixing the state $31P_{1/2}$, $m_J = +1/2$ off-resonantly with Rabi coupling $\Omega/2\pi = 3.57(3)\,\mathrm{MHz}$ and detuning $\Delta = 11.00(2)\,\mathrm{MHz}$. The magnetic field

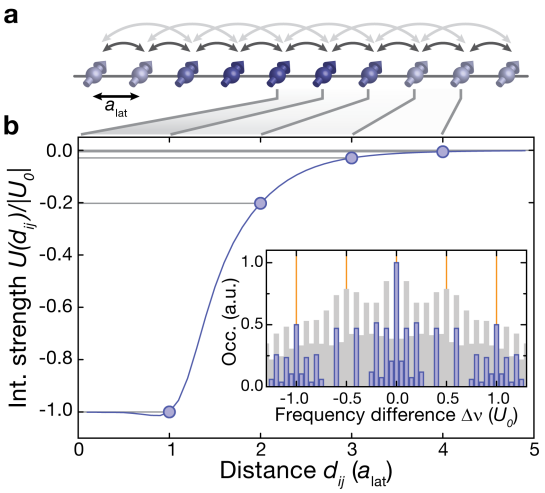

Figure 7.1: Schematic and interaction potential. **a** Illustration of a spin chain prepared in the positive S^y-direction with interactions between the spins indicated as arrows. **b** Calculated dressed potential for a Rabi coupling $\Omega/2\pi = 3.57(3)\,\mathrm{MHz}$ and a detuning $\Delta/2\pi = 11.00(2)\,\mathrm{MHz}$, normalized to the nearest-neighbor interaction strength $|U_0|/2\pi = 13.1(5)\,\mathrm{kHz}$ (blue solid line). The values of the potential at multiples of a lattice distance a_{lat} are marked by the blue points and the gray horizontal lines. The inset shows the normalized occurrence of all frequency differences $\Delta\nu$ in the many-body spectrum of the long-range interacting Ising model (gray bars), highlighting those relevant for the revival dynamics in blue. The orange lines mark the relevant frequencies for the Ising model with nearest-neighbor interactions only. Figure adapted from [76].

$B_{xy} = 0.405\,\mathrm{G}$ was oriented along the excitation beam, which had σ_+-polarization, see Fig. 6.1 a for the field and beam configuration. The calculated interaction potential for our parameters is shown in Fig. 7.1 b, exhibiting the characteristic soft-core shape.

7.2.2 Lifetime of the dressed spin chain

As discussed in chapter 6, the atom number N in the dressed two-dimensional spin system with an initial atom number $N(0)$ decayed with dressing time t with a lifetime considerably shorter than the expectation for the ideal two-level dressing approximation. Here, the atom number is expected to evolve as [74]

$$N(t) = N(0)\, e^{-\beta^2 t/2\tau} \tag{7.3}$$

for an admixture β and a bare Rydberg lifetime τ. The measurement of the atom-number lifetime in an analogous configuration for the one-dimensional spin chain

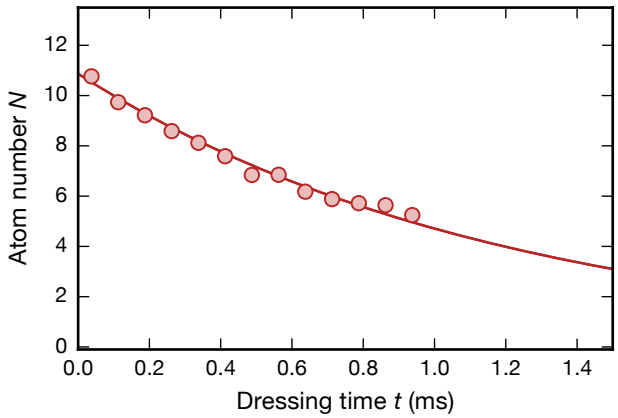

Figure 7.2: Lifetime of the dressed spin chain. A measurement of the atom number N after variable dressing times t in the echo sequence yields a lifetime of $\tau_{\text{eff}} = 1.20(4)$ ms, extracted from an exponential fit (red solid line). The error bars (smaller than data points) denote the standard error of the mean (s.e.m.). Figure adapted from [76].

is displayed in Fig. 7.2 (parameters as discussed in previous section). The extracted decay time from an exponential fit is $\tau_{\text{eff}} = 1.20(4)$ ms, reaching close to 60 % of the theoretically expected value $2\beta^{-2}\tau = 2.08(4)$ ms for the bare Rydberg lifetime $\tau = 27\,\mu$s [93]. The strongly increased lifetimes compared to the two-dimensional system can be explained by the reduced atom number, which suppresses the collective loss. A second effect could be a significantly reduced facilitation shell in the one-dimensional system, which slows down the dynamics of the avalanche triggered by the population of impurity states, see chapter 6, section 6.5.1.
In a different series of experiments, we tested the dependence of the measured lifetimes on the detuning Δ of the dressing light. The results are summarized in Fig. 7.3. We find lifetimes consistent with 67 % of $2\beta^{-2}\tau$ for all detunings. From this we conclude that also at smaller detunings no spurious resonances appear. In consequence, we expect to be able to achieve better interaction-to-decay ratios by working closer to resonance, but due to technically limited timing accuracy for short pulses, we limited ourselves to $\Delta/2\pi = 11.00(2)$ MHz for the experiments described below. Furthermore, we found a strong loss feature at the position of the sideband used to lock the SHG cavity, see also chapter 5. For this lock, the current of the seed at 1192 nm was modulated at 20 MHz. Changing this frequency allowed for shifting the loss feature. The yellow points in Fig. 7.3 were taken with modulation frequencies of 20 MHz and 16 MHz, in both cases resulting in a significantly reduced lifetime at the respective frequency. While loss occurs if the detuning matches the sideband frequency, nearby detunings are almost unaffected. If known, such loss features have to be avoided to

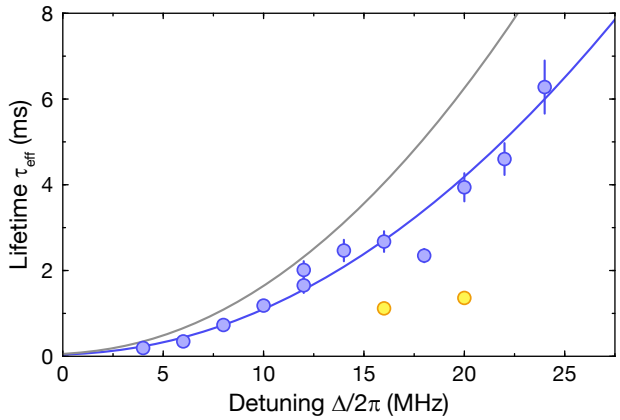

Figure 7.3: Lifetime of spin chain versus detuning. Dressed lifetimes τ_{eff} extracted from exponential fits to the decay of the atom number in a spin chain as shown in Fig. 7.2 for different detunings Δ (blue data points). The two yellow data points are below the curve due to a narrow loss feature at the position of the lock sideband employed for locking the SHG cavity. The position of these features can be tuned by changing the sideband frequency. The solid gray line is the expected dependence for a two-level system, $\tau_{\text{eff}} = 2\,\tau\beta^{-2}$, the blue includes a scaling factor of 0.67. Note that for this measurement, three echo pulses instead of one were used, but we do not expect this to influence the measured values. The error bars denote the 1σ-confidence intervals of the fit.

obtain good lifetimes.

7.2.3 Interaction quenches in a dressed Ising chain

The measured long lifetimes in the one-dimensional spin chain are a prerequisite for the observation of collapse and revival dynamics. For the latter, we prepared all spins in the initial state

$$|\psi_0\rangle = (|{\rightarrow}\rangle)^{\otimes N}. \tag{7.4}$$

Here, $|{\rightarrow}\rangle$ denotes a single-spin eigenstate of the spin operator $\hat{S}^y$ with eigenvalue $\hat{S}^y|{\rightarrow}\rangle = +\frac{1}{2}|{\rightarrow}\rangle$. The initial N-atom state is thus a coherent spin state [334] pointing in the positive S^y-direction. Experimentally, this preparation can routinely be achieved by a global microwave pulse of area $\pi/2$, see Fig. 7.4, analogous to the case shown in Fig. 6.3. Subsequently, the dressing laser was rapidly switched on for a variable time t and the initial state started evolving under the Hamiltonian (see also

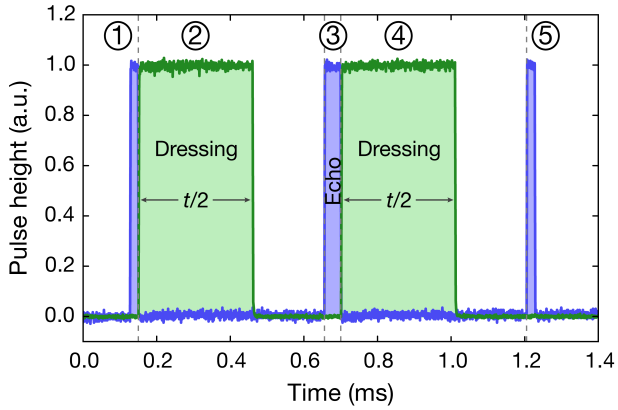

Figure 7.4: Experimental sequence. Microwave and dressing laser pulses, normalized to the maximum, are shown in blue and green. The role of the pulses in the experimental sequence was the preparation of all spins in an equal superposition of the states $|1,-1\rangle$ and $|2,-2\rangle$ in an eigenstate of $\hat{S}^y$ (1), followed by a first dressing interval of time $t/2$ (2). A spin-echo pulse (3) was used to cancel phases acquired by every spin due to the dressing laser light shift after the second dressing interval of time $t/2$ (4). The final spin readout along the S^y-direction was realized by a global spin rotation (5) identical to the one used for the preparation. To ensure the same decoherence due to magnetic field noise for measurements with different dressing times t, the time between the two $\pi/2$ pulses (1, 5) was kept constant. The microwave pulses coupling $|1,-1\rangle$ and $|2,-2\rangle$ with an area $\pi/2$ and π lasted 22 µs and 44 µs respectively. The dephasing time due to drifts of the global magnetic field was $2.8(4)$ ms. Figure adapted from [76].

equation (6.3))

$$\hat{H}_{\text{rot}} = \hbar \sum_i (\delta_{AC} + \Delta_i^{(\text{coll})}) \hat{S}_i^z + \hbar \sum_{i \neq j} \frac{U(d_{ij})}{2} \hat{S}_i^z \hat{S}_j^z = \hat{H}_s + \hat{H}. \tag{7.5}$$

Here, we have replaced the potential (6.1) by its one-dimensional equivalent $U(d_{ij})$, which only depends on the linear distance d_{ij} between two spins in the chain. The Hamiltonian $\hat{H}_s$ has been defined to capture only the longitudinal magnetic field linear in the spin operator $\hat{S}_i^z$. For the detection of purely interaction-driven revivals, it is necessary to remove the effect of the longitudinal field. This can be achieved by dividing the time t in two intervals of equal length $t/2$ and inserting a spin-echo pulse

$$\Pi = \bigotimes_i^N e^{i\pi \hat{S}_i^x} \tag{7.6}$$

after the first interval. This effectively inverts the roles of $|\uparrow\rangle$ and $|\downarrow\rangle$ after half the evolution time, and hence the terms linear in $\hat{S}_i^z$ cancel. Explicitly, we can prove this intuitive result by considering

$$\begin{aligned} e^{-it\hat{H}_{\mathrm{rot}}/2\hbar} \prod e^{-it\hat{H}_{\mathrm{rot}}/2\hbar} &= e^{-it(\hat{H}+\hat{H}_s)/2\hbar} \prod e^{-it(\hat{H}+\hat{H}_s)/2\hbar} \\ &= \prod e^{-it(\hat{H}-\hat{H}_s)/2\hbar} e^{-it(\hat{H}+\hat{H}_s)/2\hbar} \\ &= \prod e^{-it\hat{H}/\hbar}. \end{aligned} \tag{7.7}$$

We used the anti-commutator $\{\hat{S}_i^z, \hat{S}_i^x\} = 0$ for two spin operators at the same site i in the second step. Hence, up to a global redefinition of the measurement basis, the evolution of the initial state $|\psi_0\rangle$ including the spin-echo pulse is solely governed by the interactions and in the following we will therefore limit the discussion to the interaction part of the Hamiltonian,

$$\hat{H} = \hbar \sum_{i \neq j} \frac{U(d_{ij})}{2} \hat{S}_i^z \hat{S}_j^z. \tag{7.8}$$

7.2.4 Magnetization dynamics

As mentioned previously, without a full state tomography it is impossible to trace the time evolution of a quantum state $|\psi(t)\rangle$. For all but the smallest quantum systems [215, 335] full state tomography is not feasible due to the exponential scaling of the dimension of the Hilbert space with the number of particles. However, equation (7.2) shows that the revivals of the state are reflected in experimental observables. In the following, we will therefore focus on the time evolution of the transverse magnetization in our system.

Experimentally, we extracted the magnetization after time evolution for a variable time t under Hamiltonian (7.8) by an *in-situ* Stern-Gerlach sequence [72], see section 3.5.1. Upon completing the time evolution, we applied a microwave pulse of area $\pi/2$ to rotate the spins out of the equatorial plane of the Bloch sphere, such that the spin states $|\leftarrow\rangle$ and $|\rightarrow\rangle$ were mapped to the eigenstates in the S^z-direction, $|\uparrow\rangle = |2, -2\rangle$ and $|\downarrow\rangle = |1, -1\rangle$, see Fig 7.5 a. After that, we allowed the atoms to tunnel in the spatial y-direction by ramping down the respective lattice. At the same time, a magnetic field gradient was adiabatically ramped up along the same direction, separating the two spin components due to their different magnetic moments. Once enough separation had been achieved and the atoms had settled to their new equilibrium positions, the atomic distribution was frozen and a fluorescence image was recorded. This procedure allowed to read out the local magnetization $\langle \hat{S}_j^y \rangle$ at site j in the initially prepared atom chain as well as the local occupation. The detection error to detect a spin-right atom falsely as spin left and vice versa is estimated to be less

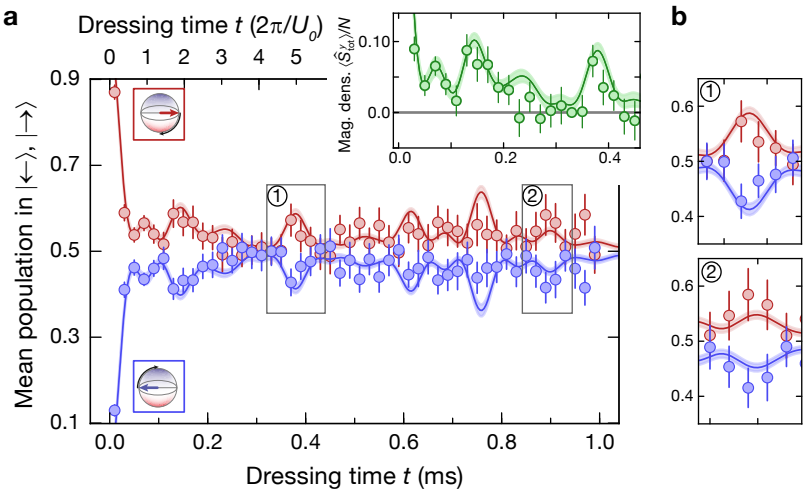

Figure 7.5: Magnetization dynamics. a The probability to measure atoms in the states $|\rightarrow\rangle$ ($|\leftarrow\rangle$) versus total dressing time t is shown as red (blue) data points. The final spin rotation before detection is indicated by the pictograms (upper and lower left corner). The total atom number was restricted to be $N < 15$ to filter out events with clear preparation errors. The solid line shows the theoretically expected dynamics, averaged over 100 initial chains randomly selected from a reference dataset with an initial filling of $87(3)\%$ and a mean atom number of $10(1.4)$. The shaded region marks the corresponding standard error of the mean (s.e.m.). The inset shows the initial dynamics of the mean transverse magnetization density $\langle \hat{S}^y_{\mathrm{tot}}\rangle/N$ (green data points) together with the theoretical prediction (green solid line). **b** Zoom into two revival features at $t \approx 10\pi/U_0$ (1) and $t \approx 24\pi/U_0$ (2), as indicated by the gray boxes in a. All error bars on the data points denote one s.e.m.. Figure adapted from [76].

than 2 %.

The probabilities for an atom to be found in states $|\rightarrow\rangle$ or $|\leftarrow\rangle$ respectively after evolution under the interaction Hamiltonian (7.8) for a time t are displayed in Fig. 7.5. This is equivalent to the transverse magnetization density of the chain,

$$\langle \hat{S}^y_{\mathrm{tot}}\rangle = \frac{1}{N}\sum_j^N \langle \hat{S}^y_j\rangle. \tag{7.9}$$

Starting at the prepared initial value close to unity, the probability to find an atom in state $|\rightarrow\rangle$ exhibits a fast decay due to interaction-induced dephasing dynamics with a first minimum in the magnetization after approximately $\pi/U_0 \approx 40\,\mu$s, before showing clear partial revivals at times $t \approx 2\pi/U_0$, $4\pi/U_0$ and $10\pi/U_0$. Even after very long times up to $24\pi/U_0$, the magnetization has not settled to its equilibrium value

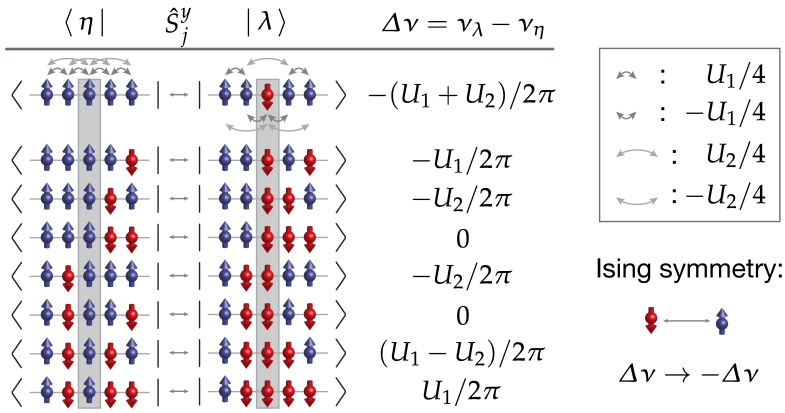

Figure 7.6: Frequencies contributing to magnetization revivals for a chain of five spins. The revival dynamics is driven by differences in the eigenfrequencies ν_η and ν_λ for spin states $|\eta\rangle$ and $|\lambda\rangle$ (represented by pictograms) which are coupled by $\hat{S}_j^y$ with $j = 3$ for the central site (marked by the gray shading), implying that only there they differ by a spin flip. The eigenfrequencies are calculated using the Ising Hamiltonian (7.8), for simplicity we only take into account nearest-neighbor ($U(a_{\text{lat}}) \equiv U_1$) and next-nearest-neighbor ($U(2a_{\text{lat}}) \equiv U_2$) contributions to the energy. They are indicated for the first set of states as curved arrows above and below for positive and negative contribution respectively. There are eight more pairs of states related to the shown ones by exchanging spin up and spin down, which leads to a sign swap in the frequency difference $\Delta\nu$. The time evolution of the transverse magnetization is obtained by summing all contributions, see equation (7.10).

$\langle \hat{S}_{\text{tot}}^y \rangle = 0$ expected in the case of strong decoherence. The dynamics is very well captured by the simulation of the exact unitary dynamics in the system without free parameters, calculated for and averaged over representative initially prepared chains taken from a reference measurement.
In order to understand the structure of the revivals, it is instructive to write out equation (7.2) explicitly for the local magnetization, yielding

$$\langle \hat{S}_j^y(t) \rangle = 2^{-N} \sum_{\lambda,\eta} e^{-i(\nu_\lambda - \nu_\eta)t} \langle \eta | \hat{S}_j^y | \lambda \rangle. \tag{7.10}$$

Here, the states $|\lambda\rangle$ and $|\nu\rangle$ denote the many-body eigenstates of the interaction Hamiltonian (7.8), which is diagonal in the product basis of single-spin eigenstates $|\uparrow\rangle$ and $|\downarrow\rangle$ of $\hat{S}^z$ with eigenenergies $\hbar\nu_\lambda$ and $\hbar\nu_\eta$ respectively. Furthermore, we have used that the initial coherent state along the S^y-direction has, up to an irrelevant phase, the same overlap $\langle \psi_0 | \lambda \rangle = \langle \psi_0 | \eta \rangle = 2^{-N/2}$ with all $|\lambda\rangle$ and $|\eta\rangle$. Naively, one could expect the time evolution to be governed by all frequency differences appearing in the exponent of the time evolution operator. In fact, according to equation (7.1), all

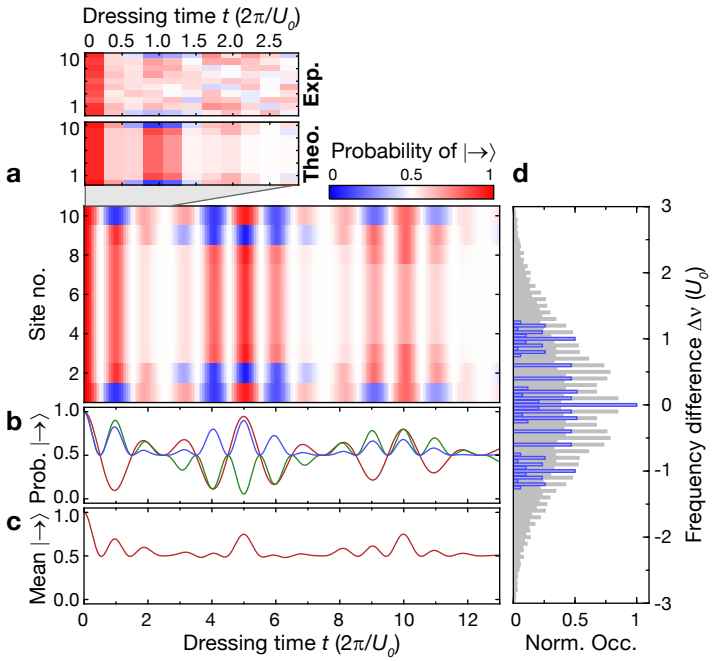

Figure 7.7: Spatially resolved magnetization dynamics in spin chain. **a** Exact diagonalization result for the evolution of the probability (color coded) for a spin at a given lattice site (labelled from 1 to 10) to point in the initially prepared S^y-direction along $|\rightarrow\rangle$ for each spin versus dressing time t in a defect-free chain of $N = 10$ atoms. Contrary to the nearest-neighbor interacting Ising chain, the bulk spin dynamics is modulated by the next-nearest-neighbor interaction $U(2a_{\mathrm{lat}}) \approx U_0/5$. Near the edge, spins show different temporal dynamics and now also the spins further in the chain are affected by the edge. Above, a zoom into the initial part of the dynamics, indicated by the gray area, shows the measured site-resolved probability for a spin at a given lattice site to point in the initially prepared S^y-direction along $|\rightarrow\rangle$ versus dressing time t (upper panel) and the corresponding theoretical expectation for a defect-free initial chain using the same binning as for the experimental data (lower panel). **b** illustrates the dynamics with single-spin time traces for an edge spin (red), the spin neighboring the edge spin (green) and spins in the bulk (blue), all taken as cuts of a. **c** The average global spin now displays an interaction-induced collapse after two weak, bulk-driven revivals at $t = 2\pi/U_0$ and $t = 4\pi/U_0$, before reviving at $t = 10\pi/U_0$ and later at $t = 20\pi/U_0$. **d** The frequency differences $\Delta\nu$ of the many-body eigenstates of the long-range interacting chain (gray bars) and those relevant for the dynamics of the transverse magnetization density (blue bars). Figure adapted from [76].

frequencies do contribute to the time evolution of the quantum state. For the magnetization, however, only few of the frequency differences are relevant, selected by

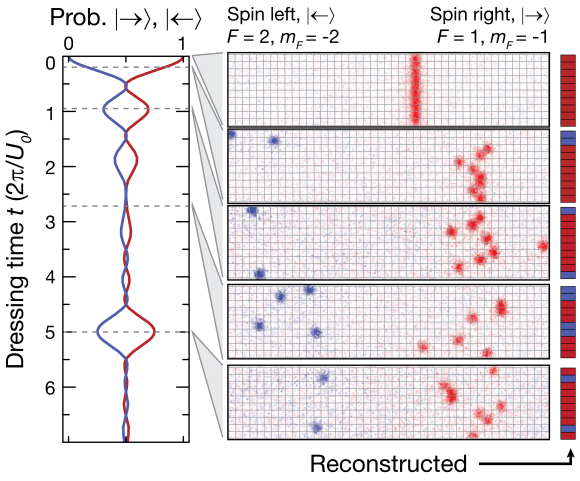

Figure 7.8: Spin-resolved measurement. Left panel: Simulated revival dynamics of the populations of spin right (red) and spin left (blue) starting from the initially fully magnetized chain in S^y-direction for a defect-free chain of ten spins and long-range interactions. Clear partial revivals are observed during the evolution. The fluorescence images to the right show characteristic spin configurations for ten spins observed during the collapse and revival dynamics at times indicated by the gray dashed lines in the time trace. The spin of the atoms was detected via an *in-situ* Stern-Gerlach sequence, which led to a spatial separation of spin-right (red) and spin-left atoms (blue). This allows for the reconstruction of the full spin and density distribution (pictograms to the right).

the many-body operator matrix element $\langle\eta|\hat{S}_j^y|\lambda\rangle$. Recalling that $\hat{S}_j^y$ applied to single-spin eigenstates of $\hat{S}^z$ induces a spin flip at position j in the chain (again up to an irrelevant phase), it is clear that in the time evolution only many-body eigenstates differing by exactly one flipped spin contribute the difference of their eigenfrequencies, see Fig. 7.6. Naturally, the energy cost for a flipped spin in an interacting system is the spin-spin interaction energy $U(d_{ij})$ and depends on the surroundings of the selected spin. In consequence, for example in an Ising system with interactions between nearest-neighbors only, the local magnetization would oscillate periodically with a frequency given by the nearest-neighbor spin interaction energy. In our system, the spin-spin interaction extends over several sites in the chain, see Fig. 7.1 b. Still, the dynamics is dominated by the interaction $U(a_{\mathrm{lat}}) \approx U_0$ with the nearest-neighbor, but it is additionally modulated with the frequency corresponding to next-nearest and next-next-nearest neighbor interactions. This can be worked out by summing all frequency contributions of coupled states according to equation (7.10) (see Fig. 7.6 for the five-spin case) and using trigonometric identities for the resulting cosines. A histogram of all relevant frequencies for our potential is shown in the inset of Fig. 7.1.

The exact solution for the local magnetization dynamics summarizes the result nicely and reads [211, 306]

$$\langle \hat{S}_j^y(t) \rangle = \frac{1}{2} \prod_{i \neq j}^{N} \cos(U(d_{ij})t/2). \tag{7.11}$$

For the spin interaction induced in our experiment, the next-nearest neighbor interaction is $U_0/5$, explaining the revival at $t \approx 10\pi/U_0$.
In view of the fact that the local magnetization dynamics can be understood by considering local spin flips, it is clear that the boundary of the spin chain as well as locally missing spins in the initially prepared chain modify the dynamics. This is confirmed by a simulation of a perfect initial spin chain shown in Fig. 7.7. One immediately recognizes that the spins located at the edge evolve differently. After one oscillation period of a bulk spin at time $t = 2\pi/U_0$, the edge spin is out of phase with the bulk due to the single missing neighbor. Even more striking, also the spin located two sites away from the edge is still modified by the edge, however only after a time $10\pi/U_0$ has it run out of phase with the bulk, consistent with the expectation based on the next-nearest neighbor interaction strength $U_0/5$. In the magnetization trace shown in Fig. 7.5 a, we average all contributions from the local magnetization, see also Fig. 7.7 b. The edge thereby causes every second revival to be suppressed compared to the bulk. Missing spins in the initially prepared chain or spins that are lost during the dynamics act similarly as an additional edge, explaining why the first (and all other odd) revival in Fig. 7.5 is smaller than the second (generally all even). Despite the difficulty of tracing the local magnetization for all spins due to limited statistics, for short times the experiment confirms the expected out-of-phase dynamics of the edge spins, see Fig. 7.7 a. Also, experimental single shots detected with the *in-situ* Stern-Gerlach technique at different times t after the quench display the expected behaviour for spins near the edge, see Fig. 7.8. These findings taken together demonstrate that, as desired, the time dynamics of the magnetization down to local features can shed light on the structure of the interaction and therefore the many-body spectrum. This is especially important for cases where the interaction potential is harder to calculate, for example in the vicinity of Förster resonances [67].
Examining the simulated local magnetization dynamics displayed in Fig. 7.7 a is also instructive in clarifying the connection between a revival of the quantum state and revivals of a specific observable. While after an evolution time $t = 2\pi/U_0$ the magnetization revives, the overlap of the quantum state at that time with the initial state is vanishing due to the out-of-phase edge spin. This shows that care has to be taken in the interpretation of the revivals of certain macroscopic observables as revivals of the quantum state, and in our case it requires microscopic knowledge of the system.

7.2.5 Correlation dynamics

The correlation dynamics in a many-body system after a quantum quench has been extensively studied both experimentally [19, 88, 89, 336, 337] and theoretically [210, 211, 338, 339]. Particularly interesting questions are related with measuring the spreading velocity of correlations, which is limited by Lieb-Robinson bounds [340], or with equilibration after the quench close to critical points [338]. In the quench considered in this chapter, the Hamiltonian (7.8), under which the quenched system evolves, is far from a critical point, as no transverse field is applied. This could, however, be implemented easily in the experiment using a continuous microwave drive, paving the way to studying the relaxation dynamics in this interesting regime.
Generally, the local, spin-resolved detection available in our experiment enables the readout of spatial correlation functions. While the detection method in two dimensions only allowed for measuring correlations within the spin-down component, see chapter 6, section 6.4.4, in one dimension we have access to the full spin distribution. This allows for evaluating connected correlations in the transverse magnetization for spins separated by a distance d,

$$C_d = \langle \hat{S}_i^y \hat{S}_{i+d}^y \rangle - \langle \hat{S}_i^y \rangle \langle \hat{S}_{i+d}^y \rangle. \tag{7.12}$$

The experimentally detected correlation dynamics, averaged over the sites i to increase statistics, is displayed in Fig. 7.9. For spins separated by one lattice site, we observe a strong increase of the correlation signal initially, explaining the fast interaction-induced dephasing observed at the same time in the magnetization dynamics, see Fig. 7.5 a. The non-zero correlation signal between spins separated by two sites, especially at the later evolution time $t = 150\,\mu$s, is a direct manifestation of the extended-range interactions. These extended-range interactions are the only way of inducing correlations and entanglement in the Ising model without a transverse field for separated spins. This can be understood by recalling that the transverse-field Ising model can be rewritten as a free-fermion model via a Jordan-Wigner transformation [210]. A vanishing transverse field corresponds in this case to a flat dispersion relation, and hence implies the absence of moving quasi-particles which could mediate entanglement.
An alternative explanation for the fast initial growth of the nearest-neighbor correlator can be obtained by re-expressing the spin operators $\hat{S}^z$ in the Hamiltonian (7.8) as spin raising and lowering operators along the S^y-direction, $\hat{\tilde{S}}_j^{\pm} = \hat{S}_j^x \pm i\hat{S}_j^z$, yielding

$$\hat{H} = \hbar \sum_{i \neq j}^{N} \frac{U(d_{ij})}{4} \left(\hat{\tilde{S}}_i^+ \hat{\tilde{S}}_j^- + \hat{\tilde{S}}_i^- \hat{\tilde{S}}_j^+ - \hat{\tilde{S}}_i^+ \hat{\tilde{S}}_j^+ - \hat{\tilde{S}}_i^- \hat{\tilde{S}}_j^- \right). \tag{7.13}$$

Because initially all spins point in the positive S^y-direction, only the combination of two lowering operators acts and induces pairwise spin-flips in the negative S^y-

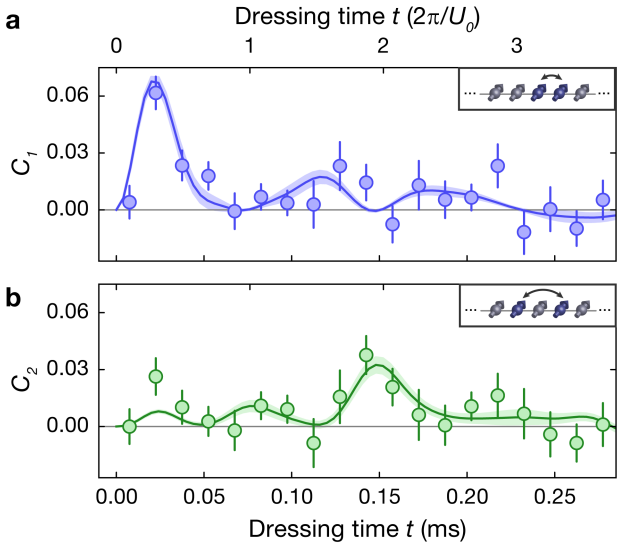

Figure 7.9: Correlation dynamics. Observed evolution of the connected correlations C_d for spins separated by **a** $d = a_{\mathrm{lat}}$ and **b** $d = 2a_{\mathrm{lat}}$, as indicated by the pictograms. The solid line with surrounding shading shows the corresponding prediction of the same theoretical calculation as used in Fig. 7.5. All error bars denote one s.e.m.. Figure adapted from [76].

direction. Once this has occurred, also the other terms become relevant, leading to pairwise spin flips in the positive S^y-direction and effective hopping of the flipped spins.

7.2.6 Parity decay

Without any coupling to the environment, the Ising model is parity conserving, in mathematical terms $[\hat{H}, \hat{P}] = 0$, for a parity operator $\hat{P}$ defined as

$$\hat{P} = e^{-i\pi \sum_{i=1}^{N} \hat{S}_i^{\leftarrow}}. \tag{7.14}$$

In a similar form, the parity operator is conventionally used in the field of quantum metrology [341, 342]. It effectively measures whether the number of spins in the chain pointing in the direction $|{\leftarrow}\rangle$ is even or odd, making it a very sensitive probe for local spin flips. According to the Hamiltonian (7.13), the number of spins in the S^y-direction only changes in even steps. Taking into account that the initial number of spins directed in the negative S^y-direction vanishes, we conclude that the number of spins pointing in this direction would remain even and the expectation value of the

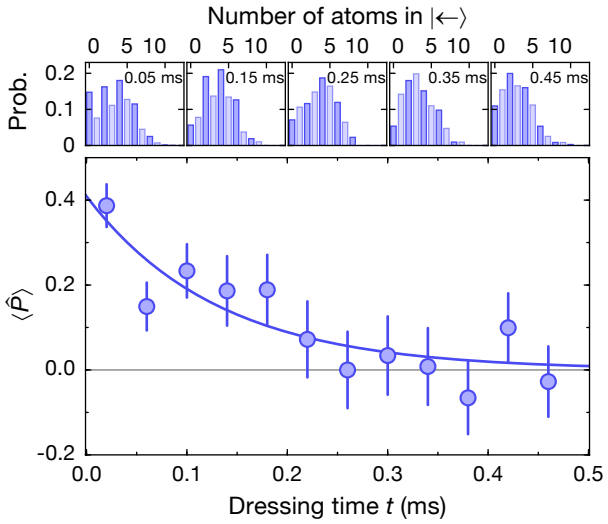

Figure 7.10: Dynamics of the parity. The histograms on top show the evolution of the number of detected atoms in the state $|\leftarrow\rangle$ with even numbers highlighted by the darker color. The data was binned in intervals of 0.1 ms and the bin centers are indicated. The main plot shows the extracted parity $\langle\hat{P}\rangle$ versus time together with an exponential fit with time constant $\tau_P = 0.13(4)$ ms (solid line). All error bars denote one s.e.m.. Figure adapted from [76].

parity operator $\hat{P}$ would equal unity in an isolated system.
As no experimentally realizable system is truly closed, we expect the parity not to be conserved exactly in our system. This is already indicated by the atom loss with rate $1/\tau_{\text{eff}} \equiv \gamma_0$ shown in Fig. 7.2, which is not compatible with a conserved parity. Yet, even in presence of dissipation, the time evolution of the parity can be straightforwardly calculated applying the formalism of Lindblad operators to treat open quantum systems used in [74, 306]. It predicts that for short times $t/\tau_{\text{eff}} \ll 1$ where the atom number is close to its initial value N_0, the expectation value of the parity, $\langle\hat{P}\rangle$, decays as

$$\langle\hat{P}(t)\rangle = P_0\, e^{-\frac{N}{2}(\gamma_0+\gamma_\downarrow+\gamma_\uparrow)t} \equiv P_0\, e^{-t/\tau_P}. \tag{7.15}$$

In addition to decoherence by the above discussed atom loss, also spin flips from the dressed ground state $|2,-2\rangle$ to the undressed ground state $|1,-1\rangle$ with rate $\gamma_\downarrow$, and dephasing of the dressed state with rate $\gamma_\uparrow$ contribute to the decay of the parity. The fact that the decay rate is proportional to the number of atoms N in the system makes the parity an immensely sensitive probe to estimate the decoherence present.
The measurement result for the expectation value of the parity operator is displayed in Fig. 7.10. Starting at an initial value of $P_0 = 0.41(7)$, the parity subsequently decays with the expected exponential dependence within a time $\tau_P = 0.13(4)$ ms. This short

decay time justifies our theoretical small-time estimate for the parity dynamics given above in equation (7.15). Scaling the parity decay time τ_P with the number of atoms $N \approx 10$ in the prepared spin chains, we find that the result matches the decay time of the atom number τ_{eff} well and, comparing with the theoretical prediction (7.15), hence conclude that most decoherence stems from the atom loss displayed in Fig. 7.2. Our identification of the effective dressed state lifetime τ_{eff} with the measured atom-loss lifetime implied in section 7.2.2 is hence supported a posteriori.
The initial parity signal different from unity is readily explained by dephasing due to magnetic field noise and initial preparation fidelity. The former can be avoided simply by minimizing the time between preparation, spin-echo and detection microwave pulses. In the present experiment, they were kept constant at the maximal dressing times $t/2$ in order to avoid time-dependent systematics not induced by the dressing, see Fig. 7.4. Working with magnetically insensitive transitions, more spin-echo pulses or better field stabilizations are other, technically more challenging options. Finally, we note that the origin of the positive parity signal is also directly visible in the number histograms of the atoms detected in the state $|\leftarrow\rangle$. They exhibit clear even-odd modulations, similar to what has been observed in experiments on the spontaneous pair creation of photons [343].

7.3 Summary and outlook

Our observation of coherent collapse and revival dynamics in a Rydberg-dressed spin chain marks an enabling step for further experiments. The demonstrated good-to-bad ratio of interaction and decoherence rate of $U_0\tau_{\text{eff}} \approx 100$ is comparable with state-of-the-art ion trap quantum simulators [88, 89]. Further experiments including a transverse field could shed light on correlation spreading near the critical point of the Ising chain [338, 339] or entanglement produced after the quench [210, 211]. Furthermore, the metrological use of the states generated during the collapse and revival dynamics could be assessed via a Loschmidt-echo sequence [344]. An entirely new class of experiments is accessible in Floquet-type systems, which are expected to host exotic non-equilibrium many-body phases [77, 78]. For these, especially the demonstrated switchability of the dressed interactions alternated with applied transverse microwave fields is crucial, and shows the clear advantage of dressed interaction over bare Rydberg interactions, were a sudden switch-off would certainly be more difficult to realize.

Chapter 8

Conclusion and outlook

8.1 Conclusion

In this thesis we have reported on microscopic experimental studies of strongly correlated ultracold gases of rubidium-87 in an optical lattice. Interactions were induced by optically coupling to Rydberg S- and P-states.
The single-atom-sensitive local detection capabilities offered by the quantum gas microscope have enabled a microscopic characterization of the superatom in the interaction-dominated regime of a frozen Rydberg gas. We have observed the characteristic square root scaling of the collectively enhanced optical coupling with the number of ground state atoms by directly detecting an atomic signal. Furthermore, we could shed light on the coherence of the superatom and infer the presence of entanglement in one of the two basis states. The observation of the coherent breakdown of Rydberg blockade bridges the gap to previously investigated crystalline structures emerging in systems which can host more than a single Rydberg excitation [55, 57].
As we have shown, the direct single-photon excitation has distinct advantages over the two-photon excitation. In particular, the higher achievable optical couplings in an experiment allowed for the implementation of Rydberg-dressed interactions by off-resonant coupling to Rydberg states. In a first set of experiments, we demonstrated the presence of Ising interactions in a spin lattice via an interferometric scheme combined with local spin-resolved detection. Exploiting the anisotropic interactions of Rydberg P-states, we could furthermore induce and demonstrate anisotropic spin-spin interactions. While these measurements on two-dimensional samples of approximately 200 atoms showed strong dissipation via atom loss, the losses were drastically reduced in one-dimensional spin chains. This allowed for the study of coherent spin dynamics in one-dimensional quantum magnets. The observation of collapse and revivals of the magnetization indicate that the coherence properties of systems with Rydberg-dressed interactions are indeed sufficient to study many-body spin physics.

8.2 Outlook

8.2.1 Resonant coupling

The explored regime of strong Rydberg blockade holds promise to realize and characterize highly entangled states different from the W-state presented in this thesis [229, 230]. Furthermore, starting from the excited superatom W-state, the recently proposed focussing of the spatially delocalized excitation via a spin lens [345] could be demonstrated. Here, the focussing of an excitation to few or even a single atom could be detected locally as a proof of principle, paving the way for subsequent local manipulations or quantum gates.
Due to the high achievable Rabi coupling together with the possibility of tailoring anisotropic interactions, direct excitation of Rydberg P-states in optical lattices is a promising avenue for studies of quantum Ising spin systems, both in one or two dimensions. The possibility of creating anisotropic crystalline structures [292], as well as exotic pair superposition states at specific "magic" distances [139] sets many-body systems based on interacting Rydberg P-states apart from those with isotropically interacting S-states. Smaller interaction strengths combined with larger Rabi couplings pave the way towards the adiabatic preparation [225, 226] and study of larger two-dimensional ordered structures with more excitations, overcoming so far limiting factors like finite system size [291] or decoherence [221].
Furthermore, combining Rydberg excitation with controllable decoherence induced by coupling Rydberg states on- or off-resonantly via the depumping transition to fast decaying states might allow for the implementation and microscopic study of interesting non-equilibrium phases [278, 281, 346] or even non-equilibrium universality in the celebrated directed percolation model [284, 347].

8.2.2 Rydberg dressing

Rydberg-dressed Ising models in principle allow for studies of most of the effects also present when Rydberg states are resonantly excited. A major advantage of dressed spins is the relative ease of preparation of initial spin states, for example by our spatial addressing technique [27, 28], as well as the availability of arbitrary global spin rotations for state detection. Local spin rotations are to be demonstrated, but are not impossible in principle. As an extension of our previous work on the preparation of crystalline ground states [57] via a complicated sweep, these states could now be prepared in a non-interacting system before switching on the dressed Ising interactions and in addition a transverse field to observe the stability or melting of the initial state [224, 348], especially on the stairs of the devil's staircase [301]. A further interesting direction is the study of correlation and entanglement growth [210, 211, 338, 339]

after a quantum quench in the transverse-field Ising chain.
Building on our initial demonstration of the revival dynamics of Rydberg-dressed spin chains, an immediate interesting extension would be the in-depth study of the generated states during the time evolution. Analogous to the strongly entangled Schrödinger cat state found in this setting for global range all-to-all interactions [176, 349], in the studied Ising model one would expect to find a so-called cluster state, which has been proposed as a building block of a novel quantum computation platform [350]. Extending the Ramsey interferometry scheme to two dimensions might enable the production of large atomic cluster states, providing an alternative route to their generation in spin-dependent lattices [351]. Going beyond the previous realization, our experiment provides local detection and manipulation, which are both necessary for a successful implementation of a one-way quantum computer [350].
Furthermore, only slight modifications of the utilized experimental sequence to detect the collapse and revivals should allow for quantifying the value of the generated states for quantum-enhanced metrology, both in terms of spin squeezing [65] or, more generally, quantum Fisher information [344].
Several ideas also exist for realizing more complex spin models. For example, a quantum spin XY-model arises naturally from the Ising model in a strong transverse field [88]. Another approach exploits the dipolar spin flips in the Rydberg manifold to engineer more exotic spin interactions [66, 67]. Dressing to Rydberg states in the vicinity of Förster resonances has in this context been discussed not only to provide larger interaction-to-decay ratios for dressing [67], but also to engineer exotic peaked potentials which could be useful to realize a coherent quantum annealer platform based on Rydberg dressing [68]. The main idea here is the implementation of local gauge constraints to limit the accessible Hilbert space via an energy penalty [352]. In a similar fashion, these local gauge constraints can be enforced to implement ice rules underlying the quantum spin ice [112].
The switchability of Rydberg-dressed interactions makes them ideal candidates to study novel quantum phases existing solely in a non-equilibrium setting with periodically modulated interactions [77, 78], among them also the recently proposed [156] and discovered [79, 80] time crystals. In our setup, the disordered magnetic fields required for the implementation of those phases could be implemented via the spatial addressing, analogous to our recent experiment [30].
One of the biggest quests for Rydberg dressing resides in complementing the demonstrated spin-spin interactions with motional dynamics in presence or absence of the optical lattice. If the lifetimes in such systems are comparable to those observed in the spin systems, the observation of the celebrated supersolid phase exhibiting both superfluid as well as crystalline properties [293] could come within reach. Numerous works have explored the possibility of realizing the supersolid with Rydberg-dressed interactions as a possible experimental platform [62, 63, 294, 353], however

the required high atomic densities in some of these proposals seem at odds with the observed collective loss. Mitigating this loss thus is one of the main challenges on the way to the supersolid. Yet, en route also other interesting effects could be investigated, for example a crystalline ordering of the atomic density [354–356], which should also be observable at lower filling. While these proposals do not require an optical lattice, so-called lattice supersolids were also studied and predicted to occur in presence of a lattice [155, 357]. Besides the supersolid, also a cluster liquid phase is predicted to exist in one-dimensional lattice systems with Rydberg-dressed soft-core interactions [170]. Finally, one-dimensional dipolar bosons were predicted to host a subtle additional phase between the Mott insulator and a crystalline charge density wave, the so-called Haldane insulator [358, 359]. This is characterized by non-local correlations, which could be directly measured in our experiment [18, 19, 171].
In summary, the first implementation of Rydberg-dressed interactions in a many-body system together with microscopic preparation and detection capabilities offer a wealth of interesting directions to explore, and it will be thrilling to see where this journey will go in the future.

Chapter A

Supplementary information for chapter 2: Two-state systems

A.1 Introduction

In this section, we briefly revisit the famous "two-level system", which is a good approximation for numerous physical systems discussed in this thesis. Examples span from the two atomic eigenstates coupled by a light field to a single spin-1/2 in a transverse field or two atoms undergoing resonant dipolar exchange dynamics. The discussion here is far from complete and the interested reader is referred to introductory courses on quantum mechanics for further reading, e.g. [128].

A.2 The model

In brief, the two-level system is described by a Hamiltonian $\hat{H}$ with two orthogonal states $|A\rangle$ and $|B\rangle$, which are coupled by a possibly complex coupling called V. Without the coupling, their eigenenergies are given by $E_A = \hbar\omega_A$ and $E_B = \hbar\omega_B$ respectively. Writing $\hat{H}$ in the basis spanned by $|A\rangle$ and $|B\rangle$ we obtain

$$H = \hbar \begin{pmatrix} \omega_A & V \\ V^\star & \omega_B \end{pmatrix}. \tag{A.1}$$

Diagonalizing H yields the eigenenergies

$$E_\pm/\hbar \equiv \omega_\pm = \omega_A - \frac{1}{2}\left(\Delta \mp \sqrt{\Delta^2 + 4|V|^2}\right) = \omega_A - \frac{1}{2}\left(\Delta \mp V_{\text{eff}}\right), \tag{A.2}$$

where we have defined the detuning $\Delta = (\omega_A - \omega_B)$ and an effective coupling $V_{\text{eff}} = \sqrt{\Delta^2 + 4|V|^2}$. The eigenstates are given as

$$|+\rangle = \sqrt{\frac{|\omega_+ - \omega_A|}{V_{\text{eff}}}} \left(\frac{|V|e^{-i\phi}}{\omega_+ - \omega_A}|A\rangle + |B\rangle \right) = \cos(\theta/2)\, e^{-i\phi}|A\rangle + \sin(\theta/2)\,|B\rangle \tag{A.3}$$

$$|-\rangle = \sqrt{\frac{|\omega_- - \omega_A|}{V_{\text{eff}}}} \left(\frac{|V|e^{-i\phi}}{\omega_- - \omega_A}|A\rangle + |B\rangle \right) = -\sin(\theta/2)\, e^{-i\phi}|A\rangle + \cos(\theta/2)\,|B\rangle,$$

introducing the mixing angle $\theta = \arctan(2|V|/\Delta)$ and $\phi = -\arg(V)$. Note that for $\Delta < 0$ the angle θ should be chosen in the interval $[\pi/2, \pi]$. In the following, we want to briefly discuss the properties of the two-level system which are important for some of the effects discussed in this thesis, see also Fig. A.1.

A.2.1 Limit of large detunings – light shifts

First, we note that in the limit of large detuning $|\Delta| \gg |V|$, $\Delta < 0$ ($\Delta > 0$), the two eigenenergies approach $\hbar\omega_+ \approx \hbar\omega_A + |\Delta|$ and $\hbar\omega_- \approx \hbar\omega_A$ ($\hbar\omega_+ \approx \hbar\omega_A$ and $\hbar\omega_- \approx \hbar\omega_A - |\Delta|$). The eigenstates are in this case close to the unperturbed eigenstates $|B\rangle$ and $|A\rangle$ ($|A\rangle$ and $|B\rangle$ respectively), see Fig. A.1 b. Decreasing the detuning, the effect of the coupling V on the eigenenergy $\hbar\omega_\pm$ can be worked out perturbatively, and, focussing for simplicity on $\Delta < 0$ one obtains in first order

$$\begin{aligned} \hbar\omega_- &\approx \hbar\left(\omega_A - \frac{|V|^2}{|\Delta|}\right) \quad (\Delta < 0, |V/\Delta| \ll 1) \\ \hbar\omega_+ &\approx \hbar\left(\omega_A + |\Delta| + \frac{|V|^2}{|\Delta|}\right). \end{aligned} \tag{A.4}$$

This energy correction is for example important for the creation of far-detuned optical dipole traps. Here, the energy correction and hence light-induced potential of a ground state $|A\rangle$ due to the off-resonant coupling of strength $|V| = \Omega/2$ to the excited state $|B\rangle$ amounts to $\hbar\delta = -\hbar|\Omega|^2/(4|\Delta|)$. Note that in this case the detuning Δ corresponds to the detuning of the coupling light. Negative detuning implies that the unperturbed ground state $|A\rangle$ lies below the excited state $|B\rangle$ and positive detuning the opposite.

A.2.2 On-resonance dynamics – exchange oscillations

For vanishing detuning, $\Delta = 0$, the two eigenenergies are simply $\hbar\omega_\pm = \pm\hbar|V|$, hence the total splitting between the two eigenenergies is $2\hbar|V|$. In this case, also the

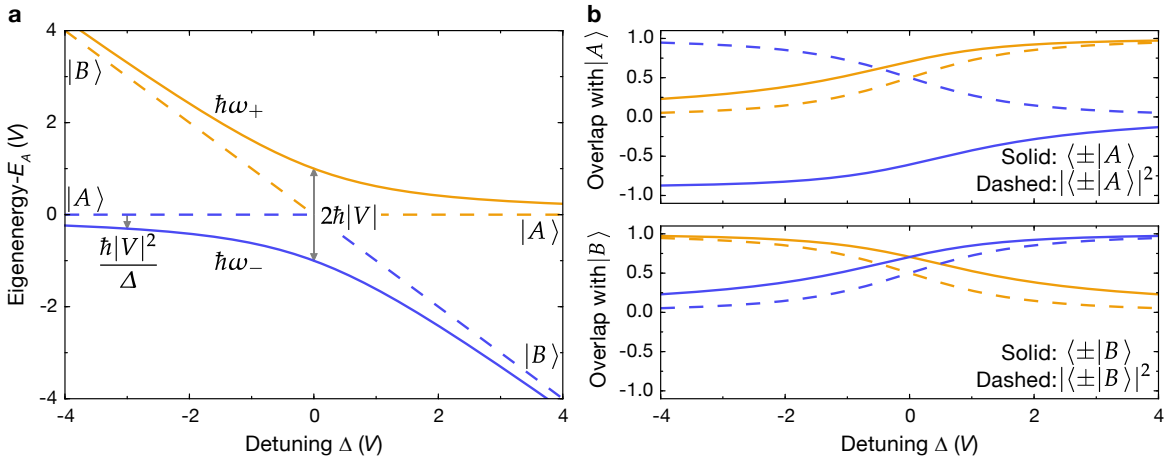

Figure A.1: Two-level system. **a** Eigenenergies $\hbar\omega_\pm$ as indicated versus detuning $\Delta = (\omega_A - \omega_B)$. For large $|\Delta|$, the eigenstates approach the uncoupled eigenstates $|A\rangle$ and $|B\rangle$. In this regime, i.e. in the limit of negligible coupling $|V/\Delta| \ll 1$, the correction to the uncoupled eigenenergy $\hbar\omega_A$ in first order amounts to $\hbar\delta = \hbar|V|^2/\Delta$, marked by an arrow at $\Delta = -3V$. On resonance for $\Delta = 0$, the splitting is given by $2\hbar|V|$ as indicated. **b** Overlaps of eigenstates $|\pm\rangle$ with the uncoupled basis. In the upper panel, blue (orange) solid lines show the amplitude $\langle -|A\rangle$ ($\langle +|A\rangle$) with $\phi = 0$, dashed lines denote the squared amplitudes (probabilities) $|\langle -|A\rangle|^2$ ($|\langle +|A\rangle|^2$). The lower panels shows the analogous quantities for $|B\rangle$.

eigenstates take a particularly simple form, becoming equal symmetric or antisymmetric superpositions

$$\hbar\omega_\pm = \pm\hbar|V| \quad (\Delta = 0) \tag{A.5}$$

$$|\pm\rangle = \frac{1}{\sqrt{2}}\left(|A\rangle \pm |B\rangle\right). \tag{A.6}$$

Finally, we investigate the time evolution of a system initially prepared in state $|A\rangle$ for the case $\Delta = 0$. Expanding in the $|\pm\rangle$-basis and using the known time evolution for the eigenstates, one obtains a periodically oscillating return probability to state $|A\rangle$,

$$p_A(t) = |\langle A|A(t)\rangle|^2 = \cos\left(|V|t\right)^2 = \frac{1}{2}\left(1 + \cos\left(2|V|t\right)\right), \tag{A.7}$$

with a frequency given by $\omega_{ex} = 2|V|$ and, as expected, the energy offset $E_A = \hbar\omega_A$ does not change the observables. Concrete examples for this scenario are the Rabi oscillation appearing for two resonantly coupled atomic states with $\Delta = 0$ and the coupling $V = \Omega/2$, or the exchange dynamics happening between two different Rydberg states due to direct dipole-dipole interaction, see chapter 2.

Chapter B

Supplementary information for chapter 4: The inhomogeneous superatom

This appendix provides some more detailed derivations for the superatom, in particular the generalization to inhomogeneous Rabi couplings for the individual particles.

B.1 Introducing inhomogenous coupling

As described in the main text (see equation (2.29) in chapter 2), in general the dynamics of a system of interacting two-level atoms in the presence of optical coupling is described by the frozen gas Hamiltonian,

$$\hat{H} = \sum_{i}^{N} \frac{\hbar}{2} \left(\Omega_i |g\rangle_i \langle r|_i + \Omega_i^\star |r\rangle_i \langle g|_i \right) - \sum_{i}^{N} \hbar \Delta_i |r\rangle_i \langle r|_i - \sum_{i<j}^{N} \frac{C_6}{R_{ij}^6} |r\rangle_i \langle r|_i |r\rangle_j \langle r|_j. \quad \text{(B.1)}$$

The vectors $\boldsymbol{i}$ and $\boldsymbol{j}$ label the position of the atoms with ground state $|g\rangle$ and interacting excited state $|r\rangle$ on the lattice and compared to equation (2.29) we have included a spatially varying Rabi coupling Ω_i, which can be experimentally relevant due to the finite curvature of the Gaussian envelope of the excitation beam. Allowing additionally for a complex Ω_i covers the presence of spatially varying laser phases, which can also be present in an experiment [54]. For simplicity we neglect an inhomogeneity in the detuning first and discuss its effects briefly in the end.

B.2 The superatom subspace

We have verified experimentally that for the initial states of up to $N = 131(5)$ particles, our system is very well described by allowing only for a single excitation, i.e. it is restricted to the subspace with $n_e = 0$ or $n_e = 1$, see Fig. 4.4 c. In this regime, the interaction part can be neglected if the basis is constrained to all (not necessarily

symmetric) $N+1$ states with $n_e = 0$ or $n_e = 1$. The single one state in the $n_e = 0$ subspace is unique and corresponds to the superatom ground state $|G\rangle = \otimes_i^N |g\rangle_i$. An appropriate basis for all singly excited states is the basis where the atom at site $|i\rangle$ is in the Rydberg state, $|R_i\rangle = |r_i\rangle \otimes_{k\neq i} |g_k\rangle$. Here, without loss of generality we have changed the notation dropping the vectorial character of i, which is from now on considered just as a label for a specific atom. Then, the Hamiltonian takes the form

$$\hat{H}_{(n=1)} = \sum_i^N \frac{\hbar}{2} \left(\Omega_i |G\rangle\langle R_i| + \Omega_i^\star |R_i\rangle\langle G|\right) - \sum_i^N \hbar\Delta_i |R_i\rangle\langle R_i|, \tag{B.2}$$

which reads in matrix form

$$H_{(n=1)} = \frac{\hbar}{2} \begin{pmatrix} 0 & \Omega_1 & \Omega_2 & \dots & \Omega_{N-1} & \Omega_N \\ \Omega_1^\star & -2\Delta & 0 & \dots & 0 & 0 \\ \Omega_2^\star & 0 & -2\Delta & \dots & 0 & 0 \\ \vdots & 0 & 0 & \ddots & 0 & 0 \\ \Omega_{N-1}^\star & 0 & 0 & \dots & -2\Delta & 0 \\ \Omega_N^\star & 0 & 0 & \dots & 0 & -2\Delta \end{pmatrix}.$$

B.3 Solution of the superatom

To find the eigenvalues it is necessary to find the zeros of the characteristic polynomial $|H_{(n=1)} - \hbar\lambda| = 0$. Due to the simple structure of $H_{(n=1)}$ the determinant is easily evaluated by expanding it as a sum of elements in the first row multiplied by their minors, which are then lower triangular matrices. Using that the determinant of a triangular matrix is just the product of its diagonal elements, the characteristic polynomial can be worked out easily and yields

$$(\Delta+\lambda)^{N-1} \left(\lambda(\Delta+\lambda) - \frac{1}{4}\sum_{k=1}^N |\Omega_k|^2\right) = 0, \tag{B.3}$$

with the solutions

$$\lambda_1 = \lambda_2 = ... = \lambda_{N-1} = -\Delta \tag{B.4}$$

$$\lambda_N \equiv E_- = -\frac{\Delta}{2} - \frac{1}{2}\sqrt{\Delta^2 + \sum_{k=1}^N |\Omega_k|^2} \equiv -\frac{\Delta}{2} - \frac{1}{2}\sqrt{\Delta^2 + \Omega_N^2} \tag{B.5}$$

$$\lambda_{N+1} \equiv E_+ = -\frac{\Delta}{2} + \frac{1}{2}\sqrt{\Delta^2 + \sum_{k=1}^N |\Omega_k|^2} \equiv -\frac{\Delta}{2} + \frac{1}{2}\sqrt{\Delta^2 + \Omega_N^2}. \tag{B.6}$$

This shows that there is a large subspace of $N-1$ dark states with energy $\lambda_1 \ldots \lambda_{N-1} = -\Delta$ which are not affected by the light coupling. The two energies E_- and E_+, in contrast, are dependent on Ω_i and hence the corresponding eigenstates do couple to the light, with a collectively enhanced Rabi frequency

$$\Omega_N = \sqrt{\sum_{k=1}^{N} |\Omega_k|^2}. \tag{B.7}$$

Obviously, in the simple case of real and equal $\Omega_i = \Omega$, the scaling (4.3) with square-root of the number of particles is recovered. It is also clear that for the case of a Gaussian envelope of the excitation beam with smaller coupling for some atoms at the edge of the experimental sample, the collective Rabi coupling is reduced compared to homogeneous case, see Fig. 4.5. Introducing $\Omega_{\text{eff}} = \sqrt{\Delta^2 + \Omega_N^2}$ for notational convenience, the two bright states with non-zero energies $E_\pm$ are given as $|\pm\rangle = \sqrt{|E_\pm|/\Omega_{\text{eff}}}\left(\Omega_N/(2E_\pm)|G\rangle + |\tilde{W}\rangle\right)$, where

$$|\tilde{W}\rangle = \frac{1}{\sqrt{\sum_{k=1}^{N}|\Omega_k|^2}} \sum_{k=1}^{N} \Omega_k |R_k\rangle \tag{B.8}$$

is a generalized W-state [360]. For the optimal configuration of homogeneous couplings, $|\tilde{W}\rangle$ is identical to a W-state. The superatom Hamiltonian can now be expressed in terms of the eigenstates $|\lambda_i\rangle$ and eigenvalues λ_i using the spectral theorem. Collecting all terms and simplifying yields as the final result

$$\hat{H}_{(n=1)} = \left(\frac{\hbar\Omega_N}{2}\left(|G\rangle\langle\tilde{W}| + |\tilde{W}\rangle\langle G|\right) - \hbar\Delta|\tilde{W}\rangle\langle\tilde{W}|\right) - \hbar\Delta\sum_{i}^{N-1}|\lambda_i\rangle\langle\lambda_i| \equiv \hat{H}_{SA} + \hat{H}_{\perp}. \tag{B.9}$$

The first part $\hat{H}_{SA}$ describes a two-level system, where the collective ground state $|G\rangle$ is coupled to the W-state $|\tilde{W}\rangle$, with a collectively enhanced coupling $\Omega_N = \sqrt{\sum_{k=1}^{N}|\Omega_k|^2}$ and the detuning Δ is equal to the single-particle detuning as there is at most one atom excited. Starting in the ground state $|G\rangle$, as we do in the experiment presented in chapter 4, only the W-state is accessible by the optical coupling. Therefore, it is justified to restrict the problem to the subspace spanned by $|\tilde{W}\rangle$ and $|G\rangle$, recovering the result presented in the main text, see equation (4.2). The situation changes if also the detuning is spatially dependent. In this case, the above derivation does not hold in general any more and couplings between $\hat{H}_{SA}$ and $\hat{H}_{\perp}$ are introduced and have to be taken into account [219]. Considering the effect on the collectively enhanced Rabi oscillations shown in Fig. 4.4, these couplings lead to a dephasing as

they cannot be coupled by light. We can furthermore exclude large detuning inhomogeneities by the visibility of the measured Ramsey fringes, see Fig. 4.6, as they would strongly damp the observed signal.

Chapter C

Supplementary information for chapter 5: Power in the SHG cavity

In this chapter, we briefly describe further methods used to characterize the second harmonic-generation cavity presented in chapter 5. We will not focus on the cavity geometry, whose optimization has been described in the respective chapter and also in a master's thesis from our group [361]. Much more background on the same subject can also be found in numerous other theses, see e.g. [261, 361, 362] for similar systems, but care has to be taken of slightly different notations and conventions.

C.1 Power round trip in the cavity

The circulating power P_{circ} in the cavity can be calculated in complete analogy to a two-mirror cavity [253] by finding the round-trip function g via the self consistency requirement for the field in the resonator after one round trip. The round-trip function contains the product of the (power) reflectivities of all mirrors (R_1 and $\mathcal{R} = \prod_{i=2}^{4} R_i$) and the linear absorption losses in the crystal ($e^{-\alpha_c d_c}$) and elsewhere (L). Furthermore, the nonlinear "loss" ($1 - \kappa_{NL} P_{\mathrm{circ}}$) by conversion of fundamental to harmonic power has to be taken into account. In total, the round-trip function for a resonant cavity reads

$$g^2 = R_1 \, (1 - \alpha)(1 - \kappa_{NL} P_{\mathrm{circ}}). \tag{C.1}$$

The square has been added as g refers to the electric field rather than the power round trip and we have introduced the total loss α containing all linear losses, $1 - \alpha = L\mathcal{R}e^{-\alpha_c d_c}$. Sources for the linear losses L are for example reflections off the crystal surface for imperfect Brewster angle or additional absorption at the crystal surface due to dirt or dust [251, 362].

C.2 Circulating power, input reflectivity and finesse

Self-consistency now allows to calculate the circulating power as a function of the incident power P_f [251]

$$P_{\text{circ}} = \frac{P_f(1-R_1)}{(1-g)^2}. \tag{C.2}$$

Due to the dependence of g on P_{circ} via the non-linear power conversion, this is an implicit relation but it can be solved numerically to obtain the round-trip power. Maximizing P_{circ} over the input reflectivity R_1 allows to find the optimal value R_1^{opt} for the latter. Polzik and Kimble [260] have also provided an explicit formula for R_1^{opt}. The optimal input reflectivity also impedance matches the cavity, implying that the power lost during one round trip in the bow-tie cavity is exactly compensated by the light coupled into the cavity [260, 363]. For perfect impedance matching, the reflected power vanishes.
Using the circulating power we can also evaluate the finesse $\mathcal{F}$ (see e.g. reference [364], but note the differences in the definition of the round trip),

$$\mathcal{F} = \frac{\pi}{2\arcsin\left((1-g)/(2\sqrt{g})\right)} \approx \frac{\pi}{1-g}. \tag{C.3}$$

The last approximate result is valid for low round-trip losses and $g \approx 1$, which is almost always the case for us. Interestingly, larger conversion efficiency can lead to a reduced finesse as the non-linear losses increase. From the performed measurement shown in chapter 5, the finesse can be extracted as $\mathcal{F} = \Delta\nu_{\text{FSR}}/\delta\nu$, i.e. the ratio of free spectral range and line width of the cavity. Typical values for the finesse of our cavity are around $\mathcal{F} \approx 280$.

C.3 Output power

Finally, the most important quantity for us is the second harmonic power P_{SH}, which is given as

$$P_{SH} = \kappa_{NL}\, P_{\text{circ}}^2. \tag{C.4}$$

Using the derived relations, we can try to understand the input versus output characteristics of our SHG cavity. To this end, we fit equations (C.4) and (C.3) to the measured values, leaving the losses α, the input mirror reflectivity R_1 and the non-linear conversion coefficient κ_{NL} as variable quantities. From this, we extract a total

intra-cavity loss $\alpha = 0.7\,\%$ and a scaled nonlinear coefficient or equivalently a scaled Boyd-Kleinman factor of 67 % of its optimal achievable value according to the Boyd-Kleinman theory [250]. The extracted input mirror reflectivity is 99.17 %, slightly above the manufacturer specification of 98.70(25)%. The reduced Boyd-Kleinman factor could be due to non-perfect beam sizes in the crystal, e.g. also due to astigmatic effects, or imperfect phase matching. From this analysis we conclude that the total intra-cavity losses α limit the cavity output power at present. Still, for the extracted parameters, we predict an intra-cavity power of $P_{\mathrm{circ}} = 65\,\mathrm{W}$, significantly above the input power $P_{in} = 0.98\,\mathrm{W}$.

Chapter D

Supplementary information for chapter 6: Stroboscopic dressing

In this appendix, we discuss scalings involved with stroboscopic dressing, where the dressing light is pulsed rather than continuously switched on. Stroboscopic dressing could be an interesting route to extend the dressing lifetimes to motional time scales, as the good-to-bad ratio of dressing can be increased for pulsed schemes.

D.1 Scalings for continuous dressing

First, we review and summarize the dependences of dressed soft-core height U_0, AC-Stark shift δ_{AC} and decoherence rate Γ on the Rydberg state admixture. We assume an ideal two-level system with ground state $|g\rangle$, coupled to an excited Rydberg state $|r\rangle$ with Rabi coupling Ω and detuning Δ. For simplicity, we will focus on the weak dressing regime, where the admixture is small, $\beta = \Omega/(2\Delta) \ll 1$. Here, we find the scalings

$$\begin{aligned} U_0 &= \frac{\Omega^4}{8\Delta^3} = \beta^3\Omega \\ \delta_{AC} &= \frac{\Omega^2}{4\Delta} = \beta\frac{\Omega}{2} \\ \Gamma_{\text{eff}} &= \frac{\Omega^2}{4\Delta^2}\gamma = \beta^2\gamma, \end{aligned} \tag{D.1}$$

where the Rydberg state decay rate is given by $\gamma = 1/\tau$ for a Rydberg lifetime τ and the effective decay rate is the inverse of the Rydberg-dressed effective lifetime, $\Gamma_{\text{eff}} = 1/\tau_{\text{eff}}$.

D.1.1 Quality factor Q

For an experiment, the first important quantity is the ratio between coherent interaction and decoherence rate, $Q = U_0/\Gamma_{\text{eff}}$, the so-called "quality factor". For this, the

scaling is

$$Q = \frac{U_0}{\Gamma_{\text{eff}}} = \frac{\beta\Omega}{\gamma} = \frac{\Omega^2}{2\Delta\gamma}. \tag{D.2}$$

We note three important points relevant for different experimental constraints:

1. The larger β, the larger the quality factor.
2. For fixed admixture β, Q increases linearly with Ω.
3. For fixed Ω, Q increases linearly with $1/\Delta$.

D.1.2 First-order light shift

A further relevant factor for experiments is the ratio between first-order (δ_{AC}) and second-order effects (U_0) induced by the dressing laser. Using the relations (D.1), we find for this

$$\frac{U_0}{\delta_{AC}} = \frac{\beta^3\Omega}{\beta\Omega/2} = 2\beta^2. \tag{D.3}$$

This implies that the interaction is a factor β^2 smaller compared to the AC-Stark shift, as we also know from the perturbative derivation of the dressed interaction presented in chapter 2. In principle this is no problem, as the first-order shift does not change the many-body physics. However, for example in the case of spin systems, noise present on the AC-Stark shift can lead to effective dephasing between spin up and spin down, acting as a fluctuating global magnetic field. Therefore, it should be ensured experimentally that the noise level is clearly smaller than the second-order effect, which naturally is easier to achieve for larger β.

D.1.3 Experimental relevance

The above scalings are relevant to find the optimal parameters for an experiment. For this, we assume that the experimentally available power and hence Ω as well as the Rydberg state decay rate γ is fixed whereas the detuning Δ can be varied. There are two cases we want to consider:

1. **Lattice or continuum physics**, where an additional time scale or respectively a rate Γ_{ext} is present, such as a hopping rate, superexchange coupling or the trap frequency. In this setting, the effective decay rate Γ_{eff} and hence also the admixture β is constrained by $\Gamma_{\text{eff}} = \beta^2\gamma \ll \Gamma_{\text{ext}}$. In consequence, for given Ω, the

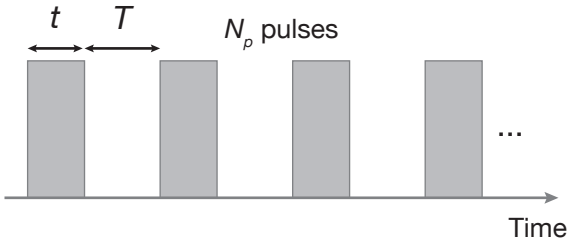

Figure D.1: Definitions for stroboscopic dressing. Definition of quantities for the sequence of N_p dressing pulses with duration t and intermediate time T.

detuning has to be increased until the desired (small) value of β is reached. As a result, inspecting equations (D.2) and (D.3) one notes that both factors decrease. This is a fundamental problem of the dressing relations in a sense that part of the quality factor has to be traded for a longer lifetime. The unfavorable scaling is the price to be paid for reducing the enormous Rydberg interaction strength to match it to other energy scales, which can in the end lead to richer physics.

2. **Spin physics**, where no external time scale like hopping rate or similar is involved. Here, the quality factor Q can (only) be maximized by maximizing the admixture β, see equation (D.2). Hence, for fixed Ω, the detuning has to be reduced leading to an increase of $Q \propto 1/\Delta$.

D.2 Scalings for stroboscopic dressing

In this section, we change the dressing protocol and the dressed interactions are now assumed to be stroboscopically switched on and off, as illustrated in Fig. D.1. For simplicity, we drop the indices for interaction, AC-Stark shift and effective decay rate and in particular for continuous dressing we write $U_0 \equiv U$, $\delta_{AC} \equiv \delta$ and $\Gamma_{\text{eff}} \equiv \Gamma$. The dressing pulses of length t are assumed to be square shaped for simplicity and consecutive pulses are interrupted by a duration T, leading to a duty cycle of $D = t/(t+T)$. In principle there is no limit to the number of pulses N_p that can be applied to the system. A prerequisite for the stroboscopic dressing scheme is that the pulses of strength U_s can be applied with a rate $1/(T+t) \gg \Gamma_{\text{ext}}$, fast compared to external time scales Γ_{ext} set for example by tunnelling or similar. In this case, we expect that the dressed interactions U_s and the associated dressing-induced decay rate Γ_s and first-order light shift δ_s can be averaged over one pulse plus the following gap (one period), to yield an average effect

$$\begin{aligned} U_{\text{s,av}} &= \frac{1}{T+t}\int_0^{T+t} U_s \,\mathrm{d}\tilde{t} = \frac{t}{T+t}U_s = DU_s \\ \delta_{\text{s,av}} &= D\delta_s \\ \Gamma_{\text{s,av}} &= D\Gamma_s. \end{aligned} \tag{D.4}$$

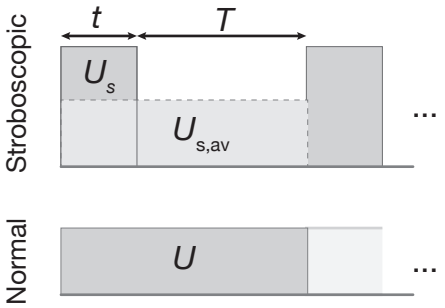

Figure D.2: Averaging procedure. Comparison of a single stroboscopic unit (top) with a pulse height U_s and averaged interaction strength $U_{\mathrm{s,av}}$ with a continuous dressing stage with the same average interaction $U = U_{\mathrm{s,av}}$ (bottom).

For these average quantities, the quality factor $Q_{\mathrm{s,av}}$ is still given by

$$Q_{\mathrm{s,av}} = \frac{U_{\mathrm{s,av}}}{\Gamma_{\mathrm{s,av}}} = \frac{\beta_s \Omega}{\gamma}, \tag{D.5}$$

and it seems like we have not gained anything. However, this is not quite true as we can now work with larger admixture β_s, which effectively increases Q as we will see. To make this quantitative we consider a comparison between a single stroboscopic unit with average $U_{\mathrm{s,av}}$ and a continuous dressing sequence of the same duration and with the interaction strength U, see Fig D.2. Motivated by experimental constraints on available power, we fix Ω to its maximal achievable value. In this case, the interaction strength can be changed by varying the detuning. To obtain the same physical effect for both configurations, we require (see also Fig. D.2)

$$U = U_{\mathrm{s,av}} \tag{D.6}$$

and obtain in terms of the respective (different) admixtures β and β_s using equations (D.1) and (D.4)

$$\begin{aligned} \beta^3 \Omega &= D \beta_s^3 \Omega \qquad (D.7) \\ \beta^3 = D\beta_s^3 &\implies \beta = D^{1/3} \beta_s. \end{aligned}$$

Because the duty cycle is smaller than one, this confirms that for the same average interaction strength, the admixture is larger in the case of pulsed dressing. Looking at the decay rate and the first-order effects, and making use of this result, we get for the comparison of continuous and stroboscopic dressing

$$\begin{aligned} \Gamma_{\mathrm{s,av}} &= D \beta_s^2 \gamma \qquad (D.8) \\ &= D (D)^{-2/3} \beta^2 \gamma \\ &= D^{1/3} \Gamma \\ \delta_{\mathrm{s,av}} &= D \beta_s \Omega / 2 \qquad (D.9) \\ &= D (D)^{-1/3} \beta \Omega / 2 \\ &= D^{2/3} \delta. \end{aligned}$$

Again, as $D \leq 1$, both the average decoherence rate $\Gamma_{s,av}$ as well as the first-order effect $\delta_{s,av}$ are smaller if the dressing light is pulsed. This is advantageous, as it tackles the two dressing problems mentioned before at once. In fact, for optimal performance, the minimal possible duty cycle should be used. However, there are some limits to this, which we discuss in the following.

D.2.1 Limits of stroboscopic dressing

In order to decrease the duty cycle D, the pulse time t can be decreased. To maintain the same average interaction strength $U_{s,av}$, this should be accompanied by a decrease in the detuning Δ to increase the admixture β_s. However, of course the admixture β_s is limited by the validity of the weak dressing regime. For larger admixture, the above scalings break down. Furthermore, for smaller detuning Δ and shorter pulses an adiabatic switching of the dressed interactions becomes difficult, resulting in real Rydberg excitations in the sample. From this we conclude that an approximate lower limit for the stroboscopic pulse time t is set by the inverse detuning $1/\Delta$. The limit of stroboscopic dressing for small detunings was recently also explored experimentally [311]. Alternatively, the dark time T can be increased, which is in the end limited by the relation $1/(T+t) \gg \Gamma_{ext}$, i.e. whether the interaction can still be considered as a time-averaged quantity with respect to external time scales.

D.2.2 Experimental relevance

Finally, we want to briefly discuss the experimental relevance for the two scenarios spin physics and lattice or continuum physics discussed already above in the context of these modified scalings for stroboscopic dressing.

1. **Spin physics**. Due to the lower bound for the pulse time t set by the adiabaticity requirement, achieving much gain with the pulsed scheme seems difficult. Generally, the best strategy for spin models seems to be increasing the admixture as far as tolerable and using continuous dressing.

2. **Lattice/continuum physics**. Contrary to the spin models, here the stroboscopic dressing could help significantly. The hopping rates in a lattice or the trap frequency are sufficiently small – reduced by about a factor of 1000 compared to the Rydberg interaction energy scale – such that the stroboscopic dressing can be applied and the average interaction would have the above discussed advantageous properties. A realistic setting could e.g. be dressing with pulse lengths of $t = 2\,\mu s$ and dark times of $T = 18\,\mu s$, resulting in a quality factor increased effectively by $D^{-1/3} \approx 2.2$.

D.3 Summary

These considerations show that a stroboscopic sequence can significantly increase the quality factor for Rydberg dressing, especially for lattice physics or physics in continuous systems. The main idea is to exploit the different dependences for the interaction U_0 and the decoherence rate Γ_{eff} on the admixture β. In addition to the advantage of using larger admixture, in the pulsed scheme atoms in spurious Rydberg S- or D-states could be depumped during the dark period T, combining two of the routes to mitigate the black-body-induced collective decay discussed in chapter 6.

Bibliography

[1] M. H. Anderson, J. R. Ensher, M. R. Matthews, C. E. Wieman, and E. A. Cornell. *Observation of Bose-Einstein Condensation in a Dilute Atomic Vapor*. Science **269**, 198–201 (1995). (Cited on page **1**)

[2] K. B. Davis, M. O. Mewes, M. R. Andrews, N. J. van Druten, D. S. Durfee, D. M. Kurn, and W. Ketterle. *Bose-Einstein Condensation in a Gas of Sodium Atoms*. Phys. Rev. Lett. **75**, 3969–3973 (1995). (Cited on page **1**)

[3] I. Bloch, J. Dalibard, and W. Zwerger. *Many-body physics with ultracold gases*. Rev. Mod. Phys. **80**, 885–964 (2008). (Cited on pages **1**, **7**, and **37**)

[4] I. Bloch, J. Dalibard, and S. Nascimbène. *Quantum simulations with ultracold quantum gases*. Nat. Phys. **8**, 267–276 (2012). (Cited on pages **1** and **7**)

[5] I. Georgescu, S. Ashhab, and F. Nori. *Quantum simulation*. Rev. Mod. Phys. **86**, 153–185 (2014). (Cited on page **1**)

[6] M. P. A. Fisher, P. B. Weichman, G. Grinstein, and D. S. Fisher. *Boson localization and the superfluid-insulator transition*. Phys. Rev. B **40**, 546–570 (1989). (Cited on page **1**)

[7] M. Greiner, O. Mandel, T. Esslinger, T. W. Hänsch, and I. Bloch. *Quantum phase transition from a superfluid to a Mott insulator in a gas of ultracold atoms*. Nature **415**, 39–44 (2002). (Cited on page **1**)

[8] A. Polkovnikov, K. Sengupta, A. Silva, and M. Vengalattore. *Colloquium : Nonequilibrium dynamics of closed interacting quantum systems*. Rev. Mod. Phys. **83**, 863–883 (2011). (Cited on pages **1** and **122**)

[9] J. Eisert, M. Friesdorf, and C. Gogolin. *Quantum many-body systems out of equilibrium*. Nat. Phys. **11**, 124–130 (2015). (Cited on pages **1** and **56**)

[10] W. S. Bakr, J. I. Gillen, A. Peng, S. Fölling, and M. Greiner. *A quantum gas microscope for detecting single atoms in a Hubbard-regime optical lattice*. Nature **462**, 74–77 (2009). (Cited on pages **1**, **37**, and **39**)

[11] J. F. Sherson, C. Weitenberg, M. Endres, M. Cheneau, I. Bloch, and S. Kuhr.

Single-atom-resolved fluorescence imaging of an atomic Mott insulator. Nature **467**, 68–72 (2010). (Cited on pages **1**, **37**, **39**, **40**, **41**, and **50**)

[12] R. Yamamoto, J. Kobayashi, T. Kuno, K. Kato, and Y. Takahashi. *An ytterbium quantum gas microscope with narrow-line laser cooling*. New J. Phys. **18**, 023016 (2016). (Cited on pages **1** and **39**)

[13] M. F. Parsons, F. Huber, A. Mazurenko, C. S. Chiu, W. Setiawan, K. Wooley-Brown, S. Blatt, and M. Greiner. *Site-Resolved Imaging of Fermionic* ^{6}Li *in an Optical Lattice*. Phys. Rev. Lett. **114**, 213002 (2015). (Cited on pages **1** and **39**)

[14] E. Haller, J. Hudson, A. Kelly, D. A. Cotta, B. Peaudecerf, G. D. Bruce, and S. Kuhr. *Single-atom imaging of fermions in a quantum-gas microscope*. Nat. Phys. **11**, 738–742 (2015). (Cited on pages **1** and **39**)

[15] L. W. Cheuk, M. A. Nichols, M. Okan, T. Gersdorf, V. V. Ramasesh, W. S. Bakr, T. Lompe, and M. W. Zwierlein. *Quantum-Gas Microscope for Fermionic Atoms*. Phys. Rev. Lett. **114**, 193001 (2015). (Cited on pages **1** and **39**)

[16] A. Omran, M. Boll, T. A. Hilker, K. Kleinlein, G. Salomon, I. Bloch, and C. Gross. *Microscopic Observation of Pauli Blocking in Degenerate Fermionic Lattice Gases*. Phys. Rev. Lett. **115**, 263001 (2015). (Cited on pages **1** and **39**)

[17] P. T. Brown, D. Mitra, E. Guardado-Sanchez, P. Schauß, S. S. Kondov, E. Khatami, T. Paiva, N. Trivedi, D. A. Huse, and W. S. Bakr. *Observation of canted antiferromagnetism with ultracold fermions in an optical lattice*. arXiv:1612.07746 (2016). (Cited on pages **1** and **39**)

[18] M. Endres, M. Cheneau, T. Fukuhara, C. Weitenberg, P. Schauß, C. Gross, L. Mazza, M. C. Bañuls, L. Pollet, I. Bloch, and S. Kuhr. *Observation of Correlated Particle-Hole Pairs and String Order in Low-Dimensional Mott Insulators*. Science **334**, 200–203 (2011). (Cited on pages **1**, **39**, and **142**)

[19] M. Cheneau, P. Barmettler, D. Poletti, M. Endres, P. Schauß, T. Fukuhara, C. Gross, I. Bloch, C. Kollath, and S. Kuhr. *Light-cone-like spreading of correlations in a quantum many-body system*. Nature **481**, 484–487 (2012). (Cited on pages **1**, **134**, and **142**)

[20] J. Simon, W. S. Bakr, R. Ma, M. E. Tai, P. M. Preiss, and M. Greiner. *Quantum simulation of antiferromagnetic spin chains in an optical lattice*. Nature **472**, 307–312 (2011). (Cited on page **1**)

[21] M. F. Parsons, A. Mazurenko, C. S. Chiu, G. Ji, D. Greif, and M. Greiner. *Site-resolved measurement of the spin-correlation function in the Fermi-Hubbard model*. Science **353**, 1253–1256 (2016). (Cited on page **1**)

[22] M. Boll, T. A. Hilker, G. Salomon, A. Omran, J. Nespolo, L. Pollet, I. Bloch, and C. Gross. *Spin- and density-resolved microscopy of antiferromagnetic correlations in Fermi-Hubbard chains*. Science **353**, 1257–1260 (2016). (Cited on pages **1** and **39**)

[23] L. W. Cheuk, M. A. Nichols, K. R. Lawrence, M. Okan, H. Zhang, E. Khatami, N. Trivedi, T. Paiva, M. Rigol, and M. W. Zwierlein. *Observation of spatial charge and spin correlations in the 2D Fermi-Hubbard model*. Science **353**, 1260–1264 (2016). (Cited on page **1**)

[24] A. Mazurenko, C. S. Chiu, G. Ji, M. F. Parsons, M. Kanász-Nagy, R. Schmidt, F. Grusdt, E. Demler, D. Greif, and M. Greiner. *A cold-atom Fermi–Hubbard antiferromagnet*. Nature **545**, 462–466 (2017). (Cited on pages **1** and **39**)

[25] T. A. Hilker, G. Salomon, F. Grusdt, A. Omran, M. Boll, E. Demler, I. Bloch, and C. Gross. *Revealing hidden antiferromagnetic correlations in doped Hubbard chains via string correlators*. Science **357**, 484–487 (2017). (Cited on pages **1** and **39**)

[26] D. Mitra, P. T. Brown, E. Guardado-Sanchez, S. S. Kondov, T. Devakul, D. A. Huse, P. Schauß, and W. S. Bakr. *Quantum gas microscopy of an attractive Fermi-Hubbard system*. arXiv:1705.02039 (2017). (Cited on pages **1** and **39**)

[27] C. Weitenberg, M. Endres, J. F. Sherson, M. Cheneau, P. Schauß, T. Fukuhara, I. Bloch, and S. Kuhr. *Single-spin addressing in an atomic Mott insulator*. Nature **471**, 319–324 (2011). (Cited on pages **1**, **40**, **42**, **50**, **123**, and **140**)

[28] T. Fukuhara, A. Kantian, M. Endres, M. Cheneau, P. Schauß, S. Hild, D. Bellem, U. Schollwöck, T. Giamarchi, C. Gross, I. Bloch, and S. Kuhr. *Quantum dynamics of a mobile spin impurity*. Nat. Phys. **9**, 235–241 (2013). (Cited on pages **1**, **3**, **39**, **43**, **102**, **123**, and **140**)

[29] T. Fukuhara, P. Schauß, M. Endres, S. Hild, M. Cheneau, I. Bloch, and C. Gross. *Microscopic observation of magnon bound states and their dynamics*. Nature **502**, 76–79 (2013). (Cited on pages **1**, **3**, **39**, **43**, and **102**)

[30] J.-y. Choi, S. Hild, J. Zeiher, P. Schauß, A. Rubio-Abadal, T. Yefsah, V. Khemani, D. A. Huse, I. Bloch, and C. Gross. *Exploring the many-body localization transition in two dimensions*. Science **352**, 1547–1552 (2016). (Cited on pages **1**, **3**, and **141**)

[31] A. M. Kaufman, M. E. Tai, A. Lukin, M. Rispoli, R. Schittko, P. M. Preiss, and M. Greiner. *Quantum thermalization through entanglement in an isolated many-body system*. Science **353**, 794–800 (2016). (Cited on pages **1** and **122**)

[32] D. Jaksch, C. Bruder, J. I. Cirac, C. W. Gardiner, and P. Zoller. *Cold Bosonic Atoms in Optical Lattices*. Phys. Rev. Lett. **81**, 3108–3111 (1998). (Cited on page **1**)

[33] D. Jaksch and P. Zoller. *The cold atom Hubbard toolbox*. Ann. of Phys. **315**, 52–79 (2005). (Cited on page **1**)

[34] C. A. Regal, C. Ticknor, J. L. Bohn, and D. S. Jin. *Creation of ultracold molecules from a Fermi gas of atoms*. Nature **424**, 47–50 (2003). (Cited on page **1**)

[35] M. W. Zwierlein, J. R. Abo-Shaeer, A. Schirotzek, C. H. Schunck, and W. Ketterle. *Vortices and superfluidity in a strongly interacting Fermi gas*. Nature **435**, 1047–1051 (2005). (Cited on page **1**)

[36] C. Chin, R. Grimm, P. Julienne, and E. Tiesinga. *Feshbach resonances in ultracold gases*. Rev. Mod. Phys. **82**, 1225–1286 (2010). (Cited on page **1**)

[37] M. Baranov. *Theoretical progress in many-body physics with ultracold dipolar gases*. Physics Reports **464**, 71–111 (2008). (Cited on pages **2** and **7**)

[38] T. Lahaye, C. Menotti, L. Santos, M. Lewenstein, and T. Pfau. *The physics of dipolar bosonic quantum gases*. Reports on Progress in Physics **72**, 126401 (2009). (Cited on page **2**)

[39] M. Baranov, M. Dalmonte, G. Pupillo, and P. Zoller. *Condensed Matter Theory of Dipolar Quantum Gases*. Chem. Rev. **112**, 5012–5061 (2012). (Cited on pages **2** and **7**)

[40] A. Griesmaier, J. Werner, S. Hensler, J. Stuhler, and T. Pfau. *Bose-Einstein Condensation of Chromium*. Phys. Rev. Lett. **94**, 160401 (2005). (Cited on pages **2** and **7**)

[41] M. Lu, N. Q. Burdick, S. H. Youn, and B. L. Lev. *Strongly Dipolar Bose-Einstein Condensate of Dysprosium*. Phys. Rev. Lett. **107** (2011). (Cited on pages **2** and **7**)

[42] M. Lu, N. Q. Burdick, and B. L. Lev. *Quantum Degenerate Dipolar Fermi Gas*. Phys. Rev. Lett. **108**, 215301 (2012). (Cited on pages **2** and **7**)

[43] K. Aikawa, A. Frisch, M. Mark, S. Baier, A. Rietzler, R. Grimm, and F. Ferlaino. *Bose-Einstein Condensation of Erbium*. Phys. Rev. Lett. **108**, 210401 (2012). (Cited on pages **2** and **7**)

[44] K.-K. Ni, S. Ospelkaus, M. H. G. d. Miranda, A. Pe'er, B. Neyenhuis, J. J. Zirbel, S. Kotochigova, P. S. Julienne, D. S. Jin, and J. Ye. *A High Phase-Space-Density Gas of Polar Molecules*. Science **322**, 231–235 (2008). (Cited on page **2**)

[45] B. Yan, S. A. Moses, B. Gadway, J. P. Covey, K. R. A. Hazzard, A. M. Rey, D. S. Jin, and J. Ye. *Observation of dipolar spin-exchange interactions with lattice-confined polar molecules*. Nature **501**, 521–525 (2013). (Cited on pages **2**, **7**, and **97**)

[46] M. Saffman, T. G. Walker, and K. Mølmer. *Quantum information with Rydberg atoms*. Rev. Mod. Phys. **82**, 2313–2363 (2010). (Cited on pages **2**, **16**, **24**, and **67**)

[47] H. Weimer, M. Müller, I. Lesanovsky, P. Zoller, and H. P. Büchler. *A Rydberg quantum simulator*. Nat. Phys. **6**, 382–388 (2010). (Cited on page **2**)

[48] A. Browaeys, D. Barredo, and T. Lahaye. *Experimental investigations of dipole-dipole interactions between a few Rydberg atoms*. J. Phys. B: At. Mol. Opt. Phys. **49**, 152001 (2016). (Cited on page **2**)

[49] I. Mourachko, D. Comparat, F. de Tomasi, A. Fioretti, P. Nosbaum, V. M. Akulin, and P. Pillet. *Many-Body Effects in a Frozen Rydberg Gas*. Phys. Rev. Lett. **80**, 253–256 (1998). (Cited on pages **2** and **115**)

[50] W. R. Anderson, J. R. Veale, and T. F. Gallagher. *Resonant Dipole-Dipole Energy Transfer in a Nearly Frozen Rydberg Gas*. Phys. Rev. Lett. **80**, 249–252 (1998). (Cited on pages **2** and **115**)

[51] E. Urban, T. A. Johnson, T. Henage, L. Isenhower, D. D. Yavuz, T. G. Walker, and M. Saffman. *Observation of Rydberg blockade between two atoms*. Nat. Phys. **5**, 110–114 (2009). (Cited on pages **2**, **37**, **47**, and **67**)

[52] A. Gaëtan, Y. Miroshnychenko, T. Wilk, A. Chotia, M. Viteau, D. Comparat, P. Pillet, A. Browaeys, and P. Grangier. *Observation of collective excitation of two individual atoms in the Rydberg blockade regime*. Nat. Phys. **5**, 115–118 (2009). (Cited on pages **2**, **37**, **47**, and **67**)

[53] L. Isenhower, E. Urban, X. L. Zhang, A. T. Gill, T. Henage, T. A. Johnson, T. G. Walker, and M. Saffman. *Demonstration of a Neutral Atom Controlled-NOT Quantum Gate*. Phys. Rev. Lett. **104**, 010503 (2010). (Cited on pages **2** and **47**)

[54] T. Wilk, A. Gaëtan, C. Evellin, J. Wolters, Y. Miroshnychenko, P. Grangier, and A. Browaeys. *Entanglement of Two Individual Neutral Atoms Using Rydberg Blockade*. Phys. Rev. Lett. **104**, 010502 (2010). (Cited on pages **2**, **47**, **59**, and **147**)

[55] P. Schauß, M. Cheneau, M. Endres, T. Fukuhara, S. Hild, A. Omran, T. Pohl, C. Gross, S. Kuhr, and I. Bloch. *Observation of spatially ordered structures in a two-dimensional Rydberg gas*. Nature **491**, 87–91 (2012). (Cited on pages **2**, **28**, **37**, **38**, **47**, **51**, **60**, **61**, **65**, **67**, **87**, **88**, **91**, **92**, **99**, **119**, and **139**)

[56] H. Labuhn, D. Barredo, S. Ravets, S. de Léséleuc, T. Macrì, T. Lahaye, and A. Browaeys. *Tunable two-dimensional arrays of single Rydberg atoms for realizing quantum Ising models*. Nature **534**, 667–670 (2016). (Cited on pages **2**, **47**, **48**, **61**, **97**, and **98**)

[57] P. Schauß, J. Zeiher, T. Fukuhara, S. Hild, M. Cheneau, T. Macrì, T. Pohl, I. Bloch, and C. Gross. *Crystallization in Ising quantum magnets*. Science **347**, 1455–1458 (2015). (Cited on pages **2**, **28**, **38**, **42**, **51**, **61**, **67**, **87**, **97**, **99**, **139**, and **140**)

[58] H. Bernien, S. Schwartz, A. Keesling, H. Levine, A. Omran, H. Pichler, S. Choi, A. S. Zibrov, M. Endres, M. Greiner, V. Vuletić, and M. D. Lukin. *Probing many-body dynamics on a 51-atom quantum simulator*. arXiv:1707.04344 (2017). (Cited on pages **2**, **37**, **47**, **48**, **61**, **64**, and **97**)

[59] M. D. Lukin, M. Fleischhauer, R. Cote, L. M. Duan, D. Jaksch, J. I. Cirac, and P. Zoller. *Dipole Blockade and Quantum Information Processing in Mesoscopic Atomic Ensembles*. Phys. Rev. Lett. **87**, 037901 (2001). (Cited on pages **2** and **48**)

[60] J. Zeiher, P. Schauß, S. Hild, T. Macrì, I. Bloch, and C. Gross. *Microscopic Characterization of Scalable Coherent Rydberg Superatoms*. Phys. Rev. X **5** (2015). (Cited on pages **2**, **47**, **65**, and **91**)

[61] L. Santos, G. V. Shlyapnikov, P. Zoller, and M. Lewenstein. *Bose-Einstein Condensation in Trapped Dipolar Gases*. Phys. Rev. Lett. **85**, 1791–1794 (2000). (Cited on pages **2**, **36**, and **95**)

[62] N. Henkel, R. Nath, and T. Pohl. *Three-Dimensional Roton Excitations and Supersolid Formation in Rydberg-Excited Bose-Einstein Condensates*. Phys. Rev. Lett. **104**, 195302 (2010). (Cited on pages **2**, **33**, **35**, **36**, **38**, **66**, **95**, **99**, **100**, and **141**)

[63] G. Pupillo, A. Micheli, M. Boninsegni, I. Lesanovsky, and P. Zoller. *Strongly Correlated Gases of Rydberg-Dressed Atoms: Quantum and Classical Dynamics*. Phys. Rev. Lett. **104**, 223002 (2010). (Cited on pages **2**, **35**, **36**, **38**, **95**, and **141**)

[64] I. Bouchoule and K. Mølmer. *Spin squeezing of atoms by the dipole interaction in virtually excited Rydberg states*. Phys. Rev. A **65** (2002). (Cited on pages **2** and **95**)

[65] L. Gil, R. Mukherjee, E. Bridge, M. Jones, and T. Pohl. *Spin Squeezing in a Rydberg Lattice Clock*. Phys. Rev. Lett. **112** (2014). (Cited on pages **2**, **95**, and **141**)

[66] A. W. Glaetzle, M. Dalmonte, R. Nath, C. Gross, I. Bloch, and P. Zoller. *Designing Frustrated Quantum Magnets with Laser-Dressed Rydberg Atoms*. Phys. Rev. Lett. **114** (2015). (Cited on pages **2**, **95**, **100**, and **141**)

[67] R. M. W. v. Bijnen and T. Pohl. *Quantum Magnetism and Topological Ordering via Rydberg Dressing near Förster Resonances*. Phys. Rev. Lett. **114** (2015). (Cited on pages **2**, **38**, **95**, **100**, **133**, and **141**)

[68] A. W. Glaetzle, R. M. W. v. Bijnen, P. Zoller, and W. Lechner. *A coherent quantum*

annealer with Rydberg atoms. Nat. Commun. **8**, 15813 (2017). (Cited on pages **2**, **38**, **119**, and **141**)

[69] S. Trotzky, P. Cheinet, S. Fölling, M. Feld, U. Schnorrberger, A. M. Rey, A. Polkovnikov, E. A. Demler, M. D. Lukin, and I. Bloch. *Time-Resolved Observation and Control of Superexchange Interactions with Ultracold Atoms in Optical Lattices*. Science **319**, 295–299 (2008). (Cited on page **3**)

[70] D. Greif, T. Uehlinger, G. Jotzu, L. Tarruell, and T. Esslinger. *Short-Range Quantum Magnetism of Ultracold Fermions in an Optical Lattice*. Science **340**, 1307–1310 (2013). (Cited on page **3**)

[71] S. Hild, T. Fukuhara, P. Schauß, J. Zeiher, M. Knap, E. Demler, I. Bloch, and C. Gross. *Far-from-Equilibrium Spin Transport in Heisenberg Quantum Magnets*. Phys. Rev. Lett. **113**, 147205 (2014). (Cited on pages **3** and **43**)

[72] T. Fukuhara, S. Hild, J. Zeiher, P. Schauß, I. Bloch, M. Endres, and C. Gross. *Spatially Resolved Detection of a Spin-Entanglement Wave in a Bose-Hubbard Chain*. Phys. Rev. Lett. **115**, 035302 (2015). (Cited on pages **3**, **43**, **56**, and **128**)

[73] Y.-Y. Jau, A. M. Hankin, T. Keating, I. H. Deutsch, and G. W. Biedermann. *Entangling atomic spins with a Rydberg-dressed spin-flip blockade*. Nat. Phys. **12**, 71–74 (2016). (Cited on pages **3**, **96**, and **117**)

[74] J. Zeiher, R. van Bijnen, P. Schauß, S. Hild, J.-y. Choi, T. Pohl, I. Bloch, and C. Gross. *Many-body interferometry of a Rydberg-dressed spin lattice*. Nat. Phys. **12**, 1095–1099 (2016). (Cited on pages **3**, **20**, **83**, **84**, **95**, **100**, **101**, **105**, **108**, **109**, **112**, **113**, **116**, **124**, and **136**)

[75] N. Ramsey. *Molecular Beams*. International series of monographs on physics. Oxford University Press (1956). (Cited on pages **3**, **55**, and **102**)

[76] J. Zeiher, J.-y. Choi, A. Rubio-Abadal, T. Pohl, R. van Bijnen, I. Bloch, and C. Gross. *Coherent many-body spin dynamics in a long-range interacting Ising chain*. arXiv:1705.08372 (2017). (Cited on pages **3**, **121**, **124**, **125**, **127**, **129**, **131**, **135**, and **136**)

[77] V. Khemani, A. Lazarides, R. Moessner, and S. Sondhi. *Phase Structure of Driven Quantum Systems*. Phys. Rev. Lett. **116**, 250401 (2016). (Cited on pages **3**, **137**, and **141**)

[78] I.-D. Potirniche, A. Potter, M. Schleier-Smith, A. Vishwanath, and N. Yao. *Floquet Symmetry-Protected Topological Phases in Cold-Atom Systems*. Phys. Rev. Lett. **119**, 123601 (2017). (Cited on pages **3**, **37**, **119**, **137**, and **141**)

[79] J. Zhang, P. W. Hess, A. Kyprianidis, P. Becker, A. Lee, J. Smith, G. Pagano, I.-D. Potirniche, A. C. Potter, A. Vishwanath, N. Y. Yao, and C. Monroe. *Observation of a discrete time crystal*. Nature **543**, 217–220 (2017). (Cited on pages **3**, **7**, and **141**)

[80] S. Choi, J. Choi, R. Landig, G. Kucsko, H. Zhou, J. Isoya, F. Jelezko, S. Onoda, H. Sumiya, V. Khemani, C. von Keyserlingk, N. Y. Yao, E. Demler, and M. D. Lukin. *Observation of discrete time-crystalline order in a disordered dipolar many-body system*. Nature **543**, 221–225 (2017). (Cited on pages **3** and **141**)

[81] H. Kadau, M. Schmitt, M. Wenzel, C. Wink, T. Maier, I. Ferrier-Barbut, and T. Pfau. *Observing the Rosensweig instability of a quantum ferrofluid*. Nature **530**, 194–197 (2016). (Cited on page **7**)

[82] M. Schmitt, M. Wenzel, F. Böttcher, I. Ferrier-Barbut, and T. Pfau. *Self-bound droplets of a dilute magnetic quantum liquid*. Nature **539**, 259–262 (2016). (Cited on page **7**)

[83] S. Baier, M. J. Mark, D. Petter, K. Aikawa, L. Chomaz, Z. Cai, M. Baranov, P. Zoller, and F. Ferlaino. *Extended Bose-Hubbard models with ultracold magnetic atoms*. Science **352**, 201–205 (2016). (Cited on page **7**)

[84] L. Chomaz, S. Baier, D. Petter, M. Mark, F. Wächtler, L. Santos, and F. Ferlaino. *Quantum-Fluctuation-Driven Crossover from a Dilute Bose-Einstein Condensate to a Macrodroplet in a Dipolar Quantum Fluid*. Phys. Rev. X **6**, 041039 (2016). (Cited on page **7**)

[85] L. Chomaz, R. M. W. van Bijnen, D. Petter, G. Faraoni, S. Baier, J. H. Becher, M. J. Mark, F. Waechtler, L. Santos, and F. Ferlaino. *Observation of the Roton Mode in a Dipolar Quantum Gas*. arXiv:1705.06914 (2017). (Cited on page **7**)

[86] R. Blatt and C. F. Roos. *Quantum simulations with trapped ions*. Nat. Phys. **8**, 277–284 (2012). (Cited on pages **7** and **97**)

[87] R. Islam, C. Senko, W. C. Campbell, S. Korenblit, J. Smith, A. Lee, E. E. Edwards, C.-C. J. Wang, J. K. Freericks, and C. Monroe. *Emergence and Frustration of Magnetism with Variable-Range Interactions in a Quantum Simulator*. Science **340**, 583–587 (2013). (Cited on pages **7** and **97**)

[88] P. Richerme, Z.-X. Gong, A. Lee, C. Senko, J. Smith, M. Foss-Feig, S. Michalakis, A. V. Gorshkov, and C. Monroe. *Non-local propagation of correlations in quantum systems with long-range interactions*. Nature **511**, 198–201 (2014). (Cited on pages **7**, **97**, **99**, **108**, **123**, **134**, **137**, and **141**)

[89] P. Jurcevic, B. P. Lanyon, P. Hauke, C. Hempel, P. Zoller, R. Blatt, and C. F. Roos.

Quasiparticle engineering and entanglement propagation in a quantum many-body system. Nature **511**, 202–205 (2014). (Cited on pages **7**, **97**, **99**, **134**, and **137**)

[90] J. R. Rydberg. *XXXIV. On the structure of the line-spectra of the chemical elements*. Philosophical Magazine **29**, 331–337 (1890). (Cited on pages **8** and **9**)

[91] T. F. Gallagher. *Rydberg Atoms*. Cambridge Monographs on Atomic, Molecular and Chemical Physics. Cambridge University Press (1994). (Cited on pages **8**, **9**, **10**, and **14**)

[92] R. Löw, H. Weimer, J. Nipper, J. B. Balewski, B. Butscher, H. P. Büchler, and T. Pfau. *An experimental and theoretical guide to strongly interacting Rydberg gases*. J. Phys. B: At. Mol. Opt. Phys. **45**, 113001 (2012). (Cited on pages **8**, **10**, **13**, **14**, **16**, **65**, and **117**)

[93] I. I. Beterov, I. I. Ryabtsev, D. B. Tretyakov, and V. M. Entin. *Quasiclassical calculations of blackbody-radiation-induced depopulation rates and effective lifetimes of Rydberg nS , nP , and nD alkali-metal atoms with* $n \leq 80$. Phys. Rev. A **79** (2009). (Cited on pages **8**, **14**, **15**, **16**, **51**, **65**, **114**, **117**, and **125**)

[94] W. E. Cooke and T. F. Gallagher. *Effects of blackbody radiation on highly excited atoms*. Phys. Rev. A **21**, 588–593 (1980). (Cited on pages **8** and **15**)

[95] N. Šibalić, J. D. Pritchard, C. S. Adams, and K. J. Weatherill. *ARC: An open-source library for calculating properties of alkali Rydberg atoms*. Computer Physics Communications **220**, 319–331 (2017). (Cited on pages **8**, **12**, **16**, **20**, **26**, **27**, **114**, and **115**)

[96] NIST. *Handbook of Basic Atomic Spectroscopic Data*. https://www.nist.gov/pml/atomic-spectra-database (2016). (Cited on page **9**)

[97] M. Mack, F. Karlewski, H. Hattermann, S. Höckh, F. Jessen, D. Cano, and J. Fortágh. *Measurement of absolute transition frequencies of* ^{87}Rb *to nS and nD Rydberg states by means of electromagnetically induced transparency*. Phys. Rev. A **83**, 052515 (2011). (Cited on pages **8**, **9**, **10**, and **11**)

[98] W. Li, I. Mourachko, M. W. Noel, and T. F. Gallagher. *Millimeter-wave spectroscopy of cold Rb Rydberg atoms in a magneto-optical trap: Quantum defects of the ns , np , and nd series*. Phys. Rev. A **67**, 052502 (2003). (Cited on pages **9**, **10**, and **83**)

[99] M. J. Seaton. *Quantum defect theory*. Rep. Prog. Phys. **46**, 167 (1983). (Cited on page **9**)

[100] C.-J. Lorenzen and K. Niemax. *Quantum Defects of the $n^2 P_{1/2,3/2}$ Levels in ^{39} K I and ^{85} Rb I*. Phys. Scr. **27**, 300 (1983). (Cited on pages **10** and **11**)

[101] B. E. King. *Angular Momentum Coupling and Rabi Frequencies for Simple Atomic Transitions*. arXiv:0804.4528 (2008). (Cited on pages **10**, **12**, and **13**)

[102] D. A. Steck. *Rubidium 87 D Line Data (revision 2.1.5, 13 January 2015)*. http://steck.us/alkalidata (2015). (Cited on pages **10**, **12**, **40**, **42**, **65**, **81**, and **90**)

[103] M. Marinescu, H. R. Sadeghpour, and A. Dalgarno. *Dispersion coefficients for alkali-metal dimers*. Phys. Rev. A **49**, 982–988 (1994). (Cited on pages **10** and **14**)

[104] B. Numerov. *Note on the numerical integration of* $\mathrm{d}^2x/\mathrm{d}t^2 = f(x,t)$. Astron. Nachr. **230**, 359–364 (1927). (Cited on page **10**)

[105] M. L. Zimmerman, M. G. Littman, M. M. Kash, and D. Kleppner. *Stark structure of the Rydberg states of alkali-metal atoms*. Phys. Rev. A **20**, 2251–2275 (1979). (Cited on pages **10** and **11**)

[106] S. A. Bhatti, C. L. Cromer, and W. E. Cooke. *Analysis of the Rydberg character of the $5d7d\,^1D_2$ state of barium*. Phys. Rev. A **24**, 161–165 (1981). (Cited on pages **10** and **11**)

[107] C. E. Theodosiou. *Lifetimes of alkali-metal–atom Rydberg states*. Phys. Rev. A **30**, 2881–2909 (1984). (Cited on page **10**)

[108] V. Bendkowsky, B. Butscher, J. Nipper, J. P. Shaffer, R. Löw, and T. Pfau. *Observation of ultralong-range Rydberg molecules*. Nature **458**, 1005–1008 (2009). (Cited on page **11**)

[109] T. Niederprüm, O. Thomas, T. Eichert, and H. Ott. *Rydberg Molecule-Induced Remote Spin Flips*. Phys. Rev. Lett. **117**, 123002 (2016). (Cited on page **11**)

[110] K. Singer, J. Stanojevic, M. Weidemüller, and R. Cŏté. *Long-range interactions between alkali Rydberg atom pairs correlated to the n s– n s, n p–n p and n d– n d asymptotes*. J. Phys. B: At. Mol. Opt. Phys. **38**, S295 (2005). (Cited on pages **12** and **25**)

[111] T. G. Walker and M. Saffman. *Consequences of Zeeman degeneracy for the van der Waals blockade between Rydberg atoms*. Phys. Rev. A **77**, 032723 (2008). (Cited on pages **12** and **25**)

[112] A. Glaetzle, M. Dalmonte, R. Nath, I. Rousochatzakis, R. Moessner, and P. Zoller. *Quantum Spin-Ice and Dimer Models with Rydberg Atoms*. Phys. Rev. X **4**, 041037 (2014). (Cited on pages **12**, **16**, **19**, and **141**)

[113] J. Deiglmayr. *Long-range interactions between Rydberg atoms*. Phys. Scr. **91**, 104007 (2016). (Cited on pages **12**, **20**, and **27**)

[114] S. Weber, C. Tresp, H. Menke, A. Urvoy, O. Firstenberg, H. P. Büchler, and S. Hofferberth. *Calculation of Rydberg interaction potentials*. J. Phys. B: At. Mol. Opt. Phys. **50**, 133001 (2017). (Cited on pages **12**, **16**, **20**, and **27**)

[115] P. Schauß. *High-resolution imaging of ordering in Rydberg many-body systems*. PhD Thesis, Ludwig-Maximilians-Universität München (2015). (Cited on pages **13**, **39**, **51**, **55**, **67**, **68**, **87**, and **119**)

[116] J. C. Weisheit. *Photoabsorption by Ground-State Alkali-Metal Atoms*. Phys. Rev. A **5**, 1621–1630 (1972). (Cited on page **14**)

[117] F. Robicheaux and J. Shaw. *Calculated electron dynamics in an electric field*. Phys. Rev. A **56**, 278–289 (1997). (Cited on page **14**)

[118] F. Robicheaux and J. Shaw. *Erratum: Calculated electron dynamics in an electric field [Phys. Rev. A 56, 278 (1997)]*. Phys. Rev. A **94**, 029904 (2016). (Cited on page **14**)

[119] M. S. Safronova, C. J. Williams, and C. W. Clark. *Relativistic many-body calculations of electric-dipole matrix elements, lifetimes, and polarizabilities in rubidium*. Phys. Rev. A **69**, 022509 (2004). (Cited on page **14**)

[120] V. A. Zilitis. *Determination of the D and F° Rydberg energy levels of rubidium-like ions by the method of interpolation of relativistic quantum defects*. Opt. Spectrosc. **97**, 849–853 (2004). (Cited on page **14**)

[121] V. A. Zilitis. *Theoretical determination of oscillator strengths for the principal series of rubidium-like ions by the Dirac-Fock method*. Opt. Spectrosc. **107**, 54–57 (2009). (Cited on page **14**)

[122] V. A. Yerokhin, S. Y. Buhmann, S. Fritzsche, and A. Surzhykov. *Electric dipole polarizabilities of Rydberg states of alkali-metal atoms*. Phys. Rev. A **94**, 032503 (2016). (Cited on page **14**)

[123] E. Caliebe and K. Niemax. *Oscillator strengths of the principal series lines of Rb*. J. Phys. B: At. Mol. Phys. **12**, L45 (1979). (Cited on page **14**)

[124] M. Mack, J. Grimmel, F. Karlewski, L. Sárkány, H. Hattermann, and J. Fortágh. *All-optical measurement of Rydberg-state lifetimes*. Phys. Rev. A **92**, 012517 (2015). (Cited on page **16**)

[125] T. L. Nguyen, J.-M. Raimond, C. Sayrin, R. Cortinas, T. Cantat-Moltrecht, F. As-

semat, I. Dotsenko, S. Gleyzes, S. Haroche, G. Roux, T. Jolicoeur, and M. Brune. *Towards quantum simulation with circular Rydberg atoms*. arXiv:1707.04397 (2017). (Cited on page **16**)

[126] J. D. Jackson. *Classical Electrodynamics*. John Wiley & Sons, Inc., Third edition (1998). (Cited on page **16**)

[127] J. Schwinger, L. Deraad, K. Milton, and W. Tsai. *Classical Electrodynamics*. Advanced book program. Avalon Publishing (1998). (Cited on pages **16**, **17**, and **18**)

[128] J. Sakurai. *Modern Quantum Mechanics*. Addison-Wesley, Revised edition (1993). (Cited on pages **17**, **19**, **33**, **98**, and **143**)

[129] H. Saßmannshausen, F. Merkt, and J. Deiglmayr. *Pulsed excitation of Rydberg-atom-pair states in an ultracold Cs gas*. Phys. Rev. A **92**, 032505 (2015). (Cited on page **18**)

[130] H. Saßmannshausen and J. Deiglmayr. *Observation of Rydberg-Atom Macrodimers: Micrometer-Sized Diatomic Molecules*. Phys. Rev. Lett. **117**, 083401 (2016). (Cited on page **18**)

[131] N. Henkel. *Rydberg-dressed Bose-Einstein condensates*. PhD Thesis, Technische Universität Dresden, Dresden (2013). (Cited on pages **18**, **33**, **66**, **99**, and **110**)

[132] S. de Léséleuc, D. Barredo, V. Lienhard, A. Browaeys, and T. Lahaye. *Optical Control of the Resonant Dipole-Dipole Interaction between Rydberg Atoms*. Phys. Rev. Lett. **119**, 053202 (2017). (Cited on page **22**)

[133] D. Barredo, H. Labuhn, S. Ravets, T. Lahaye, A. Browaeys, and C. S. Adams. *Coherent Excitation Transfer in a Spin Chain of Three Rydberg Atoms*. Phys. Rev. Lett. **114** (2015). (Cited on pages **22** and **123**)

[134] A. P. Piñeiro Orioli, A. Signoles, H. Wildhagen, G. Günter, J. Berges, S. Whitlock, and M. Weidemüller. *Relaxation of an isolated dipolar-interacting Rydberg quantum spin system*. arXiv:1703.05957 (2017). (Cited on page **22**)

[135] E. Goldschmidt, T. Boulier, R. Brown, S. Koller, J. Young, A. Gorshkov, S. Rolston, and J. Porto. *Anomalous Broadening in Driven Dissipative Rydberg Systems*. Phys. Rev. Lett. **116**, 113001 (2016). (Cited on pages **22**, **88**, **96**, **115**, and **116**)

[136] T. Förster. *Zwischenmolekulare Energiewanderung und Fluoreszenz*. Ann. Phys. **437**, 55–75 (1948). (Cited on page **24**)

[137] K. A. Safinya, J. F. Delpech, F. Gounand, W. Sandner, and T. F. Gallagher. *Reso-*

nant Rydberg-Atom-Rydberg-Atom Collisions. Phys. Rev. Lett. **47**, 405–408 (1981). (Cited on page **24**)

[138] A. Reinhard, T. C. Liebisch, B. Knuffman, and G. Raithel. *Level shifts of rubidium Rydberg states due to binary interactions*. Phys. Rev. A **75**, 032712 (2007). (Cited on page **25**)

[139] B. Vermersch, A. W. Glaetzle, and P. Zoller. *Magic distances in the blockade mechanism of Rydberg p and d states*. Phys. Rev. A **91** (2015). (Cited on pages **25**, **93**, and **140**)

[140] H. B. G. Casimir and D. Polder. *Influence of Retardation on the London-van der Waals Forces*. Nature pages 787–788 (1946). (Cited on page **26**)

[141] R. M. W. v. Bijnen. *Quantum engineering with ultracold atoms*. PhD Thesis, Technische Universiteit Eindhoven (2013). (Cited on page **27**)

[142] R. J. Le Roy. *Long-Range Potential Coefficients From RKR Turning Points: C_6 and C_8 for $B(3\Pi^+_{Ou})$-State Cl_2, Br_2, and I_2*. Can. J. Phys. **52**, 246–256 (1974). (Cited on page **27**)

[143] F. Robicheaux and J. V. Hernández. *Many-body wave function in a dipole blockade configuration*. Phys. Rev. A **72** (2005). (Cited on page **28**)

[144] H. Weimer, R. Löw, T. Pfau, and H. P. Büchler. *Quantum Critical Behavior in Strongly Interacting Rydberg Gases*. Phys. Rev. Lett. **101**, 250601 (2008). (Cited on pages **28** and **61**)

[145] J. Schachenmayer, I. Lesanovsky, A. Micheli, and A. J. Daley. *Dynamical crystal creation with polar molecules or Rydberg atoms in optical lattices*. New J. Phys. **12**, 103044 (2010). (Cited on pages **28**, **61**, and **99**)

[146] C. Ates, T. Pohl, T. Pattard, and J. M. Rost. *Antiblockade in Rydberg Excitation of an Ultracold Lattice Gas*. Phys. Rev. Lett. **98** (2007). (Cited on pages **31** and **116**)

[147] H. Schempp, G. Günter, M. Robert-de Saint-Vincent, C. S. Hofmann, D. Breyel, A. Komnik, D. W. Schönleber, M. Gärttner, J. Evers, S. Whitlock, and M. Weidemüller. *Full Counting Statistics of Laser Excited Rydberg Aggregates in a One-Dimensional Geometry*. Phys. Rev. Lett. **112** (2014). (Cited on pages **31** and **37**)

[148] N. Malossi, M. Valado, S. Scotto, P. Huillery, P. Pillet, D. Ciampini, E. Arimondo, and O. Morsch. *Full Counting Statistics and Phase Diagram of a Dissipative Rydberg Gas*. Phys. Rev. Lett. **113** (2014). (Cited on pages **31** and **37**)

[149] A. Urvoy, F. Ripka, I. Lesanovsky, D. Booth, J. Shaffer, T. Pfau, and R. Löw. *Strongly Correlated Growth of Rydberg Aggregates in a Vapor Cell*. Phys. Rev. Lett. **114** (2015). (Cited on pages **31** and **116**)

[150] M. M. Valado, C. Simonelli, M. D. Hoogerland, I. Lesanovsky, J. P. Garrahan, E. Arimondo, D. Ciampini, and O. Morsch. *Experimental observation of controllable kinetic constraints in a cold atomic gas*. Phys. Rev. A **93**, 040701 (2016). (Cited on page **31**)

[151] C. Simonelli, M. M. Valado, G. Masella, L. Asteria, E. Arimondo, D. Ciampini, and O. Morsch. *Seeded excitation avalanches in off-resonantly driven Rydberg gases*. J. Phys. B: At. Mol. Opt. Phys. **49**, 154002 (2016). (Cited on pages **31**, **88**, and **116**)

[152] R. Grimm, M. Weidemüller, and Y. B. Ovchinnikov. *Optical Dipole Traps for Neutral Atoms*. Advances In Atomic, Molecular, and Optical Physics **42**, 95–170 (2000). (Cited on pages **32** and **37**)

[153] J. E. Johnson and S. L. Rolston. *Interactions between Rydberg-dressed atoms*. Phys. Rev. A **82**, 033412 (2010). (Cited on page **35**)

[154] J. B. Balewski, A. T. Krupp, A. Gaj, S. Hofferberth, R. Löw, and T. Pfau. *Rydberg dressing: understanding of collective many-body effects and implications for experiments*. New J. Phys. **16**, 063012 (2014). (Cited on pages **35**, **96**, **110**, and **116**)

[155] A. Geißler, I. Vasić, and W. Hofstetter. *Condensation versus long-range interaction: Competing quantum phases in bosonic optical lattice systems at near-resonant Rydberg dressing*. Phys. Rev. A **95**, 063608 (2017). (Cited on pages **36** and **142**)

[156] D. V. Else, B. Bauer, and C. Nayak. *Floquet Time Crystals*. Phys. Rev. Lett. **117**, 090402 (2016). (Cited on pages **37** and **141**)

[157] S. K. Dutta, J. R. Guest, D. Feldbaum, A. Walz-Flannigan, and G. Raithel. *Ponderomotive Optical Lattice for Rydberg Atoms*. Phys. Rev. Lett. **85**, 5551–5554 (2000). (Cited on page **37**)

[158] K. C. Younge, S. E. Anderson, and G. Raithel. *Adiabatic Potentials for Rydberg Atoms in a Ponderomotive Optical Lattice*. New J. Phys. **12**, 023031 (2010). (Cited on page **37**)

[159] K. C. Younge, B. Knuffman, S. E. Anderson, and G. Raithel. *State-Dependent Energy Shifts of Rydberg Atoms in a Ponderomotive Optical Lattice*. Phys. Rev. Lett. **104**, 173001 (2010). (Cited on page **37**)

[160] S. E. Anderson, K. C. Younge, and G. Raithel. *Trapping Rydberg Atoms in an Optical Lattice*. Phys. Rev. Lett. **107** (2011). (Cited on page **37**)

[161] M. Saffman and T. G. Walker. *Analysis of a quantum logic device based on dipole-dipole interactions of optically trapped Rydberg atoms*. Phys. Rev. A **72**, 022347 (2005). (Cited on page **37**)

[162] S. Zhang, F. Robicheaux, and M. Saffman. *Magic-wavelength optical traps for Rydberg atoms*. Phys. Rev. A **84**, 043408 (2011). (Cited on page **37**)

[163] T. Topcu and A. Derevianko. *Intensity landscape and the possibility of magic trapping of alkali-metal Rydberg atoms in infrared optical lattices*. Phys. Rev. A **88**, 043407 (2013). (Cited on page **37**)

[164] T. Topcu and A. Derevianko. *Tune-out wavelengths and landscape-modulated polarizabilities of alkali-metal Rydberg atoms in infrared optical lattices*. Phys. Rev. A **88**, 053406 (2013). (Cited on page **37**)

[165] L. Li, Y. O. Dudin, and A. Kuzmich. *Entanglement between light and an optical atomic excitation*. Nature **498**, 466–469 (2013). (Cited on page **37**)

[166] T. Macrì and T. Pohl. *Rydberg dressing of atoms in optical lattices*. Phys. Rev. A **89** (2014). (Cited on page **37**)

[167] A. Schwarzkopf, D. A. Anderson, N. Thaicharoen, and G. Raithel. *Spatial correlations between Rydberg atoms in an optical dipole trap*. Phys. Rev. A **88** (2013). (Cited on page **37**)

[168] T. M. Weber, M. Höning, T. Niederprüm, T. Manthey, O. Thomas, V. Guarrera, M. Fleischhauer, G. Barontini, and H. Ott. *Mesoscopic Rydberg-blockaded ensembles in the superatom regime and beyond*. Nat. Phys. **11**, 157–161 (2015). (Cited on pages **37** and **88**)

[169] R. M. W. v. Bijnen, C. Ravensbergen, D. J. Bakker, G. J. Dijk, S. J. J. M. F. Kokkelmans, and E. J. D. Vredenbregt. *Patterned Rydberg excitation and ionization with a spatial light modulator*. New J. Phys. **17**, 023045 (2015). (Cited on page **37**)

[170] M. Mattioli, M. Dalmonte, W. Lechner, and G. Pupillo. *Cluster Luttinger Liquids of Rydberg-Dressed Atoms in Optical Lattices*. Phys. Rev. Lett. **111** (2013). (Cited on pages **38**, **95**, and **142**)

[171] M. Endres, M. Cheneau, T. Fukuhara, C. Weitenberg, P. Schauß, C. Gross, L. Mazza, M. C. Bañuls, L. Pollet, I. Bloch, and S. Kuhr. *Single-site- and single-atom-resolved measurement of correlation functions*. Appl. Phys. B **113**, 27–39 (2013). (Cited on pages **39** and **142**)

[172] C. Weitenberg. *Single-Atom Resolved Imaging and Manipulation in an Atomic Mott*

Insulator. PhD Thesis, Ludwig-Maximilians-Universität München (2011). (Cited on pages **39**, **41**, **42**, and **43**)

[173] M. Endres. *Probing correlated quantum many-body systems at the single-particle level*. PhD Thesis, Ludwig-Maximilians-Universität München (2013). (Cited on page **39**)

[174] S. Hild. *Microscopy of quantum many-body systems out of equilibrium*. PhD Thesis, Ludwig-Maximilians-Universität München (2016). (Cited on pages **39**, **42**, **43**, and **45**)

[175] K. Dieckmann, R. J. C. Spreeuw, M. Weidemüller, and J. T. M. Walraven. *Two-dimensional magneto-optical trap as a source of slow atoms*. Phys. Rev. A **58**, 3891–3895 (1998). (Cited on page **39**)

[176] M. Greiner, O. Mandel, T. W. Hänsch, and I. Bloch. *Collapse and revival of the matter wave field of a Bose–Einstein condensate*. Nature **419**, 51–54 (2002). (Cited on pages **41**, **123**, and **141**)

[177] W. S. Bakr, A. Peng, M. E. Tai, R. Ma, J. Simon, J. I. Gillen, S. Fölling, L. Pollet, and M. Greiner. *Probing the Superfluid–to–Mott Insulator Transition at the Single-Atom Level*. Science **329**, 547–550 (2010). (Cited on page **41**)

[178] J. Weiner, V. S. Bagnato, S. Zilio, and P. S. Julienne. *Experiments and theory in cold and ultracold collisions*. Rev. Mod. Phys. **71**, 1–85 (1999). (Cited on page **42**)

[179] D. Bellem. *Generation of Spatially and Temporally Varying Light Potentials in Optical Lattices*. Diploma Thesis, Ludwig-Maximilians-Universität München (2011). (Cited on pages **42** and **43**)

[180] A. Widera, F. Gerbier, S. Fölling, T. Gericke, O. Mandel, and I. Bloch. *Precision measurement of spin-dependent interaction strengths for spin-1 and spin-2 ^{87}Rb atoms*. New J. Phys. **8**, 152 (2006). (Cited on page **43**)

[181] L. Allen and J. Eberly. *Optical Resonance and Two-Level Atoms*. Interscience Monographs and Texts in Physics and Astronomy. Wiley, New York (1975). (Cited on pages **43**, **65**, and **83**)

[182] D. Tong, S. M. Farooqi, J. Stanojevic, S. Krishnan, Y. P. Zhang, R. Cŏté, E. E. Eyler, and P. L. Gould. *Local Blockade of Rydberg Excitation in an Ultracold Gas*. Phys. Rev. Lett. **93** (2004). (Cited on page **47**)

[183] K. Singer, M. Reetz-Lamour, T. Amthor, L. G. Marcassa, and M. Weidemüller. *Suppression of Excitation and Spectral Broadening Induced by Interactions in a Cold Gas of Rydberg Atoms*. Phys. Rev. Lett. **93**, 163001 (2004). (Cited on page **47**)

[184] R. Heidemann, U. Raitzsch, V. Bendkowsky, B. Butscher, R. Löw, L. Santos, and T. Pfau. *Evidence for Coherent Collective Rydberg Excitation in the Strong Blockade Regime*. Phys. Rev. Lett. **99**, 163601 (2007). (Cited on page **47**)

[185] Y. O. Dudin, L. Li, F. Bariani, and A. Kuzmich. *Observation of coherent many-body Rabi oscillations*. Nat Phys **8**, 790–794 (2012). (Cited on page **48**)

[186] T. Peyronel, O. Firstenberg, Q.-Y. Liang, S. Hofferberth, A. V. Gorshkov, T. Pohl, M. D. Lukin, and V. Vuletić. *Quantum nonlinear optics with single photons enabled by strongly interacting atoms*. Nature **488**, 57–60 (2012). (Cited on page **48**)

[187] H. Gorniaczyk, C. Tresp, J. Schmidt, H. Fedder, and S. Hofferberth. *Single-Photon Transistor Mediated by Interstate Rydberg Interactions*. Phys. Rev. Lett. **113**, 053601 (2014). (Cited on page **48**)

[188] D. Tiarks, S. Baur, K. Schneider, S. Dürr, and G. Rempe. *Single-Photon Transistor Using a Förster Resonance*. Phys. Rev. Lett. **113**, 053602 (2014). (Cited on page **48**)

[189] J. Deiglmayr, M. Reetz-Lamour, T. Amthor, S. Westermann, A. L. de Oliveira, and M. Weidemüller. *Coherent excitation of Rydberg atoms in an ultracold gas*. Opt. Commun. **264**, 293–298 (2006). (Cited on page **48**)

[190] M. Reetz-Lamour, T. Amthor, J. Deiglmayr, and M. Weidemüller. *Rabi Oscillations and Excitation Trapping in the Coherent Excitation of a Mesoscopic Frozen Rydberg Gas*. Phys. Rev. Lett. **100**, 253001 (2008). (Cited on pages **48** and **61**)

[191] T. A. Johnson, E. Urban, T. Henage, L. Isenhower, D. D. Yavuz, T. G. Walker, and M. Saffman. *Rabi Oscillations between Ground and Rydberg States with Dipole-Dipole Atomic Interactions*. Phys. Rev. Lett. **100**, 113003 (2008). (Cited on pages **48** and **61**)

[192] M. Viteau, M. G. Bason, J. Radogostowicz, N. Malossi, D. Ciampini, O. Morsch, and E. Arimondo. *Rydberg Excitations in Bose-Einstein Condensates in Quasi-One-Dimensional Potentials and Optical Lattices*. Phys. Rev. Lett. **107**, 060402 (2011). (Cited on pages **48**, **61**, and **64**)

[193] M. Ebert, A. Gill, M. Gibbons, X. Zhang, M. Saffman, and T. G. Walker. *Atomic Fock State Preparation Using Rydberg Blockade*. Phys. Rev. Lett. **112**, 043602 (2014). (Cited on page **48**)

[194] M. Ebert, M. Kwon, T. Walker, and M. Saffman. *Coherence and Rydberg Blockade of Atomic Ensemble Qubits*. Phys. Rev. Lett. **115**, 093601 (2015). (Cited on pages **48**, **55**, **59**, and **61**)

[195] M. Kitagawa and M. Ueda. *Squeezed spin states*. Phys. Rev. A **47**, 5138–5143 (1993). (Cited on pages **49** and **56**)

[196] R. H. Dicke. *Coherence in Spontaneous Radiation Processes*. Phys. Rev. **93**, 99–110 (1954). (Cited on page **49**)

[197] M. Saffman and T. G. Walker. *Entangling single- and N-atom qubits for fast quantum state detection and transmission*. Phys. Rev. A **72**, 042302 (2005). (Cited on page **49**)

[198] W. Dür, G. Vidal, and J. I. Cirac. *Three qubits can be entangled in two inequivalent ways*. Phys. Rev. A **62**, 062314 (2000). (Cited on page **49**)

[199] E. Brion, K. Mølmer, and M. Saffman. *Quantum Computing with Collective Ensembles of Multilevel Systems*. Phys. Rev. Lett. **99**, 260501 (2007). (Cited on page **50**)

[200] E. Brion, L. H. Pedersen, M. Saffman, and K. Mølmer. *Error Correction in Ensemble Registers for Quantum Repeaters and Quantum Computers*. Phys. Rev. Lett. **100**, 110506 (2008). (Cited on page **50**)

[201] S. Whitlock, A. W. Glaetzle, and P. Hannaford. *Simulating quantum spin models using Rydberg-excited atomic ensembles in magnetic microtrap arrays*. J. Phys. B: At. Mol. Opt. Phys. **50**, 074001 (2017). (Cited on page **50**)

[202] H. Häffner, W. Hänsel, C. F. Roos, J. Benhelm, D. Chek-al kar, M. Chwalla, T. Körber, U. D. Rapol, M. Riebe, P. O. Schmidt, C. Becher, O. Gühne, W. Dür, and R. Blatt. *Scalable multiparticle entanglement of trapped ions*. Nature **438**, 643–646 (2005). (Cited on pages **50** and **56**)

[203] F. Haas, J. Volz, R. Gehr, J. Reichel, and J. Estève. *Entangled States of More Than 40 Atoms in an Optical Fiber Cavity*. Science **344**, 180–183 (2014). (Cited on pages **50**, **56**, **57**, and **61**)

[204] R. McConnell, H. Zhang, J. Hu, S. Ćuk, and V. Vuletić. *Entanglement with negative Wigner function of almost 3,000 atoms heralded by one photon*. Nature **519**, 439–442 (2015). (Cited on pages **50**, **57**, and **61**)

[205] J. Alnis, A. Matveev, N. Kolachevsky, T. Udem, and T. W. Hänsch. *Subhertz linewidth diode lasers by stabilization to vibrationally and thermally compensated ultralow-expansion glass Fabry-Pérot cavities*. Phys. Rev. A **77**, 053809 (2008). (Cited on pages **52** and **77**)

[206] R. Horodecki, P. Horodecki, M. Horodecki, and K. Horodecki. *Quantum entanglement*. Rev. Mod. Phys. **81**, 865–942 (2009). (Cited on page **56**)

[207] L. Amico, R. Fazio, A. Osterloh, and V. Vedral. *Entanglement in many-body systems*. Rev. Mod. Phys. **80**, 517–576 (2008). (Cited on page **56**)

[208] A. Osterloh, L. Amico, G. Falci, and R. Fazio. *Scaling of entanglement close to a quantum phase transition*. Nature **416**, 608–610 (2002). (Cited on page **56**)

[209] T. J. Osborne and M. A. Nielsen. *Entanglement in a simple quantum phase transition*. Phys. Rev. A **66**, 032110 (2002). (Cited on page **56**)

[210] J. Schachenmayer, B. P. Lanyon, C. F. Roos, and A. J. Daley. *Entanglement Growth in Quench Dynamics with Variable Range Interactions*. Phys. Rev. X **3**, 031015 (2013). (Cited on pages **56**, **134**, **137**, and **140**)

[211] K. R. A. Hazzard, M. van den Worm, M. Foss-Feig, S. R. Manmana, E. G. Dalla Torre, T. Pfau, M. Kastner, and A. M. Rey. *Quantum correlations and entanglement in far-from-equilibrium spin systems*. Phys. Rev. A **90**, 063622 (2014). (Cited on pages **56**, **133**, **134**, **137**, and **140**)

[212] R. Nandkishore and D. A. Huse. *Many-Body Localization and Thermalization in Quantum Statistical Mechanics*. Annual Review of Condensed Matter Physics **6**, 15–38 (2015). (Cited on page **56**)

[213] V. Giovannetti, S. Lloyd, and L. Maccone. *Quantum-Enhanced Measurements: Beating the Standard Quantum Limit*. Science **306**, 1330–1336 (2004). (Cited on pages **56** and **61**)

[214] O. Gühne and G. Tóth. *Entanglement detection*. Physics Reports **474**, 1–75 (2009). (Cited on page **56**)

[215] C. F. Roos, G. P. T. Lancaster, M. Riebe, H. Häffner, W. Hänsel, S. Gulde, C. Becher, J. Eschner, F. Schmidt-Kaler, and R. Blatt. *Bell States of Atoms with Ultralong Lifetimes and Their Tomographic State Analysis*. Phys. Rev. Lett. **92**, 220402 (2004). (Cited on pages **56** and **128**)

[216] R. Islam, R. Ma, P. M. Preiss, M. Eric Tai, A. Lukin, M. Rispoli, and M. Greiner. *Measuring entanglement entropy in a quantum many-body system*. Nature **528**, 77–83 (2015). (Cited on page **56**)

[217] C. Gross, T. Zibold, E. Nicklas, J. Estève, and M. K. Oberthaler. *Nonlinear atom interferometer surpasses classical precision limit*. Nature **464**, 1165–1169 (2010). (Cited on page **56**)

[218] A. S. Sørensen and K. Mølmer. *Entanglement and Extreme Spin Squeezing*. Phys. Rev. Lett. **86**, 4431–4434 (2001). (Cited on page **57**)

[219] J. Honer, R. Löw, H. Weimer, T. Pfau, and H. P. Büchler. *Artificial Atoms Can Do More Than Atoms: Deterministic Single Photon Subtraction from Arbitrary Light Fields*. Phys. Rev. Lett. **107**, 093601 (2011). (Cited on pages **59** and **149**)

[220] C. Tresp, C. Zimmer, I. Mirgorodskiy, H. Gorniaczyk, A. Paris-Mandoki, and S. Hofferberth. *Single-Photon Absorber Based on Strongly Interacting Rydberg Atoms*. Phys. Rev. Lett. **117**, 223001 (2016). (Cited on page **59**)

[221] D. Petrosyan, K. Mølmer, and M. Fleischhauer. *On the adiabatic preparation of spatially-ordered Rydberg excitations of atoms in a one-dimensional optical lattice by laser frequency sweeps*. J. Phys. B: At. Mol. Opt. Phys. **49**, 084003 (2016). (Cited on pages **61** and **140**)

[222] P. Schauß. *Finite-range interacting Ising quantum magnets with Rydberg atoms in optical lattices - From Rydberg superatoms to crystallization*. arXiv:1706.09014 (2017). (Cited on page **61**)

[223] J. Stanojevic and R. Cŏté. *Many-body Rabi oscillations of Rydberg excitation in small mesoscopic samples*. Phys. Rev. A **80**, 033418 (2009). (Cited on page **61**)

[224] H. Weimer and H. P. Büchler. *Two-Stage Melting in Systems of Strongly Interacting Rydberg Atoms*. Phys. Rev. Lett. **105**, 230403 (2010). (Cited on pages **61** and **140**)

[225] T. Pohl, E. Demler, and M. D. Lukin. *Dynamical Crystallization in the Dipole Blockade of Ultracold Atoms*. Phys. Rev. Lett. **104** (2010). (Cited on pages **61** and **140**)

[226] R. M. W. v. Bijnen, S. Smit, K. A. H. v. Leeuwen, E. J. D. Vredenbregt, and S. J. J. M. F. Kokkelmans. *Adiabatic formation of Rydberg crystals with chirped laser pulses*. J. Phys. B: At. Mol. Opt. Phys. **44**, 184008 (2011). (Cited on pages **61** and **140**)

[227] I. Lesanovsky. *Many-Body Spin Interactions and the Ground State of a Dense Rydberg Lattice Gas*. Phys. Rev. Lett. **106** (2011). (Cited on page **61**)

[228] L. Isenhower, M. Saffman, and K. Mølmer. *Multibit C_kNOT Quantum Gates via Rydberg Blockade*. Quantum Inf. Process **10**, 755 (2011). (Cited on page **61**)

[229] T. Opatrný and K. Mølmer. *Spin squeezing and Schrödinger-cat-state generation in atomic samples with Rydberg blockade*. Phys. Rev. A **86**, 023845 (2012). (Cited on pages **61** and **140**)

[230] J. Cui, R. M. W. v. Bijnen, T. Pohl, S. Montangero, and T. Calarco. *Optimal control of Rydberg lattice gases*. Quantum Sci. Technol. **2**, 035006 (2017). (Cited on pages **61** and **140**)

[231] A. M. Hankin, Y.-Y. Jau, L. P. Parazzoli, C. W. Chou, D. J. Armstrong, A. J. Landahl, and G. W. Biedermann. *Two-atom Rydberg blockade using direct 6S to nP excitation*. Phys. Rev. A **89**, 033416 (2014). (Cited on pages **63**, **68**, **69**, and **75**)

[232] J. Bai, J. Wang, J. He, and J. Wang. *Electronic sideband locking of 318.6nm UV laser to an ultrastable optical cavity with a wide continuously tunable range*. arXiv:1606.07603 (2016). (Cited on pages **63**, **68**, **69**, and **75**)

[233] E. M. Bridge, N. C. Keegan, A. D. Bounds, D. Boddy, D. P. Sadler, and M. P. A. Jones. *Tunable cw UV laser with <35 kHz absolute frequency instability for precision spectroscopy of Sr Rydberg states*. Opt. Express **24**, 2281–2292 (2016). (Cited on pages **63** and **68**)

[234] T. Manthey, T. M. Weber, T. Niederprüm, P. Langer, V. Guarrera, G. Barontini, and H. Ott. *Scanning electron microscopy of Rydberg-excited Bose–Einstein condensates*. New J. Phys. **16**, 083034 (2014). (Cited on pages **63** and **68**)

[235] G. Günter, H. Schempp, M. Robert-de Saint-Vincent, V. Gavryusev, S. Helmrich, C. S. Hofmann, S. Whitlock, and M. Weidemüller. *Observing the Dynamics of Dipole-Mediated Energy Transport by Interaction-Enhanced Imaging*. Science **342**, 954–956 (2013). (Cited on page **64**)

[236] V. Gavryusev, A. Signoles, M. Ferreira-Cao, G. Zürn, C. S. Hofmann, G. Günter, H. Schempp, M Robert-de-Saint-Vincent, S. Whitlock, and M. Weidemüller. *Density matrix reconstruction of three-level atoms via Rydberg electromagnetically induced transparency*. J. Phys. B: At. Mol. Opt. Phys. **49**, 164002 (2016). (Cited on page **64**)

[237] S. Helmrich, A. Arias, N. Pehoviak, and S. Whitlock. *Two-body interactions and decay of three-level Rydberg-dressed atoms*. J. Phys. B: At. Mol. Opt. Phys. **49**, 03LT02 (2016). (Cited on page **64**)

[238] C. Gaul, B. DeSalvo, J. Aman, F. Dunning, T. Killian, and T. Pohl. *Resonant Rydberg Dressing of Alkaline-Earth Atoms via Electromagnetically Induced Transparency*. Phys. Rev. Lett. **116**, 243001 (2016). (Cited on page **64**)

[239] P. D. Maker, R. W. Terhune, M. Nisenoff, and C. M. Savage. *Effects of Dispersion and Focusing on the Production of Optical Harmonics*. Phys. Rev. Lett. **8**, 21–22 (1962). (Cited on page **69**)

[240] R. W. Boyd. *Nonlinear Optics*. Elsevier, Third edition (2008). (Cited on page **69**)

[241] D. N. Nikogosyan. *Beta barium borate (BBO)*. Appl. Phys. A **52**, 359–368 (1991). (Cited on pages **69** and **75**)

[242] R. Riedel, J. Rothhardt, K. Beil, B. Gronloh, A. Klenke, H. Höppner, M. Schulz, U. Teubner, C. Kränkel, J. Limpert, A. Tünnermann, M. Prandolini, and F. Tavella. *Thermal properties of borate crystals for high power optical parametric chirped-pulse amplification*. Opt. Express **22**, 17607 (2014). (Cited on pages **69** and **75**)

[243] R. C. Eckardt and R. L. Byer. *Measurement of nonlinear optical coefficients by phase-matched harmonic generation*. In *Inorganic Crystals for Optics, Electro-Optics, and Frequency Conversion*, volume 1561, pages 119–127, San Diego (1991). (Cited on page **69**)

[244] D. J. Armstrong, W. J. Alford, T. D. Raymond, and A. V. Smith. *Absolute measurement of the effective nonlinearities of KTP and BBO crystals by optical parametric amplification*. Appl. Opt. **35**, 2032–2040 (1996). (Cited on page **69**)

[245] A. Friedenauer, F. Markert, H. Schmitz, L. Petersen, S. Kahra, M. Herrmann, T. Udem, T. W. Hänsch, and T. Schätz. *High power all solid state laser system near* 280 *nm*. Appl. Phys. B **84**, 371–373 (2006). (Cited on pages **69** and **75**)

[246] Y. Kaneda, M. Fallahi, J. Hader, J. V. Moloney, S. W. Koch, B. Kunert, and W. Stoltz. *Continuous-wave single-frequency* 295 *nm laser source by a frequency-quadrupled optically pumped semiconductor laser*. Opt. Lett. **34**, 3511–3513 (2009). (Cited on page **69**)

[247] A. C. Wilson, C. Ospelkaus, A. P. VanDevender, J. A. Mlynek, K. R. Brown, D. Leibfried, and D. J. Wineland. *A 750-mW, continuous-wave, solid-state laser source at 313 nm for cooling and manipulating trapped* $^9Be^+$ *ions*. Appl. Phys. B **105**, 741–748 (2011). (Cited on pages **69**, **72**, **75**, and **80**)

[248] Y. Kaneda, J. M. Yarborough, Y. Merzlyak, A. Yamaguchi, K. Hayashida, N. Ohmae, and H. Katori. *Continuous-wave, single-frequency* 229 *nm laser source for laser cooling of cadmium atoms*. Opt. Lett. **41**, 705–708 (2016). (Cited on page **69**)

[249] D. Hanna. *Astigmatic Gaussian beams produced by axially asymmetric laser cavities*. IEEE J. Quantum Electron. **5**, 483–488 (1969). (Cited on page **71**)

[250] G. D. Boyd and D. A. Kleinman. *Parametric Interaction of Focused Gaussian Light Beams*. J. Appl. Phys. **39**, 3597–3639 (1968). (Cited on pages **69** and **153**)

[251] C. S. Adams and A. I. Ferguson. *Frequency doubling of a single frequency Ti:*Al_2O_3 *laser using an external enhancement cavity*. Opt. Commun. **79**, 219–223 (1990). (Cited on pages **69**, **74**, **75**, **151**, and **152**)

[252] Y. F. Chen and Y. C. Chen. *Analytical functions for the optimization of second-*

harmonic generation and parametric generation by focused Gaussian beams. Appl. Phys. B **76**, 645–647 (2003). (Cited on pages **69** and **70**)

[253] A. Ashkin, G. Boyd, and J. Dziedzic. *Resonant optical second harmonic generation and mixing*. IEEE J. Quantum Electron. **2**, 109–124 (1966). (Cited on pages **70** and **151**)

[254] M. M. Fejer, G. A. Magel, D. H. Jundt, and R. L. Byer. *Quasi-phase-matched second harmonic generation: tuning and tolerances*. IEEE J. Quantum Electron. **28**, 2631–2654 (1992). (Cited on page **71**)

[255] L. E. Myers, R. C. Eckardt, M. M. Fejer, R. L. Byer, W. R. Bosenberg, and J. W. Pierce. *Quasi-phase-matched optical parametric oscillators in bulk periodically poled $LiNbO_3$*. J. Opt. Soc. Am. B **12**, 2102–2116 (1995). (Cited on page **71**)

[256] Z. Burkley, C. Rasor, S. F. Cooper, A. D. Brandt, and D. C. Yost. *Yb fiber amplifier at 972.5 nm with frequency quadrupling to 243.1 nm*. Appl. Phys. B **123**, 5 (2017). (Cited on pages **71** and **75**)

[257] H. Kogelnik and T. Li. *Laser Beams and Resonators*. Appl. Opt. **5**, 1550–1567 (1966). (Cited on page **72**)

[258] D. Meschede. *Optik, Licht und Laser*. Vieweg+Teubner, Wiesbaden, Third edition (2008). (Cited on page **72**)

[259] *SNLO nonlinear optics code available from A. V. Smith*. AS-Photonics, Albuquerque, NM (2017). (Cited on page **72**)

[260] E. S. Polzik and H. J. Kimble. *Frequency doubling with $KNbO_3$ in an external cavity*. Opt. Lett. **16**, 1400–1402 (1991). (Cited on pages **73** and **152**)

[261] H. M. Meyer. *A Laser-System for Trapping and Cooling of Ytterbium-Ions*. Diploma Thesis, University of Heidelberg (2010). (Cited on pages **73** and **151**)

[262] T. C. Briles, D. C. Yost, A. Cingöz, J. Ye, and T. R. Schibli. *Simple piezoelectric-actuated mirror with 180 kHz servo bandwidth*. Opt. Express **18**, 9739–9746 (2010). (Cited on page **74**)

[263] A. Steinbach, M. Rauner, F. C. Cruz, and J. C. Bergquist. *CW second harmonic generation with elliptical Gaussian beams*. Opt. Commun. **123**, 207–214 (1996). (Cited on page **75**)

[264] T. Freegarde, J. Coutts, J. Walz, D. Leibfried, and T. W. Hänsch. *General analysis of type I second-harmonic generation with elliptical Gaussian beams*. J. Opt. Soc. Am. B **14**, 2010–2016 (1997). (Cited on page **75**)

[265] R. W. P. Drever, J. L. Hall, F. V. Kowalski, J. Hough, G. M. Ford, A. J. Munley, and H. Ward. *Laser phase and frequency stabilization using an optical resonator*. Appl. Phys. B **31**, 97–105 (1983). (Cited on pages **78** and **80**)

[266] G. H. Smith, D. Novak, and Z. Ahmed. *Overcoming chromatic-dispersion effects in fiber-wireless systems incorporating external modulators*. IEEE Trans. Microwave Theory Tech. **45**, 1410–1415 (1997). (Cited on page **78**)

[267] A. Loayssa, D. Benito, and M. J. Garde. *Single-sideband suppressed-carrier modulation using a single-electrode electrooptic modulator*. IEEE Photonics Technology Letters **13**, 869–871 (2001). (Cited on page **78**)

[268] P. Thoumany, T. Hänsch, G. Stania, L. Urbonas, and T. Becker. *Optical spectroscopy of rubidium Rydberg atoms with a 297 nm frequency-doubled dye laser*. Opt. Lett. **34**, 1621–1623 (2009). (Cited on pages **81** and **83**)

[269] H. G. Dehmelt. *Monoion oscillator as potential ultimate laser frequency standard*. IEEE Trans. Instrum. Meas. **IM-31**, 83–87 (1982). (Cited on page **81**)

[270] W. Nagourney, J. Sandberg, and H. Dehmelt. *Shelved optical electron amplifier: Observation of quantum jumps*. Phys. Rev. Lett. **56**, 2797–2799 (1986). (Cited on page **81**)

[271] J. Wang, J. Bai, J. He, and J. Wang. *Single-photon cesium Rydberg excitation spectroscopy by using of 318.6-nm UV laser and room-temperature cesium vapor cell*. arXiv:1706.06237 (2017). (Cited on pages **83** and **89**)

[272] E. Arimondo, M. Inguscio, and P. Violino. *Experimental determinations of the hyperfine structure in the alkali atoms*. Rev. Mod. Phys. **49**, 31–75 (1977). (Cited on pages **83** and **89**)

[273] J. Pritchard. *Cooperative Optical Non-Linearity in a Blockaded Rydberg Ensemble*. Springer Theses. Springer (2012). (Cited on page **83**)

[274] J. O. Day, E. Brekke, and T. G. Walker. *Dynamics of low-density ultracold Rydberg gases*. Phys. Rev. A **77**, 052712 (2008). (Cited on page **87**)

[275] C. Simonelli, M. Archimi, L. Asteria, D. Capecchi, G. Masella, E. Arimondo, D. Ciampini, and O. Morsch. *De-excitation spectroscopy of strongly interacting Rydberg gases*. arXiv:1707.01382 (2017). (Cited on page **87**)

[276] O. S. Heavens. *Radiative Transition Probabilities of the Lower Excited States of the Alkali Metals*. J. Opt. Soc. Am. **51**, 1058–1061 (1961). (Cited on pages **87** and **90**)

[277] M. Mudrich, N. Zahzam, T. Vogt, D. Comparat, and P. Pillet. *Back and Forth Transfer and Coherent Coupling in a Cold Rydberg Dipole Gas*. Phys. Rev. Lett. **95**, 233002 (2005). (Cited on pages **87** and **88**)

[278] T. E. Lee, H. Häffner, and M. C. Cross. *Antiferromagnetic phase transition in a nonequilibrium lattice of Rydberg atoms*. Phys. Rev. A **84** (2011). (Cited on pages **87** and **140**)

[279] A. W. Glaetzle, R. Nath, B. Zhao, G. Pupillo, and P. Zoller. *Driven-dissipative dynamics of a strongly interacting Rydberg gas*. Phys. Rev. A **86** (2012). (Cited on page **87**)

[280] I. Lesanovsky and J. P. Garrahan. *Kinetic Constraints, Hierarchical Relaxation, and Onset of Glassiness in Strongly Interacting and Dissipative Rydberg Gases*. Phys. Rev. Lett. **111** (2013). (Cited on page **87**)

[281] M. Hoening, W. Abdussalam, M. Fleischhauer, and T. Pohl. *Antiferromagnetic long-range order in dissipative Rydberg lattices*. Phys. Rev. A **90** (2014). (Cited on pages **87** and **140**)

[282] B. Olmos, I. Lesanovsky, and J. P. Garrahan. *Out-of-equilibrium evolution of kinetically constrained many-body quantum systems under purely dissipative dynamics*. Phys. Rev. E **90** (2014). (Cited on page **87**)

[283] H. Weimer. *Variational Principle for Steady States of Dissipative Quantum Many-Body Systems*. Phys. Rev. Lett. **114** (2015). (Cited on page **87**)

[284] M. Marcuzzi, E. Levi, W. Li, J. P. Garrahan, B. Olmos, and I. Lesanovsky. *Non-equilibrium universality in the dynamics of dissipative cold atomic gases*. New J. Phys. **17**, 072003 (2015). (Cited on pages **87** and **140**)

[285] R. Gutiérrez, J. P. Garrahan, and I. Lesanovsky. *Self-similar nonequilibrium dynamics of a many-body system with power-law interactions*. Phys. Rev. E **92**, 062144 (2015). (Cited on pages **87** and **88**)

[286] R. Gutiérrez, C. Simonelli, M. Archimi, F. Castellucci, E. Arimondo, D. Ciampini, M. Marcuzzi, I. Lesanovsky, and O. Morsch. *Experimental signatures of an absorbing-state phase transition in an open driven many-body quantum system*. arXiv:1611.03288 (2016). (Cited on page **88**)

[287] W.-K. Lee, H. S. Moon, and H. S. Suh. *Measurement of the absolute energy level and hyperfine structure of the ^{87}Rb $4D_{5/2}$ state*. Opt. Lett. **32**, 2810–2812 (2007). (Cited on pages **89** and **90**)

[288] H. S. Moon, W.-K. Lee, and H. S. Suh. *Hyperfine-structure-constant determination and absolute-frequency measurement of the Rb $4D_{3/2}$ state*. Phys. Rev. A **79**, 062503 (2009). (Cited on pages **89** and **90**)

[289] J. Wang, H. Liu, G. Yang, B. Yang, and J. Wang. *Determination of the hyperfine structure constants of the ^{87}Rb and ^{85}Rb $4D_{5/2}$ state and the isotope hyperfine anomaly*. Phys. Rev. A **90**, 052505 (2014). (Cited on pages **89** and **90**)

[290] H. S. Moon, L. Lee, and J. B. Kim. *Double-resonance optical pumping of Rb atoms*. J. Opt. Soc. Am. B **24**, 2157–2164 (2007). (Cited on page **89**)

[291] M. Gärttner, K. P. Heeg, T. Gasenzer, and J. Evers. *Finite-size effects in strongly interacting Rydberg gases*. Phys. Rev. A **86**, 033422 (2012). (Cited on pages **91** and **140**)

[292] B. Vermersch, M. Punk, A. W. Glaetzle, C. Gross, and P. Zoller. *Dynamical preparation of laser-excited anisotropic Rydberg crystals in 2D optical lattices*. New J. Phys. **17**, 013008 (2015). (Cited on pages **93** and **140**)

[293] M. Boninsegni and N. V. Prokof'ev. *Colloquium: Supersolids: What and where are they?* Rev. Mod. Phys. **84**, 759–776 (2012). (Cited on pages **95** and **141**)

[294] F. Cinti, P. Jain, M. Boninsegni, A. Micheli, P. Zoller, and G. Pupillo. *Supersolid Droplet Crystal in a Dipole-Blockaded Gas*. Phys. Rev. Lett. **105** (2010). (Cited on pages **95** and **141**)

[295] J. A. Aman, B. J. DeSalvo, F. B. Dunning, T. C. Killian, S. Yoshida, and J. Burgdörfer. *Trap losses induced by near-resonant Rydberg dressing of cold atomic gases*. Phys. Rev. A **93**, 043425 (2016). (Cited on pages **96** and **119**)

[296] E. Ising. *Beitrag zur Theorie des Ferromagnetismus*. Z. Physik **31**, 253–258 (1925). (Cited on page **96**)

[297] K. G. Wilson. *The renormalization group: Critical phenomena and the Kondo problem*. Rev. Mod. Phys. **47**, 773–840 (1975). (Cited on page **96**)

[298] L. Onsager. *Crystal Statistics. I. A Two-Dimensional Model with an Order-Disorder Transition*. Phys. Rev. **65**, 117–149 (1944). (Cited on page **96**)

[299] R. J. Glauber. *Time-Dependent Statistics of the Ising Model*. Journal of Mathematical Physics **4**, 294–307 (1963). (Cited on page **96**)

[300] W. Selke. *The ANNNI model – Theoretical analysis and experimental application*. Physics Reports **170**, 213–264 (1988). (Cited on page **96**)

[301] P. Bak and R. Bruinsma. *One-Dimensional Ising Model and the Complete Devil's Staircase*. Phys. Rev. Lett. **49**, 249–251 (1982). (Cited on pages **96** and **140**)

[302] S. Lloyd. *Universal Quantum Simulators*. Science **273**, 1073–1078 (1996). (Cited on page **97**)

[303] A. de Paz, A. Sharma, A. Chotia, E. Maréchal, J. H. Huckans, P. Pedri, L. Santos, O. Gorceix, L. Vernac, and B. Laburthe-Tolra. *Nonequilibrium Quantum Magnetism in a Dipolar Lattice Gas*. Phys. Rev. Lett. **111**, 185305 (2013). (Cited on page **97**)

[304] S. Sachdev. *Quantum Phase Transitions*. Cambridge University Press, Cambridge, second edition (2011). (Cited on page **99**)

[305] R. Mukherjee, T. C. Killian, and K. R. A. Hazzard. *Accessing Rydberg-dressed interactions using many-body Ramsey dynamics*. Phys. Rev. A **94**, 053422 (2016). (Cited on page **102**)

[306] M. Foss-Feig, K. R. A. Hazzard, J. J. Bollinger, and A. M. Rey. *Nonequilibrium dynamics of arbitrary-range Ising models with decoherence: An exact analytic solution*. Phys. Rev. A **87**, 042101 (2013). (Cited on pages **108**, **133**, and **136**)

[307] M. van den Worm, B. C. Sawyer, J. J. Bollinger, and M. Kastner. *Relaxation Timescales and Decay of Correlations in a Long-Range Interacting Quantum Simulator*. New J. Phys. **15**, 083007 (2013). (Cited on page **108**)

[308] J. Honer. *Collective Many-Body Interaction in Rydberg Dressed Atoms*. Phys. Rev. Lett. **105** (2010). (Cited on page **110**)

[309] B. Paredes, T. Keilmann, and J. I. Cirac. *Pfaffian-like Ground State for Three-Body Hard-Core Bosons in One-Dimensional Lattices*. Phys. Rev. A **75**, 053611 (2007). (Cited on page **111**)

[310] B. Capogrosso-Sansone, S. Wessel, H. P. Büchler, P. Zoller, and G. Pupillo. *Phase diagram of one-dimensional hard-core bosons with three-body interactions*. Phys. Rev. B **79**, 020503 (2009). (Cited on page **111**)

[311] T. Boulier, E. Magnan, C. Bracamontes, J. Maslek, E. A. Goldschmidt, J. T. Young, A. V. Gorshkov, S. L. Rolston, and J. V. Porto. *Spontaneous avalanche dephasing in large Rydberg ensembles*. arXiv:1709.02460 (2017). (Cited on pages **115**, **119**, and **159**)

[312] T. Amthor, C. Giese, C. S. Hofmann, and M. Weidemüller. *Evidence of Antiblockade in an Ultracold Rydberg Gas*. Phys. Rev. Lett. **104**, 013001 (2010). (Cited on page **116**)

[313] F. Letscher, O. Thomas, T. Niederprüm, M. Fleischhauer, and H. Ott. *Bistability Versus Metastability in Driven Dissipative Rydberg Gases*. Phys. Rev. X **7**, 021020 (2017). (Cited on page **116**)

[314] D. Comparat and P. Pillet. *Dipole blockade in a cold Rydberg atomic sample [Invited]*. J. Opt. Soc. Am. B **27**, A208–A232 (2010). (Cited on page **117**)

[315] J. B. Balewski, A. T. Krupp, A. Gaj, D. Peter, H. P. Büchler, R. Löw, S. Hofferberth, and T. Pfau. *Coupling a single electron to a Bose-Einstein condensate*. Nature **502**, 664–667 (2013). (Cited on page **117**)

[316] T. Keating, C. H. Baldwin, Y.-Y. Jau, J. Lee, G. W. Biedermann, and I. H. Deutsch. *Arbitrary Dicke-State Control of Symmetric Rydberg Ensembles*. Phys. Rev. Lett. **117**, 213601 (2016). (Cited on page **117**)

[317] F. Letscher, O. Thomas, T. Niederprüm, H. Ott, and M. Fleischhauer. *Anomalous excitation facilitation in inhomogeneously broadened Rydberg gases*. Phys. Rev. A **95**, 023410 (2017). (Cited on page **118**)

[318] F. Machado, G. D. Meyer, D. V. Else, C. Nayak, and N. Y. Yao. *Exponentially Slow Heating in Short and Long-range Interacting Floquet Systems*. arXiv:1708.01620 (2017). (Cited on page **119**)

[319] P. Bocchieri and A. Loinger. *Quantum Recurrence Theorem*. Phys. Rev. **107**, 337–338 (1957). (Cited on page **122**)

[320] H. Poincaré. *Sur le problème des trois corps et les équations de la dynamique*. Acta Math. 13 pages 1–270 (1890). (Cited on page **122**)

[321] E. Zermelo. *Ueber einen Satz der Dynamik und die mechanische Wärmetheorie*. Ann. Phys. **293**, 485–494 (1896). (Cited on page **122**)

[322] J. v. Neumann. *Beweis des Ergodensatzes und des H-Theorems in der neuen Mechanik*. Z. Physik **57**, 30–70 (1929). (Cited on page **122**)

[323] D. T. Haar. *Foundations of Statistical Mechanics*. Rev. Mod. Phys. **27**, 289–338 (1955). (Cited on page **122**)

[324] M. Rigol, V. Dunjko, and M. Olshanii. *Thermalization and its mechanism for generic isolated quantum systems*. Nature **452**, 854–858 (2008). (Cited on page **122**)

[325] C. Gogolin and J. Eisert. *Equilibration, thermalisation, and the emergence of statistical mechanics in closed quantum systems*. Rep. Prog. Phys. **79**, 056001 (2016). (Cited on page **122**)

[326] W. H. Zurek. *Decoherence and the Transition from Quantum to Classical*. Phys. Today (1991). (Cited on page **122**)

[327] L. F. Santos, A. Polkovnikov, and M. Rigol. *Weak and strong typicality in quantum systems*. Phys. Rev. E **86**, 010102 (2012). (Cited on page **122**)

[328] J. M. Deutsch, H. Li, and A. Sharma. *Microscopic origin of thermodynamic entropy in isolated systems*. Phys. Rev. E **87**, 042135 (2013). (Cited on page **122**)

[329] G. Kirchmair, B. Vlastakis, Z. Leghtas, S. E. Nigg, H. Paik, E. Ginossar, M. Mirrahimi, L. Frunzio, S. M. Girvin, and R. J. Schoelkopf. *Observation of quantum state collapse and revival due to the single-photon Kerr effect*. Nature **495**, 205–209 (2013). (Cited on page **122**)

[330] G. Rempe, H. Walther, and N. Klein. *Observation of quantum collapse and revival in a one-atom maser*. Phys. Rev. Lett. **58**, 353–356 (1987). (Cited on page **122**)

[331] M. Brune, F. Schmidt-Kaler, A. Maali, J. Dreyer, E. Hagley, J. M. Raimond, and S. Haroche. *Quantum Rabi Oscillation: A Direct Test of Field Quantization in a Cavity*. Phys. Rev. Lett. **76**, 1800–1803 (1996). (Cited on pages **122** and **123**)

[332] D. M. Meekhof, C. Monroe, B. E. King, W. M. Itano, and D. J. Wineland. *Generation of Nonclassical Motional States of a Trapped Atom*. Phys. Rev. Lett. **76**, 1796–1799 (1996). (Cited on page **123**)

[333] S. Will, T. Best, U. Schneider, L. Hackermüller, D.-S. Lühmann, and I. Bloch. *Time-resolved observation of coherent multi-body interactions in quantum phase revivals*. Nature **465**, 197–201 (2010). (Cited on page **123**)

[334] J. M. Radcliffe. *Some Properties of Coherent Spin States*. J. Phys. A: Gen. Phys. **4**, 313 (1971). (Cited on page **126**)

[335] P. Walther, K. J. Resch, T. Rudolph, E. Schenck, H. Weinfurter, V. Vedral, M. Aspelmeyer, and A. Zeilinger. *Experimental one-way quantum computing*. Nature **434**, 169–176 (2005). (Cited on page **128**)

[336] F. Meinert, M. J. Mark, E. Kirilov, K. Lauber, P. Weinmann, A. J. Daley, and H.-C. Nägerl. *Quantum Quench in an Atomic One-Dimensional Ising Chain*. Phys. Rev. Lett. **111**, 053003 (2013). (Cited on page **134**)

[337] P. Jurcevic, H. Shen, P. Hauke, C. Maier, T. Brydges, C. Hempel, B. Lanyon, M. Heyl, R. Blatt, and C. Roos. *Direct Observation of Dynamical Quantum Phase Transitions in an Interacting Many-Body System*. Phys. Rev. Lett. **119**, 080501 (2017). (Cited on page **134**)

[338] P. Calabrese and J. Cardy. *Time Dependence of Correlation Functions Following a Quantum Quench*. Phys. Rev. Lett. **96**, 136801 (2006). (Cited on pages **134**, **137**, and **140**)

[339] P. Calabrese, F. H. L. Essler, and M. Fagotti. *Quantum Quench in the Transverse-Field Ising Chain*. Phys. Rev. Lett. **106**, 227203 (2011). (Cited on pages **134**, **137**, and **140**)

[340] E. H. Lieb and D. W. Robinson. *The finite group velocity of quantum spin systems*. Commun. Math. Phys. **28**, 251–257 (1972). (Cited on page **134**)

[341] J. J. Bollinger, W. M. Itano, D. J. Wineland, and D. J. Heinzen. *Optimal frequency measurements with maximally correlated states*. Physical Review A **54**, R4649 (1996). (Cited on page **135**)

[342] C. C. Gerry and J. Mimih. *The parity operator in quantum optical metrology*. Contemporary Physics **51**, 497–511 (2010). (Cited on page **135**)

[343] G. Breitenbach, S. Schiller, and J. Mlynek. *Measurement of the quantum states of squeezed light*. Nature **387**, 471–475 (1997). (Cited on page **137**)

[344] T. Macrì, A. Smerzi, and L. Pezzè. *Loschmidt echo for quantum metrology*. Phys. Rev. A **94** (2016). (Cited on pages **137** and **141**)

[345] A. W. Glaetzle, K. Ender, D. S. Wild, S. Choi, H. Pichler, M. D. Lukin, and P. Zoller. *Quantum Spin Lenses in Atomic Arrays*. Phys. Rev. X **7**, 031049 (2017). (Cited on page **140**)

[346] V. R. Overbeck, M. F. Maghrebi, A. V. Gorshkov, and H. Weimer. *Multicritical behavior in dissipative Ising models*. Phys. Rev. A **95**, 042133 (2017). (Cited on page **140**)

[347] H. Hinrichsen. *Non-equilibrium critical phenomena and phase transitions into absorbing states*. Adv. Phys. **49**, 815–958 (2000). (Cited on page **140**)

[348] E. Sela, M. Punk, and M. Garst. *Dislocation-mediated melting of one-dimensional Rydberg crystals*. Phys. Rev. B **84**, 085434 (2011). (Cited on page **140**)

[349] K. Mølmer and A. Sørensen. *Multiparticle Entanglement of Hot Trapped Ions*. Phys. Rev. Lett. **82**, 1835–1838 (1999). (Cited on page **141**)

[350] R. Raussendorf and H. J. Briegel. *A One-Way Quantum Computer*. Phys. Rev. Lett. **86**, 5188–5191 (2001). (Cited on page **141**)

[351] O. Mandel, M. Greiner, A. Widera, T. Rom, T. W. Hänsch, and I. Bloch. *Controlled*

collisions for multi-particle entanglement of optically trapped atoms. Nature **425**, 937–940 (2003). (Cited on page **141**)

[352] W. Lechner, P. Hauke, and P. Zoller. *A quantum annealing architecture with all-to-all connectivity from local interactions*. Science Advances **1**, e1500838 (2015). (Cited on page **141**)

[353] N. Henkel, F. Cinti, P. Jain, G. Pupillo, and T. Pohl. *Supersolid Vortex Crystals in Rydberg-Dressed Bose-Einstein Condensates*. Phys. Rev. Lett. **108** (2012). (Cited on page **141**)

[354] H. P. Büchler, E. Demler, M. Lukin, A. Micheli, N. Prokof'ev, G. Pupillo, and P. Zoller. *Strongly Correlated 2D Quantum Phases with Cold Polar Molecules: Controlling the Shape of the Interaction Potential*. Phys. Rev. Lett. **98**, 060404 (2007). (Cited on page **142**)

[355] O. N. Osychenko, G. E. Astrakharchik, Y. Lutsyshyn, Y. E. Lozovik, and J. Boronat. *Phase diagram of Rydberg atoms with repulsive van der Waals interaction*. Phys. Rev. A **84**, 063621 (2011). (Cited on page **142**)

[356] F. Cinti, T. Macrì, W. Lechner, G. Pupillo, and T. Pohl. *Defect-induced supersolidity with soft-core bosons*. Nat. Commun. **5**, 4235 (2014). (Cited on page **142**)

[357] K. Góral, L. Santos, and M. Lewenstein. *Quantum Phases of Dipolar Bosons in Optical Lattices*. Phys. Rev. Lett. **88**, 170406 (2002). (Cited on page **142**)

[358] E. G. Dalla Torre, E. Berg, and E. Altman. *Hidden Order in 1D Bose Insulators*. Phys. Rev. Lett. **97** (2006). (Cited on page **142**)

[359] E. Berg, E. G. Dalla Torre, T. Giamarchi, and E. Altman. *Rise and fall of hidden string order of lattice bosons*. Phys. Rev. B **77**, 245119 (2008). (Cited on page **142**)

[360] J. S. Kim and B. C. Sanders. *Generalized W-Class State and Its Monogamy Relation*. J. Phys. A: Math. Theor. **41**, 495301 (2008). (Cited on page **149**)

[361] F. Seeßelberg. *A Dye Laser System for NaK-Photoassociation Spectroscopy*. Master's Thesis, Ludwig-Maximilians-Universität München (2014). (Cited on page **151**)

[362] P. Langer. *Aufbau eines Lasersystems bei 297 nm zur Einphotonenanregung von Rydbergzuständen in Rubidium*. Diploma Thesis, Technische Universität Kaiserslautern (2012). (Cited on page **151**)

[363] W. J. Kozlovsky, C. D. Nabors, and R. L. Byer. *Second-harmonic generation of a continuous-wave diode-pumped Nd:YAG laser using an externally resonant cavity*. Opt. Lett. **12**, 1014–1016 (1987). (Cited on page **152**)

[364] E. Hecht. *Optics*. Addison-Wesley, San Francisco, Fourth international edition (2002). (Cited on page **152**)

Danksagung

Ich möchte die Gelegenheit hier nutzen, um all jenen Danke zu sagen, die zum erfolgreichen Abschließen meiner Arbeit beigetragen haben. Ich hatte eine wunderbare Zeit in der Gruppe und am MPQ und habe den Entschluss, hier zu arbeiten, nie bereut.

Besonderer Dank gilt Prof. Immanuel Bloch für die Betreuung meiner Doktorarbeit und seine Unterstützung. Seine spürbare Begeisterung für so viele Facetten der Physik und seine motivierende Art waren und sind eine große Inspiration für mich. Auch die Diskussionen über Physik und darüber hinaus beim "Sunday long run" waren immer wieder Quelle für neue Ideen und Ansporn zum Nachdenken. Zudem möchte ich mich für die exzellenten Arbeitsbedingungen in der Gruppe bedanken. Sie sind sicher keine Selbstverständlichkeit und man vergisst allzu leicht, sie entsprechend zu schätzen.

Herzlich bedanken möchte ich mich auch bei Christian Groß, der uns am Single-Atoms Experiment betreut hat. Von seinem Pragmatismus, seiner Art und Weise über Physik nachzudenken, den vielen kreativen Ideen und insbesondere unseren vielen Diskussionen konnte ich unglaublich viel lernen und ich bin sehr dankbar dafür.

Natürlich will ich auch allen Kollegen und Freunden vom Single-Atoms Experiment danken. Ich denke, dass das gute Miteinander essentiell für den Erfolg des Experiments war und ist. Insbesondere danke ich Peter Schauß, der mir zu Beginn meiner Arbeit unglaublich viel über das Experiment, Rydberg Atome und Laser beigebracht hat. Auch Sebastian Hild, für die Freundschaft, die gute Zusammenarbeit am Experiment und seine kollegiale Art. Ich erinnere mich auch gerne an die Unternehmungen abseits der Arbeit im Labor, zum Beispiel unsere Skifahr-Ausflüge, diverse Wanderungen und Radtouren. Vielen Dank den Post-Docs Takeshi Fukuhara, Jae-yoon Choi und Tarik Yefsah, mit denen ich während meiner Zeit am Experiment zusammenarbeiten durfte und von deren Erfahrung ich einiges lernen konnte. Bei den beiden neuen Doktoranden Antonio Rubio Abadal und Simon Hollerith möchte ich mich besonders für die vielen Fragen bedanken, durch die man auch nach einigen Jahren am Experiment immer noch so viel Neues lernen kann, sowie das gründliche Korrekturlesen meiner Arbeit. Vielen Dank auch dem ehemaligen Single-Atoms Team um Stefan Kuhr, Christof Weitenberg, Manuel Endres, Marc Cheneau und Jacob Sherson für das tolle Experiment, das sicher noch viele wunderbare Ergebnisse hervorbringen wird.

Bei Prof. Thomas Pohl möchte ich mich für seine tolle Hilfe bei den Rydberg dressing Projekten bedanken und seine Bereitschaft, für meine Doktorprüfung extra den weiten Weg aus Aarhus auf sich zu nehmen. Danke auch an Rick van Bijnen für seine Experiment-orientierte theoretische Hilfe, die unzählig vielen Skype-Meetings zu jeder Zeit und das ein oder andere leidenschaftlich umkämpfte Tischkicker Spiel. Den Theoretikern aus der Gruppe von Peter Zoller in Innsbruck vielen Dank für die vielen Diskussionen, besonders Alex Glätzle, von dem wir sehr viel über Rydberg dressing lernen durften. Für die Zusammenarbeit beim Superatom-Projekt möchte ich Tommaso Macrì danken.

Dem aktuellen und ehemaligen Lithium-Team Ahmed Omran, Martin Boll, Timon Hilker, Guillaume Salomon, Joannis Koepsell, Jayadev Vijayan, Katharina Kleinlein, Thomas Gantner und Michael Lohse danke ich für viele interessante Diskussionen über Physik und die willkommene Abwechslung beim Keller- oder Gruppenraum-Aufräumen nach dem Mittagessen.

Den Teams vom Molekül-, Strontium- und Potassium-Experiment am MPQ für den unkomplizierten Austausch von Ideen und Laborutensilien. Besonderer Dank gilt Nikolaus Lorenz und Lorenzo Festa fürs Korrekturlesen meiner Arbeit.

Ich danke allen nicht-wissenschaftlichen Mitarbeitern am MPQ in und außerhalb der Arbeitsgruppe, insbesondere Anton Mayer für das Design der SHG-cavity und das Einbringen seiner Erfahrung bei deren Planung sowie Olivia Mödl für ihre Hilfe mit vielen kleinen elektronischen Helferlein. Danke auch an Karsten Förster, der mich zu Beginn meiner Werkstudentenzeit in der Gruppe beim Zusammenlöten verschiedenster Schaltungen betreut und jede Frage geduldig beantwortet hat. Unsren aktuellen und ehemaligen Sekretärinnen Kristina Schuldt, Doreen Seidl und Marianne Kargl am MPQ sowie Ildiko Kecskesi an der LMU, die uns die Konzentration auf die Wissenschaft ermöglichen und ohne deren Engagement sicher keine Veranstaltung in der Gruppe so reibungslos funktioniert hätte.

Dem Munich Mountaineering Team danke ich für die vielen spannenden Unternehmungen in den Bergen zum Ausgleich am Wochenende.

Zu guter Letzt möchte ich meiner Familie und besonders meinen Eltern Verena und Martin danken, die mich auch während für sie nicht so leichten Zeiten immer unterstützt haben, sowie Johanna für einfach alles. Danke, dass es Dich gibt.